Caractérisations isotopiques des voies de formation du nitrate atmosphérique et de la photochimie du nitrate dans la neige

Tesfaye Berhanu

UNIVERSITÉ DE GRENOBLE

THÈSE

Pour obtenir le grade de

DOCTEUR DE L'UNIVERSITÉ DE GRENOBLE
Spécialité : **Science de la Terre, de l'Univers et de l'Environnement**
(Arrêté ministériel du 7 août 2006)

Présentée par

TESFAYE AYALNEH BERHANU

Thèse dirigée par **Joël SAVARINO**

Thèse préparée au sein du **Laboratoire de Glaciologie et de Géophysique de l'Environnement (LGGE)** dans **l'École Doctorale Terre, Univers, Environnement** financée par une bourse **Marie Curie**

An isotopic approach towards understanding nitrate formation pathways and revealing the photochemistry of nitrate in snow

Thèse soutenue publiquement le **4 Septembre 2013,**
devant le jury compose de :

M. Thomas BLUNIER
Professeur à l'Université de Copenhague, Rapporteur
M. Christian GEORGE
Directeur de Recherche à l'Université Claude Bernard, Rapporteur
M. Christof JANSSEN
Chargé de Recherche à l' Université Pierre et Marie Curie, Examinateur
M. Didier VOISIN
Maitre de Conférence à l' Université Joseph Fourier-Grenoble 1, Examinateur
M. Catherine CHAUVEL
Directeur de Recherche à l'Université de Grenoble, Examinateur
M. Joël SAVARINO
Chargé de Recherche à l'Université de Grenoble, Directeur de thèse

Résumé

Le nitrate, produit de la fin de chaîne de réaction des oxydes d'azotes de l'atmosphère (NO_x = NO +NO_2), est l'un des ions le plus abondant de la neige et de la glace polaire. Ses rapports isotopiques stables ($\delta^{18}O$, $\delta^{15}N$ et $\Delta^{17}O$) ont été abondamment utilisés pour contraindre ses sources et les chemins réactionnels. De plus, le nitrate archivé dans les carottes de glace profondes peut apporter de nouvelles contraintes sur les conditions climatiques passées. Cependant, le dépôt de nitrate dans les régions polaires à faible accumulation est réversible en raison des processus post-dépôts, compliquant l'interprétation des enregistrements. Actuellement, il existe des enregistrements de nitrate issus de carottes de glace profonds couvrant de l'information climatique sur plusieurs milliers d'années dont leur interprétation dépend d'une quantification précise ces phénomènes post-dépôts.

Nous avons étudié expérimentalement le transfert d'excès-^{17}O de l'ozone durant la réaction en phase gaz de $NO_2 + O_3 \rightarrow NO_3 + O_2$, qui est une réaction importante de la chimie nocturne de formation du nitrate. De cette étude nous avons déterminé la fonction de transfert du $\Delta^{17}O$ donnée par : $\Delta^{17}O(O_3^*) = (1.23 \pm 0.19) \times \Delta^{17}O(O_3)_{bulk} + (9.02 \pm 0.99)$. Nous avons aussi évalué la distribution intramoléculaire des isotopes de l'oxygène de l'ozone et observé que l'excès d'enrichissement résidait de manière prépondérante sur les atomes terminaux de l'ozone. Ces résultats auront une implication importante sur la compréhension de la formation du nitrate via les mécanismes d'oxydation des précurseurs NOx.

L'impact de la photolyse sur les concentrations et les compositions isotopiques stables du nitrate est étudié dans ce travail de thèse sur la base d'étude de laboratoire et de terrain. Une étude de laboratoire a été conduite en irradiant de la neige naturelle de Dôme C avec une lampe UV à xénon et en utilisant différents filtres UV (280 nm, 305 nm et 320 nm). Sur la base des mesures des rapports isotopiques de l'oxygène et de l'azote, la dépendance aux longueurs d'onde des fractionnements isotopiques a été déterminée. En conséquence, en présence de lumière UV de haute énergie, le fractionnement isotopique est décalé vers des valeurs moins négatives et vice versa.

Sur la base des fractionnements isotopiques obtenus en laboratoire, nous avons dérivé un décalage apparent de la valeur du zéro point d'énergie (ZPE) qui apporte une meilleure contrainte sur la section efficace d'absorption du $^{15}NO_3^-$. Ce décalage apparent est obtenu en minimisant les écarts entre les observations et les fractionnements isotopiques calculés basés sur un modèle de décalage ZPE, modèle qui inclut outre le décalage ZPE, le changement des largeurs, de l'asymétrie et de l'amplitude des sections efficaces d'absorption lors de la substitution isotopique.

Nous avons validé le nouveau ZPE apparent en conduisant une étude de terrain à Dôme C, Antarctique. Dans cette étude, un dispositif expérimental a été construit sur le site et l'effet du rayonnement solaire UV sur la photolyse du nitrate de la neige investigué. Cette étude était basée sur la comparaison de deux puits remplis par de la neige soufflée homogénéisée dont l'un des deux puits n'était pas soumis aux rayonnements UV. Le fractionnement isotopique de 15N pour la neige exposée aux UV (-67.9 ± 12 ‰) est en bon accord avec le modèle de décalage ZPE estimé au cours de ce travail de thèse (-55.4 ‰). Ces valeurs sont aussi dans la gamme des fractionnements isotopiques apparents observée précédemment au Dôme C. Des calculs plus poussés pour mieux contraindre la section efficace d'absorption de $^{15}NO_3^-$ avec le décalage ZPE est en cours et nous proposons que la nouvelle valeur apparente dérivée du décalage ZPE devra être utilisée dans les études à venir. Nous pensons

que l'inclusion des ces nouvelles connaissances dans un modèle prédisant l'enrichissement du ^{15}N dans les carottes de glace permettra une interprétation quantitative de l'information préservée dans la glace.

***Mots clés*: Isotopes stables, le nitrate dans la neige, la photolyse, fractionnement isotopique**

Abstract

Nitrate, the end product of oxidation of atmospheric NO_X (= NO + NO_2), is one of the most abundant anions present in polar snow and ice. Its stable isotope ratios ($\delta^{18}O$, $\delta^{15}N$ and $\Delta^{17}O$) have been widely used to constrain its sources and oxidation pathways. In addition, the nitrate archived in deep ice cores may be an important metric to constrain past climate. However, deposition of nitrate in polar regions with low snow accumulation is reversible due to post-depositional processes, and interpretation of this record is complicated. Currently, there exist deep ice core records of nitrate encompassing climatic information of millennial time scales, and their interpretation relies on careful quantification of post-depositional effects.

We have studied the ^{17}O-excess transfer from ozone during the gas phase $NO_2 + O_3 \rightarrow NO_3 + O_2$ reaction with laboratory experiment. This reaction is an important nighttime nitrate formation pathway. From this study, we have determined the $\Delta^{17}O$ transfer function given by: $\Delta^{17}O(O_3^*) = (1.23 \pm 0.19) \times \Delta^{17}O(O_3)_{bulk} + (9.02 \pm 0.99)$. We have also evaluated the intramolecular oxygen isotope distribution of ozone and have observed that excess enrichment resides predominantly on the terminal oxygen atoms of ozone. The findings from this study have important implications for understanding nitrate formation via different NO_X oxidation mechanisms.

The impact of photolysis on the amount and stable isotope enrichments of nitrate is investigated in this thesis based on laboratory and field experiments. A laboratory study was conducted by irradiating natural snow from Dome C with a Xe UV lamp and a selection of UV-filters (280 nm, 305 nm and 320 nm). Wavelength dependent isotopic fractionations were determined based on the oxygen and nitrogen isotope ratio measurements. Accordingly, in the presence of high-energy UV light, isotopic fractionation is shifted towards less negative values and the reverse for lower energy UV photons.

Based the isotopic fractionations obtained in the laboratory study, we derived an apparent ZPE-shift value, which better constrains the absorption cross-section of $^{15}NO_3^-$. This apparent shift is derived from the best fit between the experimental observations and calculated fractionations based on the existing ZPE-shift model, and it includes actual ZPE-shift and changes in width, asymmetry and amplitude in absorption cross-section arising from isotopic substitution.

We have validated the newly derived apparent ZPE-shift model by conducting a field study at Dome C, Antarctica. In this study, an experimental setup was built on-site and the effect of solar UV photolysis on snow nitrate was investigated. This study was based on a comparison of two snow pits filled with locally drifted snow and by allowing/blocking the solar UV. The ^{15}N fractionation for the UV exposed samples (-67.9 ± 12 ‰) was in fairly good agreement with the ZPE-shift model estimate from this study (-55.4 ‰). These values are also within the range of the apparent isotopic fractionation observed at Dome C in previous studies. Further calculations to better constrain the absorption cross-section of $^{15}NO_3^-$ with the ZPE-shift are underway, and we propose that the newly derived apparent ZPE-shift value should be used in future studies. We believe that incorporating these new findings in models predicting the enrichments of ^{15}N nitrate in ice cores will allow a quantitative interpretation of the information preserved in ice.

***Key words*: Stable isotopes, nitrate in snow, photolysis, isotopic fractionation**

Acknowledgements

First, I would like to thank Thomas Blunier and Christian George for accepting to evaluate this manuscript, as well as Christof Janssen, Didier Voisin and Catherine Chauvel for being part of the jury.

The success of this PhD study would not have been possible without the active participation and strong support of many people. Foremost, I would like express my sincere gratitude to my Supervisor, Joel Savarino, for the continuous support of my PhD study and research, for his patience, motivation, enthusiasm, and immense knowledge. His guidance helped me in all time during my research and thesis writing. Matthew Johnson has been a supportive and encouraging co-supervisor during my PhD and exchange study at his lab. He has also dedicated his time proof reading this dissertation and provided insightful feedbacks. I would like to thank also his team in Copenhagen (CCAR) who were most welcoming and made my exchange study very interesting. My sincere thanks to Joseph Erbland, a good friend, colleague and mentor, and was always available for discussions. He provided fruitful comments and ideas for this thesis and he has been actively involved in method development, sample analysis and data interpretation and I thank him sincerely. I thank S.K. Bhattacharya for his significant contribution both in the laboratory and in advising on the experimental work described in chapter 2. I am very grateful to Carl Meusinger, a good friend and colleague, who has been actively providing constructive comments and inputs during our collaboration works (described in chapter 3). I owe many thanks to my officemate and close friend, William Vicars, for providing insightful comments and proof reading this manuscript. It is my pleasure to thank Remy Jost who has provided constructive feedbacks and participated on the theoretical calculations. I would like to thank Samuel Morin for his supportive advice. I would like to offer my special thanks to Markus Frey for providing field data and insightful comments. I would like to thank Erwan Vince (LTHE) who was always on time preparing the bacterial cultures for isotopic analysis graciously. I would like to express my gratitude to Sussane Preunkert and Bruno Jordan for helping to analyse snow samples, and Ghislan Picard and Quentin Libois for providing solar irradiance data from Dome C, Antarctica. It was also a pleasure to work with Samo Tamse and Dimitri Osmont who were visiting students at LGGE who helped in sample analysis and conducting experiments, and I thank them sincerely. I am also indebt to Florent Dominé, Laurent Arnaud and Manuel Barret for their contribution in setting up the photolysis experiment in the lab and providing constructive comments.

I would like to address my gratitude to the IPEV staff and different people who made my stay interesting and successful during my fieldwork at Dome C in summer 2011/12. I would like to thank Sebastian Aubin and all the 2011/12 winter over personnel at Dome C for their support on field sampling and analysis.

The research leading to these results has received funding from the European Community's Seventh Framework Programme (FP7/2007-2013) under the grant agreement number 237890. We would like to thank INSU through its LEFE program for its financial support for lab experiments. The Agence nationale de la recherche (ANR) is gratefully acknowledged for its financial support through the OPALE project (contract NT09-451281). Access to the Dome C site was possible with the financial support of the Institut Polaire Française Paul Emile Victor (IPEV) through the program 1011 (SUNITEDC).

Last but not least, I would like to express my deepest gratitude to all of the members of Initial Training in Mass Independent Fractionation (INTRAMIF) network

for their input during this PhD study and collaboration on the isotopic measurements conducted while developing a reference material.

Table of contents

Chapter 5: Conclusion and outlook

Bibliography

Annex A: Preparation of a reference material for oxygen isotopes measurement

Annex B: ^{17}O-excess transfer during the $Br + O_3 \rightarrow Br + O_2$ reaction

Annex C: Isotopic exchange in the $NO\text{-}NO_2$ equilibrium

Annex D: Protocol on preconcentration of nitrate samples

Annex E: Python algorithm for sample volume correction during isotopic measurements

CHAPTER 1

INTRODUCTION

1.1. The Polar Regions

Polar regions cover significant parts of the earth's surface, and are comprised of the Arctic and the Antarctic regions. Both the Arctic and the Antarctic extend from 66.3° North and South latitude to the respective pole. The total area covered by these regions is about 28 million sq. km. The Arctic includes the frozen Arctic Ocean, and is surrounded by the continents of Europe, Asia and, North America whereas the Antarctic atmosphere is pristine, dry and isolated from the rest of the globe by the Southern ocean (**Fig. 1.1**). The Antarctic is the fifth largest continent; 98 % of the region is covered with an ice sheet.

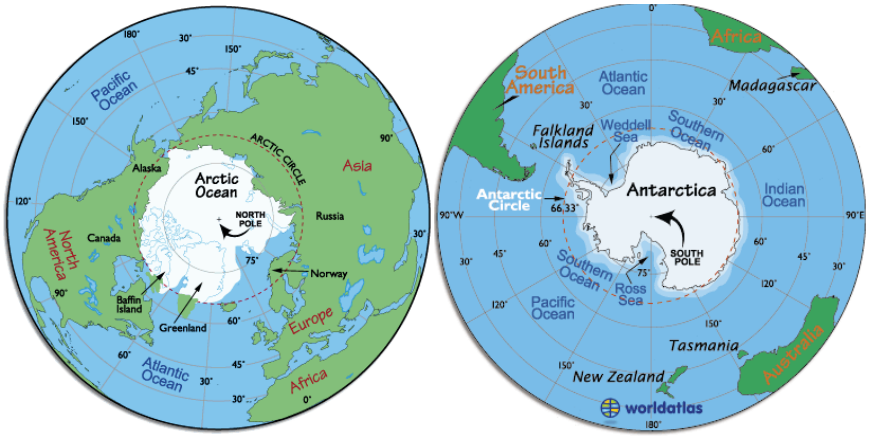

Figure 1.1 *Geographical maps of the Arctic (left) surrounded by continents and the Antarctic (right) isolated by the Southern Ocean.*

These regions have unique daytime and nighttime conditions, temperature profiles, local chemistries and other climatic conditions compared to the rest of the world and even sometimes between them.

In contrast to equatorial regions where the duration of daytime (sun) and nighttime (dark) is nearly equal throughout the year, the polar regions have varying lengths of day and night. During the Arctic summer (June-August), there are longer periods of sunlight within a day and the longest day with sunlight is at the summer solstice (20 or 21 June). In the winter, there is less sunlight and the dark period will dominate with the longest night at the winter solstice (20 or 21 December). The opposite is true for the summer and winter seasons of the Antarctic (Austral summer/winter).

These regions exhibit relatively colder temperatures throughout the year when compared to other regions of the world. There is a significant temperature difference between the two polar regions with a relatively higher temperature (mean annual temperature of about -30 °C) in the Arctic than in the Antarctic (mean annual temperature of about -50 °C). Extreme cases of low temperatures can also be observed at these regions with the coldest temperature ever recorded of -89.2 °C at Vostok station on July 21, 1983.

Polar regions act as sinks for long-range-transported chemical pollutants from mid-latitudes brought by air and sea currents. These regions can also preserve past global climatic information. During snowfall at these regions, a sequence of snow layers are built in chronological order containing a variety of information about chemicals washed away from the atmosphere and deposited in the snow.

The Arctic, which is situated close to a landmass and with permanent inhabitants (humans and wildlife), is highly influenced by seasonal atmospheric transport and anthropogenic emissions, and archived information from this site is mainly used to infer to human activities. In contrast, in the Antarctic where natural processes drive the biogeochemical cycles of the region, information relatively free from anthropogenic influences can be obtained. The archived information in these ice cores can be interpreted by various scientific techniques including visual counting of the annual layers (darker and lighter layers to correspond to seasons), analysis of the concentration of specific chemical species and their isotopes, and by matching layers with already dated events such as volcanic eruptions.

Currently, there are a number of scientific stations in both regions and different countries/institutes manage each station independently or jointly. Due to its relevance to this study, the Dome C station is briefly explained in the section below.

1.1.1. Geography of Concordia station (Dome C)

Concordia (Dome C) is a scientific station on Antarctica operated by the joint French-Italian polar institutes. The scientific station is located at the geographical coordinates 75°06'S, 123°19'E and at an altitude of 3233 m (**Fig. 1.2**). It is the third permanent continental station after Amundsen-Scott (USA) and Vostok (Russia). Its location was mainly chosen for the deep EPICA ice core drilling (3.3 km ice depth). It is also an important site for astronomical observations and chemical studies due to its clean background as well as favorable conditions for seismological and geomagnetic observations (www.institutpolaire.fr/ipev). The base is located 1200 km from the coastal French station Dumont d'Urville (DDU).

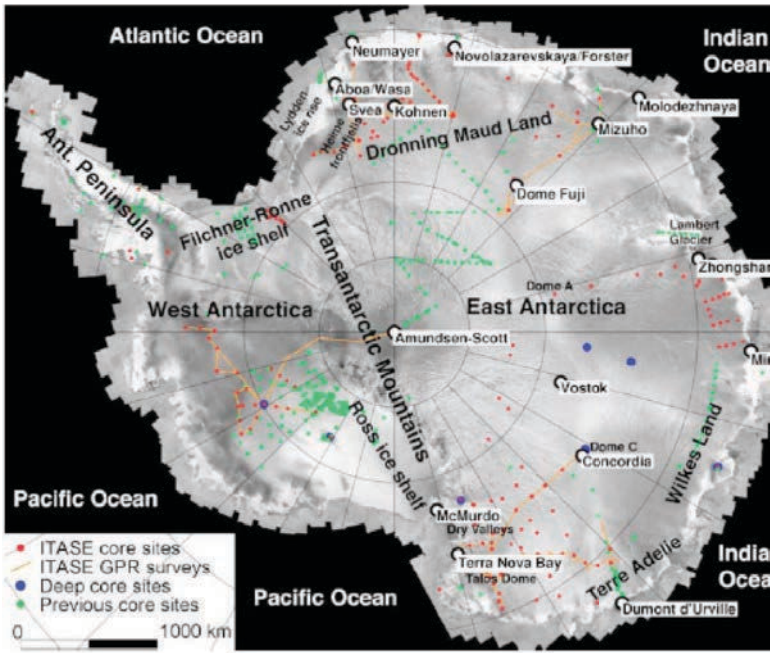

Figure 1.2. *Geographical map of the Antarctic continent showing some of the stations and ice core drilling sites (Eisen et al., 2008)*

1.1.2. Meteorology of Concordia station

Temperature

Dome C is one of the coldest places on earth due to the combined high altitude and geographical location in the continental Antarctic.

Based on the ground temperature record of Dome C, a minimum average temperature ranging -55 °C to -60 °C between April and October, and a maximum average temperature of -30 °C to -35 °C from December to February has been measured at this site (Aristidi et al., 2005). During the Austral summer where the temperature reaches its maximum, a diurnal near-surface temperature variation ranging -28 °C to -38 °C was observed during the period 16th January-31st January 2008 (Genthon et al., 2010) (**Fig. 1.4**).

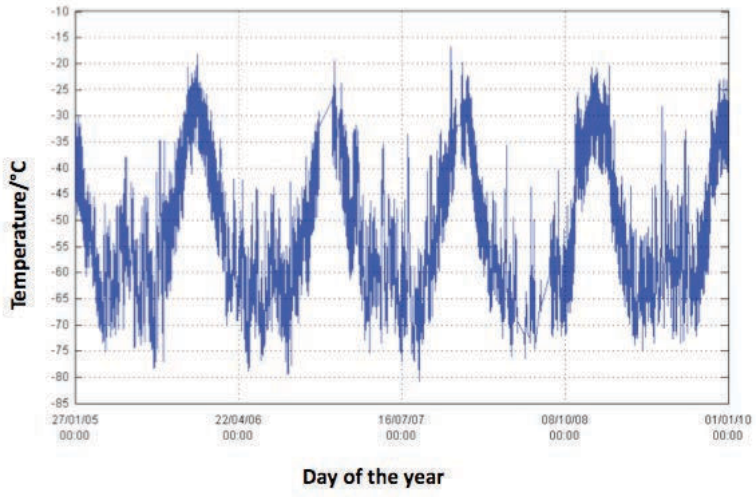

Figure 1.3. *Atmospheric temperature record at Dome C during 2005-2010 (www.climantartide.it)*

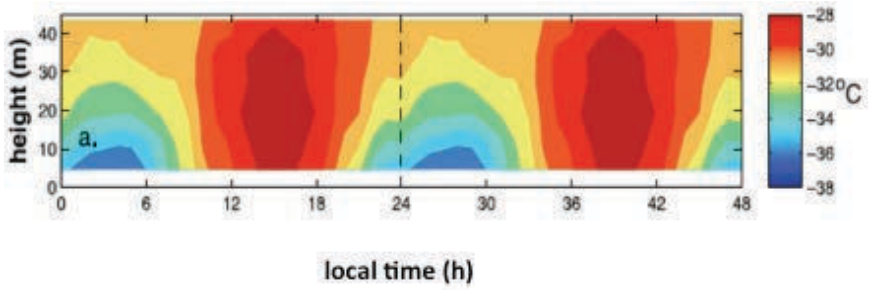

Figure 1.4 *The diurnal near surface temperature record on a tower at Dome C measured during 16th January to 31st January 2008 (Genthon et al., 2010)*

The temperature profile at Dome C was also recorded and shown in **Fig. 1.5**. Accordingly, the tropopause is found at an altitude 5.5 km from the ice surface, followed by a 1 km isothermal surface. The temperature fluctuations are more pronounced in the stratospheric layer (Aristidi et al., 2005).

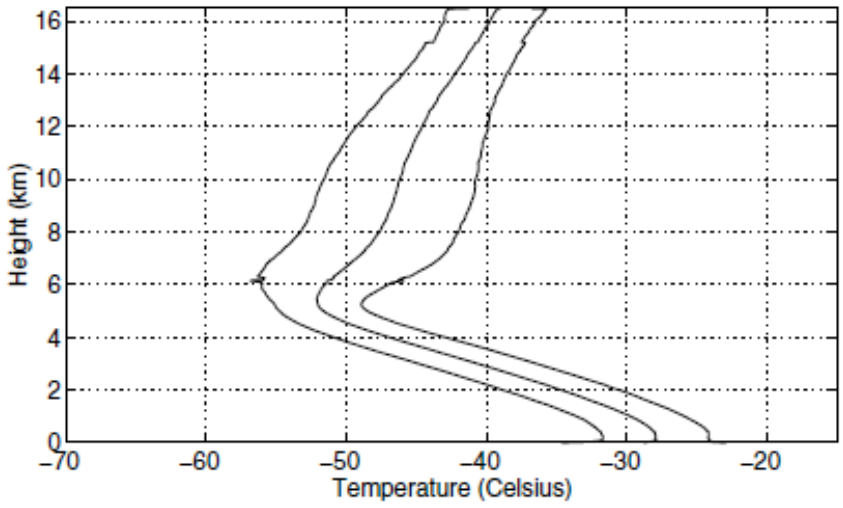

Figure 1.5. *Average summertime temperature profile at Dome C shown between the standard deviation limitation lines (Aristidi et al., 2005).*

Wind

The wind speed records from Dome C are relatively low compared to other sites such as Vostok. From wind speeds recorded in 1984-2004 at two weather stations at Dome C, an average wind speed of 2.9 m/s was measured (Aristidi et al., 2005), a value nearly half of the ground wind speed measured at Vostok or the South Pole.

Humidity and snow accumulation

Dome C is a relatively dry region with higher relative humidity during March to August when compared to the records between September and February (Gettelman et al., 2006). Looking at the diurnal cycle of humidity at the station, a positive latent heat flux during the day (sublimation) and negative heat flux in the night (deposition) are observed (Genthon et al., 2010).

Dome C is also one of the sites in Antarctica with a very low snow accumulation rate ranging 25-33 kg m^{-2} yr^{-1} (Urbini et al., 2008).

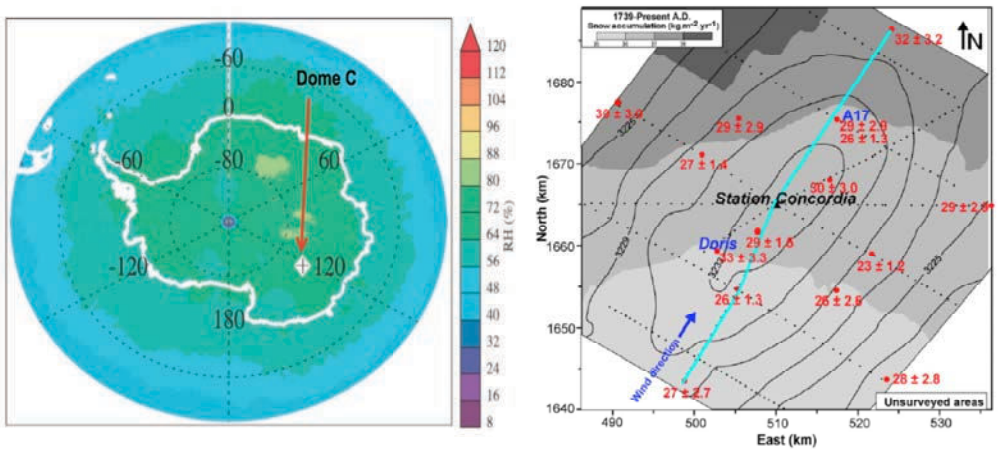

Figure 1.6. *Relative humidity measurement data for Dome C (left) during Dec-Feb (2002-2004)(Gettelman et al., 2006) and snow accumulation record for Dome C (right) based on radar data and snow accumulation values derived from firn core analysis (red). Contour lines represent surface topography within 2 m intervals. Dashed line shows snow radar profile and cyan line shows elevation (Urbini et al., 2008).*

1.2. Scientific Interests

1.2.1. The NO_X budget

The global nitrogen cycle describes the various chemical forms in which nitrogen is transformed by physical, chemical and biological processes. The major transformations include nitrogen fixation, nitrification/denitrification and ammonification.

NO_X (= NO + NO_2) can be produced from anthropogenic sources which includes mainly fossil fuels and biomass burning, and it also produced naturally via lightning and microbial activity (Horowitz and Jacob, 1999;Logan, 1983;Galloway et al., 2004). The global NO_X budget is summarized in Table 1.1, and the global inorganic nitrate deposition in the early 1990's is presented in **Fig.1.7**. The emission of anthropogenic NO_X is relatively higher in developed nations due to energy production (primarily fossil fuel combustion). However, addition of anthropogenic NO_X can have a substantial impact on biologically available N in the ecosystem, and its environmental impacts ranges from eutrophication of aquatic and terrestrial environments to global acidification (Galloway et al., 2004). Hence, it is essential to understand NO_X chemistry in order to understand the human impact on the global N-cycle, and associated environmental and health problems. An in-depth knowledge of the NO_X chemistry is also necessary to devise environmental regulations that can inhibit or prevent global NO_X emissions.

Table 1.1. The Global nitrogen sources and sinks, Tg N yr^{-1} (Galloway et al., 2004)

	1860	Early-1990s	2050
N-creation			
Natural	246	233	224
Anthropogenic	15	156	267
Total	262	389	492
Atmospheric emission			
NO_X			
Fossil fuel combustion	0.3	24.5	52.2
Lightning	5.4	5.4	5.4
Other emissions	7.4	16.1	23.9
Total	13.1	46	82
Atmospheric deposition			
NO_Y	12.8	45.8	78.5
NH_X	18.8	56.7	116.1
Total	31.6	103	195
Denitrification			
Total	125	163	221

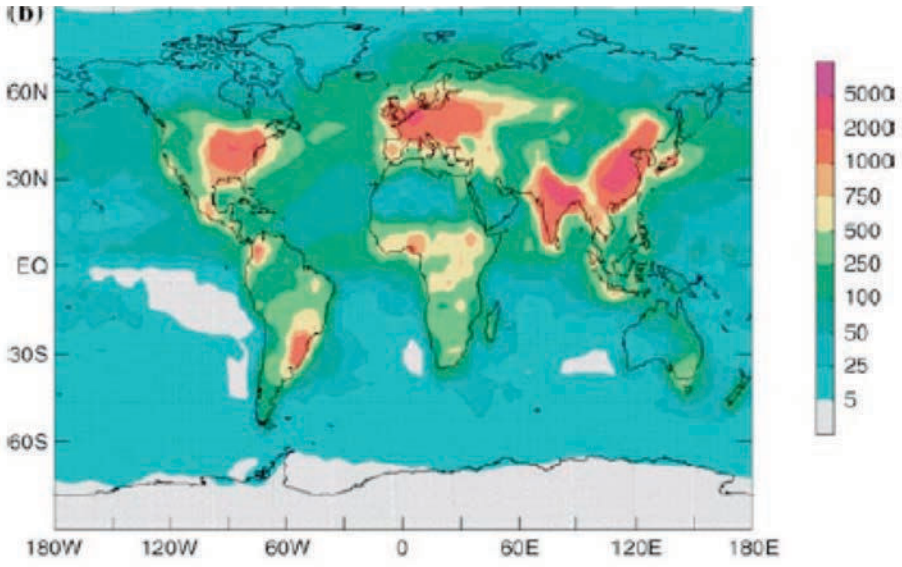

Figure 1.7. *The global inorganic nitrogen deposition in the early 90's in mgN$yr^{-1}m^{-2}$(Galloway et al., 2004). Higher emissions (marked red or pink) are mainly in North America, Europe and South East Asia, which are the most developed nations in the world.*

In the Arctic today, anthropogenic sources are the major NO_X contributors of snow nitrate, and their amount increased rapidly after the industrial revolution due to increased emissions mainly from developed nations. In the Antarctic, the sources of nitrate are not fully quantified, and currently known sources include stratospheric input

(stratosphere-troposphere exchange and precipitation of polar stratospheric clouds) and long-range transport of N-species generated at lower latitude regions (Wagenbach et al., 1998;Savarino et al., 2007;Wolff, 1995b).

Atmospheric nitrate, an oxidation product of NO_X, is removed from the atmosphere by dry or wet deposition as gas phase HNO_3 or particulate nitrate, and will be buried in the polar snow. Nitrate in the snow can be easily analyzed using ion chromatography and it is one of the most abundant anions present in the snow. Hence, buried nitrate in the polar snow carries atmospheric information of millennial timescales, and can be used in paleoclimatic studies (Wolff, 1995b;Legrand and Kirchner, 1988;Legrand et al., 1999). However, deposition of nitrate in polar regions is reversible, i.e. after being buried in the snow, its precursors and photolysis products (NO_X) will be re-emitted (**Fig. 1.8**).

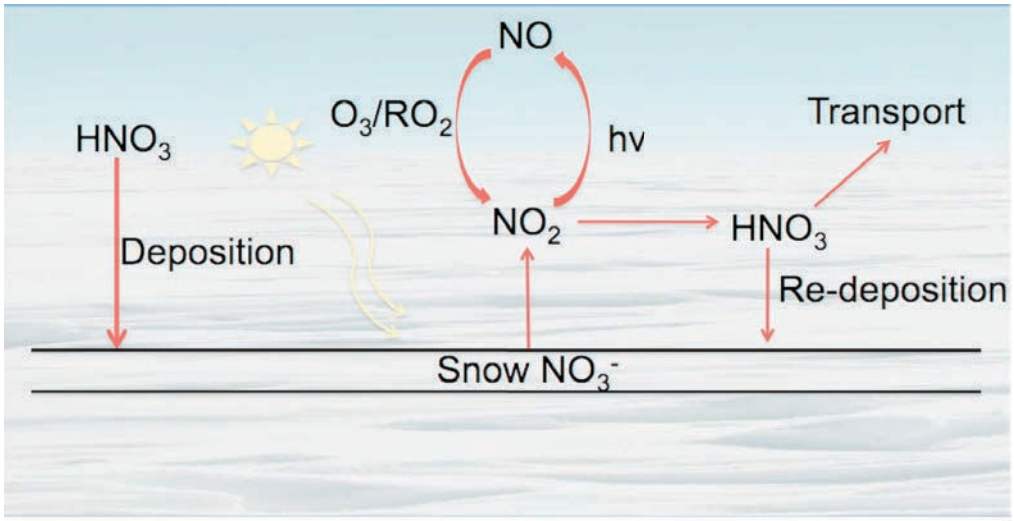

Figure 1.8. *Schematic of deposition of nitrate and emission of NO_X products which can undergo local oxidation to reform nitrate, which in turn can be re-deposited or transported.*

NO_X is an important atmospheric species mainly due to its profound effect on the tropospheric oxidation capacity via its direct influence on the two important atmospheric oxidants, OH and O_3. Today, there exists a well-documented record of high levels of emitted NO_X from the snowpack in polar regions.

During intensive investigations on atmospheric oxidants at the South Pole (ISCAT campaign), Davis et al. (2001) observed unexpectedly high levels of NO. The observed levels were 1-2 orders of magnitude higher than what was measured at other sites in Antarctica such as the Palmer station. Photodentrification of the snowpack was suggested to be the sources of the high level of NO_X.

Emissions of high levels of NO_X, which is consistent with the diurnal UV cycle, was also observed at Neumayer, Antarctica (Jones et al., 2001a;Jones et al., 2000). Accordingly, the high NO_X flux from the snowpack is dependent on the intensity of the incident radiation, and it can significantly contribute to the NO_X concentration of the lower troposphere in the Antarctic. Bauguitte and co-workers have also observed photochemistry-driven NO_X emission at Halley station in coastal Antarctica during

summer 2005 (CHABLIS campaign). The authors noted the diurnal variation of NO_X emission, and it peaked at about 5 hours after local solar noon (24 pptv) compared to its low level (5 pptv) at 4-5 hours after local midnight (Bauguitte et al., 2012).

Similar observations were also recorded at Summit, Greenland in which 3-10 times more NO_X in the interstitial air of the surface snow than the ambient air was observed (Honrath et al., 1999). It was suggested that photolysis of nitrate in the surface snow may initiate the release of NO_X.

These observations clearly show that the deposition of nitrate in the snow is reversible, and NO_X products will be emitted from the snowpack. An elevated level of NO_X has two implications: potential impacts of the emitted NO_X on the overlying boundary layer at these regions (Crawford et al., 2001), and loss or modification of archived information in the snow (Wolff et al., 2008).

Emitted NO_X products in these regions can undergo local oxidation to reform nitrate, which can be either be re-deposited or transported to other sites. Hence, the nitrate signal left in the snowpack is not the original atmospheric signature but rather a modified one.

Currently the basic NO_X chemistry is more or less known. However, its chemistry in polar regions and significance of each nitrate formation pathways are still not clear. The currently known basic NO_X chemistry is described below.

1.2.2. The atmospheric reactive NO_X cycle

Figure 1.9 shows the oxidation pathways of NO_X during the daytime and nighttime, which are described in detail below.

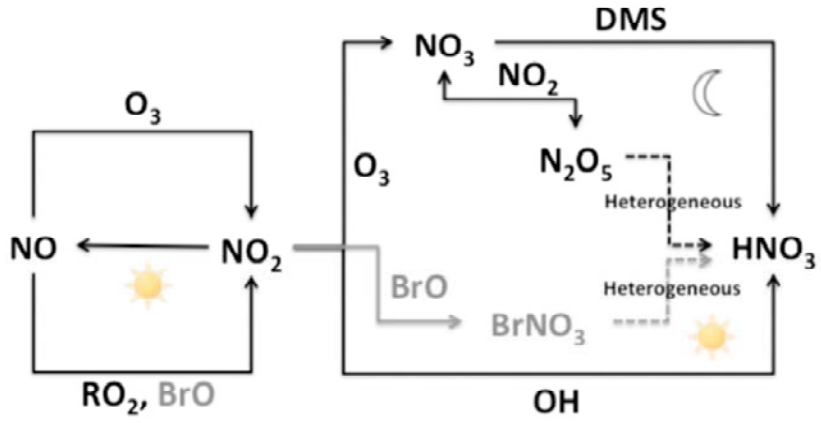

Figure 1.9. *The NO_X cycling and nitrate formation pathways in the atmosphere. The sun represents the daytime mechanism whereas nighttime pathways are shown using the moon. Dashed lines represent the heterogeneous nitrate formation pathways.*

1.2.2.1. Daytime chemistry

During the daytime, photochemical NO-NO_2 interconversion is the dominant process in which NO_2 will be photolysed to produce NO and an excited oxygen atom (R.1.1.). The oxygen atom can rapidly react with molecular oxygen to produce ozone via R.1.2. NO_2 can be reformed via R.1.3 when NO reacts with ozone. This closed photochemical cycling of NO-O_2-O_3-NO_2 is called the Leighton cycle.

$NO_2 + h\nu\ (\lambda < 424\ nm) \rightarrow NO + O$ (R.1.1)

$O + O_2 + M \rightarrow O_3 + M$ (R.1.2)

$NO + O_3 \rightarrow NO_2 + O_2$ (R.1.3)

The oxidation of NO to NO_2 and photolysis of NO_2 to NO are so rapid that steady state called a '*photostationary state'* will be achieved quickly. At steady state, the ozone concentration is given by:

$$[O_3] = \frac{j_{NO_2}[NO_2]}{k_{NO+O_3}[NO]} \quad (1.1)$$

where j_{NO2} is the photolysis rate coefficient of NO_2, and $k_{NO + O3}$ is reaction rate constant for R.1.3. Note that the steady state ozone concentration is proportional to the [NO_2]/[NO] ratio. The only known mechanism of ozone production in the troposphere is the reaction of an oxygen molecule with an oxygen atom produced by photolysis of NO_2 (R.1.2) (Seinfeld and Pandis, 2006). However, due to the reaction of NO and O_3 to reform NO_2, this is a null cycle with no net production or consumption of ozone.

In the presence of peroxy radicals such as HO_2, the conversion of NO to NO_2 is favored to form a "new" ozone molecule. This is due to the formation of NO_2 from NO via R.1.4 without involving an ozone molecule in contrary to R.1.1-R.1.3.

$NO + HO_2 \rightarrow NO_2 + OH$ (R.1.4)

Hence, the rate of ozone production can be written as:

$$P_{O_3} = k_{HO_2+NO}[HO_2][NO] \quad (1.2)$$

Net ozone production is controlled by balance between the ozone formation and destruction pathways, which depends on the concentration of NO_X and HO_X. At relatively low NO_X levels such as in the remote atmosphere, HO_2 reacts with ozone leading to a net loss of ozone via R.1.5.

$HO_2 + O_3 \rightarrow OH + 2O_2$ (R.1.5)

As shown in **Fig. 1.10**, with rising concentrations of NO_X, the production of NO_2 also increases via R.1.4, and consequently the production of ozone also increases via the photolysis of NO_2 (R.1.1-R.1.2). Above the compensation point (the concentration of NO_X at which the net ozone production is zero), the production of ozone will be the dominant process with the rate described by equation 1.2. With this increase in NO_X concentration, the net production of ozone also increases, and reaches its maximum at some level of NO_X. Above this level the net production of ozone starts to decrease and the rate of the overall photochemical cycle is controlled by the CO + OH reaction (R.1.6) which determines HO_2 production via R.1.7. Further increase in NO_X will magnify the importance of the OH + NO_2 termination reaction via R.1.8.

$$CO + OH \rightarrow H + CO_2 \qquad \text{(R.1.6)}$$

$$H + O_2 + M \rightarrow HO_2 + M \qquad \text{(R.1.7)}$$

$$NO_2 + OH \rightarrow HNO_3 \qquad \text{(R.1.8)}$$

The principal removal of NO_X during the daytime is via oxidation by OH radicals (R.1.8). At an OH concentration of 1×10^6 molecules cm^{-3}, NO_2 has an average lifetime of about 24 hours. NO_X has a lifetime of about 2 days in the pristine boundary layer and about 2 weeks in the upper troposphere. At the earth's surface NO_2 is the dominant daytime species whereas at higher altitudes the photolysis product NO is dominant.

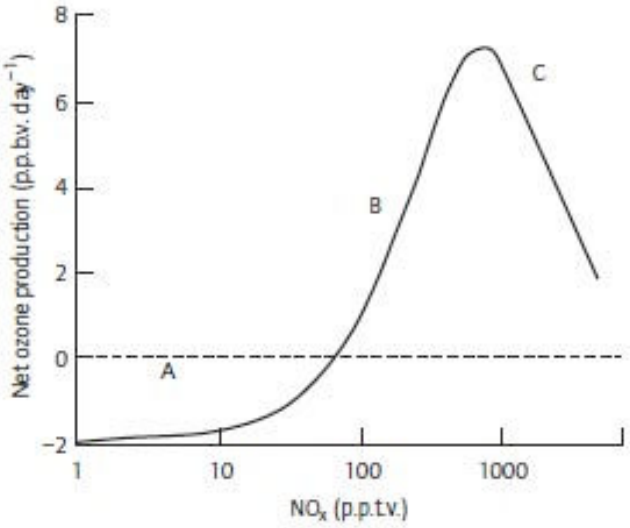

Figure 1.10. *The dependence of net ozone production on the level of NO_X. At low NO_X level, a net loss of ozone takes place (A). At increasing NO_X level above the compensation point (net ozone production = 0), net ozone production also increases (B) and reaches a maximum at a certain NO_X level. It eventually starts to decrease (C) below this point (Hewitt, 2003).*

1.2.2.2. Nighttime chemistry

The nighttime chemistry of nitrate in the troposphere is dominated by reactions of NO_3 and this is the most uncertain chemistry due to heterogeneous pathways. In contrast to daytime mechanisms, NO_2 does not photolyse readily at night but it will react with ozone forming NO_3 (R.1.9).

$$NO_2 + O_3 \rightarrow NO_3 + O_2 \qquad \text{(R.1.9)}$$

In the daytime, NO_3 photolyses readily back to NO_2 and O or NO and O_2, and it has a lifetime of 5 sec during overhead sun and clear-sky conditions at sea level (Allan et al., 2000). Additionally, the reaction of NO_3 with NO is a fast reaction with approximate photochemical steady state with NO_2 (R.1.10) during the daytime.

$$NO_3 + NO \rightarrow 2NO_2 \qquad \text{(R.1.10)}$$

During the night, the level of NO will be negligible (unless fresh local emissions are present) as all NO will be titrated by ozone and significant levels of NO_3 will be formed via R.1.9 (Allan et al., 2000). The NO_3 product can follow the following pathways to form nitrate (see **Fig. 1.9**):

Reaction with NO_2

NO_3 can undergo an addition reaction with NO_2 to form N_2O_5, which readily dissociates and establishes equilibrium with NO_3 under ambient temperatures (R.1.11). N_2O_5 is a thermally unstable compound with a life time of 40 seconds at 290 K which increases to 700 seconds at 270 K. Hence, N_2O_5 is a possible reservoir for NO_X, but with the possibility of reforming NO_2 and NO_3 depending on meteorological conditions (Brown and Stutz, 2012). N_2O_5 can undergo heterogeneous hydrolysis to form HNO_3 via R.1.13.

$$NO_2 + NO_3 \leftrightarrow N_2O_5 \qquad \text{(R.1.11)}$$

$$N_2O_5 + H_2O_{ads} \rightarrow 2HNO_3 \qquad \text{(R.1.12)}$$

Reaction with VOCs and organic sulfur species

NO_3 is reactive towards both unsaturated and saturated hydrocarbons, and sulfur-containing organic compounds. The reaction of NO_3 with unsaturated biogenic hydrocarbons such as terpenes is relatively faster than the saturated ones, and it can significantly affect the overall hydrocarbon budget (Brown and Stutz, 2012). During this reaction, NO_3 will be added to the C-C double bond, followed by recombination with O_2 to form peroxyradicals, and further add NO_X species to form stable organic nitrate products (Allan et al., 2000). The reaction of NO_3 with saturated hydrocarbons (RH) proceeds via a hydrogen atom abstraction by NO_3 to form nitrate (R.1.13).

NO_3 can also react with sulfur-containing compounds such as dimethyl sulfide (DMS) (R.1.14). DMS is the dominant natural source of atmospheric sulfur which is emitted from the oceans. Hence, oxidation of DMS by NO_3 can significantly affect the

sulfur cycle, and this reaction can be a useful sink for NO_X in marine atmosphere (Platt and LeBras, 1997).

$NO_3 + RH \rightarrow HNO_3 + R$ (R.1.13)

$NO_3 + CH_3SCH_3 \rightarrow HNO_3 + CH_3SCH_2$ (R.1.14)

1.2.2.3. Bromine Chemistry and its relation with NO_X chemistry

Bromine chemistry is relevant in polar regions where severe ozone depletion events (ODEs) take place during the polar spring (Simpson et al., 2007). During ODEs over the Arctic ocean, where such events are severe, the level of ozone can reach from very low to totally absent (Bottenheim et al., 2009). ODEs are caused by bromine species which are emitted from the sea during "bromine explosion events" via the reaction sequence (Simpson et al., 2007):

$HOBr + Br^- + H^+ \rightarrow H_2O + Br_2$ (R.1.15)

$Br_2 + h\nu \rightarrow 2Br$ (R.1.16)

$Br + O_3 \rightarrow BrO + O_2$ (R.1.17)

$BrO + HO_2 \rightarrow HOBr + O_2$ (R.1.18)

Net: $H^+ + Br^- + HO_2 + O_3 \rightarrow Br + H_2O + 2O_2$ (R.1.19)

Reaction R.1.15 consumes one reactive bromine species (HOBr) and produces Br_2 which can produce two active bromine species. This implies that in the presence of bromide each active bromine will be converted into two reactive species on ice or aerosol surfaces. This can lead to an exponential increase in the atmospheric bromine concentration (bromine explosion) and hence a depletion of ozone. Ozone depletion events and associated effects are beyond the scope of this study; here only the relationship between the bromine and nitrate chemistry will be described.

Bromine produced during these explosion events will react with ozone via R.1.20.

$Br + O_3 \rightarrow BrO + O_2$ (R.1.20)

The BrO radical has two fates: self-addition or reaction with HO_2 to produce Br_2 and HOBr. Both species are photo-labile and can be photolysed to produce Br and OH. However, BrO can also oxidize NO_X species via different mechanisms to form nitrate (Evans et al., 2003). Its reaction with NO to produce NO_2 (R.1.21) can compete with the oxidation of NO by O_3 or RO_2 (see **Fig. 1.9**).

$BrO + NO \rightarrow Br + NO_2$ (R.1.21)

BrO can also further oxidize NO_2 via:

$$BrO + NO_2 \rightarrow BrNO_3 \qquad (R.1.22)$$

Hydrolysis of $BrNO_3$ via R.1.23 is an important source of inorganic nitrate in the Arctic troposphere during spring (Morin et al., 2007b). (Note that the HOBr molecule formed during this reaction will recycle Br which will undergo multiple ODEs).

$$BrNO_3 + H_2O \rightarrow HOBr_{(aq)} + HNO_{3(aq)} \qquad (R.1.23)$$

In order to clearly understand these chemical processes, polar regions are places of interest because chemical processes are mostly driven naturally, and it has a relatively clean background associated with its remoteness from anthropogenic influences. Another unique feature of this region is 24 hours of daylight in summer and 24 hours of darkness in winter, which will simplify the interpretation of the atmospheric observations.

To generalize, NO_X is emitted from nitrate buried in the snowpack and it can play a significant role in the chemistry of the overlying boundary layer. But the precise mechanisms of NO_X emissions from the snowpack are still unknown. It is essential to understand these mechanisms in order to extract robust information from deep ice cores and to assess the impact of these emissions on the overlying atmosphere.

1.2.3. NO_X emission mechanisms from the snowpack

At the end of section 1.2.1, the field observations of elevated levels of NO_X were described. These studies and additional studies not discussed in detail in this manuscript clearly suggest that post-depositional photochemical processes during sunlit periods in these regions will tend to drive the NO_X out of the snowpack (Honrath et al., 1999;Davis et al., 2001;Bauguitte et al., 2012;Frey et al., 2012;Beine et al., 2002). However, the impacts of post-depositional processes vary for different locations in polar regions depending on the annual snow accumulation rates and other physical parameters (such as temperature and UV).

In polar sites such as Summit, Greenland with high annual snow accumulations of about (65±4.5) cm yr^{-1} (Dibb and Fahnestock, 2004), post-depositional effects may have an impact on the surface snow concentrations (and may change the atmospheric NO_X concentration) but it has a minor role on the preserved nitrate record in the snowpack (Burkhart et al., 2004). Based on the analysis of the concentration of nitrate on the surface snow and from snow pits at Summit, Greenland (Burkhart et al., 2004), over 90% of the nitrate measured in surface snow is preserved in the snow pits (**Fig. 1.11**).

In contrast, at low accumulation sites of Antarctica such as Dome C, with an annual snow accumulation of only 7.2 cm yr^{-1} (Wolff et al., 2002), nitrate deposition is reversible i.e. deposited nitrate will be modified before being buried underneath.
From measurements of nitrate concentrations in snow pits from these low accumulation sites, it can be seen that the concentration of nitrate is higher in the top few centimeters, and it diminishes rapidly below these layers (**Fig. 1.12**) (Dibb and Whitlow, 1996;Traversi et al., 2009).

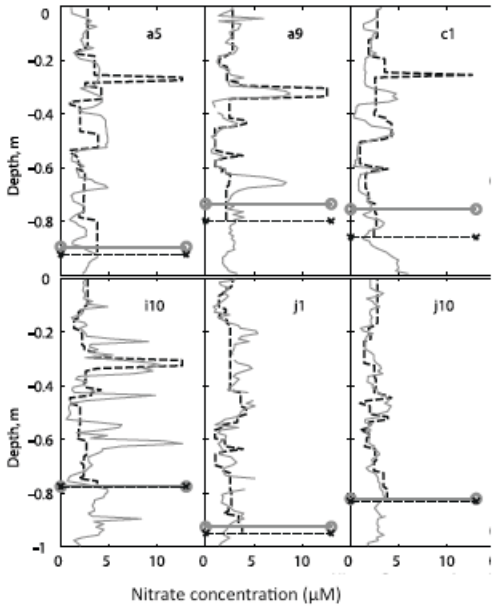

Figure 1.11. *The concentration of nitrate observed (vertical shaded) and reconstructed (vertical dashed) in snow pits at Summit, Greenland. Horizontal shaded line shows the 1- year dateline of 11 June 1997 from cumulative accumulation observation and horizontal dashed line shows the reconstructed maximum depth (Burkhart et al., 2004)*

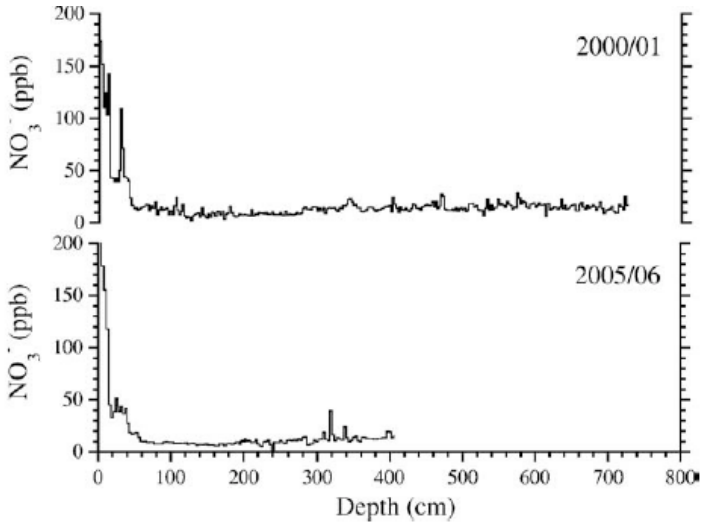

Figure 1.12. *The depth profile of nitrate in snow pits at Dome C (top 800 cm). From nitrate concentrations of 150-200 ppb in the top 20 cm, its level decreases rapidly to about 10-20 ppb below 40 cm and remains at this level in samples collected in 2000/01 and 2005/06 (Traversi et al., 2009).*

The observed huge mass loss of nitrate beneath the surface snow layers at low accumulation sites confirm that post-depositional effects are more significant at these

sites than at high accumulation sites. Hence, the focus of this thesis will be only on low accumulation sites.
Before discussing how NO_X is emitted from the snowpack, it will be useful to understand how impurities such as nitrate are incorporated in snow.

1.2.3.1. Inclusion of Impurities

Snow is a porous medium composed of ice, air, impurities and sometimes liquid water. Snow can incorporate chemical species such as HNO_3, HCl, H_2O_2 and organic compounds via three mechanisms: adsorption, dissolution in the ice matrix (formation of solid solution) and trapping of aerosol particles (Dominé et al., 2007) shown in **Fig. 1.13**. As the mechanisms of incorporation of these species into the snow are different, their lifetime in the snow also varies. For example, adsorbed species are readily available for reaction with atmospheric gases, and their lifetime in the snow is determined by the temperature, partial pressure of the species, and the surface of the snow available for gases (Specific Surface Area, SSA) (Dominé et al., 2007). In contrast, species dissolved in the ice matrix are trapped, and are the least available species for reactions. These species, which are isolated from atmospheric gases, have limited reactivity towards solid phase processes, and photochemical reactions are dampened by matrix (cage) effect (Grannas et al., 2007).

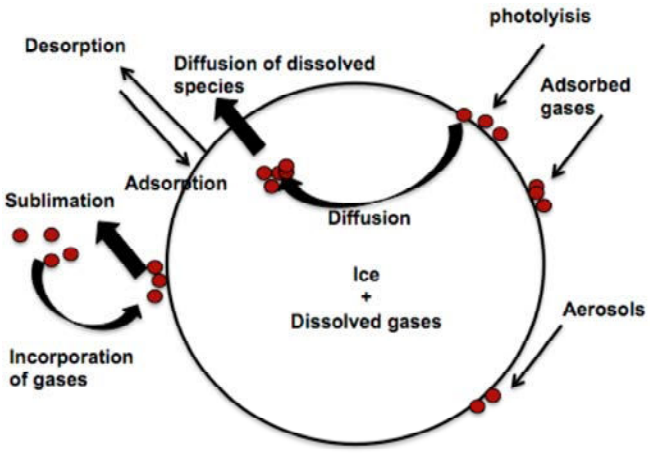

Figure 1.13. *Mechanisms of inclusion (such as adsorption and dissolution) and emission (via desorption and photolysis) of impurities in/from snow (Dominé et al., 2007).*

However, the inclusion of atmospheric species may be temporary, and physical processes and photochemistry may contribute to the emission of these species from the snowpack to the overlying atmosphere.

1.2.3.2. Emission of impurities

Emission of impurities from the snowpack occurs via incorporation of these species (which are adsorbed or dissolved in the snow crystals) into the interstitial air of the snowpack, followed by diffusion towards the surface, and then release to the boundary atmosphere. Once released into the interstitial air (air-filled pore spaces), wind pumping is the most efficient mechanism for venting these species into the boundary atmosphere.

The most important mechanisms by which impurities present in the snowpack (such as HCl, HNO_3 and H_2O_2) are emitted to the boundary atmosphere are desorption (evaporation/sublimation) and photolysis.

A. Desorption (Evaporation/Sublimation)

This process refers to the physical release of impurities from the snowpack to the boundary atmosphere due to the presence of a temperature gradient. The change in atmospheric temperature, and radiative heating and cooling of the snowpack after deposition of the snow will lead to a temperature gradient and water-vapor fluxes. These factors result in snow metamorphism which is a change in snow crystal shape and surface area (Dominé and Shepson, 2002). Snow metamorphism can induce both sublimation and condensation of ice and its solutes (Perrier et al., 2002). This can lead to loss of nitrate from the snow, and redistribution and smoothing of nitrate profiles within the snow. Snow metamorphism almost always results in change in the snow specific surface area leading to release of adsorbed species or availability of these species for gas phase or surface reactions (Grannas et al., 2007).

The physical release of HNO_3 from the snowpack in low snow accumulation sites has been invoked to explain the loss of nitrate from the snowpack (Röthlisberger et al., 2000;Blunier et al., 2005;Nakamura et al., 2000).

Even if desorption can be a loss mechanism for snow nitrate, the magnitude of its effect on the overall observed loss in low snow accumulation polar sites is an issue of debate when compared to photolysis (Grannas et al., 2007). This issue will be discussed in the later sections from an isotopic perspective.

B. Photolysis

Molecular photolysis arises from the penetration of high-energy solar photons into the snowpack which can break chemical bonds. When a molecule interacts and absorbs a photon of energy *hv*, it will be transferred into an excited state that can dissociate into products (photo fragments).

$$AB + h\nu \rightarrow [AB^*] \rightarrow A + B \qquad \text{(R.1.24)}$$

The photolysis of a molecule in a given wavelength band (λ) is described by using the photolysis rate constant (*J*) mathematically described as:

$$J = \int_{\lambda_1}^{\lambda_2} \sigma(\lambda)\phi(\lambda)I(\lambda)d\lambda \qquad (1.3)$$

where σ is the absorption cross section of a molecule (the probability that a photon is absorbed by a molecule), cm^2 $molecule^{-1}$

Φ is the quantum yield (probability that absorbed photon causes photolysis), molecules $quanta^{-1}$

I is the spectral actinic flux (the flux of photon coming from all directions), quanta cm^{-2} $s^{-1}nm^{-1}$

Solar radiation ranges through the entire electromagnetic spectrum. However, only a fraction of this light (mainly in the visible region of the spectrum) reaches the surface of the earth due to the absorption of the short wavelength region by atmospheric gases such as O_2 and O_3 (Seinfeld and Pandis, 2006). Even with these conditions, there is a small UV window allowing part of the UV light to reach the earth's surface, and the absorption cross section of nitrate overlaps within this UV window.

After absorption of UV light nitrate will be in the excited state, and can either dissipate its energy and reform nitrate or photodissociate into NO_X products depending on the wavelength of irradiation. A number of studies have been conducted in the past to understand the mechanism of photodissociation of nitrate.

From simultaneous measurement of NO and NO_2 in ambient air and air inside a snow pack, Jones et al. (2000) measured enhanced concentration of these species depending on the intensity of incident radiation. According to this study, the emission was dependent on the availability of solar radiation, and NO_X emission stopped in the dark (Jones et al., 2000). The photochemically driven emission of NO_X from the snowpack was also observed at Neumayer, Antarctica from the diurnal variation of emitted NO_X levels (Jones et al., 2001a).

Using natural snow from Halley station in Antarctica, Cotter et al. (2003) observed emission of NO_X dominated by NO_2 which ceased after irradiation at wavelengths $\lambda >$ 345 nm. The observation was in agreement with a previous laboratory study on artificial snow produced from freezing an aqueous solution of nitrate, and was irradiated around the 302 nm band (Dubowski et al., 2001). These studies confirmed the wavelength region sensitivity of photodissociation of nitrate in snow.

A similar observation on photoemission of NO_X products was also observed in different studies both in the laboratory and in the field, and a photodissociation mechanism of nitrate was proposed (Honrath et al., 2002;Beine et al., 2008;Jacobi et al., 2007;Jacobi et al., 2006).

Even if the actual mechanism of nitrate photochemistry in snow is complex, a generalized mechanism of photolysis of nitrate was devised as shown below.

Nitrate has two major absorption bands (**Fig. 1.14**): one around 200 nm (intense $\pi \rightarrow \pi^*$ band) and another one around 300 nm (weak $n \rightarrow \pi^*$ band). The 200 nm absorption band is more than 3 orders of magnitude more intense than the 300 nm absorption band (Mack and Bolton, 1999). However, short wavelength UV light in the first band does not reach the surface of the earth due to attenuation by the stratospheric ozone layer. The absorption cross-section of nitrate between the wavelength regions of 280 nm-360 nm has been measured in the liquid phase by Chu and Anastasio (2003) (**Fig. 1.16)**.

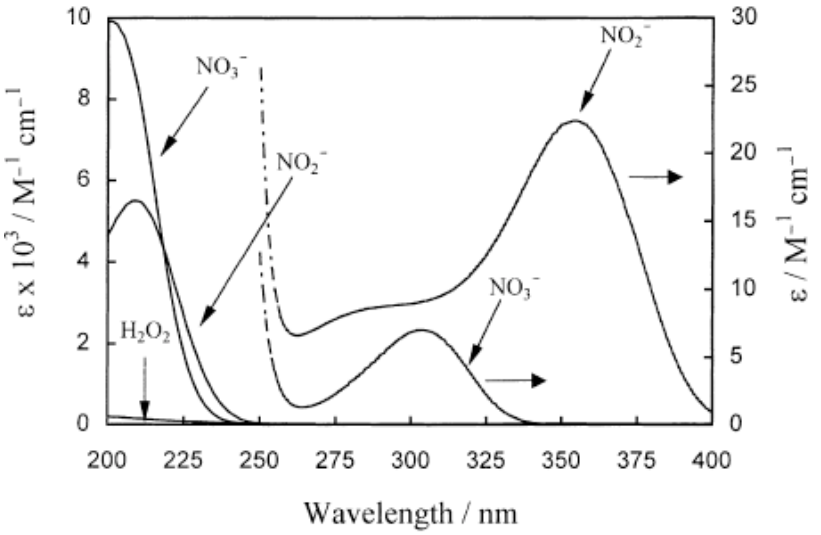

Figure 1.14. *The absorption cross-sections of NO_2^- and NO_3^- between 200 nm and 400 nm (Mack and Bolton, 1999).*

The photolysis of nitrate at wavelengths $\lambda > 290$ nm proceeds via R.1.25 producing NO_2.

$$NO_3^- + h\nu/H^+ \rightarrow NO_2 + OH \qquad \text{(R.1.25)}$$

The minor pathway R.1.26 can also take place via peroxynitrite formation at $\lambda < 290$ nm (Madsen et al., 2003). However, R.1.25 has a quantum yield 8-9 times larger than R.1.26.

$$NO_3^- + h\nu \rightarrow ONOO^- \rightarrow NO_2^- + O(^3P) \qquad \text{(R.1.26)}$$

The product NO_2 is eventually photolysed via R.1.27 and generates NO (that could be emitted) and O^- (to produce OH). With a pK_a of 3.2, in acidic matrix, NO_2^- combines with H^+ to form HONO via R.1.28.

$$NO_2^- + h\nu \rightarrow NO + O^- \qquad \text{(R.1.27)}$$

$$NO_2^- + H^+ \rightarrow HONO \qquad \text{(R.1.28)}$$

Further reactions could also take place via R.1.29-R.1.31

$$2NO_2 + H_2O \rightarrow NO_2^- + NO_3^- + 2H^+ \qquad \text{(R.1.29)}$$

$$NO_2^- + OH \rightarrow NO_2 + OH^- \qquad \text{(R.1.30)}$$

$$NO + NO_2 + H_2O \rightarrow 2HONO \qquad \text{(R.1.31)}$$

In the high-energy band, the photolysis of nitrate is dominated mainly by isomerization with the possibility of reforming ground state nitrate as shown in **Fig. 1.15** (Madsen et al., 2003). Accordingly, during photoexcitation of nitrate around 200 nm, 44 % of the molecules return rapidly to the electronic ground state. The remaining molecules will either form *cis*-$ONOO^-$ (48 %) or dissociate to NO and O_2^- or NO^- and O_2. The peroxynitrite isomer returns to its ground state or forms secondary species.

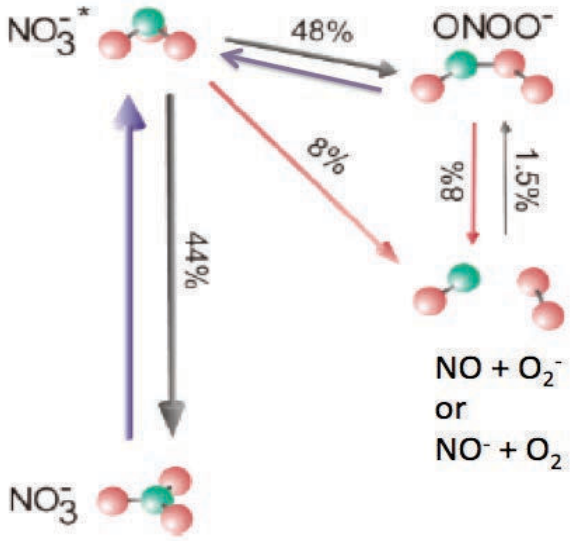

Figure 1.15. *The 200 nm photoexcited nitrate and predicted pathways for the respective product formation (Madsen et al., 2003). The purple arrows show stabilization of molecules into the ground state, and red arrows indicate alternative reaction pathways.*

The observations of these two different dissociation mechanisms indicate that the photoproducts during nitrate photodissociation are dependent on the wavelength region of irradiation (i.e. they are dependent on the absorption band).

At Dome C, as the short wavelength region of the solar spectrum is attenuated by the ozone layer, only the absorption band of nitrate around 300 nm is relevant (**Fig. 1.16**). Irradiance by the incoming light plays a significant role in the photodissociation of nitrate. An incoming light flux which reaches the surface of the snow will undergo scattering and be transformed from direct to diffuse light. The incoming solar radiation is measured as solar irradiance, and can be converted to a spherically integrated actinic flux. The actinic flux expresses the amount of light flux around a molecule from all directions. During the scattering process, the light may be reflected back, and leave the snow pack (described as the snow albedo) or enhance its penetration into the snowpack. The amount of UV light that penetrates the snow pack is dependent on the absorption and scattering properties of the snow, and the solar zenith angle (France et al., 2011b).

Ice has a very strong absorption at short wavelengths ($\lambda < 170$ nm) but its absorption capacity decreases with increasing wavelength towards the visible region (Warren, 1982;Warren et al., 2006). When encountering incoming solar UV or near-UV light, snow grains will scatter most of it. However with the presence of impurities, the absorption of radiation in natural snowpack can increase (France et al., 2012). At the top layer (near the surface) of the snowpack, multiple scattering takes place enhancing the

actinic flux and photolytic reactions. At the surface, scattering is dependent on the solar zenith angle, snow density, wavelength, and absorption and scattering coefficients. For example at higher solar zenith angles, most of the incoming solar radiation is reflected back (higher albedo) and photochemistry is very limited. In contrast, the solar zenith angle is irrelevant at large depths, and all the incoming light is attenuated exponentially (Lee-Taylor and Madronich, 2002;Simpson et al., 2002;Grannas et al., 2007). The depth at which this incoming solar irradiance is reduced to 1/e of the initial level is called the e-folding depth.

An e-folding depth at a specific wavelength η(λ) can be derived experimentally by measuring the irradiance within the snow (I_z) at a given depth z, and using the Beer-Bouger Lambert law by:

$$I_z = I_0 e^{\frac{(z-z_0)}{\eta(\lambda)}} \qquad (1.4)$$

where I_0 is the intensity of the incident light at the snow surface with depth Z_0.

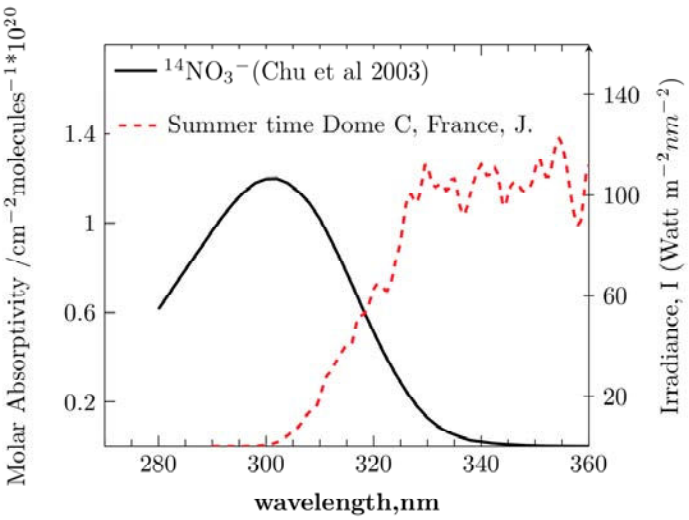

Figure 1.16. *The absorption cross-section of nitrate around 300 nm (with respect to the right y axis) measured in the liquid phase (Chu and Anastasio, 2003) and the solar irradiance at Dome C measured by J. France. The measurement was taken on 21 December 2009, which was the longest day of the year, and at the maximum solar zenith angle.*

The top 80 cm of snow pack in Dome C can be divided into three layers: soft wind pack, hard wind pack and hoar-like snow (Wolff et al., 2010;Warren, 1982;France et al., 2011b), and each layer has a unique light attenuation property. For such snowpack, France et al. (2011) determined e-folding depths of 10 cm for the soft and hard wind packs, and 20 cm for the hoar-like layer at 400 nm by experiment. However, the e-folding depth is very sensitive to the impurity content of the snowpack and wavelength in the UV/near-visible region. Recently, a factor of two difference in e-folding depth was observed between the snowpack near the base and 11 km from the base at Dome C (Zatko et al., 2013).

As discussed below, e-folding depth values have a significant influence on the overall determination from NO_X flux out of the snowpack during photolysis. For example, France et al. (2011) coupled the experimental snow e-folding depth, snow pack reflectance and snow density with the snow Tropospheric Ultraviolet Visible (TUV) model (http://cprm.acd.ucar.edu/Models/TUV/) and determined the depth integrated NO_2 production from the snow pack due to photolysis.

The TUV model is a one dimensional radiative transfer model that enables estimations of the propagation of solar light passing through different atmospheric layers in the presence of absorbers (gases such as O_3 and O_2) and scatterers (Lee-Taylor and Madronich, 2002).

According to France and colleagues, 85% of the NO_X emitted during photolysis is from the top 20 cm of the snow layer, and photolysis could reduce 80% of the surface nitrate concentration at Dome C (France et al., 2011b). This emission scenario is orders of magnitude larger than previous field studies such as that of Wolff and co-workers where only 40% of the nitrate mass loss was accounted by photolysis (Wolff et al., 2002). However, the difference between the two measurements lies mainly in the difference in the e-folding depth; a shorter e-folding depth (3.7 cm) was used in the latter case. Hence, an accurate measurement of an e-folding depth is essential to constrain the NO_X emission due to photolysis.

The main photoproducts of nitrate photolysis are NO and NO_2 where the latter is the major byproduct, which is desorbed mainly from the upper snow layers where as NO is preferably formed in the deep ice layers (Boxe et al., 2006;Jacobi et al., 2007). The probability of dissociation of nitrate into photoproducts is described using its quantum yield. Currently, only a few studies exist on the quantum yield of products of nitrate photolysis.

Chu and Anastasio (2003) derived the quantum yield of photolysis of nitrate in snow via R.1.17 ($\Phi = (1.7\pm0.3)\times10^{-3}$) by freezing an aqueous $NaNO_3$ solution at 263 K, and following the formation of OH radical using a 1 kW Hg lamp at 313 nm. However the resulting quantum yield was suggested to be higher in a different study conducted by Zhu et al. (2010). The authors determined a higher quantum yield value ($\Phi = 0.6\pm0.34$) during photolysis of HNO_3 adsorbed on ice films using 308 nm excimer laser photolysis combined with cavity ring down spectroscopy (Zhu et al., 2010).

The freeze-concentration effect is an important parameter to consider in the study by Chu and Anastasio (2003). Freeze-concentration is defined as the separation of the solutes from ice and incorporation into the liquid layers on ice crystal surfaces during freezing of a liquid solution. According to previous studies, during freezing of an aqueous solution composed of typocal organic or inorganic compounds, this effect will be present and increases the solute concentration in the liquid layer covering the ice crystals (McNeill et al., 2012;Sato et al., 2008). Furthermore, ice growth instability could occur forming dendrites and trapping of pockets of highly concentrated solutions between them. This can lead to incorporation of impurities such as NO_3^- in liquid pockets, and they can display properties similar to those expected for super cooled water (Domine et al., 2013). Hence, the very high quantum yield (150 times higher than the value from Chu and Anastasio 2003) observed by Zhu and colleagues (2010) is expected to be due to the ability of the adsorbed HNO_3 to undergo photolysis, with the photoproducts easily escaping the surrounding medium after photolysis (Domine et al., 2013).

These significant differences in the quantum yields will limit further studies on constraining the photo-production of NO_X. For example, in a field study at Dome C and determination of NO_2 emission from the snowpack during photolysis of nitrate, France et al. (2011) observed a factor of about 400 more NO_2 production while using the quantum yield derived from Zhu et al (2012) than from Chu and Anastasio (2003).

To summarize, now there are a variety of observations and proposed mechanisms that give credence to the post-depositional loss of nitrate from the snowpack in low accumulation sites, and eventually leading to the deformation of the original atmospheric signal archived in the snowpack. Desorption and photolysis processes have been suggested as the causes of the loss of nitrate from the snowpack. However, a clear understanding is lacking on these loss mechanisms and their associated effects. The photolysis of nitrate in snow is a complex process, and the parameters required to constrain the process are currently missing or are not well understood. For example, there exists only measurement of the absorption cross-section of nitrate in the liquid phase (Chu and Anastasio, 2003) which can be significantly different for the snow. Approximations made for snow chemistry based on liquid phase chemistry are inadequate. Even if the quantum yield of nitrate photolysis was measured (Chu and Anastasio, 2003;Zhu et al., 2010), the values are not in agreement with each other due to the reasons explained in the sections above. With so many unknown variables, it is difficult to constrain the NO_X emission budget, and know what information is left in the snowpack after post-depositional effects.

The photochemistry of nitrate in snow focused at Dome C is briefly evaluated in this manuscript. In this study, stable isotopes of nitrate are used as scientific tools to probe post-depositional effects on nitrate in snow but a priori we need to have the basic concepts of isotope geochemistry described below.

1.3. Scientific Approaches

In order to understand the fate of deposited nitrate in snow, recovery of the original information archived in deep ice cores and the potential impact of photo-emitted products on the atmosphere, stable isotopes of nitrate (O, N) were used in this study. Even if other approaches such as concentration measurement of different N-containing species in the snow or in the overlying atmosphere also exists, isotopes are chosen in this study because of the unique information which can be obtained i.e. the oxygen isotope ratios provide information about the oxidation pathways during nitrate formation and the N isotope ratios depicts the source/origin of nitrate. In order to know how it is possible to obtain such information, let us first introduce basic definitions and notations of stable isotopes geochemistry.

1.3.1. Basics and Definitions in isotope geochemistry

An atom is composed of a positively charged nucleus and negatively charged electrons around it. The mass number of an element (A) is described as the sum of the number of protons (Z) and the number of neutrons (N). Isotopes (Greek word meaning "*equal places"* to reflect they occupy same place in periodic table) are atoms containing the same number of protons but different number of neutrons (Hoefs, 2009). Isotopes

could also be defined as nuclides of a single element with different atomic weight where nuclide referring to any type of atom (Criss, 1999).

Isotopes can be divided as radioactive or stable, a relative term depending on the detection limit of radio active decay times (Hoefs, 2009) where the former decays into daughter atoms at statistically predictable rates, and the latter do not decay or could be decaying but their half-lives are so long that it is not possible to detect (Criss, 1999). Stable nuclides can further be divided into radiogenic and non-radiogenic based on their origin. Radiogenic stable nuclides such as ^{40}Ar and ^{207}Pb are formed continuously by decay of radioactive parent element. The abundance of radiogenic nuclides depends on the available amounts of the parent material and the amount of time. To the contrary, non-radiogenic stable isotopes abundance is time independent (Criss, 1999).

The non-radiogenic stable isotopes (simply called stable isotopes throughout this thesis) of oxygen and nitrogen are the focus of this PhD thesis.

The natural abundances for major constituents of the Earth's atmosphere (H, C, N and O) are given in table 1.2.

Table 1.2. The natural abundance of selected stable isotopes

Element	**Isotope**	**Abundance (atom%)**
Hydrogen	^{1}H	99.985
Hydrogen	^{2}H	0.015
Carbon	^{12}C	98.90
Carbon	^{13}C	1.10
Nitrogen	^{14}N	99.63
Nitrogen	^{15}N	0.37
Oxygen	^{16}N	99.76
Oxygen	^{17}N	0.04
Oxygen	^{18}N	0.20

According to Muller 1994 (IUPAC recommendations 1994), a given molecule can have an isotopomer or an isotopologue. Accordingly, isotopologues are molecular entity differing only in isotopic composition such $^{16}O^{16}O$, $^{16}O^{17}O$, $^{16}O^{18}O$ and $^{17}O^{18}O$, and isotopomers are isotopes with same number of each isotope but different position in the given molecule ($^{16}O^{17}O^{16}O$ and $^{16}O^{16}O^{17}O$ for ozone molecule) (Muller, 1994).

Isotope ratios (R) and the delta notation (δ)

The isotopic composition of a given chemical element can be expressed as percentage or more conventionally as a ratio. Isotope ratios refers to the atomic

abundance ratio of a heavy (less abundant or rare) to a light (most abundant) isotopes of an element. For oxygen and nitrogen these ratios can be written as $^{17}R = n(^{17}O)/n(^{16}O)$, $^{18}R = n(^{18}O)/n(^{16}O)$ and $^{15}R = n(^{15}N)/n(^{14}N)$ respectively.
However, the isotopic composition of most natural samples is usually expressed in terms of delta values using the small delta notation (δ) defined as the relative isotopic enrichment of a sample relative to a reference material, defined mathematically as:

$$\delta = \frac{R_{sample}}{R_{reference}} - 1 \qquad (1.5)$$

where R_{sample} and $R_{reference}$ are the heavy to light isotope ratios of the sample and the reference respectively. The delta values are often reported in units of per mille (10^{-3}, ‰) or per meg (10^{-6}).
Some of the importances of using reference materials to measure and report the isotopic composition of a given compound are (Criss, 1999):

- As it is difficult to measure the absolute abundance of heavy isotopes due to their very rare availability (for eg., D/H ∼ 0.00015), performing a relative measurement with a reference of known/accepted isotopic composition will make it easier
- It can account for system variability during isotopic measurements. Measuring differences rather than an absolute ratio is more precise and minimize instrumental or sample preparation biases, as variations of isotopic content in nature are very small.
- Interlaboratory comparisons can be made relatively easily leading to interpretations of results from different laboratories coherent

For the oxygen and nitrogen isotopic measurements, Vienna Standard Mean Ocean Water (VSMOW) and Air-Nitrogen are the corresponding reference scales respectively, and they are used while reporting the isotopic measurements in this thesis. (Reference materials are briefly discussed in the Annex of this manuscript)

1.3.2. Isotope Effect

The chemical behavior of an element is basically determined by the electronic structure and minimal difference is expected between isotopes. However, this minor difference causes a significant physico-chemical behavioral variation between isotopes. The difference in mass number leading to variation in physical and chemical properties between isotopes is called isotope effect. The effect is more pronounced in lighter atoms such as hydrogen and oxygen.

The difference in physico-chemical property arises due to quantum mechanical effects. A diatomic molecule exhibits an energy restricted to certain discrete energy levels described as shown in **Fig.1.17** below. The lowest energy level is described by 1/2hν (which is above the minimum energy curve by 1/2hν) where h is the Plank's constant and ν is the vibrational frequency of the two atoms to each other.
The vibrational frequency is quantified by:

$$v = \frac{1}{2\Pi}\sqrt{\frac{k}{\mu}} \qquad (1.6)$$

where k is the reduced mass of the two atoms calculated by:

$$\mu = \frac{m_1 \times m_2}{m_1 + m_2} \qquad (1.7)$$

Hence a vibrating molecule, even at ground state with absolute zero temperature, exhibits certain zero point energy higher than the minimum in the potential energy curve called Zero Point Energy (ZPE). During isotopic substitution of a lighter atom by the heavier one in a given molecule, the ZPE of the molecule with the heavier atom will be reduced. This implies weaker bonds will be formed with molecules involving lighter isotopes than the heavier ones, and during chemical reactions molecules with the lighter isotopes mostly react relatively faster (Hoefs, 2009).

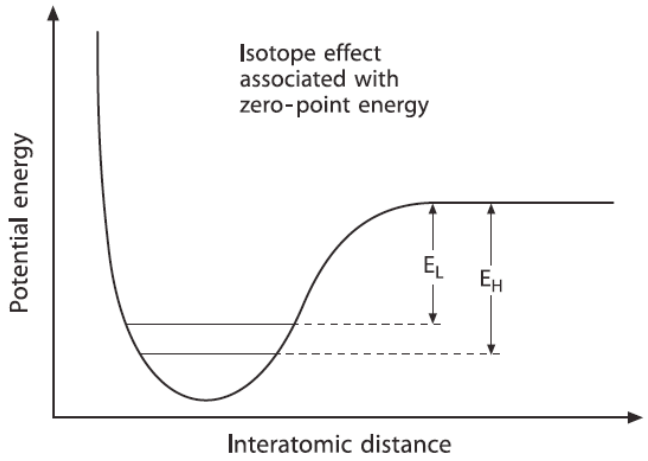

Figure 1.17. *The shift in zero point energy associated with substitution of a light isotope with a heavier one in a given molecule (Hoefs, 2009).*

1.3.3. Isotopic fractionation

Isotopic fractionation is defined as the partitioning of a sample in two or more parts with different isotopic ratios of heavy and light isotopes than the original ratio. Isotopic fractionation can be caused by equilibrium or non-equilibrium effects (kinetic) (Criss, 1999).

1.3.3.1. Equilibrium fractionation (Isotopic exchange)

These are the types of reactions which involves transfer of isotopes between different phases, different chemical substances or between individual molecules but without a net reaction.

Chemical equilibria

Isotopic exchange reaction involving chemical equilibria can be expressed as:

$$aA_1 + bB_2 \Leftrightarrow aA_2 + bB_1 \qquad \text{(R.1.32)}$$

where the subscripts 1 and 2 denotes the species A and B containing either the light or heavy isotope 1 or 2 respectively. The equilibrium constant for such reaction can be expressed as:

$$K = \frac{\left(\frac{A_2}{A_1}\right)^a}{\left(\frac{B_2}{B_1}\right)^b} \qquad (1.8)$$

Equilibrium fractionations are largest for elements with low atomic weight such as H, C, O, N and S. Because of this low atomic weight, a variation in one or more neutrons can induce a significant difference in the masses of the isotopologues containing the given element.

For isotopic exchange reactions, the equilibrium constant *K* is often replaced with the fractionation factor α. Isotopic fractionation factor refers to the partitioning of isotopes between two separate phases or two parts of a system (A and B), and it can be described mathematically as:

$$\alpha_{A\text{-}B} = R_A/R_B \qquad (1.9)$$

where R represents the atomic ratio of heavy to light species (Criss, 1999).
For isotopes randomly distributed overall positions between compounds A and B, the fractionation factor is related to the equilibrium constant K by:

$$\alpha = K^{1/n} \qquad (1.10)$$

where n is the number of atoms exchanged.
Note that for isotopic exchange reactions involving a single atom, the fractionation factor is same as the equilibrium constant. Additionally, isotopic fractionation effects tend to be small, and the value is usually very close to one (Hoefs, 2009). Hence, it is usually expressed by the fractionation constant (ε) as:

$$\varepsilon = 1 - \alpha \qquad (1.11)$$

ε is usually reported in units of "permil, ‰" and sometimes in "permeg"

Physical equilibria

In contrary to chemical equilibria where isotopic exchange takes place between different chemical species, physical equilibria takes place within molecules of the same species but in different phases. For example the isotopic exchange of ^{18}O between the liquid water and water vapor.

$$H_2{}^{16}O(l) + H_2{}^{18}O(g) \leftrightarrow H_2{}^{18}O(l) + H_2{}^{16}O(g) \qquad \text{(R.1.33)}$$

The equilibrium fractionation factor for this reaction can be expressed as:

$$\alpha_{gas\text{-}liquid} = (^{18}O/^{16}O)_{gas} / {}^{18}O/^{16}O)_{liquid} \qquad (1.12)$$

The difference in vapor pressure between isotopic compounds can lead to an isotopic fractionation. For example ^1H_2O has a higher vapor pressure than ^2H_2O, and hence the vapor will be enriched in light isotopes than the liquid. It should be noted that α is strongly dependent on temperature, and hence determines the isotopic composition of atmospheric water vapor. This is the basis for using the stable isotopes of water as metrics for global hydrological cycles (Rozanski et al., 2001).

Open and closed systems

In a closed system isotopic fractionation is accompanied by conservation of mass and isotopic composition of the system i.e. δ_{system} is constant. For a system composed of liquid and vapor phases:

$$\delta_{vapor} = \delta_{system} + f\,\varepsilon \qquad (1.13)$$

where f is the mass fraction in the liquid reservoir. When the entire system is in the vapor form ($f = 0$) and $\delta_{vapor} = \delta_{system}$. In contrary, when the entire system is condensed into the liquid phase ($f = 1$), $\delta_{vapor} = \delta_{system} + \varepsilon$.
However, the Earth's system is mostly open and may not conserve mass and isotopic composition. For such processes involving an open system where a trace substance is removed from a large reservoir continuously, the isotopic fractionation process is called Rayleigh fractionation, and it can be treated theoretically using the Rayleigh equation (Criss, 1999). For a condensation process this equation can be written as:

$$\left(\frac{R}{R_i}\right) = f^{\alpha-1} \qquad (1.14)$$

where f represents the fraction of the residual vapor, R_i is the isotope ratio of the bulk composition, and R is the instantaneous ratio of the remaining vapor (Hoefs, 2009). This equation is valid when a given material is removed from the system continuously, the fractionation associated with the removal process can be described using the fractionation factor, and if this factor does not change during the process at constant temperature. Equation 1.14 can also be expressed in terms of δ-values as:

$$\frac{\delta + 1}{\delta_0 + 1} = f^{\alpha - 1} \qquad (1.15)$$

Figure 1.18 shows a Rayleigh plot for liquid-vapor equilibrium in open and closed systems (Criss, 1999). As condensation occurs progressively, heavy isotopes will be removed from the vapor phase, and eventually the residual vapor becomes depleted in heavy isotopes.

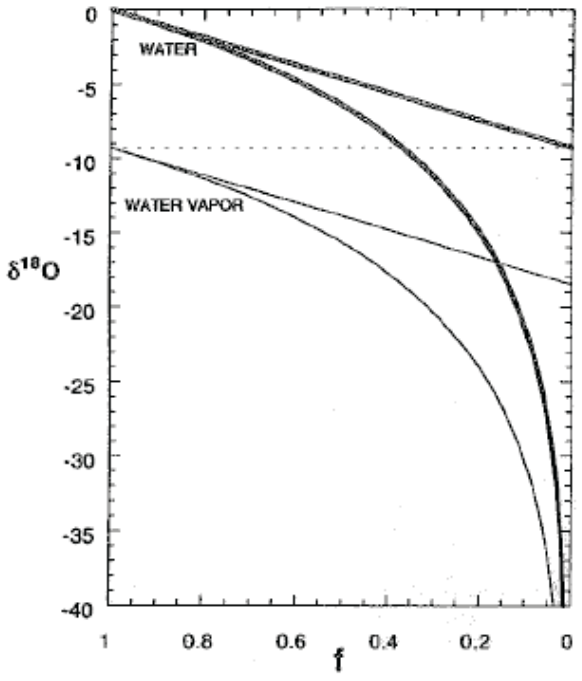

Figure 1.18. *The $\delta^{18}O$ of liquid water (thick lines) and water vapor (thin lines) versus the fraction of water vapor remaining in an open system (curved lines) and closed systems (straight lines). The dotted line represents the δ-values of the initial vapor.*

A simple natural log of equation 1.15 and substituting ε for (α-1) allows the determination of the fractionation constant:

$$\ln(\delta + 1) = \varepsilon \ln f + \ln(\delta_0 + 1) \qquad (1.16)$$

where δ_0 and δ are the isotopic composition at the beginning and at the end of the process respectively. Equation 1.16 will be repeatedly used in this manuscript.

1.3.3.2. Non-equilibrium Fractionation

These are processes associated with isotopic systems out of equilibrium and even products may become physically isolated from the reactants (unidirectional) such as diffusion, evaporation, and dissociation reactions which arises due to difference in mass

and zero point energy (Criss, 1999). The knowledge of these effects enables to understand various atmospheric chemical reaction pathways.

Diffusion

Diffusion of molecules could lead to distribution of isotopes in different proportion simply due to the difference in the mass of the isotopes. At a given gas temperature, lighter species diffuse faster than heavier species. Referring to the gas law, the translational velocity of molecules is indirectly related the square roots of their respective masses. Hence, lighter molecules will escape faster a given system than the heavier ones, leading to an enrichment of the reservoir with time.

Evaporation

Evaporation is associated with molecules escaping from the bulk liquid, and similar to diffusion where the lighter isotopes with higher translational velocity preferentially escape the bulk leaving it enriched with time.

Kinetic Isotopic Effects

These effects are related to the difference in dissociation energies of molecules containing different isotopes. For example species containing light isotopes have relatively weaker bonds (higher vibrational frequency) than species with heavier isotopes. During bond breaking reactions such as photolysis where weaker bonds are broken primarily, the light isotopes will be preferentially incorporated into the product side leaving the residue enriched in heavy isotopes.

1.3.4. Mass Independent Fractionation (MIF)

For two isotopically substituted molecules, the difference in their physical and chemical property is expected to arise only due to their difference in mass and termed as Mass Dependent Fractionation. For oxygen, one of the most abundant atmospheric gases, this can be expressed as the enrichment of the ^{18}O relative to ^{16}O is about twice that of the enrichment of ^{17}O relative to ^{16}O and it can be mathematically defined as:

$$\delta^{17}O = \lambda\delta^{18}O \qquad (1.17)$$

where λ is the slope of the $\delta^{17}O$ versus $\delta^{18}O$ plot called three isotopic plot. For molecular oxygen with three isotopes, the value of λ can be approximated by equation 1.18 (Young et al., 2002;Thiemens, 1999).

$$\frac{\delta^{17}O}{\delta^{18}O} \cong \frac{\left(\frac{1}{32}-\frac{1}{33}\right)}{\left(\frac{1}{32}-\frac{1}{34}\right)} = 0.516 \qquad (1.18)$$

Depending on the molecular mass and nature of process, the value of the coefficient for oxygen can vary between 0.529 (for atomic oxygen) and 0.500 (for higher molecular weight species) (Thiemens, 1999).

Different atmospheric species and minerals obey this rule and lies along the Terresterial Fractionation Line (TFL) with a slope $\lambda \approx 0.52$, in agreement with Urey's model prediction (Urey, 1947). However, this rule is not respected by few atmospheric species. After analyzing the multiple oxygen isotopic composition in Chondrules, the deviation from the TFL was first revealed by (Clayton et al., 1983) (**Fig. 1.19**). Accordingly, a $\delta^{17}O \approx \delta^{18}O$ relation was observed and it was suggested that it is due to nuclear processes rather than chemical processes. Later on, Thiemens and Heidenreich observed $\delta^{17}O$ values comparable to the $\delta^{18}O$ in ozone generated in the laboratory from molecular oxygen using an electrical discharge demonstrating that such effect can also arises chemically (Thiemens and Heidenreich, 1983).

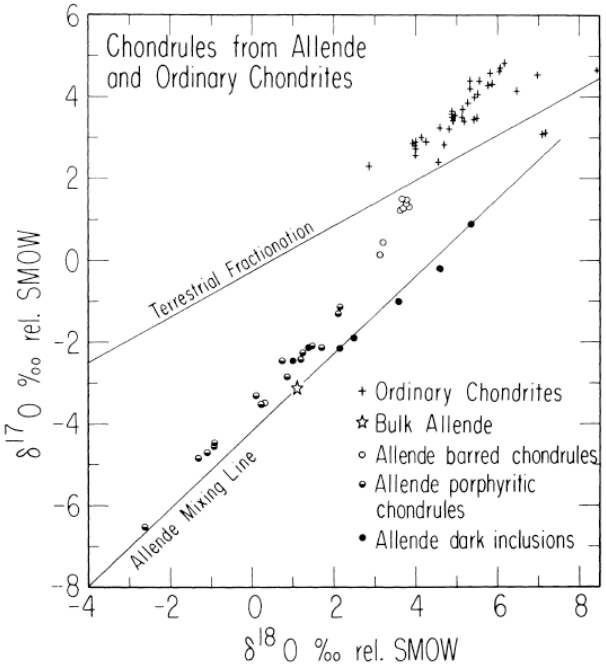

Figure 1.19. *The oxygen isotopic composition from different Chondrules sources (Clayton et al., 1983)*

The process responsible for this deviation is named as "Mass Independent Fractionation, MIF", or "Non-mass Dependent Fractionation" and quantified using the term "^{17}O-excess" denoted as $\Delta^{17}O$ and expressed mathematically as:

$$\Delta^{17}O = \delta^{17}O - \lambda \times \delta^{18}O \qquad (1.19)$$

Equation 1.19 is derived from its original MDF relation and it has significant limitations. Firstly, the slope $\lambda = 0.52$ used in this equation, which has emerged from the measurement of terrestrial and water samples which yielded a slope of 0.5164 ± 0.0033 reviewed in (Miller, 2002), has been a subject of debate due to its inconsistency as it is

fractionation process or origin dependent. Different λ values have been obtained for variety of water and rock samples and different studies apply different λ values. However, for atmospheric species with higher ^{17}O-excess (typically $\Delta^{17}O > 20$ ‰), the choice of slope of 0.52 has been widely accepted due to its minor impact on the overall $\Delta^{17}O$ values.

Secondly, expression of the ^{17}O-excess is not consistent between different studies in which linear, logarithmic or power-law form of approximations exist. Miller (2002) used the power-law derived ^{17}O-excess definition as:

$$\Delta^{17}O + 1 = \frac{1+\delta^{17}O}{(1+\delta^{18}O)^{\lambda}} \qquad (1.20)$$

Equation 1.20 has been suggested to be preferable expression as the slope of the fractionation line is invariant to the magnitude of the δ-values and the choice of the reference gas (provided all the references lie at the same MDF line) (Kaiser et al., 2004;Miller, 2002). However, in the case of nitrate and in this thesis, the application of equation 1.19 is practical and the difference is minor in $\Delta^{17}O$ if equation 1.20 was used. Besides, equation 1.19 has been implemented widely in previous studies in this field (Savarino et al., 2007;Morin et al., 2009;Michalski et al., 2003), and hence it will ensure consistency and eases comparison between the findings from this study with the existing measurement values. Additionally, the linear form is mathematically simple to make calculations.

In addition to ozone, other atmospheric species were also found carrying this ^{17}O-excess (**Fig. 1.20**). However, laboratory and field observations verified that their ^{17}O-excess was not directly generated but inherited/transferred from ozone during various atmospheric oxidation processes (Michalski et al., 2003;Röckmann et al., 2001;Yung et al., 1991;Savarino et al., 2000). While this conclusion is widely accepted today, the quantification of this transfer remains mainly on untested hypothesis.

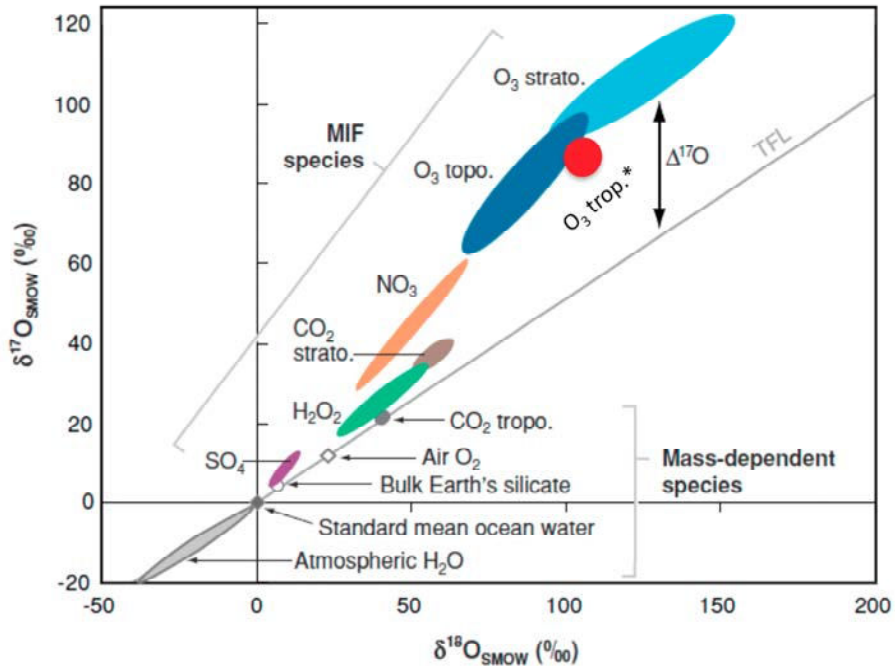

Figure 1.20. *The three isotopic plot showing the different species that obey or do not obey the mass dependent rule (Thiemens, 2006). The red circle for O_3 trop* is an updated measurement of tropospheric ozone based on the analysis of the oxygen isotopes of tropospheric ozone at different geographical locations using the nitrite coated filter method (Vicars et al., 2012) as well as measurements in the early 90's (Krankowsky et al., 1995;Johnston and Thiemens, 1997).*

1.3.5. MIF in ozone

Ozone is an important atmospheric oxidant which possesses a large ^{17}O-excess described in previous sections. There have been a number of studies conducted to understand why there exists ^{17}O-excess in ozone. A brief analysis and historical development/measurement towards understanding MIF in ozone can be found in literatures (Thiemens, 2006;Brenninkmeijer et al., 2003;Marcus, 2008;Janssen et al., 2001), and only a brief summary will be provided in this manuscript.

Thiemens and Heidenreich (1983) generated ozone from molecular oxygen via electrical discharge. After cryogenically separated the ozone molecule and converted it to oxygen, they have analyzed its triple oxygen isotopes using isotope ratio mass spectrometer. They have obtained a slope of 1 on their three-isotope plot. This was the first experimental/labaratory observation of MIF in ozone due to chemical mechanism. Their experimental study was the benchmark for further experimental studies on ozone which are employed until today.

Further experiments were also carried out to understand how temperature and pressure play a role on the enrichments in $\delta^{17}O$ and $\delta^{18}O$ in mass-independent fashion observed in ozone. Thiemens and Jackson (1987) observed the pressure dependence of isotopic enrichment in ozone produced by UV light photolysis of O_2. Accordingly, $\delta^{17}O = \delta^{18}O = 90$ ‰ which was dominant above 20 torr, and $\delta^{17}O = -27.5$ ‰ and $\delta^{18}O = -55$‰

dominant below 6 torr were observed. With further experimental studies (Thiemens and Jackson, 1990, 1987;Morton et al., 1990;Bainssahota and Thiemens, 1987), the pressure dependence of enrichment in ozone was briefly described. These studies showed that at low pressure ranges (below 100 torr) enrichment in ozone is more or less constant but higher than enrichments at higher pressure ranges (see **Fig. 1.21a**). Enrichment is intermediate at pressure range of about 100 torr to 600 torr.

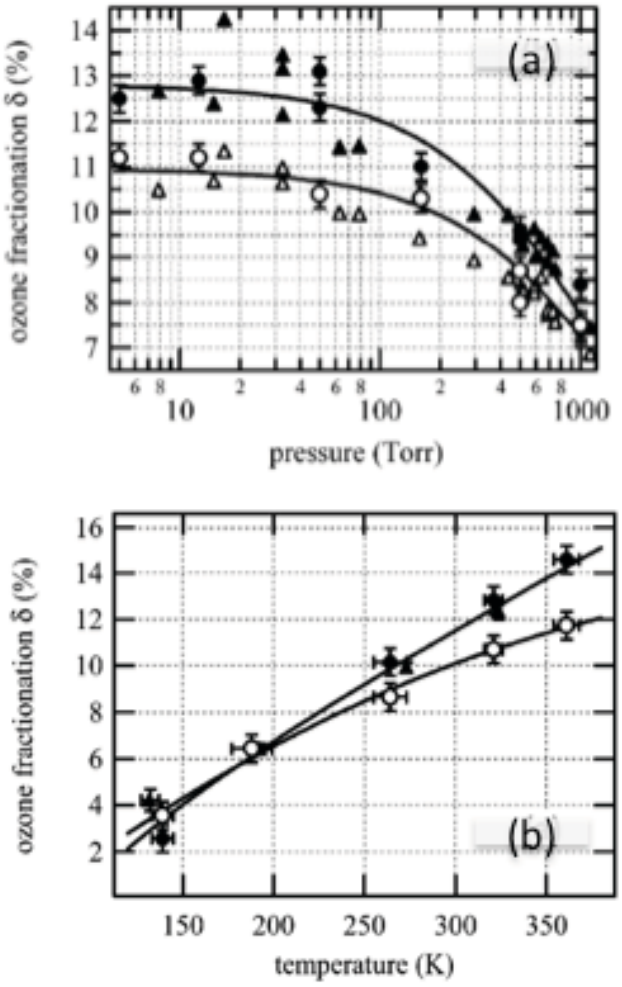

Figure 1.21. *The pressure and temperature dependence in enrichments in $\delta^{17}O$ (open symbols) and $\delta^{18}O$ (closed symbols) in ozone formed from pure oxygen or air (Brenninkmeijer et al., 2003).* ***Top panel (a)****: $\delta^{17}O$ and $\delta^{18}O$ values between 5-1000 torr. Circles and triangles represent values obtained at 321 K (Morton et al., 1990) and at room temperature (Thiemens and Jackson, 1990, 1988) respectively. Best fit curves for the data from Morton et al. (1990) are obtained from (Guenther et al., 1999).* ***Bottom panel (b)****: $\delta^{17}O$ and $\delta^{18}O$ values between 130 K and 360 K. Circles and triangles represent values obtained at oxygen pressures of 50 torr (Morton et al., 1990) and at 45 torr (Janssen et al., 2003).*

The direct effect of temperature in the observed enrichments in ozone was also experimentally verified (Morton et al., 1990;Janssen et al., 2003) with a different

experimental set-up than the previous electric discharge experiments. In the previous experiments (Thiemens and Jackson, 1990, 1988), there was no control over temperature, and as the ozone is formed in a trap immersed in liquid nitrogen, its temperature is expected to vary between the discharge temperature and the liquid nitrogen temperature. Morton and co-workers designed a photolysis recycling experiment where the temperature and pressure can be controlled. At a constant oxygen gas pressure of 50 torr, observed the temperature dependence enrichment of $\delta^{17}O$ = 36 ‰ and $\delta^{18}O$ = 26 ‰ at 130 K to $\delta^{17}O$ = 117 ‰ and $\delta^{18}O$ = 146 ‰ at 361 K (Morton et al., 1990) (see **Fig. 1.21b**).

The studies mentioned above were the bench marks for further laboratory and field studies due to the possibility of interpolating these values to the required temperature and pressure regimes as needed. In chapter 2 of this manuscript, pressure and temperature of ozone formation were manipulated to generate ozone with different ^{17}O-excess values.

In order to have an advanced understanding and provide supporting information for the experimental observations of strangely large enrichment in ozone, different theoretical approaches were also provided. The RRKM theory (Rice-Ramsperger-Kassel-Markus) developed by Marcus and co-workers was the most successful describing the isotopic effect in ozone and is discussed below (Marcus, 2008;Hathorn and Marcus, 1999;Gao and Marcus, 2001).

Ozone can be formed from atomic oxygen produced from photolysis of molecular oxygen via:

$$O + O_2 \leftrightarrow O_3^* \qquad \text{(R.1.33)}$$

$$O_3^* + M \rightarrow O_3 + M \qquad \text{(R.1.34)}$$

After formation of an excited ozone molecule, an intramolecular energy redistribution will take place between the rotational and vibrational energy levels which depends on the molecular symmetry. According to the RRKM theory, symmetric species ($^{16}O^{16}O^{16}O$, $^{16}O^{17}O^{16}O$, etc) have fewer intramolecular couplings for energy redistributions due to symmetry restrictions. This will lead to shorter lifetime of the O_3^*, and consequently lower rate of stabilized O_3 formation associated with reduced probability of collision to loose the excess energy. In contrary, the asymmetric isotopomers have longer lifetimes due to increased probability for energy redistribution. This will lead to higher rate of stabilized ozone formation with an equal fractionation of the heavy isotopes. However, this is a semi-empirical model which uses an adjustable parameter η =1.18 (Gao and Marcus, 2001). The physical meaning behind the RRKM theory is that enrichment in ozone is symmetry driven i.e. only the asymmetric isotopomers exhibit non-zero ^{17}O-excess. For ozone molecule composed of two terminal (O_{ter}) and one central atom (O_{cen}), a mass balance equation can written as:

$$3\,\Delta^{17}O\,(O_3) = 2\,\Delta^{17}O\,(O_{ter}) + \Delta^{17}O\,(O_{cen}) \qquad (1.22)$$

As the theory states that the ^{17}O-excess on the central atom is zero, equation 1.22 will be reduced to:

$$\Delta^{17}O\ (O_{ter}) = 1.5 \times \Delta^{17}O\ (O_3) \qquad (1.23)$$

This theory has been tested experimentally in different studies via reaction of ozone with Ag (Savarino et al., 2008;Michalski and Bhattacharya, 2009;Bhattacharya et al., 2008), NO (Savarino et al., 2008) and NO_2^- (Michalski and Bhattacharya, 2009). These studies were based on previously existing study which states that during oxidation of atmospheric species, it is preferably the terminal atom will be transferred to other species (Liu et al., 2001). Even if their results agree on the existence of ^{17}O-excess mainly on the terminal atom, the transferable quantity is not always equal to the ^{17}O-excess of the terminal atom. In order to account for this possibility, the transferable ^{17}O-excess can be represented by $\Delta^{17}O\ (O_3^*)$ expressed as:

$$\Delta^{17}O\ (O_3^*) = \alpha\ \Delta^{17}O\ (O_3) + b \qquad (1.24)$$

where α is a factor representing fraction of ^{17}O-excess transferable from the bulk and b is introduced to account for the fact when $\Delta^{17}O\ (O_3) = 0$, it does not necessarily imply that $\Delta^{17}O\ (O_{ter})$ and $\Delta^{17}O\ (O_{cent})$ are zero as proposed by the theory (Savarino et al., 2008). Other mechanisms during ozone formation (rotation, exchange, cyclic ozone) can lead to atom scrambling within the metastable ozone intermediate, generating artificial non-zero $\Delta^{17}O\ (O_{cen})$. In cases where $\alpha = 1.5$ is observed, it will be a direct indication that the reaction takes place with the transfer of the terminal atom transfer exclusively (Savarino et al., 2008).

The transferable ^{17}O-excess is an important tool in the chemistry of many chemical species in the atmosphere as it can provide information about their oxidation pathways. The implication of this quantity in nitrate samples measured at different geographical locations will be briefly discussed in the sections below but in prior, the knowledge of ^{17}O-excess in atmospheric ozone is essential.

1.3.6. Measurements of ^{17}O-excess in tropospheric ozone

Measuring the isotopic composition of tropospheric ozone is a complicated task due to the high oxygen to ozone ratio. Krankowsky et al. (1995) measured the isotopic composition of tropospheric ozone (Heidelberg, Germany) for the first time. Ozone collected via cryogenic trapping and converted to oxygen gas had average value of $\delta^{17}O = 71$ ‰ and $\delta^{18}O = 91$ ‰. This measurement was in good agreement with the prediction in $\delta^{17}O$ values from laboratory studies but has lower enrichment in $\delta^{18}O$ values which could be attributed to extra fractionations in tropospheric ozone and systematic errors (Brenninkmeijer et al., 2003). Following this, Johnston and Thiemens (1997) performed similar studies at three sites: Pasadena, La Jolla and White Sand. Accordingly, $\delta^{17}O$ values ranging 66-78 ‰ and $\delta^{18}O$ values ranging 82-90 ‰ were measured at these sites (see **Fig. 1.22**). The authors suggested ozone decomposition variability between the three sites as the source of differences observed in the isotopic composition of ozone. However, low sample collection efficiency, interference from Xenon during isotopic measurement and sample storage were suggested as possible factors for the observed variability (Brenninkmeijer et al., 2003). Both datasets from Krankowsky, and Johnston

and Thiemens measurements were in good agreement in the average $\Delta^{17}O$ about 25‰ excluding the White Sand measurement (due to high altitude) (Brenninkmeijer et al., 2003). This average value of $\Delta^{17}O$ of tropospheric ozone is used today in different modeling calculations which use the ^{17}O-excess in ozone to model the isotopic anomaly in other species such as nitrate (Morin et al., 2009;Alexander et al., 2009). However, theoretical calculations set this value even higher for example $\Delta^{17}O(O3)$ = 35 ‰ (Lyons, 2001). The variation in the $\Delta^{17}O$ values of ozone has a significant effect in modeling calculations of determination of isotopic anomaly in other atmospheric species such as nitrate (discussed below).

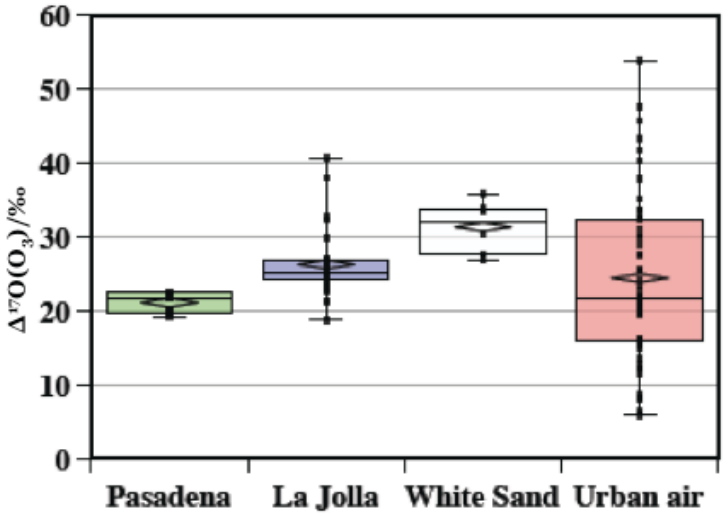

Figure 1.22. *The ^{17}O-excess values of tropospheric ozone measured at Pasadena, La Jolla and White Sand (Johnston and Thiemens, 1997) as well as in Urban air (Krankowsky et al., 1995). (Adapted from: Morin et al., 2007).*

1.3.7. Atmospheric observations of ^{17}O-excess in nitrate

The $\Delta^{17}O$ signal of atmospheric ozone is a conserved quantity (i.e., it cannot be altered via mass-dependent fractionation processes), which can be partially or completely transferred to other species through oxidation reactions (Thiemens, 2006;Michalski and Bhattacharya, 2009;Lyons, 2001). Ozone is an important atmospheric oxidant and during this process it transfers its ^{17}O-excees to the other atmospheric species. As a result of this ^{17}O-excess transfer, $\Delta^{17}O$ values of oxygen-bearing atmospheric species serve as proxies for the influence of ozone in their chemical formation pathways. This provides a unique approach for tracing chemical oxidation pathways in the atmosphere, and it has yielded valuable insight into the atmospheric dynamics of several key species such as nitrate.

Nitrate is the end product of atmospheric NO_X oxidation and possesses high ^{17}O-excess inherited from ozone (Savarino et al., 2007;Morin et al., 2008b;Morin et al., 2007b;Michalski et al., 2003). During the oxidation reactions of NO_X with ozone, the ^{17}O-excess of ozone is ultimately transferred to nitrate.

Large oxygen isotope anomalies have been measured in nitrate samples obtained from various parts of the globe, however; the amount of ^{17}O-excess in the nitrate samples

is highly variable. $\Delta^{17}O$ values for atmospheric nitrate varying from 20 ‰ to 31 ‰ was measured in samples from the Atacama desert in Chile and La Jolla, California (Michalski et al., 2003). A relatively higher ^{17}O-excess was measured in nitrate samples from polar sites. From a set of aerosol samples collected in coastal Antarctica over a year, Savarino et al. (Savarino et al., 2007) measured $\Delta^{17}O$ of 24 ‰ – 39 ‰. McCabe et al. (2007) established a seasonal variation of $\Delta^{17}O$ of aerosol nitrate from 22.6 ‰ – 28.5 ‰ in summer and 38.1 ‰ in winter in Antarctic snow. All these measurements showed that atmospheric nitrate is characterized by a highly positive anomaly and there is a large variation among samples. The observed variation ^{17}O-excess is attributed to the variation in the nitrate formation pathways which is in turn dependent on space and time. Currently, a theoretical approach is widely applied which uses the ^{17}O-excess signal to infer to the high $\Delta^{17}O$ of nitrate samples associated with nitrate formation pathways. This model which was originally developed by Lyons (Lyons, 2001) and further adopted by many scientific studies (Morin et al., 2009;Michalski et al., 2003;Alexander et al., 2009;Morin et al., 2011) is based on the basic principle that sink reactions do not induce isotopic fractionations in a mass independent fashion, and every source reaction induces a transfer of a given $\Delta^{17}O$ value to the newly formed species. Hence, simple mass balance calculations can be employed to identify the nitrate formation pathways based on the measured $\Delta^{17}O$ values.

1.3.8. Mass balance calculations for $\Delta^{17}O$ of nitrate

In section 1.2.2, a brief discussion is given regarding the atmospheric chemistry of NO_X and nitrate formation pathways. Accordingly, nitrate formation can follow either daytime or nighttime oxidation pathway. For clarity, the schematic on NO_X oxidation pathways is shown below (re-plot of **Fig. 1.9**). Detailed mass balance calculations can be found in the literature (Morin et al., 2007b;Morin et al., 2011), and here a short revision is provided.

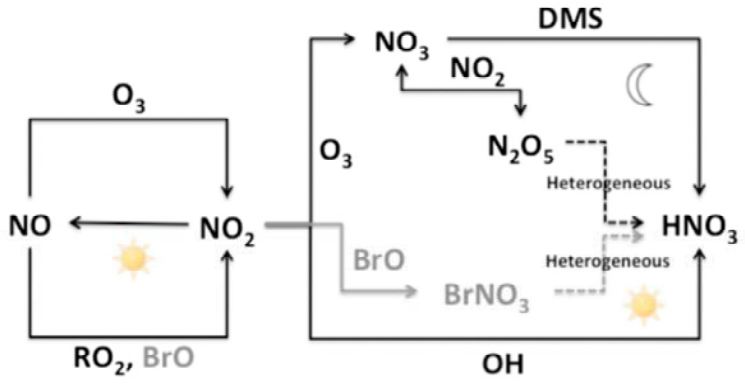

Figure 1.23. *The NO_X cycling and nitrate formation pathways in the atmosphere. The sun represents the daytime mechanism whereas nighttime pathways are shown using the moon. Dashed lines represent the heterogeneous nitrate formation pathways.*

The general mass balance equation governing the ^{17}O-excess in nitrate can be written as:

$$\Delta^{17}O\ (NO_3^-) = 2/3 \times \Delta^{17}O\ (NO_2) + 1/3 \times \Delta^{17}O\ (O_{add}) \qquad (1.25)$$

where $\Delta^{17}O\ (NO_2)$ refers to the ^{17}O-excess originating from NO_2 and $\Delta^{17}O\ (O_{add})$ describes the ^{17}O-excess contribution to nitrate from the additional oxygen atom. This contribution depends on the mechanisms of conversions of NO_2 to nitrate shown in **Fig. 1.23**. Referring to this figure, the formation of $\Delta^{17}O\ (NO_2)$ depends on the concentration and rate of formations of O_3 and RO_2/HO_2 (In the first approach, the Bromine chemistry is not considered). During photochemical steady state, $\Delta^{17}O\ (NO_2)$ can be described by:

$$\Delta^{17}O\ (NO_2) = \alpha\, \Delta^{17}O\ (O_3^*) \qquad (1.26)$$

where $\Delta^{17}O\ (O_3^*)$ denoted the transferable ^{17}O-excess from O_3 to NO_2 during oxidation of NO and α is expressed by:

$$\alpha = \frac{k_{NO+O_3}[O_3]}{k_{NO+O_3}[O_3] + k_{NO+HO_2}[HO_2] + k_{NO+RO_2}[RO_2]} \qquad (1.27)$$

where k denotes the reaction rate constants for the reaction between NO and its oxidants (O_3, HO_2 and RO_2) and α can vary between values less than one (during daytime when RO_2 is involved in oxidation of NO_2) and close to one (during the night when photochemical steady state breaks down) (Morin et al., 2009). In these equations, the $\Delta^{17}O\ (RO_2/HO_2)$ is set to 0 ‰ as the peroxy radicals are produced from O_2 which possesses ^{17}O-excess value nearly zero (Savarino and Thiemens, 1999).

The nitrate formation pathways with contribution of an additional oxygen atom can be described with the following reactions:

$NO_2 + OH + M \rightarrow HNO_3 + M$ (R.1.34)

$NO_2 + O_3 \rightarrow NO_3 + O_2$ (R.1.35)

$NO_3 + RH \rightarrow HNO_3 + R$ (R.1.36)

$NO_2 + NO_3 \leftrightarrow N_2O_5$ (R.1.37)

$N_2O_5 + H_2O_{liq} \rightarrow 2HNO_{3,aq}$ (R.1.38)

To determine the mass balance equation for nitrate formation pathways (R.1.34-R.1.38), we will need the ^{17}O-excess contributions from OH, H_2O, O_2 and O_3.
OH can be formed via (R.1.40.a-c):

$O_3 + h\nu \rightarrow O(^1D) + O_2$ (R.1.39)

$O(^1D) + H_2O \rightarrow 2OH$ (R.1.40.a)

$$NO + HO_2 \rightarrow NO_2 + OH \qquad \text{(R.1.40.b)}$$

$$O_3 + HO_2 \rightarrow 2O_2 + OH \qquad \text{(R.1.40.c)}$$

The OH radical formed via R.1.40.a should carry a $\Delta^{17}O$ (OH) = 0.5 × $\Delta^{17}O$ ($O(^1D)$). However, rapid exchange of OH with tropospheric water (Dubey et al., 1997) which possess a ^{17}O-excess value of zero (Zahn, 2006) will lead to $\Delta^{17}O$ (OH) = 0 ‰. The OH produced via the two other reactions, R.1.40 b and c, will also possess negligible $\Delta^{17}O$ values due to the $\Delta^{17}O$ (HO_2/RO_2) (Savarino and Thiemens, 1999). Hence, for nitrate formation via R.1.34, an important mass balance approximation can be given by:

$$\Delta^{17}O\ (NO_3^-) = 2/3\ \alpha\ \Delta^{17}O\ (O_3^*) \qquad (1.25)$$

For nitrate formation via R.1.35-36, which involves the transfer of additional terminal oxygen atom from ozone, the $\Delta^{17}O$ of nitrate can be expressed by:

$$\Delta^{17}O\ (NO_3^-) = 2/3\ \alpha\ \Delta^{17}O\ (O_3^*) + 1/3\ \Delta^{17}O\ (O_3^*) \qquad (1.26)$$

Similarly, for nitrate formed from hydrolysis of N_2O_5 (R.1.37-38), the mass balance equation describing the ^{17}O-excess in nitrate can be written as:

$$\Delta^{17}O\ (NO_3^-) = 1/3\ \alpha\ \Delta^{17}O\ (O_3^*) + ½\ [2/3\ \alpha\ \Delta^{17}O\ (O_3^*) + 1/3\ \Delta^{17}O\ (O_3^*)] \qquad (1.27)$$

The mass balance calculations for nitrate will be modified during special conditions when the bromine chemistry will become relevant (mainly during polar spring) in nitrate formation pathways. Much attention has been given to the role of bromine chemistry in the ^{17}O-excess record of nitrate from polar regions more recently. Briefly, the BrO molecule produced during the reaction of Br with ozone (*see section* 1.2.2.3) will react with NO/NO_2 to produce $BrNO_3$ which will eventually undergo hydrolysis to produce nitrate. This hydrolysis reaction is an important mechanism which can incorporate an oxygen atom carrying a ^{17}O-excess from ozone into nitrate i.e. during hydrolysis of $BrNO_3$, a nucleophillic attack by water molecule will extract the bromine atom leaving the oxygen from BrO to be incorporated into the HNO_3 produced (Gane et al., 2001). As BrO is formed exclusively via R.1.20, and during its formation it abstracts most likely the terminal oxygen of ozone (Zhang et al., 1997), a higher ^{17}O-excess is predicted in nitrate from polar regions in the presence of bromine chemistry (Morin et al., 2007b). Hence, the $\Delta^{17}O$ (NO_3^-) can be described by:

$$\Delta^{17}O\ (NO_3^-) = (2\alpha+1)/3 \times \Delta^{17}O\ (O_3^*) \qquad (1.28)$$

where α can be expressed as:

$$\alpha = \frac{k_{NO+O_3}[O_3] + k_{NO+BrO}[BrO]}{k_{NO+O_3}[O_3] + k_{NO+BrO}[BrO] + k_{NO+RO_2}[RO_2] + k_{NO+HO_2}[HO_2]} \qquad (1.29)$$

Equations 1.25-1.28 express the possible contribution of ^{17}O-excess from individual pathways forming nitrate. However, in atmospheric conditions rather than individual pathways, multiple nitrate formation pathways exist and depending on space and time each pathway can be a dominant nitrate formation mechanism. Hence, the final isotopic composition of nitrate will be determined by the weight of each reaction pathway. These mass balance equations play a fundamental role in the modelling studies discussed below.

1.3.9. Modelling of the $\Delta^{17}O$ (NO_3^-)

Few studies exist on modelling the ^{17}O-excess in nitrate samples obtained from different geographical regions. Michalski and co-workers (2003) used a modelling approach to evaluate the $\Delta^{17}O$ (NO_3^-) measured in aerosol nitrate samples from coastal La Jolla, CA which ranges 20-30.8 ‰. Based on individual reaction pathways and transfer mechanisms of ^{17}O-excess explained in section 1.3.8, they have modelled the seasonal variation of $\Delta^{17}O$ (NO_3^-). The calculations are based on a strong assumption of the $\Delta^{17}O$ (O*) values and $\Delta^{17}O$ values are generated only by mass transfer of oxygen atoms from ozone to products during oxidation. The authors were able reproduce the winter and spring observations with their model. However, the late summer and fall values were overestimated due to a seasonal shift from about 50 % homogeneous (R.1.34) during spring to more than 90 % heterogeneous (R.1.38) reaction pathway during the winter (Michalski et al., 2003). This was the first isotopic evidence which supports the available NO_X models stating hydrolysis of N_2O_5 dominates the production of HNO_3 in winter.

Morin et al. (2008) also conducted a year round study on the NO_X/nitrate chemistry at Alert, Canada. From the analysis of the triple oxygen isotopes of atmospheric nitrate samples, a clear seasonal trend was observed in the $\Delta^{17}O$ of nitrate values (*see* **Fig. 1. 24**). The highest $\Delta^{17}O$ (NO_3^-) values were observed in the spring and the lowest values were on summer. According to this study, three dominant nitrate formation mechanisms from NO_2 were proposed for each season, and were tested for their contribution to the observed ^{17}O-excess in nitrate at this site. These are reactions with OH (summer), O_3 (winter) and BrO dominant reactions during surface ozone depletion events (spring). The observations in winter and summer were in good agreement based on their model predictions for these seasons and considering the long-range transport of atmospheric nitrate from mid-latitude regions. However, the measured spring $\Delta^{17}O$ (NO_3^-) are higher than predicted by the model. The only possible nitrate formation mechanism which was not considered in the model was the nitrate formation via hydrolysis of $BrNO_3$. These discrepancies strongly suggest the importance of the oxidation of NO_X with BrO and eventually formation of nitrate via hydrolysis of $BrNO_3$. Such chemistry was also provided as the explanation for the discrepancy observed between the measured and modelled values of the ^{17}O-excess in nitrate from Summit, Greenland (Kunasek et al., 2008). During this study, the authors observed good agreement between the measured and modelled values in winter but not in summer with a difference of about 2-7 ‰ in the $\Delta^{17}O$ of nitrate.

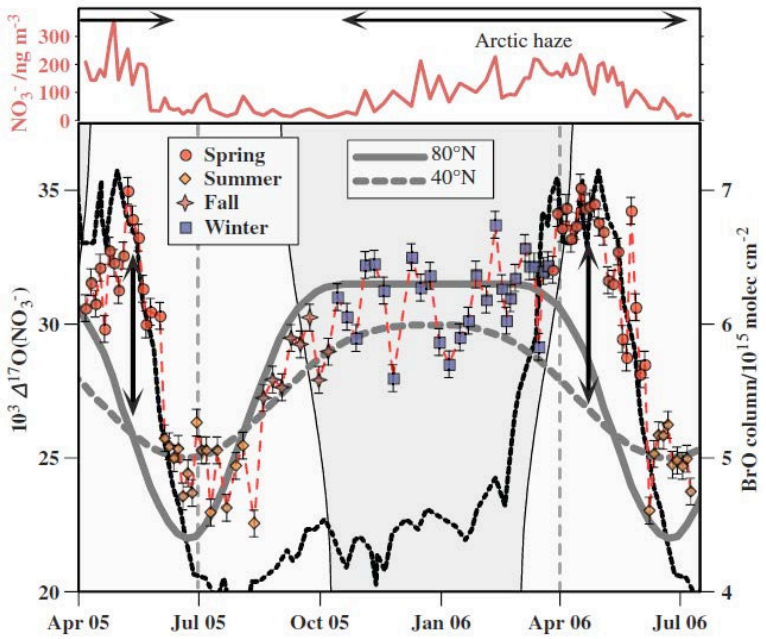

Figure 1.24. *The concentration and $\Delta^{17}O$ (NO_3^-) values from atmospheric nitrate collected at Alert, Canada (Morin et al. 2008). The black dashed line represents satellite retrieved BrO measurement data. Solid and dashed grey lines represent calculated $\Delta^{17}O$ (NO_3^-) values at 80°N and 40°N latitudes respectively. The strong deviations from these calculations during spring caused by interaction between snowpack emitted NO_X and BrO are shown using the vertical thick black arrows.*

Recently, Savarino and co-workers established the yearly profile of nitrate from a tropical marine boundary coupling both field observations and modelling calculations. The authors determined $\Delta^{17}O$ values ranging 26-30 ‰ for nitrate samples at the Cape Verde observatory with minimum $\Delta^{17}O(NO_3^-)$ in summer and maximum in winter (Savarino et al., 2013) (**Fig .1.25**). Accordingly, summer was accompanied by maximum $\Delta^{17}O$ values of nitrate (27 ‰) than any other region in the globe. The authors used a steady state box model (SSM) and a 3D-chemical transport model (CTM) to model the concentration and oxygen isotopes of nitrate by coupling various nitrate formation pathways with local measurements of NO_X and O_3 into the models. The models well reproduced the observed field nitrate concentration. However, a discrepancy between the modeled values and measurements in $\Delta^{17}O(NO_3^-)$ was observed arising mainly from the weight of nitrate formation pathways (daytime or nighttime emphasis) and amount of other species such as DMS in the two models. By using mass balance calculations, the authors determined an average nitrate production rate of 20 ± 10 % for the pathway involving bromine chemistry ($BrNO_3$ hydrolysis). Additionally, it was shown that the nitrate formation pathway via N_2O_5 pathway is negligible at this site.

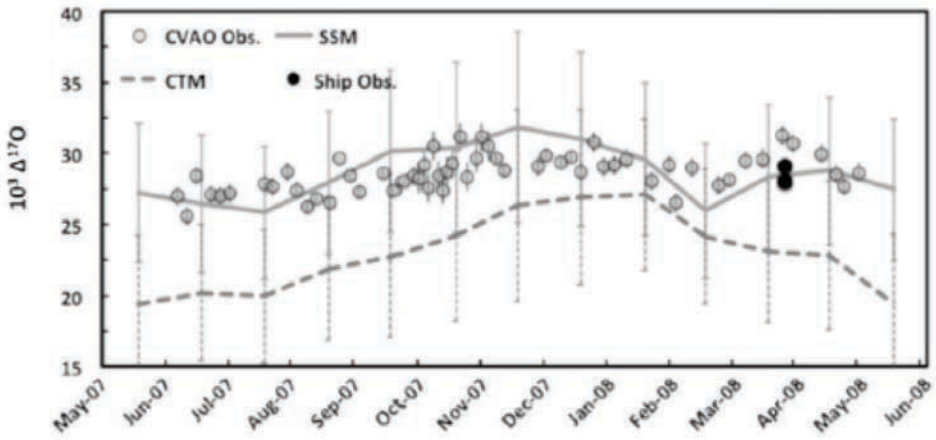

Figure 1.25. *A year round ^{17}O-excess profile of atmospheric nitrate during 2007/08 from Cape Verde Atmospheric Observatory (CVAO), Steady State atmospheric Model (SSM), 3D-Chemical Transport Model (CTM) and collection from three cruises (2007, 2008 and 2012) on south-north Atlantic transects (Savarino et al., 2013). The authors noted that the CTM model underestimation is associated with the chemistry in the model favoring pathways with low ^{17}O-excess contribution to nitrate.*

Alexander et al. (2009) also used GEOS-Chem global 3D to simulate the observations of ^{17}O-excess in nitrate. The model considers different nitrate formation pathways and used $\Delta^{17}O(O_3)$ values of 25 and 35 ‰ to simulate the atmospheric observations. Additionally, they have included the experimentally derived transfer functions for the NO + O_3 reaction (Savarino et al., 2008) and applied similar function for the missing NO_2 + O_3 reaction transfer function. The authors observed good agreement between their model and observations while using a $\Delta^{17}O(O_3)$ value of 35 ‰ with the transfer function developed by Savarino et al. (2008). Accordingly, the NO_2 + OH reaction dominates the global annual-mean tropospheric inorganic nitrate burden (76 %), followed by the N_2O_5 hydrolysis reaction which accounts for about 18 %. A small contribution (4 %) was also observed for the NO_3 + DMS reaction pathway.

Looking at each nitrate formation pathway specific to a given geographic location and its contribution to the annual mean nitrate concentration at the lowest model layer (0-200 m above the surface), nitrate production in the tropics is dominated by the NO_2 + OH pathway (87 %) due to the high OH concentration (**Fig. 1.26**) (Alexander et al., 2009). The production of nitrate via hydrolysis of N_2O_5 was found to be dominant (74 %) in high northern latitudes over the continents and the Arctic, and the high latitude marine boundary layer nitrate formation was dominated (up to 46 %) by the NO_3 + DMS reaction pathway. The stratospheric nitrate contribution was found to be negligible with an average annual maximum contribution of 2 % over Antarctica.

However, the model underestimated the $\Delta^{17}O$ of nitrate values (0-5 ‰) during summer and spring in polar regions as it ignores the bromine chemistry which may have a significant contribution to the high $\Delta^{17}O$ values of nitrate from this region. Morin et al. (2007) showed that hydrolysis of $BrNO_3$ can have a significant contribution to the formation of nitrate with higher $\Delta^{17}O$ values. Additionally local snowpack emissions of

NO_X which are not included in the model may have introduced additional discrepancy with the model output (Alexander et al., 2009).

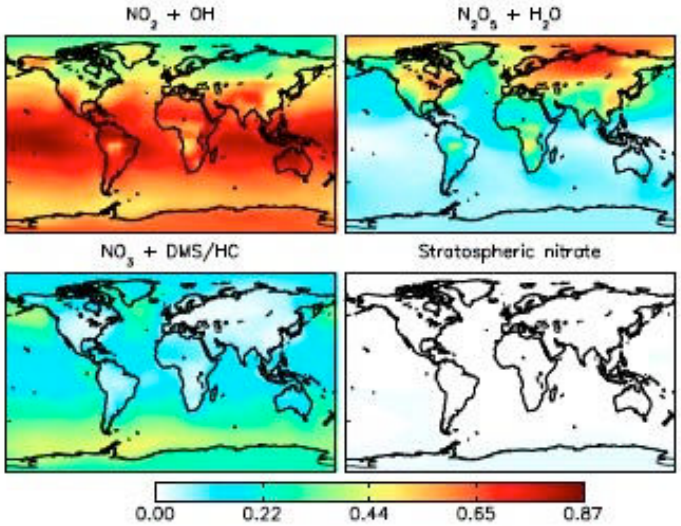

Figure 1.26. *The model output for the annual-mean fractional importance of the different nitrate formation pathways to the total inorganic surface nitrate (Alexander et al., 2009).*

In general, these modelling approaches provide significant information regarding the nitrate formation pathways and the seasonal trends observed in different geographical locations based on the knowledge of the $\Delta^{17}O$ of nitrate and ozone. However, there are some gaps in these studies mainly due to unavailability of experimental data. For example, for the gas phase oxidation reaction of NO + O_3 → NO_2 + O_3, experimental ^{17}O-excess transfer formalism was developed (Savarino et al., 2008). Accordingly, the transferable ^{17}O-excess from ozone to NO_2 was quantified by $\Delta^{17}O(O_3^*) = (1.18 \pm 0.07) \times \Delta^{17}O(O_3)_{bulk} + (6.6 \pm 1.5)$. However, this formalism is missing for some other oxidation pathways such as the NO_2 + O_3 → NO_3 + O_2 reaction or Br + O_3 → BrO + O_2 reactions. Therefore, currently existing studies employ assumptions for the transferable ^{17}O-excess during these reactions based on existing thermodynamic and spectroscopic studies or use transfer values from similar reactions with already existing transfer mechanisms (Alexander et al., 2009;Morin et al., 2011). Hence, a credible experimental study is required to fill these gaps in modeling the regional and global $\Delta^{17}O$ of nitrate. Chapter 2 of this manuscript will address the ^{17}O-excess transfer during the gas phase NO_2 + O_3 reaction.

1.3.10. Isotopic effects in Photolysis

In section 1.2.1 records of high NO_X levels in the overlying boundary layer of polar regions were briefly discussed. These observations were also reflected in the field observations of nitrate mass loss from the snowpack (section 1.2.3). In those sections, desorption and photolysis was pointed as the two important processes for post-depositional modification of snow nitrate. In the section below, first the observations of stable isotope profiles of nitrate based on the studies conducted at Dome C or in the

laboratory will be revised. Then, the findings from these studies and their respective explanations will be described. Finally, the limitations of the existing studies will be pointed out and what is required will be suggested.

Photolysis (briefly defined in section 1.2.3.2) describes breaking of a chemical bond in a given molecule after absorption of light of appropriate energy. During bond breaking, the chemical bond with the light isotope (relatively weaker bond) will be preferentially broken than with the heavy isotope. In case of snow nitrate, this will lead to enrichment in ^{15}N in the nitrate remaining in the snow.

To visualize the isotopic effects associated with photolysis, isotopic fractionation factor (α) was introduced which represents the partitioning of isotopes between two pools and related to isotopic fractionation constant (ε) by ε = (1-α) (Criss, 1999). (Note that the term "isotopic fractionation" will be used instead of "isotopic fractionation constant" throughout this manuscript (Coplen, 2011).

Field observations of isotopic fractionations

In order to understand the possible causes of nitrate mass loss form the snow, Blunier and co-workers (2005) used stable isotopes of nitrate as interpretive tools. From two 15 cm long firn ice cores obtained from Dome C, they have analyzed the nitrogen isotope ratios of nitrate. They have also estimated the concentration of nitrate in these samples from the mass spectrometry measurements. The authors observed similar nitrate concentration profile with previous study at the same site (Röthlisberger et al., 2000) where the concentration showed a sharp decrease to below 10 % of initial nitrate remaining at 10 cm depth. In this study, rapid decrease in nitrate concentration from high surface concentration (maximum of 360 ppb) reaching low values (below 100 ppb) at about 8 cm depth (see **Fig. 1.27**) was also observed. From their measurement of the N isotope ratios depth profile, the $\delta^{15}N$ increased from about 10 ‰ at the surface to about 200 ‰ at 15 cm depth. The isotopic fractionation for N isotopes was determined assuming a Rayleigh type fractionation (described in section 1.3.3.1) where nitrate will be removed from the firn air irreversibly and using equation 1.16 which is rewritten here for clarity:

$$\ln(\delta + 1) = \varepsilon \ln f + \ln(\delta_0 + 1) \qquad (1.30)$$

where δ and δ_0 represents the $\delta^{15}N$ after and before photolysis and f is the fraction of nitrate concentration left in the snow. As the N isotopic composition of nitrate at the beginning was not known in this study, equation 1.30 was modified by substituting f with C/C_0 where C and C_0 represents concentration of nitrate after and before photolysis as:

$$\ln(\delta + 1) = \varepsilon \ln C + \left[\ln(\delta_0 + 1) - \varepsilon \ln C_0\right] \qquad (1.31)$$

Equation 1.31 is a linear equation of the form y = ax + b, and the authors approximated the second term of the equation as a constant term b. Hence, a linear plot of the ln $(\delta + 1)$ versus ln C will be a straight line with slope ε. This approach has been followed in proceeding publications to determine the isotopic fractionations associated with

photolysis which will be discussed below (Frey et al., 2009;Erbland et al., 2013). Based on this approach, the authors derived an isotopic fractionation of -54 ‰.

In order to understand the mechanism behind the observed isotopic fractionation and to reproduce the field result in the laboratory, Blunier and co-workers took a further step and conducted an experimental study. Their approach was the first of its kind and is used as a benchmark for current researches in similar topics including experimental studies conducted in this manuscript. In their laboratory experiment, an artificial snow doped with $NaNO_3$ was prepared and was irradiated with a UV lamp for few hours. Based on the nitrate concentration and N isotopes measurement before and after photolysis, the authors derived an isotopic fractionation of -11.7 ± 1.4 ‰. As this value is significantly different than their field observation, the authors ruled out photolysis as the dominant mechanism for the observed nitrate mass loss and isotopic fractionation.

Frey et al. (2009) also conducted similar study at Dome C. In their study, two snow pits were sampled in two summer campaigns (DC 04 and DC 09), and measured both the oxygen and nitrogen isotopes of nitrate. From these campaigns, an average isotopic fractionation of 8 ± 2 ‰, 1 ±1 ‰ and -60 ± 15 ‰, were determined for $\delta^{18}O$, $\Delta^{17}O$ and $\delta^{15}N$ respectively. In order to explain the mechanisms for these isotopic fractionations, a zero point energy shift (ΔZPE) theoretical model was employed which is described briefly below.

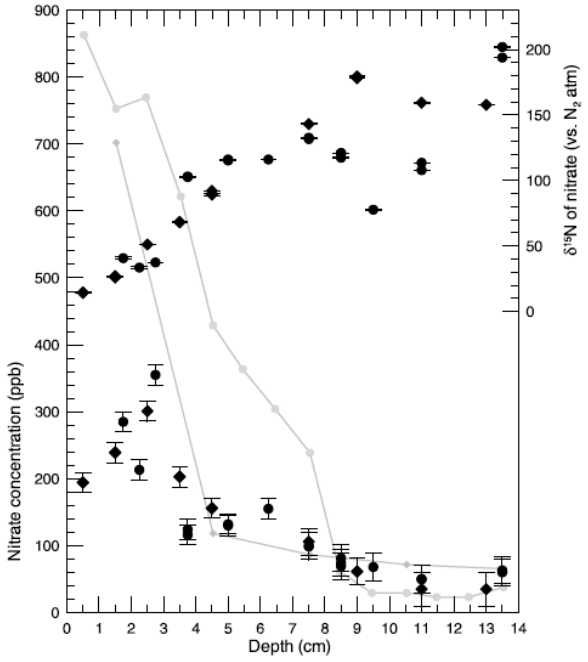

Figure 1.27. *The nitrate concentration and $\delta^{15}N$ profile with depth for two ice cores extracted from Dome C. Concentration measurements were estimated from mass spectrometer measurements and error bars show one sigma from analytical errors (Blunier et al., 2005). Previous concentration measurements by (Röthlisberger et al., 2000) are shown in grey dots and diamonds.*

The ZPE shift model and theoretical determination of ε

In order to understand isotopic fractionations induced by photolysis of nitrate in snow, Frey and co-workers implemented the ZPE-shift model. The model is based on the observation that, with substitution of a light isotope by a heavier one, the vibrational zero point energy (energy associated with a molecule at the lowest vibrational energy level) of the heavier isotopologue is reduced. Zero point energy can be expressed by:

$$ZPE = \frac{\hbar\omega_0}{2} \qquad (1.32)$$

where ω_0 is the vibrational frequency and k is the ground state potential curvature (also called spring or force constant) evaluated at the bond length R_0 expressed mathematically as:

$$\omega_0 = \sqrt{\frac{k}{\mu}} \qquad (1.33)$$

where μ is the reduced mass defined by $(m_1m_2)/(m_1+m_2)$ for the masses of the heavy and the lights isotopes.
During isotopic substitution, the molecule possessing the heavier isotope will have its wave function at lower energy level as shown in **Fig. 1.28**. Hence, an isotopically substituted molecule will have a distinct electronic absorption spectra than the original molecule (Miller, 2000).

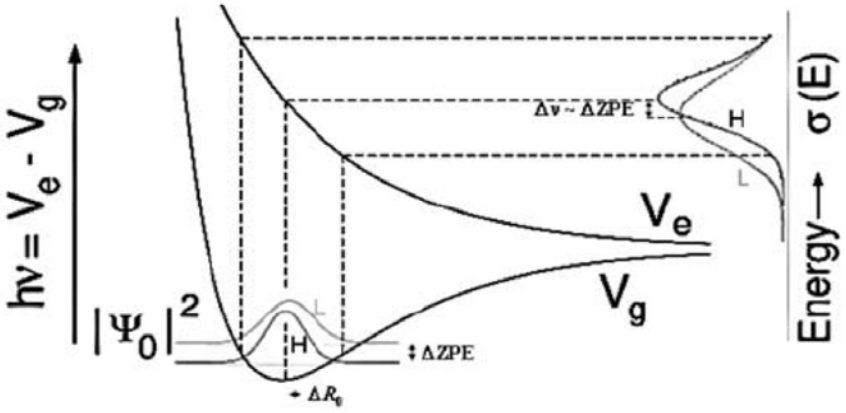

Figure 1.28. *Schematic of the direct photo dissociation process and the expected shift in the absorption cross-section of the heavier isotopologue (H) from the lighter (L) due to the change in the Zero Point Energy (ΔZPE). $/\Psi_0/^2$, V_g and V_e denotes the ground state wave function, ground state electronic potential and dissociating electronic potential respectively (Liang, 2004)*

The model states that this difference in ZPE results in a blue shift of the UV absorption cross-section for the heavier isotopologue. Hence, with the knowledge of the absorption cross-section of the most abundant isotopologue (σ), which is easier to measure experimentally, the absorption cross-section of the least abundant isotopologue (σ') can be derived by shifting the UV spectra of the most abundant isotopologue by a value corresponding to the difference in ZPE between them.
Given that each isotopologue has a unique absorption cross-section, the rate of their photodissociation (*J* and *J'*) can be expressed as:

$$J = \int \sigma(\lambda,T)\phi(\lambda,T)I(\lambda)d\lambda \qquad (1.30)$$

$$J' = \int \sigma'(\lambda,T)\phi(\lambda,T)I(\lambda)d\lambda \qquad (1.31)$$

where $\phi(\lambda)$ is the quantum yield and $I(\lambda)$ is the measured actinic flux of the source of UV light causing photolysis (For example, the solar actinic flux at Dome C conditions).
The isotopic fractionation ε can be determined mathematically from the ratios of the photolysis rate constants of the heavy (*J'*) and the light (*J*) isotopes by:

$$\varepsilon = \frac{J'}{J} - 1 \qquad (1.32)$$

However, this conceptual model is based on simplified principles which do not take into account the full complexity of the quantum mechanics behind isotopic substitutions. Previous laboratory studies observed a factor of two difference between the isotopic fractionation derived from this model and observations (Kaiser et al., 2003). Applying the time-dependent Hermite Propagation (HP) method and introducing the Franck-Condon model, which states that isotopic substitution has a significant effect on the wave function of the upper state, Johnson and co-workers were able to better reproduce the observations (Johnson et al., 2001). Their results were better than the predictions from the ZPE model but still with limitations associated with the 2D-potential energy surface (Kaiser et al., 2003). Later, with an improved photo-dissociation dynamics of their model, (Nanbu and Johnson, 2004) obtained a very good agreement between their isotopic fractionation and the ones observed in the laboratory, pointing to the importance of taking into account the dynamics of the transition into the upper dissociation state and not only the ground state level. More recently, an empirical model using four parameters (ZPE, width, amplitude and asymmetry) was developed by Jost and co-workers in order to calculate the absorption cross-sections of isotopically substituted species (Jost, 2008;Ndengue et al., 2010). The designed model successfully determines the absorption cross-sections of isotopologues of triatomic molecules.

In aim of determining the processes responsible for the observed enrichments in ^{15}N in snow nitrate associated with post-depositional effects, Frey et al. (2009) employed the ZPE-shift model. The authors applied a simple ΔZPE shift of about -44.8 cm^{-1} (an average shift of about 0.5 nm) in the 280-360 nm ranges, constrained by the vibrational energies of each state mentioned in previous studies. The absorption spectrum of $^{15}NO_3^-$

was determined by shifting the known $^{14}NO_3^-$ cross-section (Chu and Anastasio, 2003) by the ZPE (**Fig. 1.29**).

Using the absorption cross-section values derived above, Frey and co-workers determined the isotopic fractionations for nitrogen isotopes using the solar actinic flux determined for Dome C conditions obtained using the snow TUV model (see end of section 1.2.3.2) and assuming a quantum yield of 1. They have obtained an isotopic fractionation $^{15}\varepsilon$ value of -48 ‰. With the agreement of this value to the field observation, the authors suggested that photolysis is the major process behind isotopic fractionation and mass loss of snow nitrate (Frey et al., 2009).

Frey et al. (2009) also studied the oxygen isotopic fractionations. In contrary to the increasing trend (enrichment) in $\delta^{15}N$, a decreasing profile was observed in $\delta^{18}O$ and $\Delta^{17}O$ profiles with depth. The authors suggested besides photolysis, matrix effect plays a dominant role in oxygen isotopic fractionation pointing out previous studies which showed depletion in oxygen isotopes due to isotopic exchange with surrounding matrix (McCabe et al., 2005a) i.e. photoproducts of nitrate photolysis (NO and NO_2) will undergo oxygen isotopic exchange with surrounding OH/water and reform nitrate. In case of complete isotopic exchange (100 % exchanged), the reformed nitrate will have $\delta^{18}O$ values close to Dome C water (less than -40 ‰ (Masson-Delmotte et al., 2008)) and $\Delta^{17}O$ values close to zero as both reservoirs exhibit $\Delta^{17}O$ values close to zero (Frey et al., 2009).

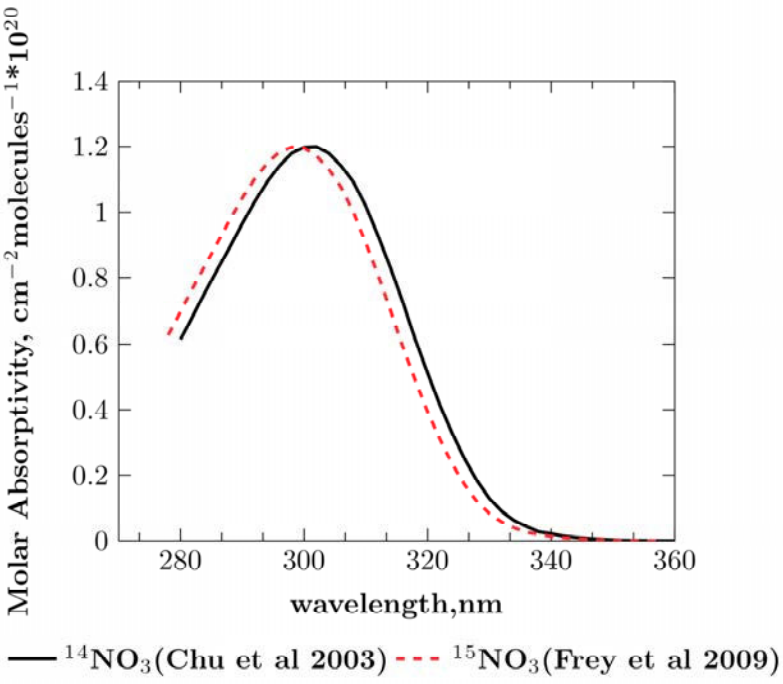

Figure 1.29. *The absorption cross section of $^{14}NO_3$ measured experimentally (Chu and Anastasio, 2003) and $^{15}NO_3$ derived applying the ZPE model (Frey et al., 2009). The absorption spectras are manually manipulated to show the shift but in reality they overlay on each other.*

More recently, an intensive field study was conducted in the East Antarctic Plateau (EAP) on determination of isotopic fractionations (Erbland et al., 2013). This study went one step ahead and conducted simple experimental study on the effect of desorption (evaporation/sublimation) in the isotopic fractionations. Accordingly, at -30°C (close to summer time average temperature at Dome C) they have obtained a nitrogen isotopic fractionation of 1.8 ± 3.8 ‰. The authors also sampled different sites at the EAP and derived an average apparent isotopic fractionations of -59 ± 10 ‰, 2 ± 1 ‰ and 8.7 ± 2.4 ‰ for $\delta^{15}N$, $\Delta^{17}O$ and $\delta^{18}O$ respectively. These values are in agreement with the previous study by Frey et al. (2009) field observations and ZPE-shift model. Noting the significant difference between the measured values and the values derived for desorption, the authors suggested photolysis (which is associated with large negative isotopic fractionations) as the dominant process behind post-depositional loss of snow nitrate and isotopic fractionation in EAP. However, in coastal Antarctica where the observed loss is small, both processes can be significant.

In general, these studies clearly observed the isotopic effects associated with post-depositional processes. They have also derived apparent isotopic fractionations for different sites in Antarctica and suggested desorption and photolysis as responsible processes with their respective reasons. However, these mentioned studies also have their limitations.

The disagreement between the field observation and the laboratory experiment (Blunier et al., 2005) was suggested to arise from the experimental setup i.e. the lamp used for photolysis was unable to reproduce field conditions and it includes the absorption band of nitrate at 200 nm (Frey et al., 2009). Hence, photolysis rate spectrum spectrum will be shifted towards short wavelength regions leading to less negative or even positive isotopic fractionations. Additionally, photoproducts were not flushed from the system, and hence secondary chemistry was inevitable.

The ZPE-shift model approach by Frey et al. (2009) was a novel approach but it was too simplified. The ZPE-shift model has been previously criticized as it does not take into account for changes in shape and intensity of absorption spectras during isotopic substitution (Miller and Yung, 2000). Hence, the predictions from the model may give a direction of the isotopic fractionations but the accuracy remains to be tested.

The isotopic fractionations determined for the field measurements (Frey et al., 2009;Erbland et al., 2013;Blunier et al., 2005) were also unable to derive purely photolysis driven isotopic fractionations rather an apparent value where besides photolysis additional process such as desorption can play a role.

Chapter 3 and 4 of this manuscript are dedicated to clarify these scientific gaps in photochemistry of nitrate in snow. In chapter 3, an experimental study which employs similar principle as Blunier et al. (2005) will be described. However, this study uses natural snow from Dome C, and had better control in parameters such as temperature, pressure and removal of photoproducts as well as it uses UV filters to better mimic field conditions. This will enable to derive a purely photolytic isotopic fractionation close to field conditions. We will also test the validity of the ZPE-shift model using the experimentally obtained values. In chapter 4, a field study, which isolates photolysis process, is described. In this study, the effect of photolysis in mass and stable isotopes of nitrate will be evaluated at Dome C, and a purely photolytic isotopic fractionation will be

derived. The findings from the laboratory studies will be used to explain the observations in the field.

1.3.11. Structure of the manuscript and the PhD project

1.3.11.1. Structure of the manuscript

In the introduction section, the basic backgrounds regarding the atmospheric chemistry of NO_X and isotope geochemistry are briefly explained. From the discovery of isotopic anomaly in ozone to the current knowledge of experimental and theoretical explanations for MIF in ozone, and mass balance equations to determine ^{17}O-excess in nitrate are described in detail. Additionally, the current state of the art in snow photochemistry and the limitations of the currently existing studies in this field are also pointed out.

The fundamental questions in manuscript includes:

- How does the isotopic anomaly transfer proceeds for the $NO_2 + O_3 \rightarrow NO_3 + O_2$ reaction? Is it similar to the $NO + O_3 \rightarrow NO_2 + O_2$ reaction?
- How can we account for the observed mass loss and isotopic fractionation of nitrate in snow?
- Which processes significantly play a role in post-depositional modification of nitrate in snow?
- What are the limitations of the currently existing studies and how can we improve them?

This manuscript is comprised of three main chapters of experimental studies and an annex which describes the experiments conducted under this PhD study but were not successfully finished. A short overview for each chapter is given below.

Chapter 2: ^{17}O excess transfer during the $NO_2 + O_3 \rightarrow NO_3 + O_2$ reaction

In this chapter, the ^{17}O-excess transfer during the gas phase reaction of $NO_2 + O_3 \rightarrow NO_3 + O_2$ is described. This is an important nighttime nitrate formation pathway but its isotopic transfer function has not been experimentally studied in the gas phase. The knowledge of this transfer function is a useful tool to understand the nocturnal nitrate formation pathways. Additionally, this reaction can also be used to evaluate the internal isotopic distribution of ozone. Michalski and Bhattacharya (2009) conducted a similar study for the liquid phase $NO_2^- + O_3$ reaction. However, this reaction does not truly represent the actual gas phase reaction in the atmosphere. Currently, modeling studies on $\Delta^{17}O(NO_3)$ use simple assumptions based on similar reactions. Following similar experimental protocol as the $NO + O_3 \rightarrow NO_2 + O_2$ reaction isotopic transfer function by Savarino et al. (2008), the transferable ^{17}O-excess will be computed from measurements of the triple oxygen isotopes of initial ozone and oxygen product. Isotopic ratios will be measured using the MAT-253 IRMS available at LGGE. Additionally, the intramolecular isotopic distribution of ozone will be evaluated and will be compared to previous studies (Michalski and Bhattacharya, 2009;Bhattacharya et al., 2008;Savarino et al., 2008).

Chapter 3: Laboratory Study of Nitrate Photolysis in Antarctic Snow, Part 2: Isotope Effects and Wavelength Dependence

In Chapter 3, the photochemistry of nitrate in snow is briefly investigated from an isotopic perspective. Currently, only few experimental studies exist on constraining the post-depositional loss of nitrate from snowpack in low snow accumulation sites. However, these studies were unable to derive a purely photolytic isotopic fractionation (Frey et al., 2009;Erbland et al., 2013). The laboratory study, which was conducted by irradiating an artificial snow doped with $NaNO_3$ (Blunier et al., 2005), did not well reproduce the field conditions in terms of light conditions mainly and secondary effect due to photoproduct recycling. The theoretical ZPE-shift model invoked to explain observed isotopic fractionations (Frey et al. 2009) is also a very simplified estimation. In Chapter 3 of this manuscript, a modified setup with better control on temperature, pressure and product removal is designed, and UV filters were used to match wavelength regions of specific interests (the field conditions at Dome C). Hence, irradiating this natural Dome C snow with selection of UV-filters at different wavelengths, we can evaluate the changes in mass and isotopic composition of nitrate in the snow. The results from this study are presented in two parts. The first part which focuses on the nitrate quantum yield (Meuasinger et al.) and the second part (chapter 3 of this manuscript) which describes the isotopic effects. Further, based on the experimental observations, the predictions of the ZPE-shift model will also be tested if it can reproduce the laboratory results or if limitations of ZPE-shift model to reproduce field observations can be improved with this experimental work combined theoretical calculations.

Chapter 4: Isotopic effects of nitrate photochemistry in snow: A field study at Dome C, Antarctica

In this chapter, we present the study on the photochemistry of nitrate in snow at Dome C, Antarctica during Austral summer 2011/12. As in chapter 3, where only photolytic effect was studied excluding other post-depositional effects, similar principle was also applied in this field study. Two snow pits with identical snow nitrate concentration and isotopic composition profiles were studied by exposing/blocking solar UV light to derive a purely photolytic fractionation. Sampling was conducted in 2-5 cm depth resolution until 30 cm in 10 days frequency during 02/12/2011-30/01/2012. These samples were analyzed for the concentration and the O and N isotopic composition of nitrate. The purely photolytic isotopic fractionations obtained from these measurements will be compared with the an apparent isotopic fractionations derived from previous studies (Frey et al., 2009;Erbland et al., 2013;Blunier et al., 2005) where besides photolysis additional processes such as evaporation are also present. Based on the results from this study, variation of isotopic fractionation with time or depth is also evaluated. We will also compare these observations with the laboratory study findings (Chapter 3) and with the ZPE-shift model predictions under the field conditions.

At the end of this manuscript, conclusions from these studies and outlooks for future work are given.

1.3.11.2. The PhD project

This PhD project is part of the Initial Training in Mass Independent Fractionation (INTRAMIF) funded by the European Union Marie Curie grant. The project is composed of 13 PhD students and 8 laboratories in Europe. All the PhD projects are focused on MIF in different atmospheric species with ozone the central piece. The overall project preview is described in the charts below, and this PhD project (ESR 4) is assigned at LGGE (Grenoble) and CCAR (Grenoble).

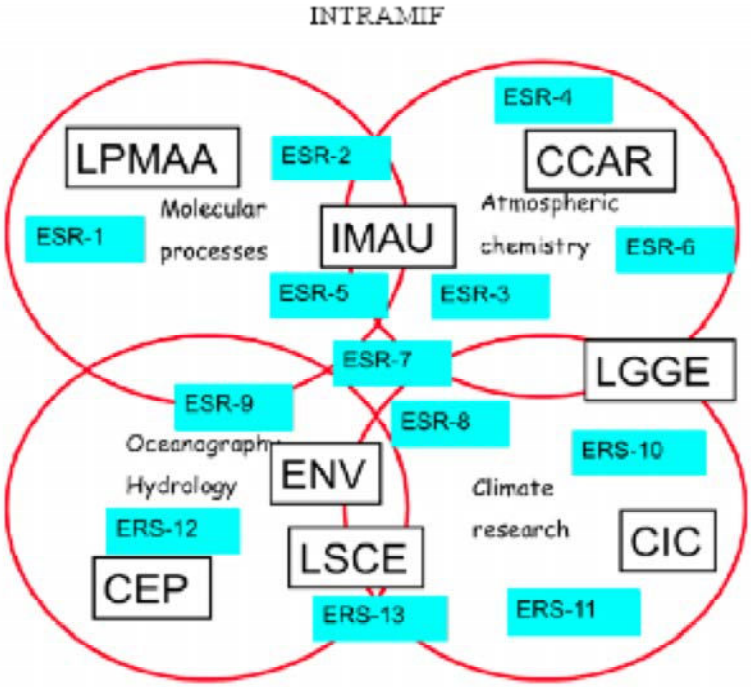

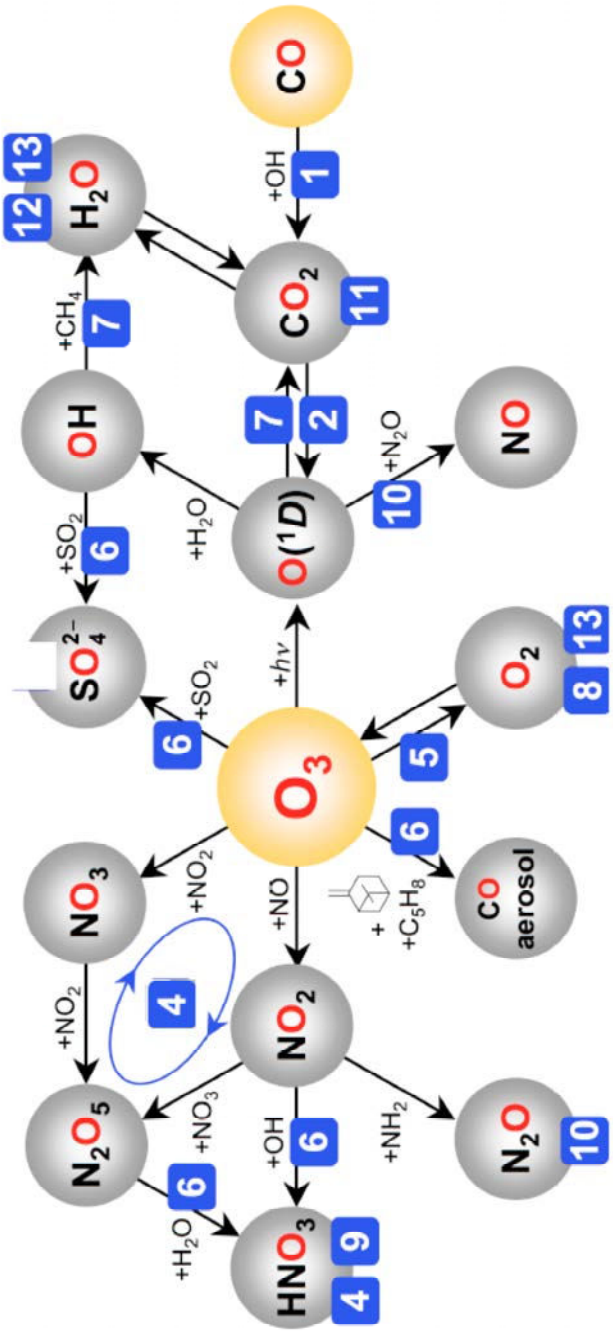
CO
+OH
1
H2O
12
13
CO2
11
+CH4
7
OH
7
2
NO
+N2O
10
+SO2
6
+H2O
O(1D)
SO4 2−
6
+SO2
+hν
O2
8
13
5
O3
6
NO3
+NO2
+NO
+C5H8
CO aerosol
+NO2
4
NO2
N2O5
+NO3
+OH
6
+NH2
N2O
10
+H2O
6
HNO3
9
4

CHAPTER 2

^{17}O excess transfer during the $NO_2 + O_3 \rightarrow NO_3 + O_2$ reaction

This chapter is based on:

Tesfaye Ayalneh Berhanu, Joël Savarino, S.K.Bhattacharya, Willliam C. Vicars. ^{17}O excess transfer during the $NO_2 + O_3 \rightarrow NO_3 + O_2$ reaction**.** *Journal of chemical Physics, 2012, 4, 136.*

Abstract

The ozone molecule possesses a unique and distinctive ^{17}O excess ($\Delta^{17}O$) which can be transferred to some of the atmospheric molecules via oxidation. This isotopic signal can be used to trace oxidation reactions in the atmosphere. However, such an approach depends on a robust and quantitative understanding of the oxygen transfer mechanism, which is currently lacking for the gas-phase $NO_2 + O_3$ reaction, an important step in the nocturnal production of atmospheric nitrate. In the present study, the transfer of $\Delta^{17}O$ from ozone to nitrate radical (NO_3) during the gas-phase $NO_2 + O_3 \rightarrow NO_3 + O_2$ reaction was investigated in a series of laboratory experiments. The isotopic composition ($\delta^{17}O$, $\delta^{18}O$) of the bulk ozone and the oxygen gas produced in the reaction was determined via isotope ratio mass spectrometry. The $\Delta^{17}O$ transfer function for the $NO_2 + O_3$ reaction was determined to be: $\Delta^{17}O(O_3^*) = (1.23 \pm 0.19) \times \Delta^{17}O(O_3)_{bulk} + (9.02 \pm 0.99)$. The intramolecular oxygen isotope distribution of ozone was evaluated and results suggest that the excess enrichment resides predominantly on the terminal oxygen atoms of ozone. The results obtained in this study will be useful in the interpretation of high $\Delta^{17}O$ values measured for atmospheric nitrate, thus leading to a better understanding of the natural cycling of atmospheric reactive nitrogen.

2.1. Introduction

Oxygen isotopes (^{16}O, ^{17}O, ^{18}O) in most natural compounds are distributed in such a way that the change in the $^{17}O/^{16}O$ ratio is approximately half of the change in the $^{18}O/^{16}O$ ratio. When the ratios for such samples are expressed in the relative scale of δ-values (where δ (‰) = 10^3 ($R_{sample}/R_{standard} - 1$) and R is the $^{x}O/^{16}O$ ratio, where x = 17 or 18) we obtain a linear array in a plot of $\delta^{17}O$ versus $\delta^{18}O$ which has a slope of 0.52 (Terrestrial Fractionation Line) (Thiemens, 1999). Strictly speaking, the relation between $\delta^{17}O$ and $\delta^{18}O$ values is a power law (Miller, 2002); however, a linear relationship with a slope 0.52 is a good approximation over a small range of δ-values. Any deviation from this line is indicative of a ^{17}O-excess, commonly referred to as an oxygen isotope anomaly caused by contribution from a mass-independent fractionation (MIF) or transfer processes. ^{17}O excess is usually expressed in its linearized form as $\Delta^{17}O = \delta^{17}O - 0.52 \times \delta^{18}O$, and signifies an excess or depletion of ^{17}O from the amount expected for a mass dependent isotopic distribution.

Atmospheric ozone (O_3) possesses large ^{17}O-excess, with $\Delta^{17}O$ values ranging from 20-40 ‰ (Mauersberger et al., 2001;Krankowsky et al., 1995;Thiemens and Heidenreich, 1983;Johnston and Thiemens, 1997). The $\Delta^{17}O$ signal of atmospheric ozone is a conserved quantity (i.e., it cannot be altered via mass-dependent fractionation processes), which can be partially or completely transferred to other species through oxidation reactions (Thiemens, 2006;Michalski and Bhattacharya, 2009;Lyons, 2001). As a result of this ^{17}O-excess transfer, $\Delta^{17}O$ values of oxygen-bearing atmospheric species serve as proxies for the influence of ozone in their chemical formation pathways. This provides a unique approach for tracing chemical oxidation pathways in the atmosphere and has yielded valuable insight into the atmospheric dynamics of several key species such as nitrate, the end product of atmospheric NO_X oxidation (Savarino et al., 2007;Morin et al., 2008b;Morin et al., 2007b;Michalski et al., 2003) as well as N_2O(Röckmann et al., 2001), CO_2(Alexander et al., 2004) and sulfates (Savarino et al., 2000;Strauss et al., 2007;Farquhar and Wing, 2005;Farquhar et al., 2007).

Ozone is a bent molecule with two distinctive types of oxygen atoms: the two "terminal" atoms and the "central" atom, which is bonded to both terminal atoms. The anomalous isotopic enrichment is not distributed statistically in the ozone molecule (Janssen, 2005). In particular, it is believed that the ^{17}O-excess resides on the terminal atom alone (Michalski and Bhattacharya, 2009). It is also believed that during oxidation reactions, there is a preference for reaction of the terminal oxygen atom of ozone (Liu et al., 2001). Hence the excess enrichment on this oxygen atom will be transferred to the oxidized compound and can be used as interpretive tool to study various atmospheric reactions (Savarino et al., 2008;Michalski et al., 2003). Therefore, a quantitative understanding of ^{17}O-excess transfer in atmospheric reactions involving ozone is essential to verify the validity of these two key assumptions in particular cases.

The present study concerns atmospheric NO_X ($NO + NO_2$), which is emitted primarily through biomass burning, soil emission, fossil fuel combustion or formed in situ by lightning and it is strongly related to atmospheric ozone(Seinfeld and Pandis, 2006). The atmospheric NO_X cycle follows well-known daytime and nighttime reaction pathways and eventually results in the formation of a stable HNO_3 product through the following reactions.

$$NO + O_3 \rightarrow NO_2 + O_2 \quad \text{(R.2.1)}$$

$$NO + RO_2 \rightarrow NO_2 + RO \quad \text{(R.2.1a)}$$

$$NO + HO_2 \rightarrow NO_2 + OH \quad \text{(R.2.1b)}$$

$$NO_2 + hv \rightarrow NO + O \quad \text{(R.2.2)}$$

$$O + O_2 \rightarrow O_3 \quad \text{(R.2.3)}$$

During the daytime, NO is oxidized by O_3 and peroxy radicals to produce NO_2, which is readily photolyzed back to NO. A photo-stationary state between NO and NO_2 is achieved quickly, in less than 100 seconds (Roberts, 1990). The reaction pathways R.2.1 and R.2.2 followed by R.2.3 constitute null cycle for ozone with no net loss or production. However, in the presence of volatile organic compounds (VOCs), where degradation intermediates HO_2/RO_2 are formed, NO oxidation follows pathways R.2.1a and R.2.1b producing NO_2(Atkinson, 2000). Photolysis of NO_2 and formation of ozone via R.2.3 is a major ozone formation mechanism in the troposphere.
NO_2 can be further oxidized by O_3 to NO_3 during the daytime. But due to rapid photolysis of NO_3, its concentration is insignificant.

$$NO_2 + O_3 \rightarrow NO_3 + O_2 \quad \text{(R.2.4)}$$

Reaction with OH (R.2.5) is the dominant daytime removal mechanism for NOx, resulting in a 1-2 day lifetime in the lower troposphere(Roberts, 1990).

$$NO_2 + OH \rightarrow HNO_3 \quad \text{(R.2.5)}$$

At night, the NO_3 radical thus produced may react with organic compounds (RH) such as VOCs or DMS to form stable HNO_3 product (R.2.6), or may react with NO_2 (R.2.7).

$$NO_3 + RH \rightarrow HNO_3 \quad \text{(R.2.6)}$$

$$NO_2 + NO_3 \leftrightarrow N_2O_5 \quad \text{(R.2.7)}$$

$$N_2O_5 + H_2Oads \rightarrow 2HNO_3 \quad \text{(R.2.8)}$$

R.2.7 attains equilibrium within a few minutes; low temperature and the absence of sunlight favors the forward reaction(Seinfeld and Pandis, 2006). N_2O_5 can undergo hydrolysis on aerosols via R.2.8 forming a stable nitrate product. This stable HNO_3 is then removed from the atmosphere through dry and wet deposition (Galloway et al., 2008). Reactivation of deposited nitrate can take place via photolysis mainly from snow or ice emitting active gaseous NOx in the polar environment which can be oxidized by local oxidants such as ozone and re deposited or transported to other locations(Jarvis et al., 2009;Abida et al., 2011).

R.2.3 is the ozone formation reaction that produces the anomalous non-zero $\Delta^{17}O$. During the oxidation reactions of NO_X with ozone, the ^{17}O-excess of ozone is transferred to nitrate.

Large oxygen isotope anomalies have been detected in nitrate samples obtained from various parts of the globe. Michalski et al(Michalski et al., 2003;Michalski et al., 2002) measured $\Delta^{17}O$ values for atmospheric nitrate varying from 20 ‰ to 31 ‰ in samples from the Atacama desert in Chile and La Jolla, California. From a set of aerosol samples collected in coastal Antarctica over a year, (Savarino et al., 2007) measured $\Delta^{17}O$ of 24 ‰ – 39 ‰. McCabe et al(McCabe et al., 2007) established a seasonal variation of $\Delta^{17}O$ of aerosol nitrate from 22.6 ‰ – 28.5 ‰ in summer and 38.1 ‰ in winter in Antarctic snow. Morin et al (Morin et al., 2007b) also measured $\Delta^{17}O$ of 29 ‰ – 35 ‰ in nitrate samples from the Arctic. All these measurements showed that atmospheric nitrate is characterized by a highly positive anomaly and there is a large variation among samples depending on space and time.

Though it is known that the oxygen isotope anomaly of atmospheric nitrate is inherited from ozone, the exact amount of transferable anomaly is still an issue of debate considering the wide range of $\Delta^{17}O$ values observed in atmospheric nitrate mentioned above. The variation may originate from the local ozone source or may be due to reaction conditions. Nitrate formation follows different reaction pathways in the atmosphere depending on various factors(Alexander et al., 2009). Hence, it is important to investigate isotopic anomaly transfer for each reaction pathway in order to clearly understand and explain the high and variable $\Delta^{17}O$ values observed for atmospheric nitrate. A breakthrough was made in an investigation of the gas phase reaction of NO with O_3 (R.2.1). Data obtained during this experiment was used to explain the anomaly transfer from ozone to NO_2 in the context of an earlier study on the intramolecular isotopic distribution of ozone (Savarino et al., 2008).

Presently there is no analogous study of anomaly transfer study during the gas phase reaction of NO_2 with O_3 (R.2.5). Michalski and Bhattacharya (Michalski and Bhattacharya, 2009) have recently studied the aqueous phase NO_2^- reaction with ozone in order to investigate the intramolecular oxygen isotope distribution of ozone and anomaly transfer during formation of NO_3^-. This study suggests that the ozone isotopic anomaly resides entirely on terminal atoms of ozone when a limited range of $\Delta^{17}O$ values of ozone is considered (20-40 ‰). However, the aqueous phase oxidation of NO_2^- anion with ozone is not chemically equivalent to the gas phase atmospheric oxidation of NO_2 radical by ozone. Therefore, an experimental quantification of ^{17}O-excess transfer from O_3 to NO_3 is necessary in order to use an isotopic approach to investigate the nitrate chemistry and related compounds. This is the main objective of the study described here.

2.2. Experimental

A. Experimental setup

The $NO_2 + O_3$ reaction was carried out in a custom made vacuum line (**Fig. 2.1**) using Pyrex glass components. A turbomolecular pump (Model Pfeiffer TMH071), backed by a rotary oil pump (Alcatel), was used to obtain vacuum at the level of 1.3 Pa (10 mTorr) within a few minutes. The system was equipped with two spherical glass chambers (C1:

10 L and C2: 1 L), two Baratron gauges (MKS, PR4000, 0-10 Torr and 0-1000 Torr ranges), vacuum gauges (Varian 801, thermocouple), and three cold traps T1, T2 and T3. A Tesla coil (ETP, BD 50E) was used to generate ozone via electrical discharge in oxygen (obtained from a tank, Messer, 99.999% purity). A glass bulb containing NO_2 (Air Liquide, 98% purity) was attached to the system. NO_2 was purified by cycles of freezing with alcohol slush (-100 °C) and pumping away non-condensable gases until any blue or brown/yellow colors have disappeared before its use. The line was covered with aluminum foil to avoid decomposition of ozone as well as NO_2 caused by exposure to light.

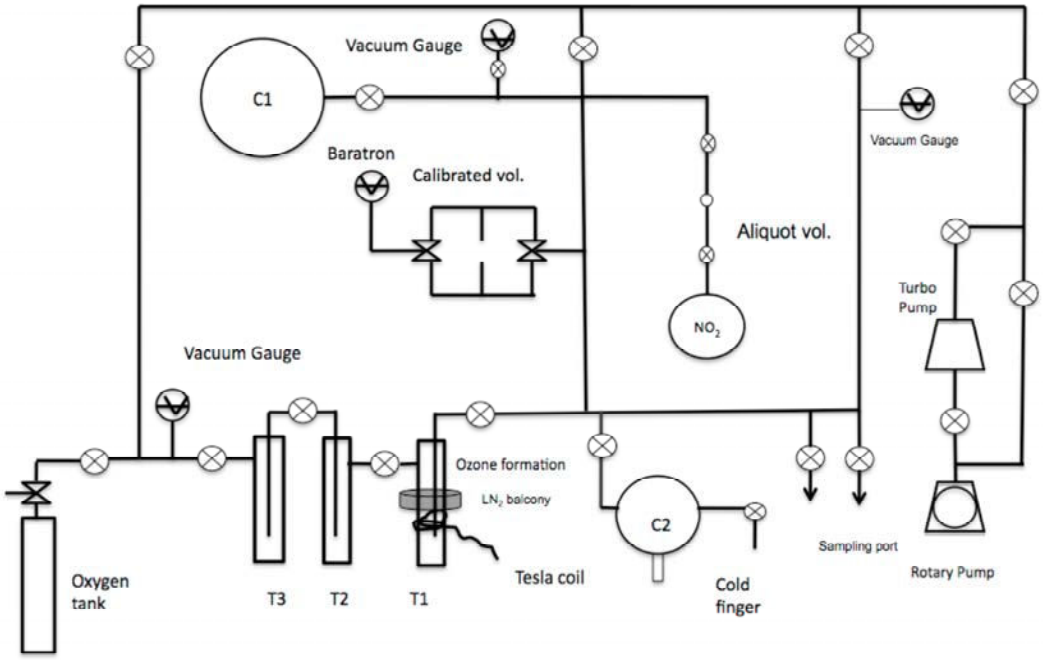

Figure 2.1. *Simplified sketch of the vacuum line used in the present study where T1, T2, T3 are the cylindrical traps and C1 and C2 are spherical glass chambers.*

B. Preparation of ozone

Ozone was generated via electrical discharge at various pressures (1.3 kPa to 13kPa read by the Baratron gauge) and temperatures (77 K to 340 K) in order to obtain $\Delta^{17}O(O_3)_{bulk}$ values ranging from 0 to 40 ‰ (Savarino et al., 2008). The vacuum line volume was rather small (about 500 ml) but inclusion of the 10 L bulb as a reservoir allowed for an essentially constant pressure during ozone generation. This avoided any pressure change effect on delta values and associated changes in the internal isotope distribution of ozone. Discharge was carried out in the cylindrical glass trap (T1), having a Styrofoam balcony in the middle containing liquid nitrogen (LN_2) to trap the ozone as it was formed. To obtain higher enrichment values oxygen was made to flow through the system during discharge (in trap T2) using a diaphragm pump (**Fig. 2.2**) while ozone was collected in trap T1. Heating the glass trap with hot air gun as well as making the discharge at various

distances from the cold trap induced temperature variations at the ozone formation site. In this way, different enrichment values were produced as the $\Delta^{17}O$ of ozone is sensitive to variations in temperature (Morton et al., 1990). As a special case ozone with $\Delta^{17}O \approx 0$ was produced by electrolysis of acidified water (Bhattacharya et al., 2009).

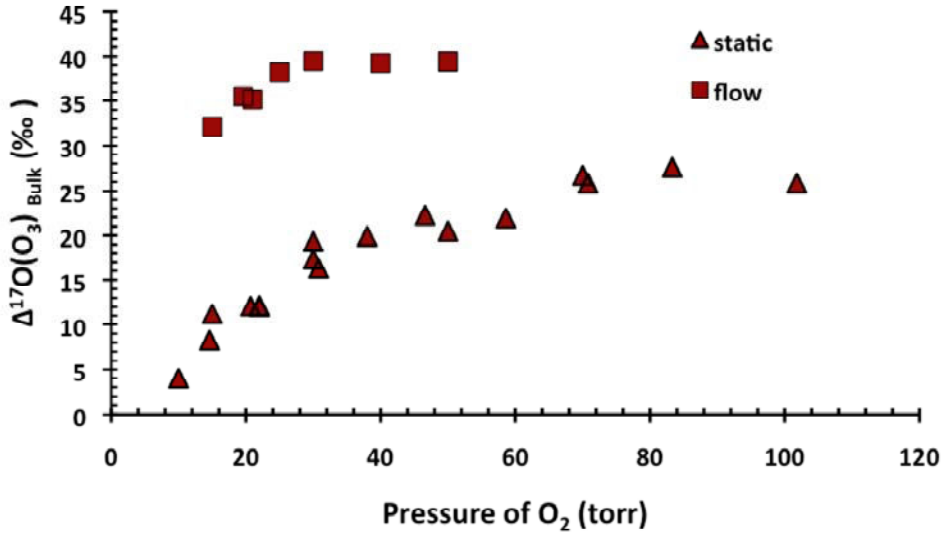

Figure 2.2. *Production of ozone having various $\Delta^{17}O$ values were obtained by manipulating pressure and temperature of ozone formation using static (LN_2 temperature) and flow systems (room temperature). Static experiments were used to generate $\Delta^{17}O\ (O_3)_{bulk}$ below 30‰ and flow experiments for $\Delta^{17}O\ (O_3)_{bulk}$ of 30-40‰.*

C. Reaction procedure

After ozone was produced (typically 30 μmole-120 μmole) and trapped at T1, the left over oxygen was pumped away until a vacuum of 10 mTorr was obtained. T1 was then isolated and the ozone was brought to gas phase by removing the LN_2. Next, the ozone was allowed to equilibrate between T1 and T2 for ~ 10 minutes. T1 was then isolated and its ozone was taken to the cold finger at C2 and isolated from the main bulb. The ozone aliquot left at T2 was taken to a cold finger (containing molecular sieve, MS) attached to the Baratron (pre-calibrated). This ozone was converted to oxygen by warming the MS and oxygen amount was measured with the Baratron. This oxygen was collected in a sample vial (with MS) and analyzed in the mass spectrometer to obtain the isotopic composition of the starting ozone assuming that this ozone aliquot represents the ozone that would react with the NO_2 in C2. The volume ratio of T1 and T2 also allows us to determine the amount of ozone in C2 to be used for the reaction. An excess amount (about twice) of gaseous NO_2 was taken from the NO_2 bulb and transferred to C2 by freezing at the bottom finger with LN_2. Next, the LN_2 in both fingers of C2 were removed and the stopcock separating the cold finger with ozone was slowly opened, allowing the NO_2 and O_3 to mix. The reaction was allowed to proceed for 30 minutes. The estimated

time for completion was determined with a chemical kinetics model (KINTECUS). Afterwards, LN_2 was used at the bottom finger of C2 to trap all possible products (except O_2) as well as left over NO_2 and O_3, if any remained. The O_2 thus produced was transferred to a sample vial with MS and its isotopic composition was determined via mass spectrometry.

D. Isotopic Measurements

The aliquots of ozone and O_2 produced from the $NO_2 + O_3$ reaction were analyzed using a MAT 253 IRMS in dual inlet mode. An LGGE standard oxygen gas (calibrated against VSMOW: $\delta^{17}O_{SMOW}$ = 3.53 ‰, $\delta^{18}O_{SMOW}$ =7.52 ‰) was used as the reference gas. Each analysis comprises eight pairs of sample-reference ratio measurements to obtain average $\delta^{17}O$ and $\delta^{18}O$ values. These were in turn used to determine the enrichment relative to tank O_2 ($\delta^{17}O_{SMOW}$ = 5.97 ‰, $\delta^{18}O_{SMOW}$ =12.14 ‰). As mentioned before, the linear expression $\Delta^{17}O = \delta^{17}O - 0.52 \times \delta^{18}O$ was used for calculating $\Delta^{17}O$ values.

E. Control Experiments

As mentioned before, the ozone that reacts in C2 is assumed to have the same δ- values as the aliquot. However, there could be some minor change during the transfer from T1 to C2 associated with ozone dissociation or equilibration between T1 and T2. To investigate this possibility, we did nine control experiments in which ozone having various $\Delta^{17}O$ values was produced and allowed to equilibrate between T1 and T2 and transferred to C2. The ozone gases in T2 and C2 were collected separately and analysed for $\delta^{17}O$ and $\delta^{18}O$ values. These experiments showed that on average there is usually a small but significant (0.74‰) increase in $\Delta^{17}O$ value during equilibration. The ozone reacting in flask C2 had little less δ-values: average changes were -1.38 ‰ in $\delta^{17}O$ and -4.22 ‰ in $\delta^{18}O$ (Table 2.1) which implies slightly more $\Delta^{17}O$ values than computed from aliquots. These corrections were applied to the measured aliquot values to obtain the reacting ozone values.

Table 2.1. Control experiment results in order to observe an aliquot- effect. Change in $\delta^{17}O$ and $\delta^{18}O$ of reacting ozone (in C2) from aliquot values (in T2) observed from the 9 control experiments. The average change in δ values was used to correct for this effect. The mean change in $\Delta^{17}O$ is 0.74‰.

Expt.	Ozone in T2		Ozone in C2		Change in $\delta^{17}O$	Change in $\delta^{18}O$
No	$\delta^{17}O$	$\delta^{18}O$	$\delta^{17}O$	$\delta^{18}O$		
81	59.62	71.49	58.83	68.07	0.79	3.42
82	60.25	73.33	57.49	66.00	2.75	7.33
83	47.60	58.62	46.49	55.04	1.10	3.58
84	32.67	40.04	30.44	34.34	2.22	5.70
85	29.84	39.23	28.13	34.63	1.72	4.60
87	100.58	122.99	99.33	119.72	1.25	3.27
88	101.23	120.10	100.90	117.13	0.33	2.97
90	73.61	85.50	73.17	82.72	0.44	2.78
91	59.62	71.49	58.83	68.07	0.79	3.42
				Average	1.38	4.22

2.3. Results and Analysis

2.3.1. Isotopic measurements

Results for $\delta^{17}O$, $\delta^{18}O$, and $\Delta^{17}O$ during the isotope transfer experiments are summarized in Table 2.2. Ozone produced for individual experiments had $\Delta^{17}O$ values ranging from 6.13‰ to 41.02‰. The oxygen gas produced via R4 was also analyzed and had $\Delta^{17}O$ values ranging -0.15‰ to 31.43‰.

Table 2.2. Measured and calculated $\delta^{17}O$, $\delta^{18}O$, and $\Delta^{17}O$ for Bulk Ozone, O_2 and NO_3 produced by the $NO_2 + O_3 \rightarrow NO_3 + O_2$ reaction and terminal oxygen atoms of ozone. The values are in units of ‰ (per mil) with respect to tank oxygen and recalculated based on the control experiments.

Expt.	O_3, Bulk			O_2, Produced			$^{\ddagger}\Delta^{17}O$,	$^{\ddagger}\Delta^{17}O$,
No	$\delta^{18}O$	$\delta^{17}O$	$\Delta^{17}O$	$\delta^{18}O$	$\delta^{17}O$	$\Delta^{17}O$	NO_3	terminal
1	7.50	10.07	6.17	10.43	5.26	-0.15	6.28	18.84
2	8.66	13.66	9.15	17.45	12.10	3.03	7.14	21.41
3	11.23	15.40	9.56	24.26	15.76	3.17	7.47	22.40
4	24.49	22.53	9.80	31.96	18.42	1.90	8.60	25.79
5	20.66	20.75	10.00	34.72	22.85	4.84	6.81	20.44
6	17.36	20.66	11.64	29.65	20.76	5.36	8.07	24.22
7	35.89	32.54	13.88	38.58	28.81	8.72	8.05	24.14
8	44.90	40.92	17.57	39.83	32.48	11.65	9.73	29.20
9	43.88	40.46	17.64	43.83	34.35	11.47	9.93	29.80
10	34.26	38.31	20.49	44.76	37.29	13.84	11.15	33.45
11	33.09	37.71	20.50	45.73	36.64	12.74	11.92	35.77
12	52.63	49.03	21.66	63.82	49.92	16.55	10.50	31.51
13	53.78	50.09	22.12	57.16	46.37	16.42	11.02	33.07
14	47.70	48.51	23.71	56.89	46.70	16.87	12.30	36.89
15	43.57	46.65	23.99	41.80	37.61	15.63	13.40	40.21
16	71.00	65.13	28.21	74.90	61.07	21.72	13.46	40.38
17	55.56	57.14	28.24	63.71	54.35	20.81	14.10	42.29
18	73.41	68.95	30.78	78.99	65.26	23.69	14.66	43.97

19	86.58	77.88	32.86	93.13	72.82	23.99	16.60	49.80
20	89.78	81.59	34.90	99.52	77.58	25.38	17.69	53.06
21	107.03	92.28	36.62	111.86	84.86	26.31	18.82	56.47
22	107.14	93.24	37.53	107.97	84.24	27.57	18.80	56.39
23	106.58	93.20	37.77	111.04	85.38	27.17	19.35	58.06
24	103.25	91.86	38.16	109.12	85.37	28.07	19.08	57.24
25	102.48	92.16	38.87	98.94	80.54	28.40	19.48	58.43
26	107.77	95.54	39.50	111.84	87.64	28.88	19.85	59.54
27	110.78	98.04	40.44	116.36	92.17	30.93	19.32	57.97
28	105.95	96.71	41.62	111.33	90.15	31.43	20.11	60.33
29*	-41.16	-20.22	1.18	-16.58	-32.6	-0.18	0.92	2.76
30*	-44.54	-21.93	1.23	-14.97	-30.3	0.77	0.72	2.15
31*	-41.23	-20.20	1.24	-14.51	-27.6	-0.18	1.36	1.60

2.3.2. Analysis

A. Anomaly Transfer

The ^{17}O excess present in NO_3 is a function of the ^{17}O-excess in NO_2 ($\Delta^{17}O(NO_2)$) and $\Delta^{17}O(O_3*)$. We have defined $\Delta^{17}O(O_3*)$ as the ^{17}O-excess transferrable from ozone via terminal or central oxygen atom (expressed in equation 2.3 below) and it is not same as $\Delta^{17}O(O_3)$ (Savarino et al., 2008;Janssen, 2005). This can be expressed mathematically using a mass balance equation as:

$$3\Delta^{17}O(NO_3) = 2\Delta^{17}O(NO_2) + \Delta^{17}O(O_3*) \qquad (2.1)$$

However, the ^{17}O excess in NO_2 radical used in this study is negligible ($\Delta^{17}O(NO_2)$ = -0.7 ± 1.4 ‰) (Savarino et al., 2008) compared to the higher $\Delta^{17}O$ values we are interested in and we can fairly assume that $\Delta^{17}O(NO_2)$ is zero.
The transferred oxygen isotopic anomaly can be written as a function of the isotopic anomaly in bulk ozone and the O_2 produced by the reaction:

$$\Delta^{17}O(O_3^*) = 3\Delta^{17}O(O_3) - 2\Delta^{17}O(O_2) \quad (2.2)$$

where $\Delta^{17}O(O_3)$ and $\Delta^{17}O(O_2)$ are the values obtained from this experiment.

Fig. 2.3 represents a plot of the $\Delta^{17}O(O_3^*)$ versus $\Delta^{17}O(O_3)_{bulk}$ and shows that the two are linearly related. The best fit linear equation over the whole range of bulk $\Delta^{17}O(O_3)$ values is: $\Delta^{17}O(O_3^*) = (1.23\pm0.19) \times \Delta^{17}O(O_3)_{bulk} + (9.02\pm0.99)$. However, if we narrow the range to the average tropospheric ozone $\Delta^{17}O$ values of 20-40 ‰ (Johnston and Thiemens, 1997;Krankowsky et al., 1995), the linear fit is given by $\Delta^{17}O(O_3^*) = (1.41\pm0.25) \times \Delta^{17}O(O_3)_{bulk} + (3.34\pm1.42)$. This equation is in good agreement with the equation $\Delta^{17}O(O_3^*) = 1.5 \times \Delta^{17}O(O_3)_{bulk}$ whose implication is discussed below.

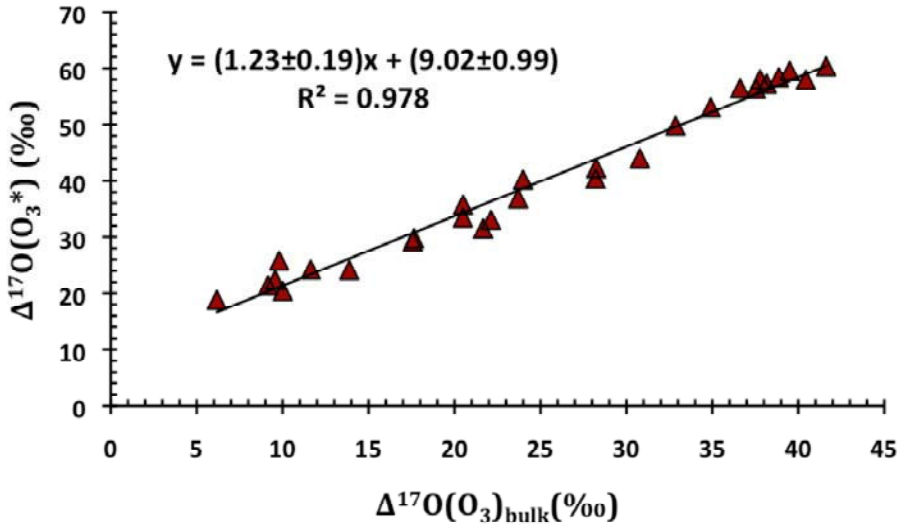

Figure 2.3. *Plot of* $\Delta^{17}O(O_3^*)$ *versus* $\Delta^{17}O(O_3)_{bulk}$ *for the whole range of data points. The* $\Delta^{17}O(O_3^*)$ *is calculated using the equation* $\Delta^{17}O(O_3^*) = 3\Delta^{17}O(O_3) - 2\Delta^{17}O(O_2)$. *The best fit y = (1.23±0.19)x + (9.02±0.99) represents pure experimental conclusion without any assumptions.*

B. Reaction Mechanism

The $NO_2 + O_3 \rightarrow NO_3 + O_2$ oxidation reaction proceeds via transfer of one of the three oxygen atoms of ozone to NO_3. We assume a probability p for the terminal oxygen atom transfer and (1-p) for the transfer of the central atom. This can be described by an isotopic transfer function as follows:

$$\Delta^{17}O(O_3^*) = p\Delta^{17}O(O)_{terminal} + (1\text{-}p)\Delta^{17}O(O)_{central} \quad (2.3)$$

The ozone mass balance is given as:

$$\Delta^{17}O(O_3)_{bulk} = 2\Delta^{17}O(O)_{terminal} + \Delta^{17}O(O)_{central} \quad (2.4)$$

It is clear that the three unknowns p, $\Delta^{17}O(O)_{terminal}$ and $\Delta^{17}O(O)_{central}$ cannot be determined based on these two equations. However, it is known that ozone does not exhibit a statistically distributed isotopic anomaly. The Gao–Marcus theory (Gao and Marcus, 2001) postulates that the asymmetric ozone molecule is favored during ozone formation due to the symmetry-driven restriction of the couplings between the rotational-vibrational energy levels of the symmetric molecule. The key point is that asymmetric ozone O_3* has a longer lifetime due to more rapid randomization of the energy (relative to symmetric O_3*), enhancing the yield of asymmetric O_3 from collisional stabilization. From a quantification of isotope transfer for the $NO + O_3 \rightarrow NO_2 + O_2$ reaction, Savarino et al. (2008) found that the terminal oxygen atom of ozone was preferentially transferred with only a low probability (8±5)% for central atom abstraction during this oxidation reaction. In an experimental study of the aqueous phase NO_2^- /O_3 oxidation reaction, (Michalski and Bhattacharya, 2009) determined that it is the terminal oxygen atom that is transferred during oxidation reactions and the isotopic anomaly resides only on the terminal oxygen atom of ozone.

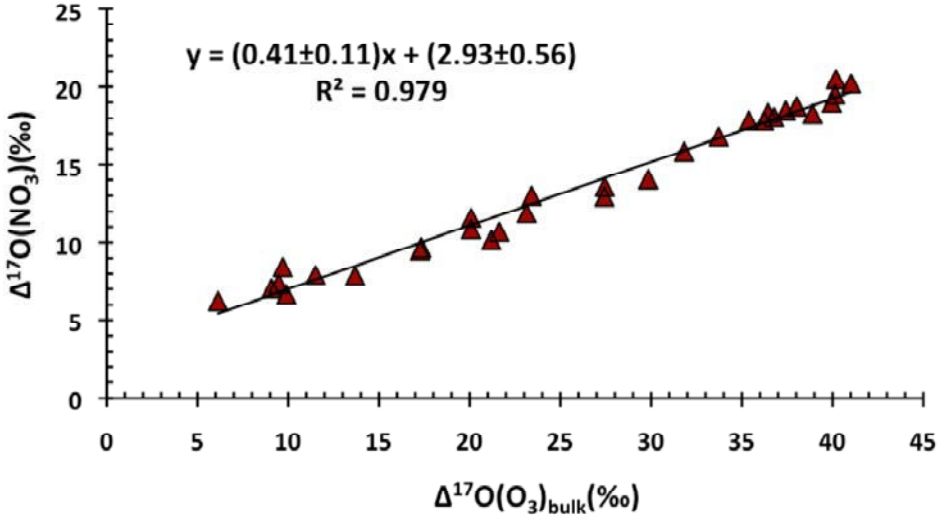

Figure 2.4. *Plot for $\Delta^{17}O(NO_3)$ versus $\Delta^{17}O(O_3)_{bulk}$ for the whole range of data points. $\Delta^{17}O(NO_3)$ is calculated using the equation $3\Delta^{17}O(NO_3) = 3\Delta^{17}O(O_3)_{bulk} - 2\Delta^{17}O(O_2)_{produced}$ and it is the diluted $\Delta^{17}O$ due to the contribution of two zero $\Delta^{17}O$ oxygen atoms from NO_2. The slope from this graph is compared with the theoretically expected slope (0.5) based on the two assumptions mentioned in the text.*

Based on the above studies we made the two assumptions given below and validate them according to our experimental observation from the gas phase $NO_2 + O_3 \rightarrow NO_3 + O_2$ reaction.

i) The oxygen isotope anomaly of O_3 exists only on terminal position ($\Delta^{17}O(O)_{central} = 0$) and ii) the reaction of O_3 with NO_2 occurs only with the terminal oxygen atoms (i.e. p = 1).

Hence, the oxygen molecule produced by reaction 1 is composed of two kinds of oxygen atoms and its $\Delta^{17}O$ value is given by:

$$2\Delta^{17}O(O_2) = \Delta^{17}O(O)_{terminal} + \Delta^{17}O(O)_{central} \quad (2.5)$$

The $\Delta^{17}O$ values for the NO_3 produced can also be calculated by:

$$3\Delta^{17}O(NO_3) = 3\Delta^{17}O(O_3)_{bulk} - 2\Delta^{17}O(O_2)_{produced} \quad (2.6)$$

where the $\Delta^{17}O$ values of $(O_3)_{bulk}$ and $(O_2)_{produced}$ are the experimental values.
Combining equations 2.4-2.6 and using the above-mentioned assumptions we obtain:

$$\Delta^{17}O(NO_3) = 1/2\Delta^{17}O(O_3)_{bulk} \quad (2.7)$$

Equation 2.7 implies that under the above assumptions, if a linear fit is made for $\Delta^{17}O$ (NO_3) versus $\Delta^{17}O(O_3)_{bulk}$, a slope of 0.5 should be obtained. Based on the observed experimental values and using equation 2.6, a linear fit of $\Delta^{17}O(NO_3) = (0.41\pm 0.11) \times \Delta^{17}O(O_3)_{bulk} + (3.00\pm0.57)$ was obtained (**Fig. 2.4**) for the whole range of data points. The $\Delta^{17}O(NO_3)$ given here is a diluted $\Delta^{17}O$ value due to the two oxygen atoms already present in the NO_2 which carries no ^{17}O excess. If we restrict the range to the narrow tropospheric ozone $\Delta^{17}O$ values (**Fig. 2.5**) the fit is given by: $\Delta^{17}O(NO_3) = (0.47\pm 0.15) \times \Delta^{17}O(O_3)_{bulk} + (1.11\pm0.82)$ which matches closely to the expected relation. This implies that the two assumptions can be considered valid as far as the restricted tropospheric ozone $\Delta^{17}O$ range is concerned.

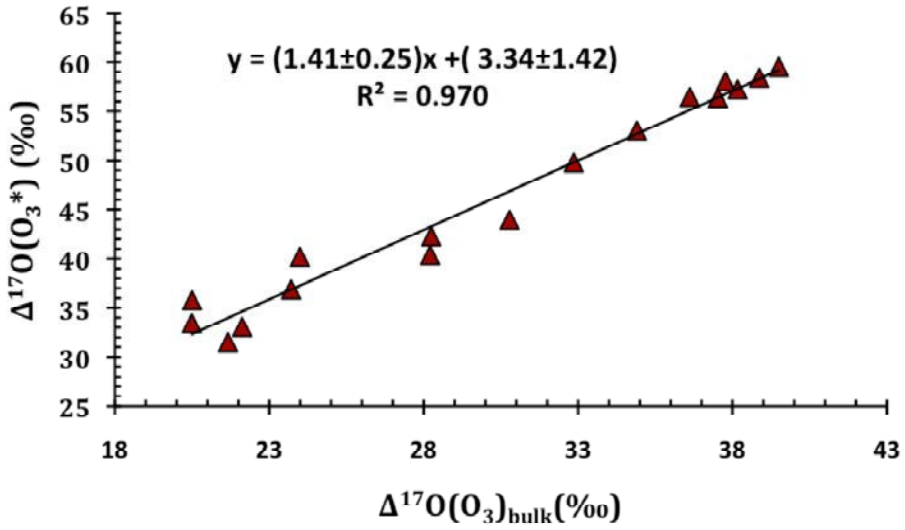

Figure 2.5. *Plot of* $\Delta^{17}O(O_3^*)$ *versus* $\Delta^{17}O(O_3)_{bulk}$ *for tropospheric ozone* $\Delta^{17}O$ range (20-40‰ . *The* $\Delta^{17}O(O_3^*)$ *is calculated using the equation* $\Delta^{17}O(O_3^*) = 3\Delta^{17}O(O_3) - 2\Delta^{17}O(O_2)$. *The best y =(1.41±0.25)x + (3.34±0.1.42) represents a pure experimental conclusion without any assumptions.*

However, we note that both linear equations expressing nitrate $\Delta^{17}O$ in terms of ozone $\Delta^{17}O$ have a small non-zero intercept. This would suggest that even at low $\Delta^{17}O(O_3)_{bulk}$ values nitrate radical formed via reaction with O_3 would have a small $\Delta^{17}O$. Due to our inability to produce ozone with zero $\Delta^{17}O$ via electrical discharge of oxygen gas the non-

zero intercept is inferred based on higher $\Delta^{17}O$ values. It is possible that this observation may be at least partly accounted by experimental error e.g., incomplete trapping and/or aliquot sampling, etc. Based on a set of control experiments we estimated the aliquot-effect, which showed that the aliquot was on average enriched compared to the real sample by 4.22 ‰ and 1.38 ‰ in ^{18}O and ^{17}O respectively.

To investigate this issue further, ozone was produced through the electrolysis of acidified water, which produces ozone of mass-dependent composition(Bhattacharya et al., 2009) and this ozone was used for reaction with NO_2. The results obtained for $\Delta^{17}O(O_3*)$ (experiments 29-31) are in good agreement with the transfer function for the narrowed range considering the small contribution from the $\Delta^{17}O(NO_2)$ (-0.7±1.4 ‰). The above observations suggest that our assumptions are reasonably valid within a certain range of bulk ozone $\Delta^{17}O$ values (typically 20-40 ‰ range). However, for the lower $\Delta^{17}O$ range (below 20 ‰) the observation deviate to some extent. Therefore, it is still an open question if the terminal only enrichment or terminal atom transfer only theories are valid. We have generated ozone with $\Delta^{17}O$ below 20 ‰ at relatively lower temperature and pressure ranges. We believe that this might interfere with the reaction pathways. A thorough analysis of this apparent discrepancy is beyond the scope of this paper. However, this is certainly a topic that merits further study.

Generally, our experimental observations agree well with previous studies in a limited bulk ozone $\Delta^{17}O$ range (Savarino et al., 2008;Michalski and Bhattacharya, 2009;Bhattacharya et al., 2009) with respect to terminal atom only transfer and excess enrichment residing on only the terminal atom.

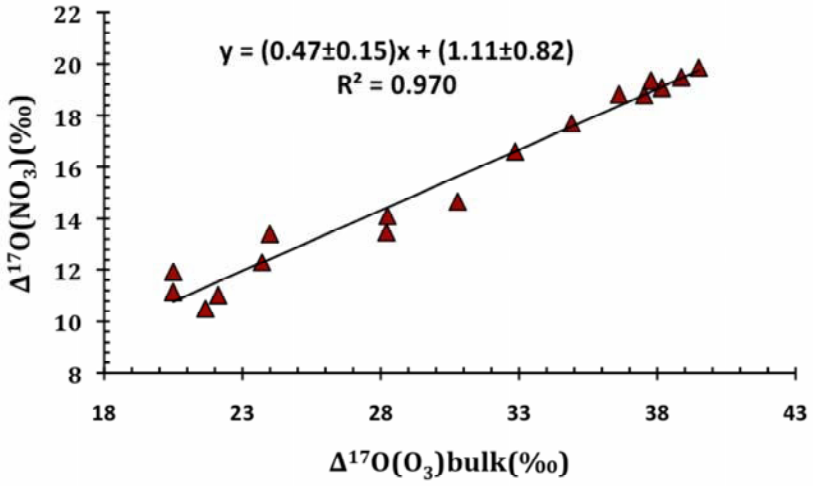

Figure 2.6. *Plot for $\Delta^{17}O$ (NO_3) versus $\Delta^{17}O(O_3)_{bulk}$ for the tropospheric ozone $\Delta^{17}O$ range (20-40‰). $\Delta^{17}O$ (NO_3) is calculated using the equation $3\Delta^{17}O(NO_3) = 3\Delta^{17}O(O_3)_{bulk} - 2\Delta^{17}O(O_2)_{produced}$ and it is the diluted $\Delta^{17}O$ due to the contribution of two zero $\Delta^{17}O$ oxygen atoms from NO_2. The slope from this graph is compared with the theoretically expected slope (0.5) based on the two assumptions mentioned in the text.*

Another critical issue in this study was possible mechanisms that can have direct or indirect effects on the measured δ-values. In this study we have assumed that the

contribution of additional oxygen from other processes such as decomposition of the NO_3 produced is negligible due to the reasons discussed below.

The major fate of the NO_3 radical is reaction with NO_2 to attain equilibrium with N_2O_5. Even if there might be some water on the walls of the reaction chamber, this will lead to the formation of HNO_3 which will further push the equilibrium towards rapid consumption of the NO_3 radicals.

By applying mass balance, for every micromole of ozone that reacts with NO_2 we should expect an O_2 product in 1:1 ratio. Based on our experimental observation we obtain a slope of 0.88 for the plot of the amount of ozone consumed with respect to the amount of O_2 produced by the reaction (**Fig. 2.7**). This shows that we did not produce any additional oxygen. In most of the data points, we observe smaller amounts of oxygen than expected. This is possibly due to an over estimation of the initial amount of ozone transferred to the reaction chamber. Oxygen is measured directly at the end of the reaction via collection on MS. However, ozone is determined indirectly from trap 2. As some of the ozone decomposes on the wall during the transfer process to reaction chamber, there is always some loss of ozone that is not included in the indirect method of calculating amount of ozone transferred. Though oxygen is formed from this process, it is pumped out in every step by freezing the ozone in a liquid nitrogen trap. The larger deviation observed at relatively higher points is due to a decrease in ozone trapping efficiency of the MS at higher amount of ozone or oxygen. Additionally, we have modeled our system with Kintecus assuming 1% of the NO_3 produced is decomposed to NO_2 and O rather than forming N_2O_5. We have observed no difference in the amount of O_2 produced. These points have enabled us to rule out the possibility of additional oxygen atom contribution from NO_3 decomposition.

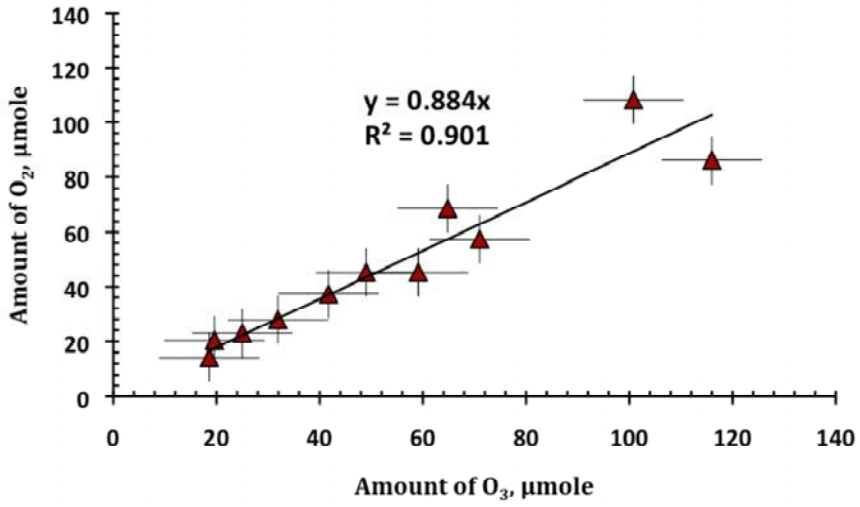

Figure 2.7. *Plot of* amount of Ozone reacting *versus amount of oxygen produced during the NO_2 + O_3 reaction to produce NO_3 and O_2. The error bars show the uncertainty of measurements of the amounts of initial ozone and oxygen produced.*

2.4. Discussion

2.4.1. Reaction Dynamics

Various studies have been undertaken to study the $NO_2 + O_3 \rightarrow NO_3 + O_2$ reaction due to its relevance in atmospheric chemistry and in particular to evaluate the rate of this reaction. The IUPAC has recommended $k = 1.4 \times 10^{-13}\ e^{-2470/T}\ cm^3\ molecule^{-1}\ s^{-1}$ over the temperature range of 230 K – 360 K ($k = 3.5 \times 10^{-17}\ cm^3\ molecule^{-1}\ s^{-1}$ at 298 K) and E_a = 20.54 kJ mol^{-1}(Atkinson et al., 2004).
Based on ab-initio studies, the reaction of NO_2 with O_3 seems to be determined by the π orbital of the terminal oxygen atom of ozone(Peiro-Garcia and Nebot-Gil, 2003). Accordingly, NO_2 attacks the terminal oxygen of ozone and forms a single transition state (TS1), the rate-determining step. On the contrary, the $NO + O_3$ reaction proceeds through two transition states (TS1 and TS2) as well as an intermediate (A)(Peiro-Garcia and Nebot-Gil, 2002, 2003). Application of the single-reference higher correlated QCISD methodology(Peiro-Garcia and Nebot-Gil, 2003) for the computation of the reaction mechanism in case of $NO_2 + O_3$ shows that the overall reaction is a direct process with no intermediate (A) and transition state TS2. It establishes firmly that abstraction of the central atom does not take place.

2.4.2. Atmospheric Implications

NO_X plays a major role in the production of tropospheric ozone and destruction of stratospheric ozone(Crutzen, 1979). The $NO_2 + O_3 \rightarrow NO_3 + O_2$ in particular has been investigated widely due to its importance in the nighttime chemistry of the troposphere. The atmospheric chemistry of nitrates can be explained by studying their oxygen and nitrogen isotopic composition. The relative involvement of ozone in the formation of atmospheric nitrate can be inferred based on ^{17}O excess transfer studies.
The correlation $\Delta^{17}O(O_3^*) = (1.23\pm0.19) \times \Delta^{17}O(O_3)_{bulk} + (9.02\pm0.99)$ should be applied to quantify the anomaly transfer during the NO_2 reaction with O_3. However, this equation underestimates the results due to the strange intramolecular isotopic distribution of ozone at low $\Delta^{17}O$ values (typically below 20 ‰). Instead, we propose the equation $\Delta^{17}O(O_3^*) = (1.41\pm0.25) \times \Delta^{17}O(O_3)_{bulk} + (3.34\pm1.42)$ as appropriate in the 20-40 ‰ range of bulk ozone, which is considered relevant for tropospheric ozone.
We can estimate the $\Delta^{17}O$ value of the final NO_X cycle product, HNO_3, by using isotopic anomaly transfer functions derived experimentally for the 0-40 ‰ range in order to keep consistency between the two experimental results and applying mass balance equations defined below:

- $\Delta^{17}O(O_3^*)(NO + O_3) = (1.18\pm 0.07) \times \Delta^{17}O(O_3)_{bulk} + (6.6\pm1.5)$ for the $NO + O_3 \rightarrow NO_2 + O_2$ reaction (Savarino et al., 2008)

- $\Delta^{17}O(O_3^*)(NO_2 + O_3) = (1.23\pm0.19) \times \Delta^{17}O(O_3)_{bulk} + (9.02\pm0.99)$ for the $NO_2 + O_3 \rightarrow NO_3 + O_2$ reaction (from this study)

- $\Delta^{17}O(NO_2) = 1/2\Delta^{17}O(NO) + 1/2\Delta^{17}O(O_3^*)(NO + O_3)$
- $\Delta^{17}O(NO_3) = 2/3\Delta^{17}O(NO_2) + 1/3\Delta^{17}O(O_3^*)(NO_2 + O_3)$
- $\Delta^{17}O(N_2O_5) = 1/3\Delta^{17}O(NO_2) + 1/2\Delta^{17}O(NO_3)$

Using $\Delta^{17}O(O_3)$ values of 25 ‰ (Krankowsky et al., 1995;Johnston and Thiemens, 1997) and 35 ‰ (Lyons, 2001), we have estimated the $\Delta^{17}O(O)$ of nitrate produced via the termination reaction $NO_3 + RH \rightarrow HNO_3$ to be 25 ‰ and 33 ‰ respectively. If the termination reaction is via hydrolysis of N_2O_5, we obtain lower $\Delta^{17}O$ for nitrate, 18.5 ‰ and 24.5 ‰, for $\Delta^{17}O(O_3)$ values of 25 ‰ and 35 ‰ respectively.
However, the two nitrate formation pathways mentioned above accounts for only 22 % of global annual mean tropospheric nitrate formation based on modeling calculations (Alexander et al., 2009) assuming a tropospheric ozone $\Delta^{17}O$ value of 35 ‰. The NO_3 + DMS termination reaction can account for up to 46 % in high latitude marine boundary layer where as the N_2O_5 hydrolysis can account for up to 74 % at high northern latitudes over the continental and the arctic regions(Alexander et al., 2009).
Nitrate formation pathways vary in time and space, which in turn leads to variation in the measured $\Delta^{17}O$ value of different nitrate samples. This fact should be emphasized while using such isotopic anomaly transfer studies.

2.5. Conclusions

The use of ^{17}O-excess to study various atmospheric reactions is currently a widely employed technique. The chemical cycling of many important atmospheric compounds can be investigated and quantified through the use of this method. We have studied the $NO_2 + O_3 \rightarrow NO_3 + O_2$ gas phase reaction, in particular, in order to quantify the incorporation of anomaly from O_3 to nitrate. The experimental results obtained in this study should serve as useful tools for studying the atmospheric chemistry of nitrate. The results obtained in this study show that during oxidation ozone transfers its ^{17}O excess to NO_3 in a fashion that can be quantified by the function $\Delta^{17}O(O_3^*) = (1.23\pm0.19) \times \Delta^{17}O(O_3)_{bulk} + (9.02\pm0.99)$. We would like to point out that the $NO_2 + O_3$ reaction should not be treated as similar to the $NO + O_3$ reaction as the former proceeds only through terminal atom transfer. In order to explain the overall high atmospheric nitrate anomaly, a detailed study of the different nitrate formation reaction pathways of nitrate formation should be carried out. By coupling experimental results with modeling work, an accurate quantitative explanation of the ^{17}O excess of nitrate samples can be obtained.

Appendix

KINTECUS Modeling

In order to understand how the NO_2 reaction with ozone proceeds in the reaction chamber, we have used a modeling program called Kintecus (V.3.9) that is available at http://www.kintecus.com/. We have incorporated our experimental values for initial concentrations of reactants (20-35 µmole ozone and 65 µmole NO_2) and possible reaction pathways with their reaction rates available in the literature (Table A.1). At the end of our experiment (30 minutes of reaction time), our model showed that all ozone is consumed and there is some left over NO_2. Complete reaction of ozone at the end of the process confirms that there is no oxygen contribution due to left over ozone avoiding procedural bias. The reaction of NO_2 and NO_3 to produce N_2O_5 also has no influence on the oxygen collected, as this equilibrium does not lead to any oxygen incorporation for the system.

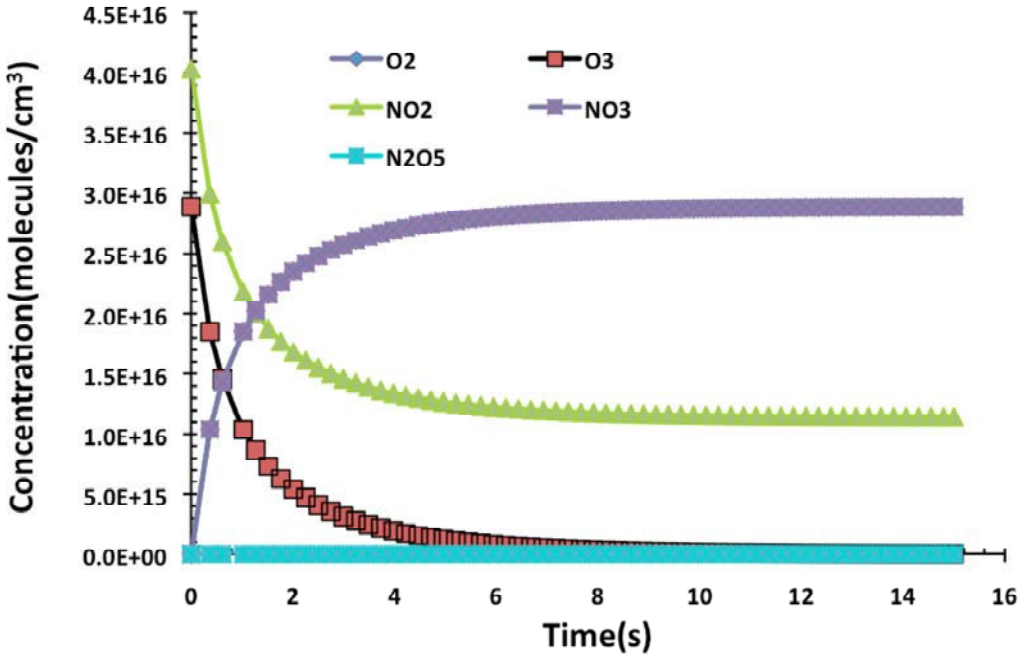

Figure 2.8. *Kintecus model output for the reaction of NO_2 with ozone (first 15 seconds) under the present experimental conditions. A rapid decrease in concentration of ozone and NO_2 is accompanied by fast increase in O_2 and NO_3.The O_2 and NO_3 lines are overlapping because they are in the same concentration range.*

Table A.1. *Reactions with their rate constant (k) values as incorporated in the kintecus model described in the text.*

Reaction	*k*, $cm^3 molecules^{-1} s^{-1}$	Reference
$NO_2 + O_3 \rightarrow NO_3 + O_2$	3.5×10^{-17}	Atkinson et al., 2004
$NO_2 + NO_2 \rightarrow N_2O_4$	1.4×10^{-33}	Atkinson et al., 1997
$N_2O_4 \rightarrow NO_2 + NO_2$	6.89×10^{-15}	Atkinson et al., 1997
$NO_2 + NO_3 \rightarrow N_2O_5$	3.6×10^{-30}	Hahn et al., 2000
$N_2O_5 \rightarrow NO_2 + NO_3$	1.2×10^{-19}	Atkinson et al., 1997

CHAPTER 3

Laboratory study of nitrate photolysis in Antarctic snow, Part 2: Isotopic effects and wavelength dependence

This chapter is based on:

Tesfaye A Berhanu[1], Carl Meusinger[2], Joseph Erbland[1], Joel Savarino[1] and Matthew S Johnson[2], Rémy Jost[3]. Laboratory study of nitrate photolysis in Antarctic snow, Part 2: Isotopic effects and wavelength dependence. *Journal of Chemical Physics* ***(to be submitted)***

Abstract

Atmospheric nitrate is preserved in Antarctic snow firn and ice. However, in low snow accumulation sites post-depositional processes initiated by UV photolysis obscure the interpretation of its record in ice cores. The goal of these studies (see also companion paper in the annex by Meusinger et al. In prep.) is to describe nitrate photochemistry in Antarctic snow in sufficient detail to improve the interpretation of this record. Naturally occurring stable isotopes such as ^{15}N and ^{18}O provide additional information concerning post-depositional processes. In this paper we present results from studies of the wavelength-dependent isotope effects due to photolysis of nitrate in a matrix of natural snow. The experimental setup included a Xe UV lamp as light source with a selection of spectral filters, an environmental chamber with temperature controller, and an inert flow system to flush away gas phase photoproducts. Natural snow from Dome C, Antarctica was irradiated within selected wavelength regions. The irradiated snow column was sampled in 1 cm sections and analyzed for nitrate concentration and isotopic composition ($\delta^{15}N$, $\delta^{18}O$ and $\Delta^{17}O$). From these measurements, an average photolytic isotopic fractionation of $^{15}\varepsilon$ = -15 ± 1.2 ‰ was found for broadband Xe lamp photolysis. These results are ascribed to excitation of the intense absorption band of nitrate around 200 nm. For the photolysis experiments conducted with 280 nm and 305 nm UV-filters, we have determined isotopic fractionations of -23.2 ± 1.0 ‰ and -38.6 ± 2.8 ‰ respectively. An experiment with a filter blocking wavelengths shorter than 320 nm, approximating the actinic flux spectrum at Dome C, showed a photolytic fractionation constant of $^{15}\varepsilon$ = -47.9 ± 6.8 ‰ in good agreement with fractionations determined for the East Antarctic Plateau, ranging from -40 to -74.3 ‰(Erbland et al., 2013). The isotopic fractionations

obtained from this study are compared to theoretical estimates derived by applying the zero point energy shift model coupled with measured actinic fluxes at each depth. The results confirm that the photolytic fractionation of nitrate isotopes in snow is very sensitive to the actinic flux spectrum and indicate limitations in previous laboratory studies. This work demonstrates that the spectrum of the excitation source is a key parameter determining nitrogen isotope fractionation in the photolysis of nitrate in snow.

3.1. Introduction

Nitrate (NO_3^-) is the end product of atmospheric NO_X ($NO + NO_2$) oxidation and its precursors are strongly coupled with OH and O_3 chemistry in the atmosphere. The oxygen isotope ratios in nitrate provide information about the oxidation pathways of nitrate formation, and incorporate the isotopic signature of ozone during this process (Michalski et al., 2003;Savarino et al., 2007). As nitrogen isotopes are conserved from source to sink during nitrate formation, they can be used as metrics to trace the sources of NO_X(Heaton, 1990).

In polar regions, nitrate is one of the most abundant anions in snow, and has a significant potential in documenting past climate change including the oxidation capacity of the atmosphere (Wolff, 1995b;Legrand et al., 1999).

The stable isotope ratios (R) ($n(^{18}O)/n(^{16}O)$, $n(^{17}O)/n(^{16}O)$ and $n(^{15}N)/n(^{14}N)$, where n is the amount of each isotope) of nitrate are expressed as δ-values ($\delta^{17}O$, $\delta^{18}O$ and $\Delta^{17}O$) where $\delta = (R_{spl}/R_{ref})-1$ is the ratio of R of the sample (R_{spl}) and reference (R_{ref}) with references being AIR_N_2 and VSMOW for N and O respectively . The ^{17}O-excess is determined by the linear relation $\Delta^{17}O = \delta^{17}O - 0.52 \times \delta^{18}O$. These stable isotope ratios of nitrate in snow have been used to investigate the sources and formation pathways of snow nitrate in polar regions (Hastings et al., 2004;Hastings et al., 2009;Savarino et al., 2007). However, the large loss of snow nitrate (Dibb and Whitlow, 1996;Röthlisberger et al., 2000) and simultaneous isotopic fractionations in low accumulation sites (Frey et al., 2009;Blunier et al., 2005) indicate post-depositional processes significantly modify nitrate and quantitative interpretation of these signals is not straightforward. Processes including evaporation/sublimation and photolysis change the original nitrate mass and isotopic signal, especially in low snow accumulation sites such as Dome C. This conclusion is supported by the high atmospheric NO_X levels, and the profiles of nitrate concentration and stable isotope ratios in snow at these regions (Wolff et al., 2002;Röthlisberger et al., 2002;Röthlisberger et al., 2000;Frey et al., 2009;Blunier et al., 2005) described below.

Multiple field studies in both the Arctic and Antarctic showed elevated NO_X levels in association with sunlight and determined the snowpack to be the source (Jones et al., 2001b;Honrath et al., 1999;Wang et al., 2007) but the production mechanism is not well constrained. A series of laboratory and field studies have studied these mechanisms. Using natural snow from Halley station in Antarctica, (Cotter et al., 2003) observed emission of NO_X dominated by NO_2 which ceased in the absence of UV radiation below 345 nm, in agreement with a previous laboratory study on artificial snow doped with nitrate (Dubowski et al., 2001). The diurnal variation of NO_X emission from a snow sample exposed to solar UV was monitored in a field study at Neumayer station in Antarctica. In this study, Jones et al. (2000) observed that NO_X emission is driven by

photochemistry (Jones et al., 2000). Additional studies were conducted to determine the mechanism of photolysis of nitrate deposited in snow (Jacobi et al., 2006;Jacobi and Hilker, 2007;Honrath et al., 2000a;Honrath et al., 2000b).
Photolysis of nitrate involves these elementary reactions:

$$NO_3^- + h\nu \rightarrow NO_2 + O^- \quad \text{(R.3.1)}$$

$$NO_3^- + h\nu \rightarrow NO_2^- + O(^3P) \quad \text{(R.3.2)}$$

$$NO_2^- + h\nu \rightarrow NO + O^- \quad \text{(R.3.3)}$$

$$NO_2^- + OH \rightarrow NO_2 + OH^- \quad \text{(R.3.4)}$$

NO_2 is the primary photoproduct of nitrate photolysis (Boxe et al., 2006); R.3.1 is 8-9 times faster than R.3.2 (Grannas et al., 2007). Nitrite produced via R.3.2 may be photolyzed producing NO (R.3.3) or it may react with a hydroxyl radical to produce NO_2 (R.3.4). NO_X products from nitrate photolysis are emitted to the atmosphere where they influence O_3 and HO_X chemistry and have a significant impact on the composition of the boundary layer, further complicating the interpretation of information archived in deep ice cores (Cotter, 2003;Davis et al., 2008;Jacobi and Hilker, 2007;McCabe et al., 2005b;Qiu et al., 2002;Dominé and Shepson, 2002;Wolff et al., 2002;Grannas et al., 2007).

A series of studies have used stable isotope distributions to investigate nitrate and nitrate-related photochemistry in snow. Blunier et al. (2005)(Blunier et al., 2005) investigated nitrate mass loss and isotopic fractionation ($^{15}\varepsilon$) in artificial snow that was doped with $NaNO_3$ and irradiated with a Xe UV lamp. The laboratory isotopic fractionations did not agree with the field observations leading the authors to rule out photolysis as the main mechanism driving post depositional modification of nitrate. However, in a later study by Frey et al. (2009)(Frey et al., 2009), it was shown that the isotopic fractionation obtained from the laboratory study by Blunier et al. (2005)(Blunier et al., 2005) was not a true representation of the field conditions; and the observed isotope effects were due to the nature of the Xenon excitation lamp spectrum and the lack of removal of photoproducts. Based on field measurements, Frey et al. (2009)(Frey et al., 2009) determined an apparent isotopic fractionation ($^{15}\varepsilon_{app}$) and proposed that photolysis is the main mechanism responsible for the observed isotopic fractionation of stable isotopes of nitrate based on a theoretical approach. These authors applied a simple zero point energy shift model(Yung and Miller, 1997) to derive an isotopic fractionation in the wavelength region of interest (-48 ‰) and observed good agreement with the field observation (-60 ± 15 ‰ (Frey et al., 2009) and -54 ± 10 ‰ (Blunier et al., 2005)). More recently, Erbland et al. (2012)(Erbland et al., 2013) derived an average apparent nitrogen isotopic fractionation of -59 ± 10 ‰ for the East Antarctic Plateau (EAP). However, the variability of field conditions limited the field studies making it problematic to extract a purely photolytic fractionation constant including wavelength dependence (Frey et al., 2009;Erbland et al., 2013). Additionally, the theoretical model of photolytic isotopic fractionation made by Frey et al. (2009) is simplistic and neglects the change in shape and intensity of the absorption cross-section from isotopic substitution (Ndengue et al.,

2010;Jost, 2008), and should therefore be confirmed by an experimental study. The aforementioned limitations of the existing studies clearly demonstrate the need for a laboratory study with improved experimental setup.

The companion paper by Meusinger et al. focuses on the physical chemistry of photolysis of nitrate in snow and specifically on the quantum yield during photodissociation of nitrate in natural snow in the solid phase. The main goal of this paper is to understand the effect of photolysis on the stable isotope enrichments in nitrate in an experimental setup that controls key parameters including temperature, excitation spectrum and product removal.

In this study we investigate the fractionation of oxygen and nitrogen stable isotopes in nitrate in natural Dome C snow in response to photolysis in different UV wavelength regions. We discuss these results using the zero point energy shift model developed by Frey et al. (2009)(Frey et al., 2009). In addition, we re-evaluate previous works using our results and model, and discuss directions for future work.

3.2. Methods

3.2.1. Experimental set up and sample handling

The detailed experimental set up is described in the companion paper (Meusinger et al.) and will only be briefly described here. Wind blown snow from the vicinity of the EPICA warm laboratory at Dome C, Antarctica (75°S 06' and 124°E 33') was collected and homogenized on 6th December 2011 and transported to France. Snow temperatures were always maintained around -20 °C during transport and storage, except during transfer of the sample containers which could occasionally raise the snow temperature to -15 °C for periods of less than an hour. Nitrate concentration measurements at the time of collection (29 nmol ml^{-1}) and before the photolysis experiments (27 nmol ml^{-1}) show identical concentrations within the analytical uncertainty (<3 %)(Frey et al., 2009), confirming temperature and environmental variation had no effect on the snow nitrate, an indicator that the majority of nitrate is probably not physically sorbed in the form of HNO_3 on the surface of the grain crystal.

For each experiment, a sample of 110-120 g of snow was homogenized and transferred into a cylindrical Pyrex glass cell of 30 cm length and 6 cm internal diameter (**Fig. 3.1**). The cell is equipped with two end-clamped cells with Suprasil UV windows (L.O.T. Oriel). The four ports on the upper side of the cell were used as inlets and outlets for a water saturated N_2 flow (to flush gaseous reaction products) and to monitor temperature and pressure during the experiment. A 16 cm long, 10 cm wide Teflon sleeve was formed into the same shape as the glass cell and used to line the snow column inside the cell (**Fig. 3.2**). The sleeve helped to prevent the snow sample from sticking to the glass cell and eased sampling after the experiments.

All experiments were performed in an environmental chamber at -30°C with a side port to mount the Xe lamp. A flow of N_2 saturated with water vapor continuously swept through the snow. Water vapor saturation was maintained by combining a dry N_2 flow with a wet flow generated by passing a fraction of the dry nitrogen flow through a water bubbler giving a combined flow of 2.2 L min^{-1} directed through a cold condensation trap placed inside the environmental chamber to remove the excess water

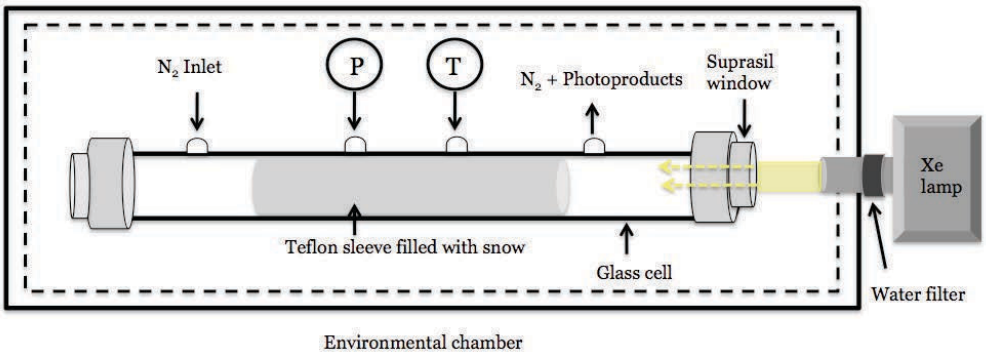

Figure 3.1. *Schematic of the experimental setup used in this study. Natural snow was filled in the glass cell (total length of about 30 cm and internal diameter of 6 cm) with T and P probes (to monitor temperature and pressure) and irradiated with a Xe lamp. A flow of nitrogen (relative humidity of 100%) was used to remove the photoproducts. The water filter at the front of the lamp enabled removal of the infrared (IR) part of the incoming light.*

A Xe lamp (L.O.T. Oriel, 300 Watt) with the spectral range of 200-900 nm was used as light source with a water filter at the front to minimize the IR heat flux into the snow. UV filters were attached at the front of the lamp (LOT Oriel, Andover Corporation). The filters have different cut-off wavelengths; the cut-off function is gradual rather than sharp.

Figure 3.2. *Photo of the glass cell filled with a snow within the teflon sleeve and the four ports*

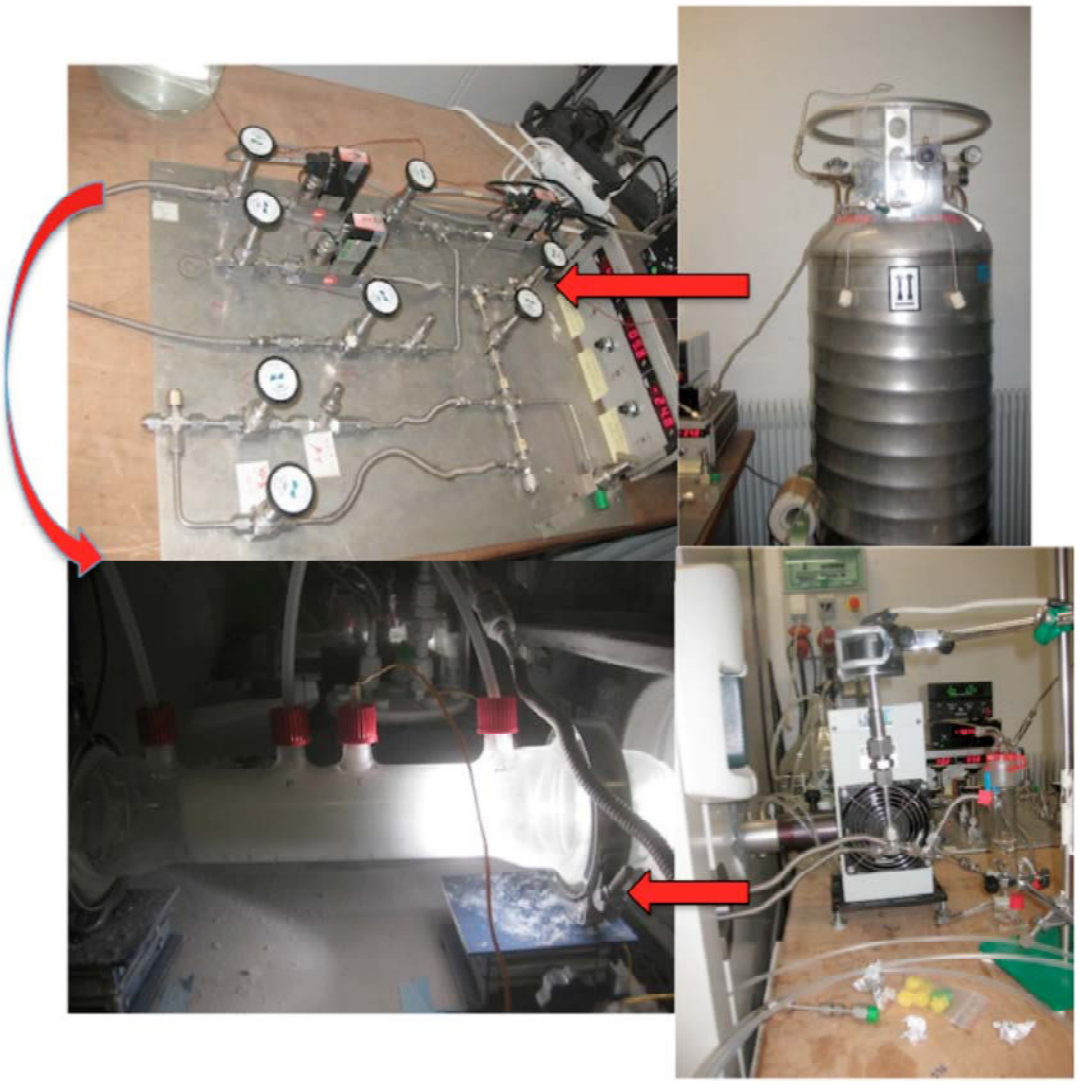

Figure 3.3. *A combined picture of the photolysis experiment set up. From right nitrogen is flushed via the mass flow controllers that are manually adjusted. The main flow is separated into two: dry flow and wet flow generated by bubbling through water. The combined flow is directed towards the glass cell filled with snow after the excess water is removed at the water trap placed inside the cold chamber. The Xe lamp is turned on after all the experimental requirements are met.*

At the end of an experiment, post processing of the snow samples was done in a cold room at -15°C. The snow was slowly pushed out of the Teflon sleeve and sampled in 1-2 cm slices with a scalpel (**Fig. 3.4**). From the side close to the lamp, the first 7 cm was sampled at 1 cm intervals as no significant light flux penetrates deeper into the snow column. Each sub sample (5-10 g) was homogenized and divided into two parts. One part

was used for concentration measurements. The rest of the sample was weighed and sealed in a plastic bag for later isotopic analysis.

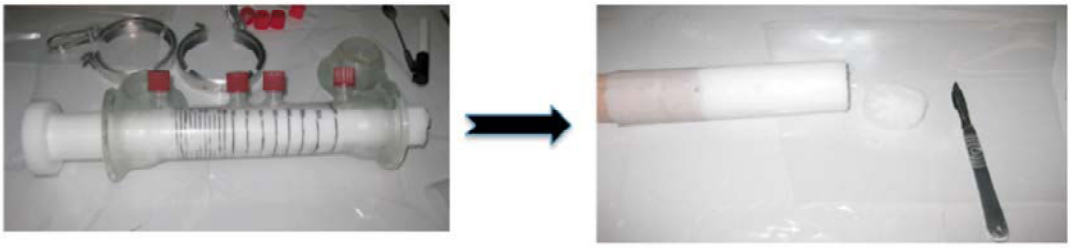

Figure 3.4. *Picture of the post processing of the snow. The snow column is pushed out of the glass cell with the Teflon sleeve that is again sub-sampled at 1-2 cm depth resolution using a scalpel.*

The nitrate absorption cross section has two main peaks: one at about 200 nm and another around 305 nm (**Fig. 1.12**). The former is 3 orders of magnitude larger than the latter (Mark et al., 1996). In order to observe the wavelength dependence of photolysis of nitrate we used long-pass UV filters with cut off wavelengths at 280 nm, 305 nm and 320 nm. An overview of the experimental conditions is provided in Table 3.1.

Table 3.1. Experimental conditions for the experiments. In each case a flow rate of 2.2 L min^{-1} is used to flush out the NO_X by-products. Experiments are performed at -30°C with natural snow from Dome C.

No.	Expt type	duration, hr
1	Dark experiment	139.5
2	No filter	20.3
3	No filter	162.8
4	280 nm filter	164.0
5	305 nm filter	187.2
6	320 nm filter	283.2

3.2.2. Sample Analysis

The snow samples were analyzed for nitrate concentration using an Ion Chromatography system (850 Professional IC, Metroholm). The stable isotope ratios of nitrate were measured using the well established bacterial denitrifier method developed by Sigman et al.(Sigman et al., 2001) and Casicotti et al.(Casciotti et al., 2002) and further improved by Kaiser et al.(Kaiser et al., 2007) and Morin et al(Morin et al., 2009). Briefly, a bacterial culture strain (Pseudomonas Aureofaciens) was grown for 5-7 days in a temperature controlled shaker and then concentrated 8 times. Two ml of this bacterial

suspension was transferred into a 20 ml glass vial, sealed with a PTFE septum and degassed with He (Air Liquide, 99.9%) for 3 hours. The volume of sample necessary to obtain 50 nmol of nitrate was calculated based on the nitrate concentration measurement. The system at the laboratory at LGGE is designed for samples containing 100 nmol of nitrate; however, lower sample amounts were also analyzed using an additional correction to compensate for the blank effect and isotopic exchange. As we have a small sample volume in each slice of snow (typically 5-10 ml) with a nitrate concentration of 8-25 nmol ml^{-1}, sample volumes corresponding to 50 nmol were injected into the vials containing the bacteria. However, few samples were below the minimum amount of nitrate required for isotopic analysis and it was not possible to measure their isotopic composition. After overnight incubation, 0.5 ml of 1 M NaOH was added to inactivate the bacteria. The N_2O in the headspace of the sample vials was flushed with He into a gold tube at 900°C where it decomposed into O_2 and N_2. The resulting gas mixture was injected into a GC column that separate the two species, and passed into a MAT253 IRMS (Thermo) for dual analysis of the oxygen and nitrogen isotope ratios in continuous flow mode (**Fig. 3.5**). An algorithm was used to calibrate the results to account for blank effects and isotopic exchange that could arise due to the small sample size. To correct for isotope effects associated with sample analysis, we have included certified standards of USGS 32, USGS 34 and USGS 35(Böhlke et al., 2003;Michalski et al., 2002) (Table 3.2) which are treated in the exact same way as the samples and prepared in the same matrix as the samples (MQ water)(Morin et al., 2009), at a range of concentrations (20 – 100 nmol). This enabled us to perform a non-linear calibration for some of the samples not falling in the 50 nmol range which would be uncalibrated otherwise. Using the same algorithm the overall accuracy of the method is determined from the standard deviations of the residuals of the linear regression between the measured and expected isotopic values of the references. For the samples analyzed in this study the associated average uncertainties are 2.25 ‰, 0.6 ‰ and 0.6 ‰ for $\delta^{18}O$, $\Delta^{17}O$ and $\delta^{15}N$ respectively. The larger uncertainties observed in these measurements relative to typical values are due to the use of samples smaller than the usual 100 nmol range.

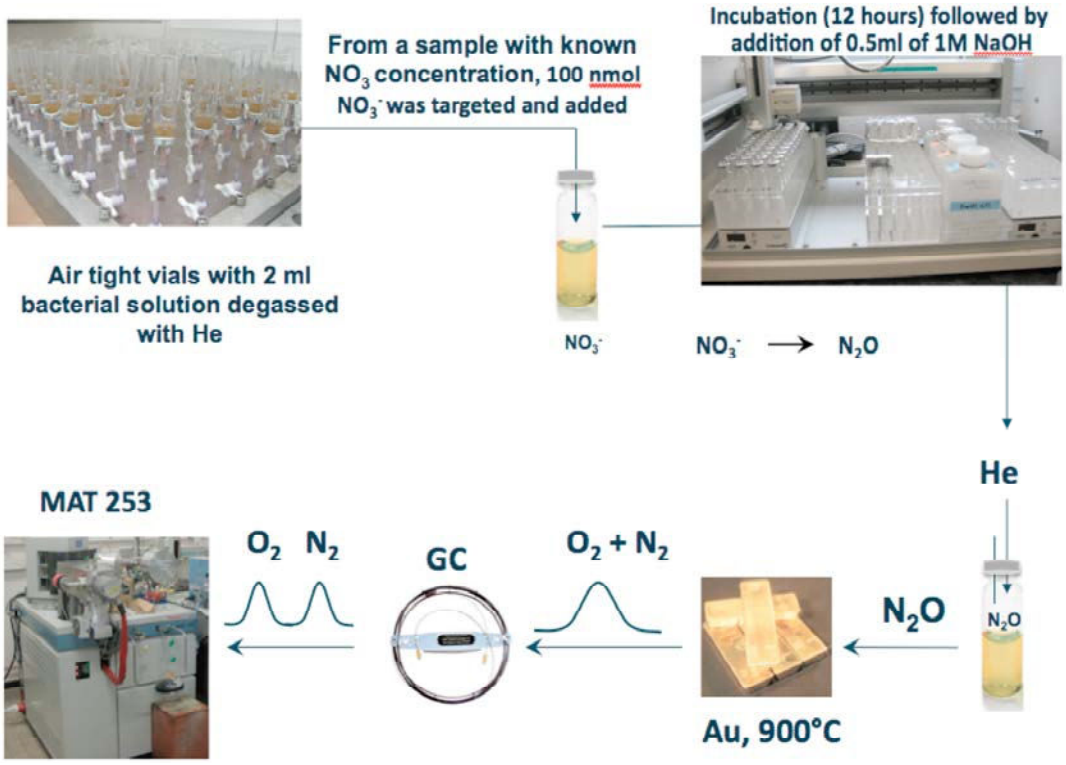

Figure 3.5. *Schematic of steps followed during analysis of snow nitrate by the bacterial denitrifier method*

Table 3.2. Isotopic composition of the standards (in units of ‰) used for isotopic analysis

Code	standard name	$\delta^{17}O$	$\delta^{18}O$	$\Delta^{17}O$	$\delta^{15}N$
A	USGS 35	51.46	57.5[b]	21.56[a]	2.7
C	USGS 35+USGS 34	18.33	14.79	10.64	0.45
F	USGS 32+USGS 34	-0.72	-1.12	-0.14	90.70
Z	USGS 32	13.4[c]	25.7[b]	0.0	180.0[b]

[a]Michalski et al 2002, [b]Bohlke et al 2003, [c]Morin,Phd thesis, 2008

3.2.3. Data reduction

Photolysis rate constants (J) are determined by:

$$J = \int \sigma(\lambda,T)\phi(\lambda,T)I(\lambda)d\lambda \qquad (3.1)$$

where $\sigma(\lambda)$ is the absorption cross section of $^{14}NO_3^-$, $\phi(\lambda)$ is the quantum yield and $I(\lambda)$ is the measured actinic flux of the filtered UV Xe lamp in appropriate units (**Fig. 3.6a**). The calculated photolysis rates (i.e. the integrand of equation 1) are shown in **Fig. 3.6b** as a function of wavelength for the different filters.
The fractionation factor ($^{15}\varepsilon$) is determined using the Rayleigh equation (Frey et al., 2009;Blunier, 2005) assuming NO_X produced by photolysis of nitrate is irreversibly removed from the system with the flow of nitrogen:

$$\frac{R}{R_0} = \frac{\delta + 1}{\delta_0 + 1} = f^{\varepsilon} \qquad (3.2)$$

where R_0 and R are the isotope ratios $^{15}N/^{14}N$ in nitrate before and after photolysis. Note that f denotes the extent of reaction as well as the nitrate fraction left in the snow and determined by $f = C/C_0$, where the initial nitrate in snow has concentration C_0 (and isotopic composition δ_0) and the nitrate after irradiation has concentration C (and isotopic enrichment δ). From equation (1) the following relationship is obtained:

$$\ln(\delta + 1) = \varepsilon \ln(f) + \ln(\delta_0 + 1) \qquad (3.3)$$

Plotting $\ln(\delta+1)$ versus $\ln(f)$ gives the isotopic fractionation ε as the slope. (Note that ε is related to the fractionation factor α by $\varepsilon = \alpha - 1$). The (1-σ) uncertainty in ε is based on the propagation of the error in the isotope ratios, as in Frey et al. (2009)(Frey et al., 2009) based on Taylor (1997)(Taylor, 1997).
The isotopic fractionation is determined theoretically using the equation:

$$\varepsilon = \frac{J'}{J} - 1 \qquad (3.4)$$

where J' and J are the photolytic rate constants for the heavy ($^{15}NO_3^-$) and the light ($^{14}NO_3^-$) isotopologues respectively determined using equation 1 from their corresponding absorption cross-sections of $\sigma(\lambda)$ and $\sigma'(\lambda)$ (**Fig. 3.6a**) and the spectral actinic flux $I(\lambda)$. Note that if the quantum yield ($\phi(\lambda)$) is assumed to be independent of wavelength and to be similar for $^{14}NO_3^-$ and $^{15}NO_3^-$, then there is no need to know its exact value to determine the isotopic fractionation.

The isotopic fractionations ($^{15}\varepsilon_{pho}$) were calculated as a function of filter type and snow column depth by using equation 3.4. We have measured the actinic flux of the pure Xe lamp in the snow column and in the presence of the UV filters (Meusinger et al.). The absorption cross section of $^{14}NO_3^-$ was obtained from Chu et al (2003)(Chu and Anastasio, 2003) and the absorption cross section of $^{15}NO_3^-$ was taken from Frey et al (2009)(Frey et al., 2009).

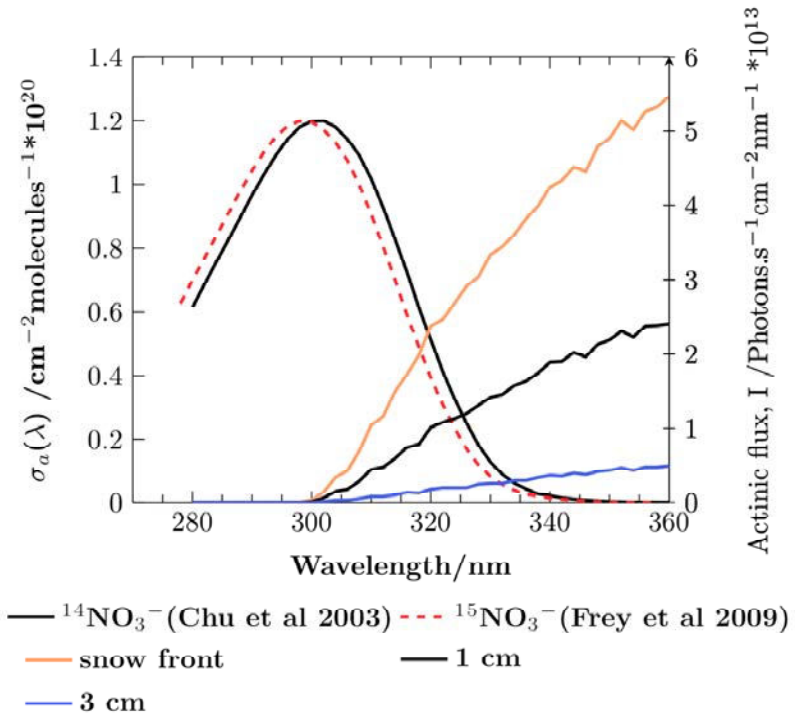

Figure 3.6a. *The absorption cross-section of $^{14}NO_3^-$ measured in the liquid phase(Chu and Anastasio, 2003) and $^{15}NO_3^-$ derived from the ZPE-shift model(Frey et al., 2009) as a function of wavelength referring to the left y-axis as well as the actinic flux (right y-aixs) of the filtered lamp spectra (using the 320 nm filter) at the front of the snow (depth = 0 cm) and at depths of 1 cm and 3 cm. Note that the ZPE-shift is exaggerated (≈ 2 nm) for visual purpose but the actual shift calculated by Frey et al. (2009) is ≈ 0.5 nm.*

3.3. Results

3.3.1. Nitrate concentration measurements

Snow samples were homogenized at the beginning of each experiment to minimize the natural variability in nitrate concentration and isotopic composition. We have also determined the difference in total snow mass before photolysis in each experiment, and the total snow mass obtained from the sum of each sub-sample at the end of the photolysis experiment. The variability was less than 1 % of the total snow mass, indicating sublimation is negligible during the experiment and sample handling error is also minimal. Data for the change in nitrate concentration was discussed in Meusinger et al. (In prep.); here we will summarize the relevant conclusions. The actual nitrate concentration for each experiment is given in the Annex (**Fig. A.1**).

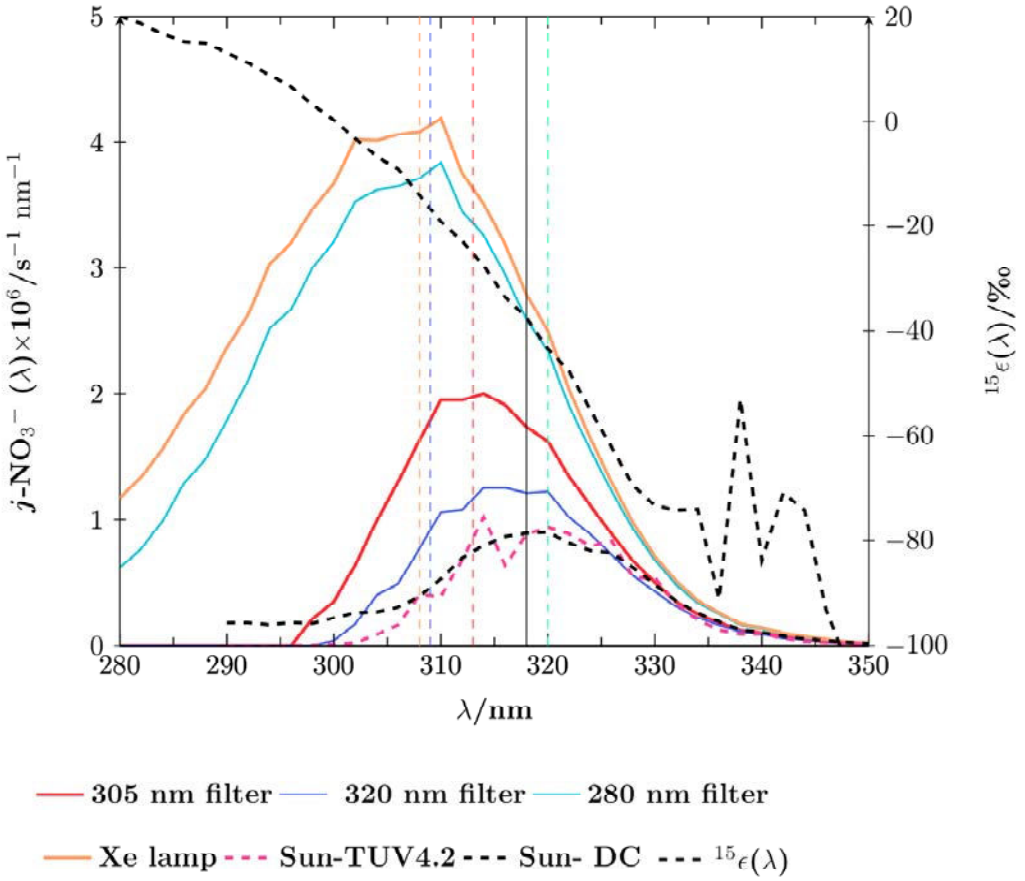

Figure 3.6b. *Photolysis rates j(λ) of $^{14}NO_3^-$ determined for each UV filter calculated from measured irradiance of the lamp in the presence of the different filters (Meusinger et al, In prep) and using the absorption cross section of nitrate determined by Chu and Anastasio 2003(Chu and Anastasio, 2003). The solar photolysis rate of nitrate is determined by using the solar actinic flux at Dome C derived using TUV model 4.4 for January 15, 2004, with 297 DU ozone column and with an albedo of 0.9 (as used in Frey et al. 2009). Sun-DC is derived from the solar irradiance measured at Dome C on 8th January 2013 at 2 pm local time (Picard G. and Libois Q., personal communication). The thin vertical lines shows the maxima of j(λ). The corresponding $^{15}\varepsilon$ can be inferred from where the vertical lines cut the $^{15}\varepsilon(\lambda)$ curve (right axis). The flat line at λ < 300 nm in the Sun-Dc from irradiance measurement at Dome C is associated with the instrumental noise.*

As it is relevant for the calculations in the forthcoming sections, the nitrate fraction left at the end of each experiment (*f*) is re-plotted in **Figure 3.7**.

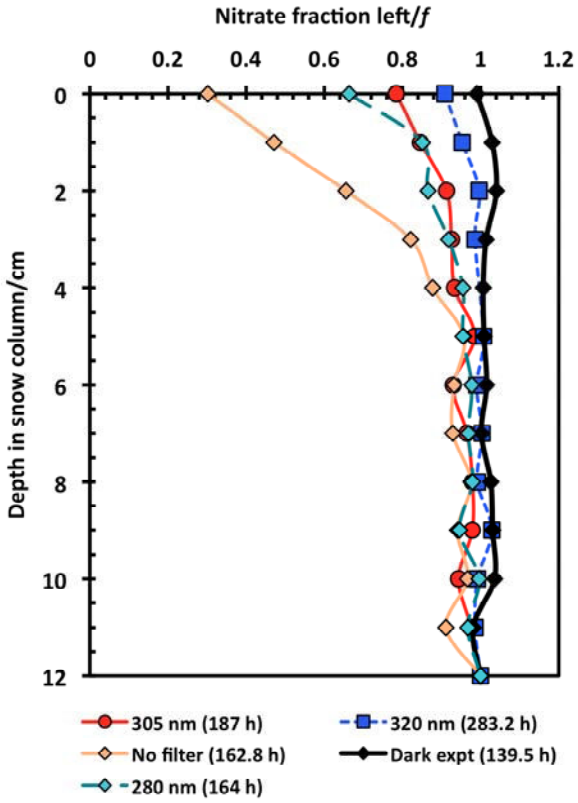

Figure 3.7. *Nitrate concentration profile (fraction of nitrate left, f) versus depth in the snow column plotted for the experiments conducted using different filters.'0' represents the side of snow column closer to the lamp.*

A dark experiment (control) was performed to quantify sublimation and possible loss of nitrate. The experiment was conducted with the same conditions as the photolysis experiments for ~ 140 h. It showed no change in the concentration of nitrate confirming the observed loss is only associated with the UV light.

The experiment conducted without a UV filter shows about 70 % nitrate loss for the front sample of experiment #3, with decreasing loss with depth in the snow column. The experiments using the 280 nm and 305 nm filters also showed varying losses depending on the duration of UV exposure and the fraction of UV light around 300 nm that was attenuated by the filters. The 320 nm filter experiment showed only a small loss after 12 days of irradiation. We conducted this experiment for longer duration, as the nitrate mass loss was minor (less than 2 % in 2 days) in shorter experiments.

3.3.2. Isotopic measurements

$\delta^{15}N$

The $\delta^{15}N$ profile for the experiments is shown in **Figure 3.8**. For the experiment conducted using the Xe lamp without a UV-filter, $\delta^{15}N$ increases from the initial value of -3.8 ‰ to about +3.0 ‰ for the sample at 3 cm depth. The $\delta^{15}N$ values for the top two

samples could not be measured due to the strong loss of nitrate mass (**Fig. 3.7**) leading to a nitrate concentration (6 nmol ml^{-1}) below the analysis limit.

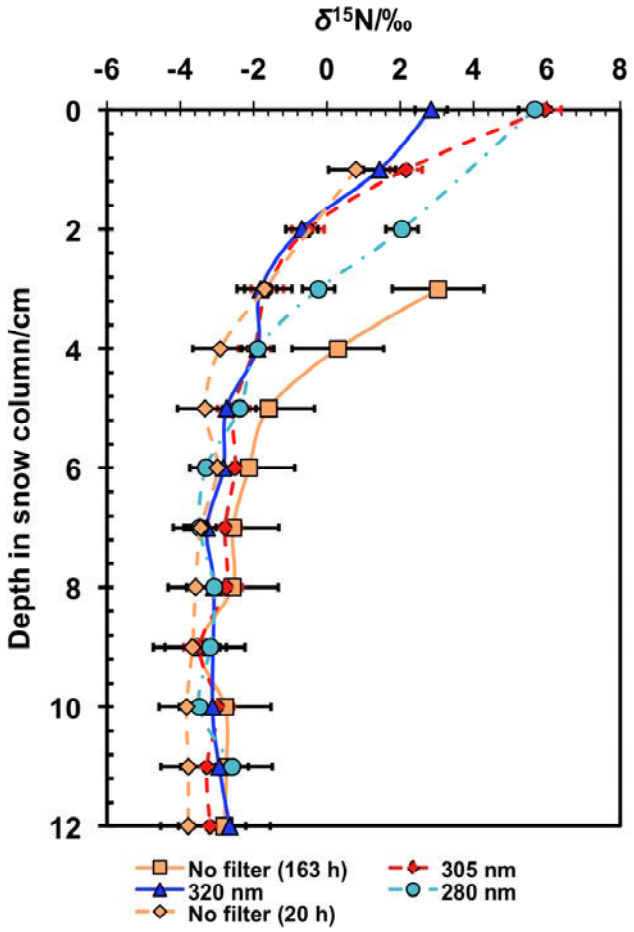

Figure 3.8. *The $\delta^{15}N(NO_3^-)$ profile with depth in the snow column for the experiments conducted using different filters.*

Both the 280 nm and 305 nm filter experiments cut off irradiation in the 200 nm nitrate absorption band and show similar patterns of isotopic enrichments, with enrichments to about +5.9 ‰ for the top samples. A smaller enrichment follows up to 4 cm depth, and $\delta^{15}N$ is stable below 5 cm. The 320 nm filter experiment also shows enrichment in $\delta^{15}N$, to a value of +2.8 ‰, for the top samples after 12 days of irradiation.

The isotopic fractionation associated with photolysis for each experiment ($^{15}\varepsilon_n$, where n is the cut off wavelength of 280 nm, 305 nm and 320 nm, and 'Xe' in the case of no filter) was determined from the Rayleigh plots generated using equations 3.1 and 3.2. Most of the Rayleigh plots display a good correlation (usually $R^2 > 0.8$). A typical example of a Rayleigh plot is shown in **Figure 3.9**. For experiments conducted for 7-12 days duration and with/without a UV filter, we derived $^{15}\varepsilon_{Xe}$, $^{15}\varepsilon_{280}$, $^{15}\varepsilon_{305}$ and $^{15}\varepsilon_{320}$ values of (-15 ± 1.2) ‰, (-23.2 ± 1.0) ‰, (-38.6 ± 2.8) ‰ and (-47.9 ± 6.8) ‰ respectively (Table 3.3).

Table 3.3. $^{15}\varepsilon$ values observed in this study and the predicted values from the ΔZPE-model.

Filter type	Experimental $^{15}\epsilon(\pm(1\text{-}\sigma))/‰$	R^2	ZPE $^{15}\epsilon/‰$
No filter (20.3 h)	-14.1±1.0	0.95	-
No filter (163.8 h)	-16.0±1.4	0.95	-
280 nm	-23.2±1.0	0.98	-16.8
305 nm	-38.6±2.8	0.95	-36.8
320 nm	-47.9±6.8	0.83	-42.8
Dark expt	-4.2±5.9	0.05	

$\delta^{18}O$ and $\Delta^{17}O$

The determination of the oxygen isotopes was affected by the small sample size and the results are associated with large error bars. In contrast to the observed clear trend in the $\delta^{15}N$ measurements, $\delta^{18}O$ and $\Delta^{17}O$ showed no such profile, as shown in Appendix A.1 and A.2.

The oxygen isotopic fractionations, $^{18}\varepsilon$ and ^{17}E (expressed by $^{17}E = {}^{17}\varepsilon - 0.52 \times {}^{18}\varepsilon$) for most of the experiments were associated with large error bars and it was not possible to draw meaningful Rayleigh plots for most of the experiments. However, the measured ^{17}E values are consistently positive and the experiments conducted with the pure Xe lamp (162.8 h) and the 280 nm UV-filter have ^{17}E values with acceptable error bars (1.8 ± 2.1 ‰ and 2.8 ± 1.4 ‰). The actual values obtained from this study are shown in the Appendix (table A.3).

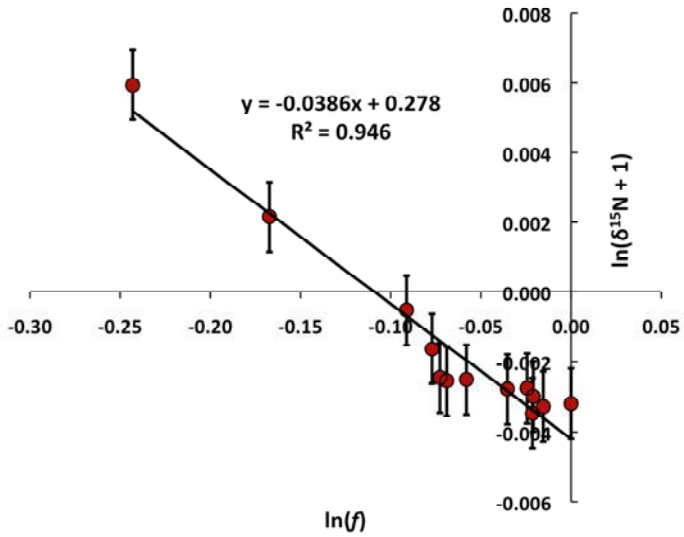

Figure 3.9. *A typical Rayleigh plot for the experiment conducted using 305 nm UV-filter for 187.2 hours. An isotopic fractionation of (-38.6 ± 2.2) ‰ was obtained for this experiment.*

Depth dependence of the isotopic fractionation

As observed in the concentration and isotope profile plots, neither measurement shows a significant change below 7 cm. This is due to the loss of light within the first few centimeters of depth (and hence shorter depth penetration), as the boundary conditions are not semi-infinite in contrast to the field conditions (France et al., 2011a) (see also Meusinger et al.). Hence, we have considered only the top 7 cm to evaluate the depth dependence of the isotopic fractionations.

Based on the irradiance measurements at every 1 cm depth starting from the front side (close to the lamp), we have observed a uniform attenuation of the incoming light flux by the snow layers. We have calculated isotopic fractionation in nitrogen using the measured irradiances at every 1 cm and the absorption cross-sections of $^{14}NO_3^-$ (Chu and Anastasio, 2003) and $^{15}NO_3^-$ (Frey et al., 2009) for the first 7 cm samples closer to the lamp, and the obtained results are not significantly different for a given filter. Results for experiments 4 and 5 (305 nm and 320 nm UV filters) are presented in Table 3.4. Accordingly, for the 305 nm filter, we have calculated a fractionation constant of -33.5 ‰ at the top of the snow column, decreasing to -34.5 ‰ at 7 cm depth. Similarly, for the 320 nm filter, a fractionation constant ranging from -39.3 ‰ to -40.7 ‰ was calculated.

Table 3.4 Calculated isotopic fractionation constants at different depth in the snow column for the 305 nm and 320 nm filter experiments

Depth, cm	305 nm filter $^{15}\epsilon$/‰	320 nm filter $^{15}\epsilon$/‰
0	-36.75	-42.80
1	-36.86	-42.95
2	-36.97	-43.10
3	-37.08	-43.25
4	-37.18	-43.39
5	-37.28	-43.53
6	-37.43	-43.74
7	-37.70	-44.12
	(-38.6±2.8)*	(-47.9±6.8)*

**Values observed in the laboratory experiment with the respective UV filters*

3.4. Discussions and Implications

3.4.1. Isotopic Fractionation

The experiment conducted without a filter showed a strong enrichment in $\delta^{15}N$ probably due to excitation of the 200 nm nitrate absorption band. For the other

experiments, in which this part of the spectrum is blocked by the UV filters, the enrichment in $\delta^{15}N$ is smaller.

The isotopic fractionations obtained from all photolysis experiments are generally negative implying the remaining nitrate in the snow is enriched in ^{15}N. However, the isotopic fractionations differ depending on the UV filter used in the experiment. For the two unfiltered Xe lamp experiments, conducted with durations of 20 and 163 hours, we calculated an average isotopic fractionation of $^{15}\varepsilon_{Xe}$ = (-15 ± 1.2) ‰. This value is in good agreement with the result obtained by Blunier et al. (2005)(Blunier, 2005) where an $^{15}\varepsilon_{Xe}$ value of -11.7 ± 1.4 ‰ was determined using a more powerful Xe lamp and artificial snow doped with nitrate, instead of natural snow. However, these laboratory observations disagree with the values observed in the field (Frey et al., 2009;Erbland et al., 2013;Blunier et al., 2005). Our experimental studies show that the $^{15}\varepsilon_{Xe}$ value observed in the experimental study by Blunier et al. (2005) is mainly due to significant excitation of the nitrate absorption band around 200 nm by the Xe lamp, in agreement with the prediction by Frey et al 2009(Frey et al., 2009). However, the use of artificial snow and product recycling (due to a closed system) in the laboratory study from Blunier et al. (2005) may have an additional but minor impact on their laboratory observations. Since the mechanism of the 200 nm band photolysis is most likely isomerization (with the possibility of decaying back to nitrate) (Madsen et al., 2003), additional post-excitation mechanisms including exchange may also affect the observed fractionation; the isotope-dependent absorption cross section will not be the only factor in that case. The use of UV filters was partly motivated by this observation. The use of UV filters has two important consequences. First it avoids excitation of the short wavelength absorption band where dissociation mechanisms are radically different from those occurring during the photo-excitation of the low energy band (Madsen et al., 2003). Second, it better replicates the solar UV at Dome C by shielding the 300 nm band.

According to solar irradiance measurement at Dome C on the 8th January 2013 at 2 pm (local time) (Ghislan Picard and Quentin Libois, Personal Communication), shown in **Fig. 3.2**, the photolysis experiment conducted with the 320 nm filter is the best match to the field conditions of Dome C, in particular because it blocks the entire UV region below 300 nm. This experiment also gives the best agreement between laboratory experiments and previous field studies conducted at Dome C for isotopic fractionations (Frey et al., 2009;Blunier, 2005), and in the East part of the Antarctic Plateau a $^{15}\varepsilon$ range of -40.0 to -74.3 ‰ was determined by Erbland et al. (2012)(Erbland et al., 2013) (see Table 3.5).

Table 3.5. $^{15}\varepsilon$ values determined in different studies in comparison to our observations using identical light spectrum (Xe and sun)

$^{15}\epsilon(\pm 1\text{-}\sigma/‰)$	**UV source**	**Reference**
(-15±1.2)	Xe lamp(No filter)	This study[a]
(-11.7±1.4)	Xe lamp(No filter)	Blunier et al[b]
(-40 to -74.3)	Sun	Erbland et al[c]
(-47.9±6.8)	Xe lamp (320 nm filter)	This study[d]

[a]*Isotopic fractionation constant derived for the unfiltered Xe lamp experiment*

[b]*Isotopic fractionation constant derived by Blunier et al., 2005 for the unfiltered Xe lamp used in their experiment*
[c]*Apparent isotopic fractionation constant observation range for the East Antarctic Plateau by Erbland et al., 2013*
[d]*Isotopic fractionation constant derived for the Xe lamp using the 320 nm filter in this laboratory study*

The very small isotopic fractionations observed for the oxygen isotopes compared to the fractionation in ^{15}N makes it difficult to observe the effects in these isotopes and draw strong conclusions from the experimental results (Table A.1). However, it is important to note that all the experiments show small positive isotopic fractionations; most of these values have large error bars. The two experiments in which the loss of nitrate mass was significantly higher, the Xe lamp (162.8 h) and 280 nm experiments, have ^{17}E values of 1.8 ± 2.1 ‰ and 2.8 ± 1.4 ‰ respectively. These values are in good agreement with the observations in the field (2.0 ±1.0 ‰(Erbland et al., 2013) and ^{17}E = 1 ± 1 ‰ (Frey et al., 2009)). However, we note that even if the actinic flux spectra in these two experiments and Dome C is significantly different, the small ^{17}E values are suspected to be linked to the cage (matrix) effect in which photoproducts of nitrate photolysis undergo isotopic exchange with the surrounding OH/H_2O (with ^{17}O-excess values close to zero), reforming nitrate(McCabe et al., 2005b). In addition, we note that the lack of significant oxygen fractionation observed in the laboratory is in qualitative agreement with the field observations where the oxygen isotope fractionations are significantly smaller than the nitrogen isotope fractionations (for example $^{18}\varepsilon$ = 8 ± 2 ‰ and ^{17}E = 1 ± 1 ‰(Frey et al., 2009)).

3.4.2. Comparison with theoretical estimates

A theoretical model was constructed to characterize the wavelength dependence of the observed fractionations based on the work of Frey and co-workers(Frey et al., 2009). In this model $^{15}\varepsilon_{pho}$ was estimated using the Zero Point Energy-shift (ΔZPE) approach(Yung and Miller, 1997;Schmidt et al., 2011). The model is based on the observation that, with substitution of a light isotope by a heavier one, the vibrational zero point energy of the heavier isotopologue is reduced. This difference in ZPE results in a blue shift of the UV absorption cross-section for the heavier isotopologue. Frey et al (2009)(Frey et al., 2009) determined a ΔZPE = -44.8 cm^{-1} for $^{15}NO_3^-$ corresponding to a blue shift of approximately 0.5 nm in the absorption cross-section. Accordingly, using the absorption cross section of $^{14}NO_3^-$ in the liquid phase(Chu and Anastasio, 2003), they estimated the absorption cross section of $^{15}NO_3^-$.

Using this modeled cross-section and the solar actinic flux determined from the TUV model (TUV 4.2)(Lee-Taylor and Madronich, 2002) (http://cprm.acd.ucar.edu/Models/TUV/Interactive_TUV/) at Dome C conditions, Frey et al (2009)(Frey et al., 2009) determined a photolytic isotopic fractionation of -48 ‰ that was very close to the apparent (effective) fractionation observed in the field ($^{15}\varepsilon_{app}$ = -60 ±15 ‰). However, the observation in the field is a cumulative value, where in addition to photolysis, processes such as evaporation, deposition and removal of nitrate by the wind may play a role.

In this study, we used a similar procedure and determine the photolytic isotopic fractionation for each UV-filter specific actinic flux (i.e. using the ZPE-shift derived

absorption cross-section and measured actinic flux of the lamp in the presence of the UV-filters) and compare the result with the corresponding laboratory observation.

As explained in detail in Meusinger et al. a significant decrease in the amplitude of the actinic flux was observed with depth in our experiment with a limited wavelength dependency. In agreement with the model result, the experimental isotopic fractionations are insensitive to the small change in the actinic flux spectrum with depth; the predicted difference is less than 1.5 ‰ between top and bottom. As the isotopic fractionations are nearly constant, we can directly compare the experimental $^{15}\varepsilon_n$ values and the predicted $^{15}\varepsilon_{pho}$ values.

The photolysis experiments show a clear correlation between the wavelength-dependent photolysis rate ($j(\lambda)$) controlled by the UV filters and $^{15}\varepsilon_n$, with a clear decrease in $^{15}\varepsilon_n$ as $j(\lambda)$ is red shifted. This trend was also predicted by Frey et al. (2009)(Frey et al., 2009) using the ZPE shift model (**Figure 3.6**).

The estimates obtained from the ΔZPE-shift model are in excellent agreement with the observed values for the unfiltered Xe lamp. As the series of filters progressively shield more of the high-energy UV photons, the deviation of the experimentally observed values from the predicted values of the ZPE-shift model grows (Table 3.3).

As the isotopic fractionation is derived from the absorption cross sections using the ZPE-shift model, the magnitude of the shift has a significant effect on the process isotopic fractionation constant. According to the four parameter model of absorption cross-section determination for isotopically substituted species created by Jost and co-workers(Jost, 2008), the absorption cross-section of a given molecule can be expressed using an asymmetric Gaussian function σ/E (the absorption cross-section divided by the photon energy, E) which is dependent on the amplitude (A), center (C), width (W) and asymmetry term (S)(Ndengue et al., 2010;Jost, 2008) of the cross-section. These four parameters mainly depend on the initial ground state wave function, the vertical excitation energy and the slope and curvature of the upper electronic state. The ZPE shift model disregards factors other than the shift (center) and can only give a rough estimate of the absorption cross-section of the isotopically substituted species. In addition, the ZPE-shift (-44.8 cm^{-1}) derived by Frey and co-workers based on previous measurements of the fundamental vibrational frequencies of $^{14}NO_3^-$ and $^{15}NO_3^-$ in the aqueous phase (Begun and Fletcher, 1960) may not be accurate. The ZPE-shift may be higher than -44.8 cm^{-1} (Remy Jost, personal communication). Accordingly, the vibrational frequencies used to determine the ZPE for the nitrate isotopologues do not include the anharmonicities, and the partition function ratios were less accurate for $^{14}NO_3^-$ and $^{15}NO_3^-$(Begun and Fletcher, 1960) and by including anharmonicities the recalculated ZPE-shift become -47.5 cm^{-1}. Because of these concerns, we have followed a new approach to obtain an apparent ZPE-shift value obtained by fitting the theoretically predicted isotopic fractionations to the $^{15}\varepsilon_n$ values derived from the laboratory study. The best agreement between the experimental and ZPE-shift model observations was for $\Delta ZPE = -53.7$ cm^{-1} (**Figure 3.10**). However, it should be noted that this apparent ZPE-shift value includes all the changes associated with isotopic substitutions such as the actual ZPE-shift and change in width and amplitude during isotopic substitutions. We have tested the veracity of this value by comparison with the fractionations observed in the field conditions. Using the solar actinic flux and absorption cross-sections of nitrate isotopologues given by Frey et al. (2009) and applying a ZPE-shift = -53.7 cm^{-1}, an average isotopic fractionation of -

52.3 ‰ was derived for Dome C using actinic flux measured during 09 December 2011-13 January 2012 (Jaime Elías Gil Roca, personal communication). This is in good agreement with the field observations of -60 ± 15 ‰ (Frey et al., 2009) at this site.

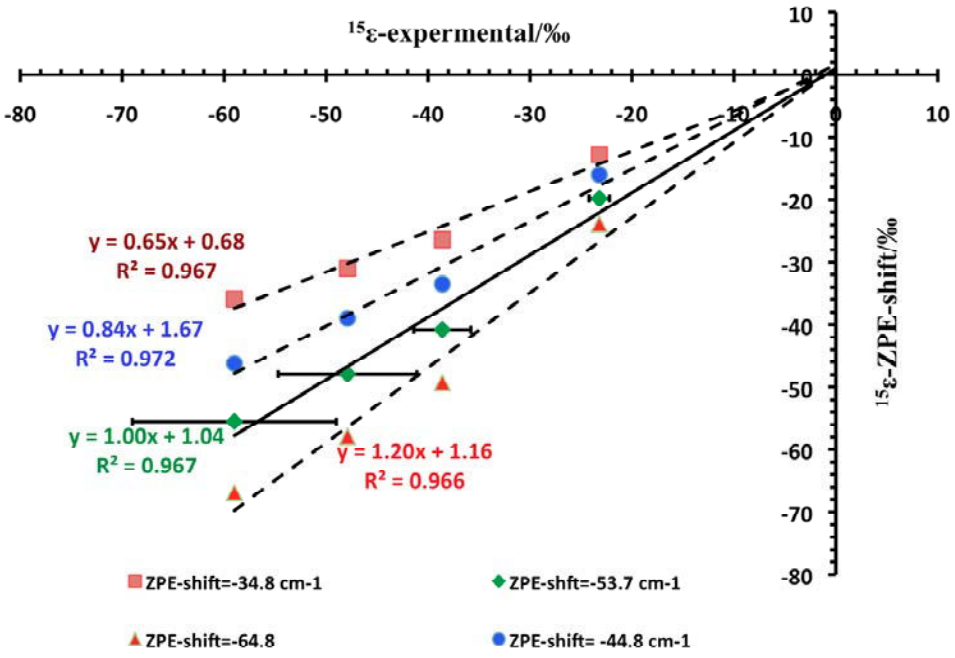

Figure 3.10. *Plot showing the experimentally obtained $^{15}\varepsilon$ values for the 280 nm, 305 and 320 nm filters and the average $^{15}\varepsilon$ value determined for the East Antarctic Plateau(Erbland et al., 2013) and versus their respective $^{15}\varepsilon$ values as predicted by the ΔZPE model using different ZPE-shift values. The best fit was observed at ZPE-shift = -53.8 cm^{-1}.*

Additionally, isotopic fractionation at the tails of the absorption cross-section is extremely sensitive to model parameters compared to fractionation close to the maximum of the absorption peak. As shown in **Fig. 3.6b**, the asymmetric actinic spectrum favoring the low-energy side of the band and the steeper slope of the fractionation constant (ε(λ)) in this region drives the fractionation constant towards more negative values in the longer wavelength regions relative to fractionations obtained using a pure Gaussian envelope. Accordingly, the experiments using the 305 nm filter show stronger fractionation than those using the 280 nm filter, and a more negative fractionation than the prediction of the pure ZPE-shift model. This trend continues for the 320 nm filter experiment and for the sun's spectrum. The predictions of the ZPE-shift model and the laboratory results must be taken as an upper limit for field observations. Recently, Erbland et al. reported an apparent isotopic fractionation ranging from -40 to -74.3 ‰ for the East Antarctic Plateau(Erbland et al., 2013). The discrepancies observed between laboratory, theory and field observations can most likely be explained by the difference in the actinic flux spectra and cross-sections used for the laboratory and modeling experiments respectively. However, the apparent isotopic fractionations derived for the field are influenced by a variety of processes in addition to a unidirectional Rayleigh process. While desorption of

HNO_3 is still a process that will blur the photolytic isotopic fractionation measurements, our dark experiment indicates that such process only has a minor effect, in line with a study by Erbland et al. (2012)(Erbland et al., 2013). Product recycling and re-deposition in the strongly stratified boundary layer of Dome C is another process which may give rise to deviation from a purely open system. The laboratory study has better control of temperature, light flux and photoproduct removal associated with the purely photolytic fractionation. Additionally it should be noted that the ZPE-shift model uses the absorption cross-section of liquid phase nitrate (Chu and Anastasio, 2003) which could be significantly different than the solid phase nitrate absorption spectrum (Kahan and Donaldson, 2007).

3.5. Summary and Conclusion

We have studied the isotopic fractionation of nitrate photolysis in natural snow in a series of experiments. From the analysis of the nitrogen isotope ratios in nitrate as a function of depth in the snow column we derived $^{15}\varepsilon_{Xe}$, $^{15}\varepsilon_{280}$, $^{15}\varepsilon_{305}$ and $^{15}\varepsilon_{320}$ values of (-15 ± 1.2) ‰, (-23.2 ± 1.0) ‰, (-38.6 ± 2.8) ‰ and (-47.9 ± 6.8) ‰ for unfiltered Xe lamp and 280, 305 and 320 nm filters respectively. The isotopic fractionation constant determined for the unfiltered Xe lamp is in excellent agreement with a previously determined value of (-11.7 ± 1.4) ‰ by Blunier et al (2005)(Blunier, 2005). This result is attributed to excitation of the strong absorption peak of nitrate around 200 nm, which is strongly attenuated in nature by O_2 and O_3 absorptions. The observed isotopic fractionation of nitrate is strongly dependent on the wavelength spectrum of irradiation, with an increase towards more negative values in the fractionation constant as the actinic flux spectrum is red shifted, in agreement with the prediction by Frey et al. (2009)(Frey et al., 2009). A model of the depth resolved photolytic isotopic fractionation shows insensitivity of $^{15}\varepsilon_{photo}$ to depth in the snow column, even if a significant decrease in the actinic flux is observed with depth. This is in agreement with the near wavelength independent e-folding depths reported by Meusinger et al. We believe that the results of this study accurately describe the photochemistry of nitrate and associated effects on the mass and isotopic composition of snow nitrate. Further, the presented results contribute to efforts to correctly account for isotopic fractionation in post-depositional processes affecting the preservation of nitrate record in ice core, and thus its interpretation in context of past climatic conditions and solar variability. We believe that further experimental studies on the temperature dependence of isotopic fractionation are required to better understand nitrate photolysis in snow. Additionally, with improved techniques for small sample analysis or by modifying the setup such that a higher sample amount could be obtained, the photolytic effect on oxygen isotopes could be better evaluated. Finally, our group has recently collected field samples with an experimental set up tending to maximize the photolysis of nitrate in Dome C snow. Findings from this study will help to better constrain and deconvoluate the processes behind the field apparent fractionation.

Supplementary data

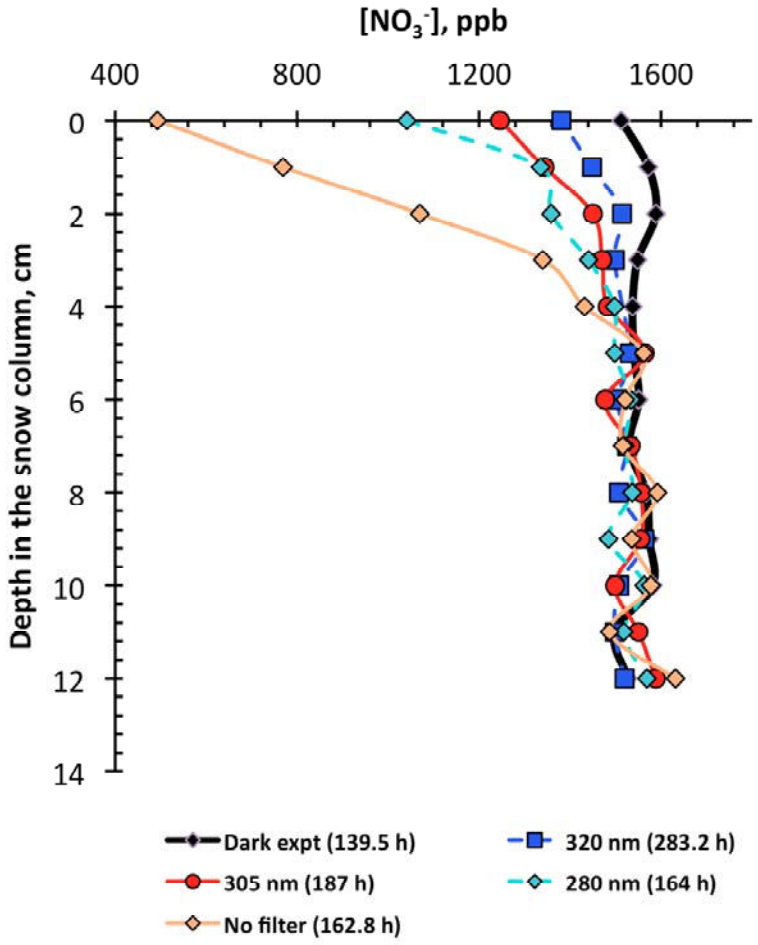

Figure A.1. *Plot for the nitrate concentration for each experiment versus depth in the snow column*

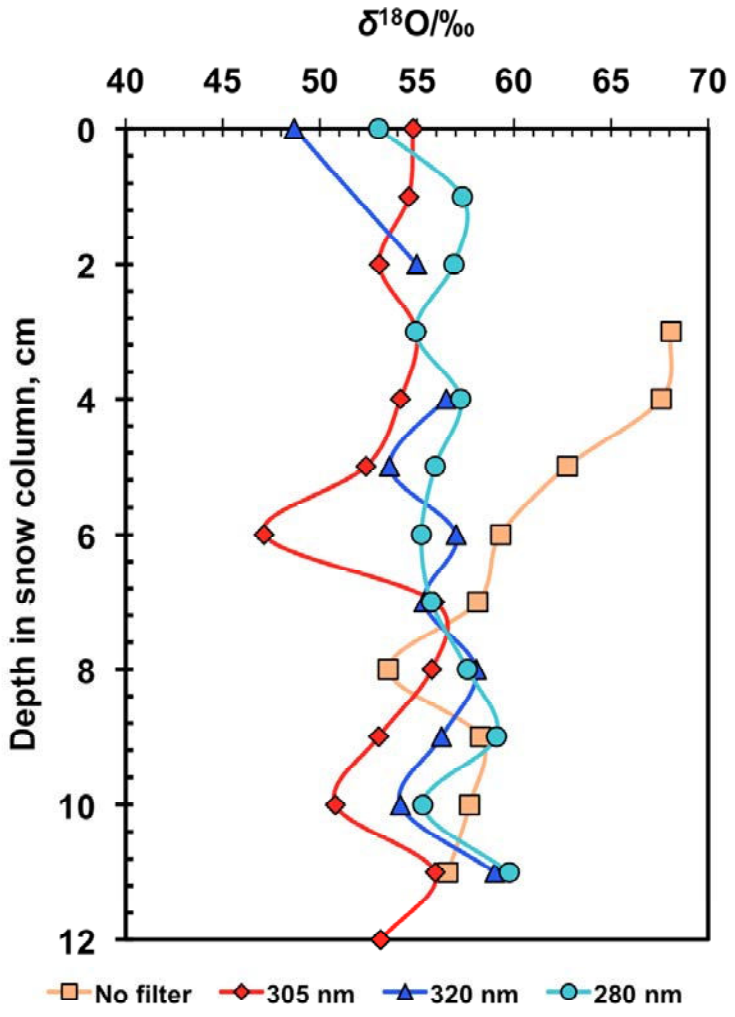

Figure A.2. *Plot for the $\delta^{18}O$ values versus depth in the snow column for the Xe lamp and the three UV-filters.*

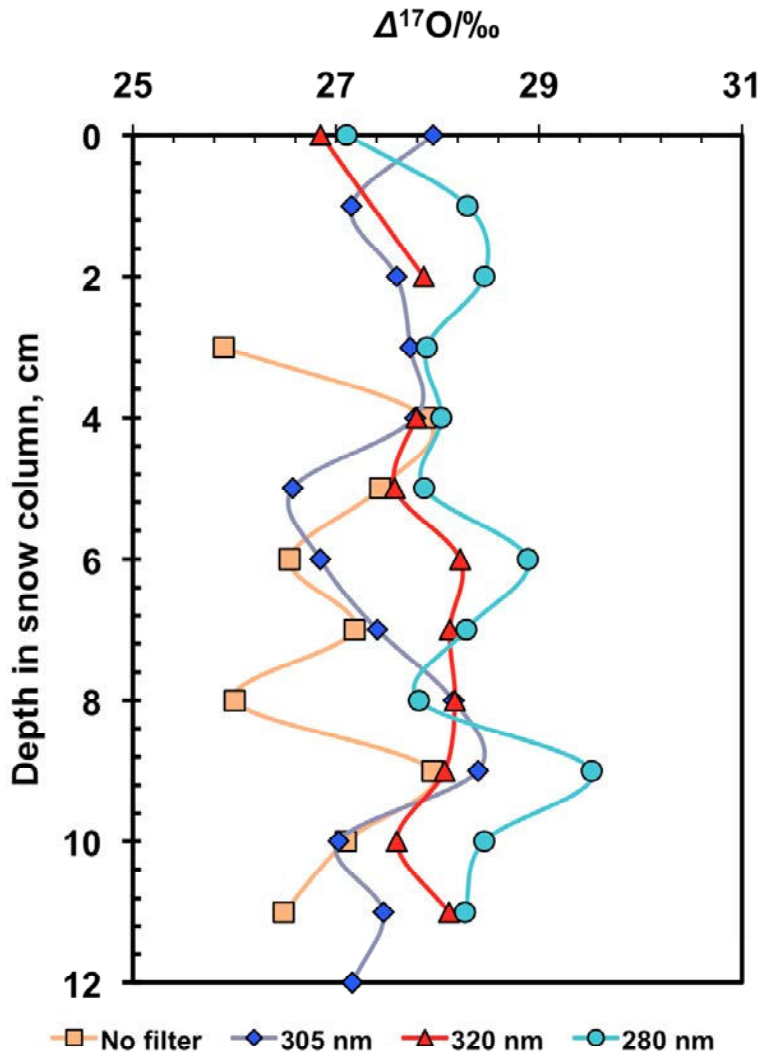

Figure A.3. *Plot for the $\Delta^{17}O$ values versus depth in the snow column for the Xe lamp and the three UV-filters.*

Table A.3. The $^{18}\varepsilon$ and ^{17}E values determined in this study

Expt	$^{18}\epsilon$/‰	$^{17}\epsilon$/‰
Xe (20.3 h)	3.4±6.9	10.8±2.1
Xe (162.8 h)	-30.2±8	1.8±2.1
280 nm	7.8±4.3	2.8±1.4
305 nm	- 4.6±10.2	2.0±11.8
320 nm	31.7±63	5.1±10.4

CHAPTER 4

Isotopic effects of nitrate photochemistry in snow: Results from field experiments at Dome C, Antarctica

This chapter is based on:

Tesfaye A Berhanu, Joseph Erbland, Joel Savarino and William C. Vicars. Isotopic effects of nitrate photochemistry in snow: Results from field experiments at Dome C, Antarctica. *Atmospheric Chemistry and Physics Discussions* ***(to be submitted)***

Abstract

Stable isotope ratios of nitrate in snow are expected to provide unique and valuable information regarding atmospheric processes and further the interpretation of information archived in deep ice cores. However, with post- depositional modification of snow nitrate, this information may be erased or significantly modified by physical or photochemical processes. We have investigated the role of UV-photolysis in the post-depositional processing of nitrate mass and stable isotope ratios at Dome C, Antarctica during the Austral summer 2011/12. In our experimental approach, two 30 cm snow pits were filled with homogenized drifted snow from the vicinity of the base. One of these pits was covered with a plexi-glass plate that transmits solar UV radiation, while the other was covered with a plate that blocks incoming UV. Samples were then collected from each pit every 10 days at a 2-5 cm depth resolution. From the nitrate stable isotope ratios ($\delta^{15}N$, $\delta^{18}O$ and $\Delta^{17}O$) determined for snow the samples exposed to solar UV, we have derived average apparent isotopic fractionations ($^{15}\varepsilon$, $^{18}\varepsilon$ and ^{17}E) of (-67.8 ± 12) ‰, (12.5 ± 6.7) ‰ and (2.2 ± 1.4) ‰ respectively. The ε values derived from our measurements were relatively constant throughout the field season and are in close agreement with the values obtained in previous studies at Dome C. Meanwhile, for the samples where the UV light is blocked, average $^{15}\varepsilon$, $^{18}\varepsilon$ and ^{17}E values of -13.3 ± 2.4 ‰, 0.2 ± 2.6 ‰ and -0.5 ± 0.8 ‰ respectively were obtained. The differences in the observed apparent $^{15}\varepsilon$ values between the UV-exposed and non-UV pits indicate a quantitatively dominant role of solar UV photolysis in nitrate post-depositional processing. However, the small and negative ε values derived for the non-UV samples reflect an impact of non-photolytic processes including surface snow mixing with drifted snow, desorption and/or

a minor effect from photolysis. We have also experimentally observed the depth independence of the $^{15}\varepsilon$ values averaged (-59.9 ± 24.7) ‰ at the 7-30 cm depth.

4.1. Introduction

Nitrate (NO_3^-) is the final product of the oxidation of atmospheric reactive nitrogen (NO_X = NO + NO_2) and is one of the most abundant ions present in polar ice and snow. Ice core records of nitrate offer the potential to provide quantitative constraints on past variations in atmospheric NO_X cycling and the oxidative capacity of the atmosphere (Mayewski and Legrand, 1990;Wolff, 1995a). However, the interpretation of these paleo-records is problematic at sites where snow accumulation rates are low and post-depositional processes such as desorption (evaporation/sublimation) and photolysis can have a major influence on the nitrate signal archived at depth (Röthlisberger et al., 2002;Honrath et al., 1999;Dibb et al., 1998;Zhou et al., 2001;Frey et al., 2009;Blunier, 2005;McCabe et al., 2005b). Additionally, the products of nitrate photolysis particularly NO_X and the hydroxyl (OH) radical can alter the oxidative capacity of the overlying atmosphere (Crawford et al., 2001;Chen et al., 2001;Dominé and Shepson, 2002;Grannas et al., 2007).

The stable isotope ratios (R) ($n(^{18}O)/n(^{16}O)$, $n(^{17}O)/n(^{16}O)$ and $n(^{15}N)/n(^{14}N)$) of nitrate are expressed as δ-values ($\delta^{17}O$, $\delta^{18}O$ and $\Delta^{17}O$) where $\delta = (R_{spl}/R_{ref})-1$ is the ratio of R of the sample (R_{spl}) and reference (R_{ref}) and n is the amount (molar concentration) of each isotope. The $\Delta^{17}O$ value is determined by the linear relationship $\Delta^{17}O = \delta^{17}O - 0.52 \times \delta^{18}O$. Recently, stable isotope ratios of nitrate ($\delta^{18}O$, $\Delta^{17}O$ and $\delta^{15}N$) have been identified as useful metrics to constrain the NO_X chemistry (Morin et al., 2008a;Hastings et al., 2009;Savarino et al., 2007) and the post-depositional processing of nitrate in snow (Frey et al., 2009;Erbland et al., 2013;Blunier et al., 2005). The potential for extending these interpretations into the past using ice cores relies upon a quantitative understanding of the impact of post-depositional processes on the isotopic composition of nitrate archived in snow.

While desorption is manifested by the physical release of HNO_3 from the snowpack, photolysis involves bond breaking in NO_3^- and emission of the photoproducts into the overlying atmosphere. The UV-photolysis of nitrate can take place mainly via (R.4.1), which produces NO_2, the major product of nitrate photolysis, or via (R.4.2) to produce nitrite, with the (R.4.1) reaction proceeding about 8-9 times faster than (R.4.2) (Grannas et al., 2007):

$$NO_3^- + h\nu \rightarrow NO_2 + O^- \qquad \text{(R.4.1)}$$

$$NO_3^- + h\nu \rightarrow NO_2^- + O(^3P) \qquad \text{(R.4.2)}$$

The photo-product NO_2^- can either undergo photolysis (R.4.3) to produce NO or react with the OH radical to produce NO_2 product (R.4.4).

$$NO_2^- + h\nu \rightarrow NO + O^- \qquad \text{(R.3)}$$

$$NO_2^- + OH \rightarrow NO_2 + OH^- \qquad \text{(R.4)}$$

In acidic conditions ($pK_a < 3.2$), nitrite can also be protonated to form HONO (R.4.5):

$$NO_2^- + H^+ \rightarrow HONO \qquad \text{(R.4.5)}$$

In order to constrain post-depositional effects on nitrate mass and stable isotope ratios, the isotopic fractionations for specific post-depositional processes must be known. Blunier and co-workers analyzed two surface cores from Dome C, Antarctica and determined a nitrogen isotopic fractionation (denoted as $^{15}\varepsilon$) of -54 ‰ (Blunier et al., 2005). In an attempt to reproduce this field observation in the laboratory, an artificial snow was irradiated with UV light in the 200–900 nm wavelength range and a $^{15}\varepsilon$ value of -11 ‰ was determined. The authors concluded based on the difference in $^{15}\varepsilon$ value that post-depositional modification must therefore result primarily from evaporation, with only a minor contribution from photolysis. However, it was later confirmed that the laboratory study of (Blunier et al., 2005) did not adequately replicate the relevant field conditions, particularly the spectral distribution of the experimental UV source used for photolysis and the removal of photo-products (Frey et al., 2009).

In a field study at Dome C, Frey et al. (2009) determined nitrogen isotopic fractionations of (-50 ± 10) ‰ and (-71 ± 12) ‰ for snow samples collected at Dome C during the summer campaigns of 2004 and 2007 respectively in close agreement with the field observations of Blunier et al. (2005). They have also presented a theoretical estimate of the isotopic fractionations due to photolysis by applying the Zero Point Energy-shift model (ΔZPE)(Yung and Miller, 1997). Applying this simple model and using the solar irradiance for the summer solstice at Dome C, a $^{15}\varepsilon$ value of -48 ‰ was determined, consistent with their field observations. The authors therefore suggested that photolysis is the key factor governing the nitrogen isotopic fractionation associated with the post-depositional processing of nitrate at Dome C. Meanwhile, photolytic isotopic fractionations derived solely from the ZPE-shift model carry high uncertainties due to the limitations of the model, which does not account for the change in shape and intensity of absorption cross-sections during isotopic substitutions (Nanbu and Johnson, 2004;Frey et al., 2009) (Berhanu et al. In prep).

Erbland and colleagues also determined an average apparent $^{15}\varepsilon$ value of -59 ± 10 ‰ for snow pits on the East Antarctic Plateau (EAP) and it was shown that photolysis is the primary mechanism driving the mass loss and isotopic fractionation of nitrate (Erbland et al., 2013). The authors also showed that evaporation plays a minor role with isotopic fractionations closer to zero ($^{15}\varepsilon = 0.9 \pm 1.5$ ‰ at -30 °C).

In a recent laboratory study by (Berhanu et al. In prep.), nitrogen isotopic fractionations during photolysis of nitrate was determined experimentally in Dome C snow. The authors used a Xe lamp with various UV-filters to better replicate field conditions and evaluated the wavelength sensitivity of nitrogen isotopic fractionations. The $^{15}\varepsilon$ value of -47.9 ± 6.8 ‰ derived for the experiment conducted using 320 nm filter (closer to Dome C solar irradiance conditions), was in good agreement with the field observations.

However, the currently existing field studies (Frey et al., 2009;Erbland et al., 2013;Blunier et al., 2005) derived apparent isotopic fractionations, values that incorporate not only the isotopic effects of photolysis but also other processes with

potential to induce isotopic fractionation (evaporation, reoxidation and surface deposition, etc.). Therefore, further experimental and modelling studies are required to constrain the effects of post-depositional processes on stable isotope ratios of nitrate in snow and to advance the interpretation of these measurements in the snow and ice.

We have conducted a field study at Concordia (Dome C), Antarctica (75°06' S and 123°19' E, elevation 3233 m) during the Austral Summer 2011/2012. The UV-photolysis of snow nitrate and the associated impacts on its stable isotopic composition were investigated in this study. We have employed an isolation technique to produce solar UV-exposed and non-UV exposed samples in order to understand the role of photolysis in the post-depositional processing of snow nitrate. To the best of our knowledge, this is the first field study that has employed an isolation strategy to constrain specifically the nitrate mass loss and isotopic fractionation induced only by photolysis from solar UV radiation.

4.2. Methods

4.2.1. Field setup and sampling

Wind-blown snow (drifted snow) was collected on 02 December 2011 at the Dome C station and was physically homogenized. This drifted snow possessed a high nitrate concentration of approximately 1600 ppb, which ensured levels adequate for isotopic analysis. Two snow pits of 1m × 2m surface and 30 cm depth were excavated within close proximity (~10 meters) and filled with the drifted homogenized snow. A rectangular wooden frame was used to mark each surface level at a fixed position (i.e., depth = 0 cm). Hence, any additional windblown snow accumulating above this wooden mark could be removed at least on a weekly basis. The pits were covered with plexi-glass plates of different UV transmittances (**Fig. 4.1**), one having only minor transmittance (10 - 15 %) below 380 nm and the other allowing for the transmittances of all solar UV-radiation down to 290 nm (**Fig. 4.2)**. The samples were named UV-exposed and non-UV referring to the presence and absence of solar UV respectively. The choice of the plexi-plate transmittance is based on the UV absorption cross-section of nitrate. Note that other non-UV light associated effects are expected to affect both pits equally. Nitrate has UV absorption peaks around 200 nm and 305 nm in which the 200 nm band is 3 orders of magnitude stronger than the latter (Mack and Bolton, 1999). However, this strong 200 nm band does not reach the earth's surface due to its absorbance by the stratospheric ozone layer. The non-UV plexi-plates block the secondary absorption band in contrary to the UV plexi-plates, which allow this band to reach the snow beneath. The plexi-glass plates were placed on a metallic frame at 20 cm above the snow surface, which is expected to be an optimum height because it minimizes both the warming effect on the underlying snow and trapping of emitted NOx products. Placing the plates at a higher level could increase the possibility of snow deposition at the sides; furthermore, at higher solar zenith angles there may be solar UV radiation reaching the UV-unexposed samples. Vertical plates were not placed at the sides to avoid trapping drifted snow.

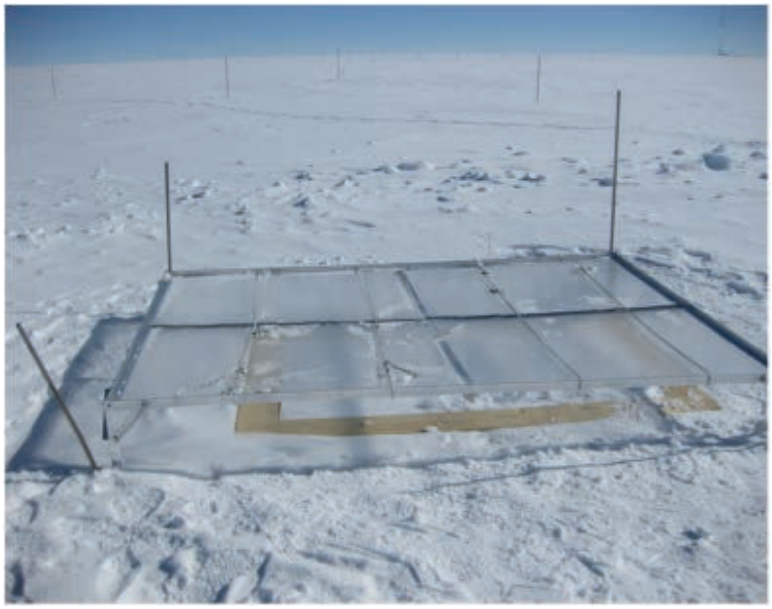

Figure 4.1. *Picture of the field experimental set-up at Dome C, Antarctica showing the pit filled with drifted snow and covered with a plexi-plate.*

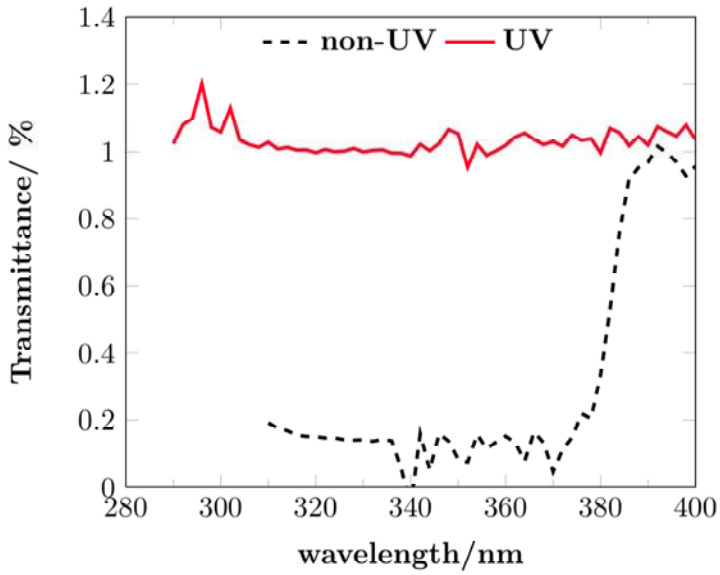

Figure 4.2. *The measured transmittance of the plates covering non-UV and the UV-exposed fields. The Solar UV light above 290 nm can pass through the plate covering the UV-exposed samples whereas the plate above the non-UV samples has a cut off wavelength around 375 nm (Note that on average 15 % of the UV below 375 nm is transmitted into the non-UV samples).*

Snow pit sampling was conducted every 10 days (from 02 December 2011 to 30 January 2012) at a 2 - 5 cm depth resolution to a depth of 30 cm for all samples and continued to a depth of 50 cm for several samples. This is denoted using numbers 0 - 6 to

indicate sampling between the beginning and the end of the season respectively. For each sampling, about 40 cm × 40 cm of the surface was used and a wall of 10 cm was left between the individual collections. After sampling, the remaining hole was filled with nearby snow of a similar nitrate concentration range. The detailed sampling dates are given in Table 1.

Table 1. Experiment numbers and their respective sampling dates during the field sample collection in Austral summer 2011/12 at Dome C, Antarctica.

Sample	Sampling date
0	02/12/2011
1	10/12/2011
2	21/12/2011
3	31/12/2011
4	10/01/2012
5	20/01/2012
6	30/01/2012

For each sample, a snow mass of 0.5 - 1.0 kg was collected, placed in 1-liter bags (Whirl-Pack^{TM}) and stored frozen in a temporary storage at Dome C. The samples were later melted at room temperature and the concentration of nitrate in each sample was determined in a warm laboratory at the Dome C station using a continuous flow analysis method. This technique is employed routinely at Dome C and has a precision of < 3% and a detection limit of 5 ng g^{-1} (Frey et al., 2009;Erbland et al., 2013). In order to obtain a nitrate concentration range high enough for the isotopic analysis each sample (> 10 μmol mL^{-1}), all the samples were preconcentrated in the warm lab at Dome C following the procedure of (Silva et al., 2000). Briefly, nitrate in the melted snow samples was concentrated via quantitative trapping using 0.3 mL of anion exchange resin AG 1-X8 (Bio-Rad 200-400 mesh chloride form), followed by elution with 10 mL of 1.0 mol L^{-1} NaCl solution (Frey et al., 2009;Erbland et al., 2013). The pre-concentrated samples were then stored in plastic tubes in the dark and shipped frozen to our laboratory in Grenoble for isotopic analysis.

4.2.2. Isotopic analysis

The oxygen and nitrogen isotopic composition of nitrate was determined using the bacterial denitrifier method (Sigman et al., 2001;Kaiser et al., 2007;Casciotti et al., 2002;Morin et al., 2008a) as modified by Kaiser et al. (2007) and Morin et al. (2009). Briefly, a bacteria culture strain (*Pseudomonas aureofaciens*) was concentrated 8 times by centrifugation following a 5-day growth period. 2 mL of the bacterial cultures were then transferred to a 20 mL glass vial, which was crimp-sealed with a PTFE septum. The vials were then degassed using He (Air Liquide, 99.99 %) for 3 hours. 100 nmol of each preconcentrated nitrate sample was then injected into the vials using an automated

injection system (Gilson Liquid Handler 215). After an overnight incubation, which allowed for the complete conversion of NO_3^- to N_2O (Sigman et al., 2001), 0.5 mL of 1 M NaOH was added to each vial to inactivate the bacteria. The N_2O in the sample vial headspace was then flushed with purified He (99.999 %) into a gold tube at 900°C where it was decomposed to O_2 and N_2 sample gases (Kaiser et al., 2007), which were then separated in a GC column and passed to a MAT253 IRMS (Thermo Scientific) to determine the stable oxygen and nitrogen isotope ratios (Morin et al., 2009).

To correct for isotopic effects associated with sample analysis, we have included certified standards of USGS 32, USGS 34 and USGS 35 (Michalski et al., 2002;Böhlke et al., 2003) treated in the same way as the samples and prepared in the same matrix as the samples (1M NaCl solution prepared using DC water to match the same water isotopic composition) (Morin et al., 2009;Werner and Brand, 2001). A Python algorithm was used to correct for blank effects and isotopic exchange which can arise in cases of small sample size (Details of this algorithm are given in the Supplementary materials). We have determined the overall accuracy of the method as the standard deviation of the residuals derived from the linear regression between the measured and expected values of the reference materials (Morin et al., 2009). For the samples analyzed in this study, the associated average uncertainties are 2.0 ‰, 0.4 ‰ and 0.6 ‰ for $\delta^{18}O$, $\Delta^{17}O$ and $\delta^{15}N$ respectively.

4.2.3. Data reduction

We have calculated apparent isotopic fractionations (i.e. isotopic fractionations derived for field samples irrespective of the process inducing fractionation) for O and N isotopes. These values are denoted as $^{15}\varepsilon_{app,}$ $^{18}\varepsilon_{app}$ and $^{17}E_{app}$ for $\delta^{15}N$, $\delta^{18}O$ and $\Delta^{17}O$ for nitrate respectively where $^{17}E = {}^{17}\varepsilon - 0.52 \times {}^{18}\varepsilon$. In this calculation, we have assumed an open system where NO_X products emitted during photolysis of nitrate will be removed as soon as they are formed and nitrate is lost from the pits irreversibly and adopting the following linear relationship (Erbland et al., 2013):

$$\ln(\delta + 1) = \varepsilon \ln(f) + \ln(\delta_0 + 1) \qquad (4.1)$$

where f is the nitrate fraction remaining in snow and defined as the ratio of the final (C) and initial nitrate (C_0) amount in the snow, $f = C/C_0$ and δ_0 and δ are the isotopic values for the initial and final snow respectively. The initial nitrate amount was calculated using the average nitrate concentration at 25 - 30 cm depth assuming that there is no change in the amount of nitrate. The slope of the $\ln(\delta+1)$ versus $\ln(f)$ plot is the isotopic fractionation ε (note that $\varepsilon = \alpha - 1$, where α is the fractionation factor).

Isotopic fractionations due to photolysis (denoted as $^{15}\varepsilon_{photo}$) have also been determined using the Zero Point Energy shift-model (ΔZPE) as in Frey et al. (2009). According to this model, during isotopic substitution of a light isotope with a heavier one, the ZPE of the heavier isotopologue is reduced and this shift leads to a small blue shift in the absorption spectrum of the heavier isotopologue relative to the lighter one. Hence, from a light isotopologue with measured absorption cross-section ($^{14}NO_3^-$) it will be possible to derive the absorption cross section of the heavier isotopologue ($^{15}NO_3^-$) (**Fig.**

4.3) (Yung and Miller, 1997;Miller, 2000). Isotopic fractionations (ε) were determined by:

$$\varepsilon = \frac{J'}{J} - 1 \qquad (4.2)$$

where *J'* and *J* are the photolytic rate constants of the heavier and lighter isotopologues are defined mathematically as:

$$J(T,\theta,z) = \int \phi(\lambda,T)\sigma(\lambda,T)I(\lambda,\theta,z)d\lambda \qquad (4.3a)$$

$$J'(T,\theta,z) = \int \phi(\lambda,T)\sigma'(\lambda,T)I(\lambda,\theta,z)d\lambda \qquad (4.3b)$$

where σ and σ' are the absorption cross-sections of the light and heavy isotopologues respectively. $\phi(\lambda)$ is the quantum yield and *I* is the actinic flux in the given wavelength ranges, which is dependent on solar zenith angle (θ) and depth (z). Note that if the quantum yield ($\phi(\lambda)$) is assumed to be independent of wavelength and is same for $^{14}NO_3^-$ and $^{15}NO_3^-$, there is no need to know its value to determine the isotopic fractionations.

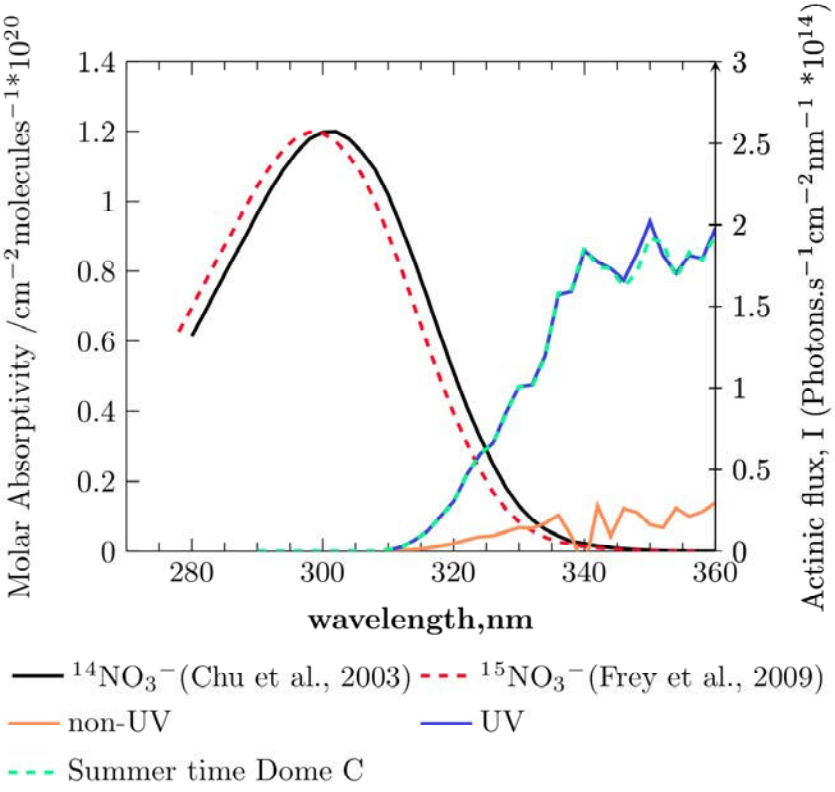

Figure 4.3. *Measured absorption cross-section of $^{14}NO_3^-$ in liquid phase, absorption cross-section of $^{15}NO_3^-$ determined using ZPE shift model as well as solar spectra derived using TUV model at Dome C conditions and expected UV fluxes in the presence of the plexi filters. The absorption cross section of $^{15}NO_3^-$ was derived by applying an average shift of 0.5 nm on the $^{14}NO_3^-$ and in this figure the shift is exaggerated (2 nm shift) to visualize this shift.*

4.2.4. Experimental precautions

Several experimental precautions were applied in this study in order to minimize possible experimental artifacts. The two experimental setups were open to the atmosphere in spite of plexi-plates placed on top of them. Therefore, the deposition of snow and associated nitrate was prevented from the top; however, wind could deposit snow at the surface of the pits as the sides were not closed. In order to minimize this effect, we placed wooden frames at the sides of each snow pits so that it was possible to track the surface level (i.e. depth = 0 cm) over time, and snow above this frames was carefully removed or sampled as surface snow. In addition, wind blown snow during this period could be deposited on the plexi-glass and prevent penetration of light via absorption/reflection. To avoid this, the snow deposited on the plexi-plates was manually removed with a broom 1 - 2 times a week. In a few instances snow was also carried away from the top few mm of the snow pit and hence our starting level (depth = 0 cm) may have been shifted to lower depths relative to subsequent samplings.

4.3. RESULTS

4.3.1. Concentration profiles

Fig. 4.4 shows the fraction of nitrate remaining in the two snow pits at each sampling time (Plots showing the nitrate fraction remaining at depth in the snow and the actual concentration for individual collections are shown in **Figs. A.1** and **A.2** of the supplementary material respectively). Accordingly, at the beginning of the sampling season (02/12/2011) the concentration of nitrate is uniform with depth ($f \approx 1$). This corresponds to an average nitrate concentration of (1431 ± 46.8) ng g^{-1} and (1478 ± 34.5) ng g^{-1} for the UV-exposed and non-UV pits respectively.

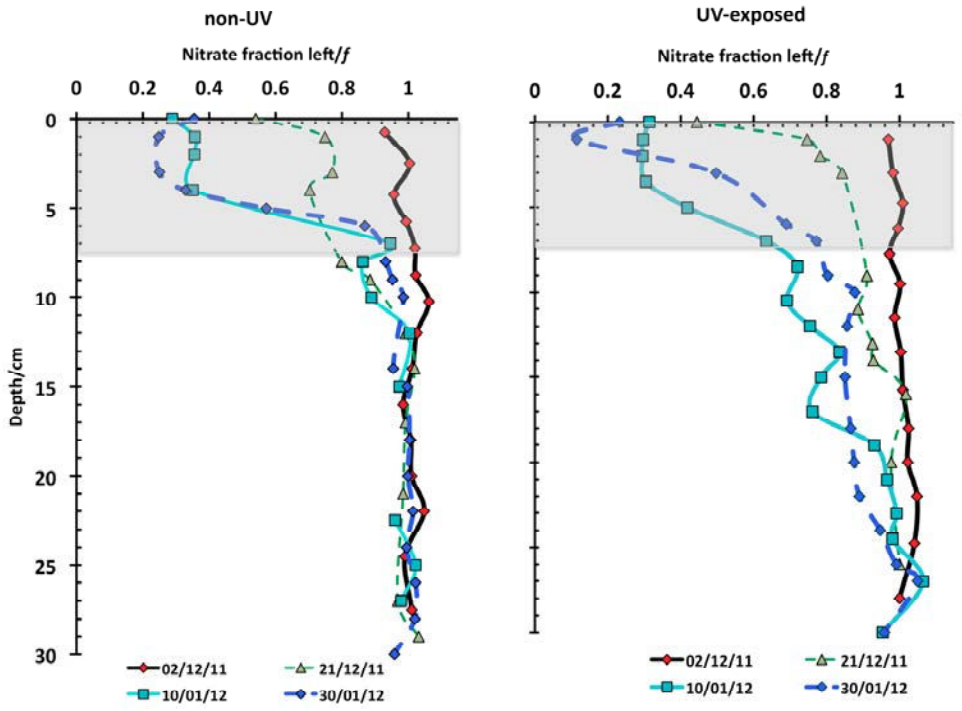

Figure 4.4 *Plot for the nitrate fraction left the snow (f) with depth. The left plot is for the samples that are not exposed to the solar UV and the right plot for the one exposed to UV light. The grey shaded region shows the depth where other factors may play a significant role.*

For the non-UV samples collected on 21/12/2011, f began to decrease to about 0.75 for the top 5 cm samples, but the profile became stable below 10 cm ($f \approx 1$). A significant nitrate loss was observed for the samples of the same pit collected on 10/01/2012 and 30/01/2012, with f reaching 0.15 - 0.25 in the top 4 cm, but only minor loss ($f > 0.8$) below 5 cm. The maximum nitrate loss ($f < 0.3$) was observed at the surface.

In contrast, the samples from the pits exposed to the UV radiation showed a significant decrease in nitrate amount until a depth of 20 cm. For samples collected on 21/12/2011, a nitrate loss of $f \approx 0.5$ was observed at the surface. However, at depths

below 3 cm, only minor losses were observed ($f > 0.8$). Maximum nitrate loss ($f < 0.2$) were observed in the top 0 - 3 cm samples collected on 10/01/2012 and 30/01/2012. This loss continued until a 7-cm depth, with f increasing to 0.4. Further minor losses ($f > 0.75$) were observed to a depth of 20 cm and the loss of nitrate ceased below 25 cm.

From the general profile of the nitrate fraction remaining in the snow in both pits, the loss of nitrate in the top 7 cm is comparable for both the UV-exposed and non-UV samples. However, the nitrate loss was minor below 7 cm in the non-UV samples where as UV-exposed samples lost a significant amount of nitrate below this depth. Additionally, the amount of nitrate mass loss was different within each pit depending on depth and sampling period.

4.3.2. Isotopic Analysis

Figure 4.5 shows the δ^{15}N profiles of the two pits for the samples collected in 20 days interval (δ^{15}N values for the entire sampling season are shown in **Fig. A.3**). Non-UV samples from 02/12/2011 and 21/12/2011 showed fairly uniform δ^{15}N profiles, with values ranging -2 ‰ to -8 ‰. However, the samples from 10/01/2012 and 30/01/2012 exhibited δ^{15}N values up to +15 ‰ at the surface (0-1 cm depth) extending to a depth of about 7 cm, with only subtle changes below a 10 cm depth.

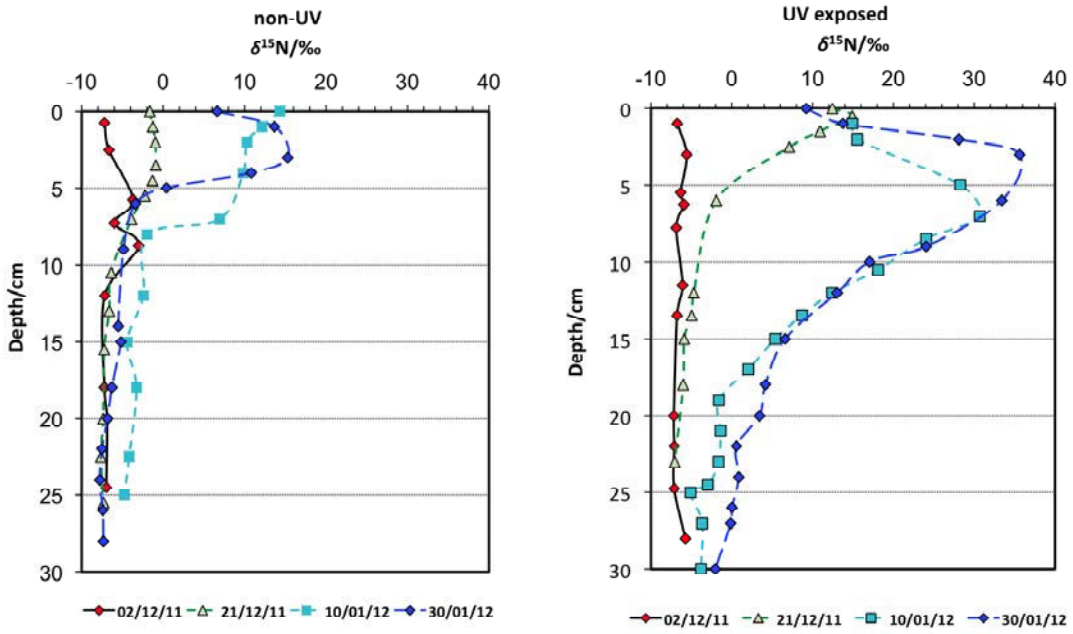

Figure 4.5 *The δ^{15}N nitrate profile in the snow with depth. The top plot is for the samples that are not exposed to the solar UV and the bottom plot for those exposed to UV light.*

In the case of UV-exposed samples, only the first collection showed stability until a 30-cm depth with δ^{15}N values ranging between -6 ‰ and -8 ‰. For the top 5 cm samples from 21/12/2011, the δ^{15}N values showed an increasing pattern, with maximum values at the surface (-12 ‰), and a stable δ^{15}N profile below 5 cm depth. Comparable

δ^{15}N values and similar profiles were observed for the collections of 10/01/2012 and 30/01/2012, with a maximum δ^{15}N value of +35 ‰ at a depth of 2 - 4 cm. However, a decrease in δ^{15}N values towards the surface level was observed. Most of the UV-exposed samples (except numbers 0 - 2) exhibit a decreasing pattern in δ^{15}N values form their respective maximum values to about +8 ‰ - +14 ‰ near the snow surface, irrespective of the sampling period. Meanwhile, this pattern is also observed for the 10/01/2012 and 30/01/2012 samples from non-UV pit.

Figure 4.6 shows the δ^{18}O values for all field samples, which ranged from 52 ‰ to 68 ‰, in good agreement the 55-70 ‰ range measured during a year-round skin layer snow nitrate (first few mm) measurement at Dome C (Erbland et al., 2013). From the figures, it is difficult to discern a trend between the δ^{18}O values and depth or sampling period in either the UV-exposed or non-UV pits.

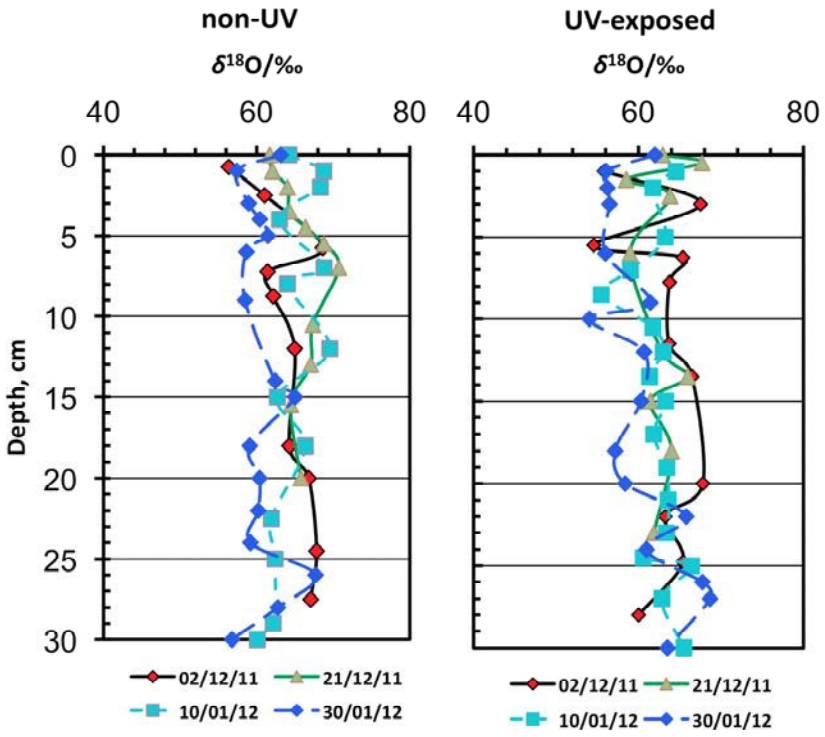

Figure 4.6 *The δ^{18}O of nitrate in the snow samples 0, 2, 4 and 6 with depth. The left plot is for the samples that are not exposed to the solar UV and the right plot for the one exposed to UV light.*

Similar to the δ^{18}O observations, the measured Δ^{17}O values also showed no significant pattern with values ranging between 26 ‰ and 30 ‰ in both pits (**Fig. 4.7**). When comparing the non-UV and UV-exposed samples, more variability is observed in the Δ^{17}O values of the latter samples.

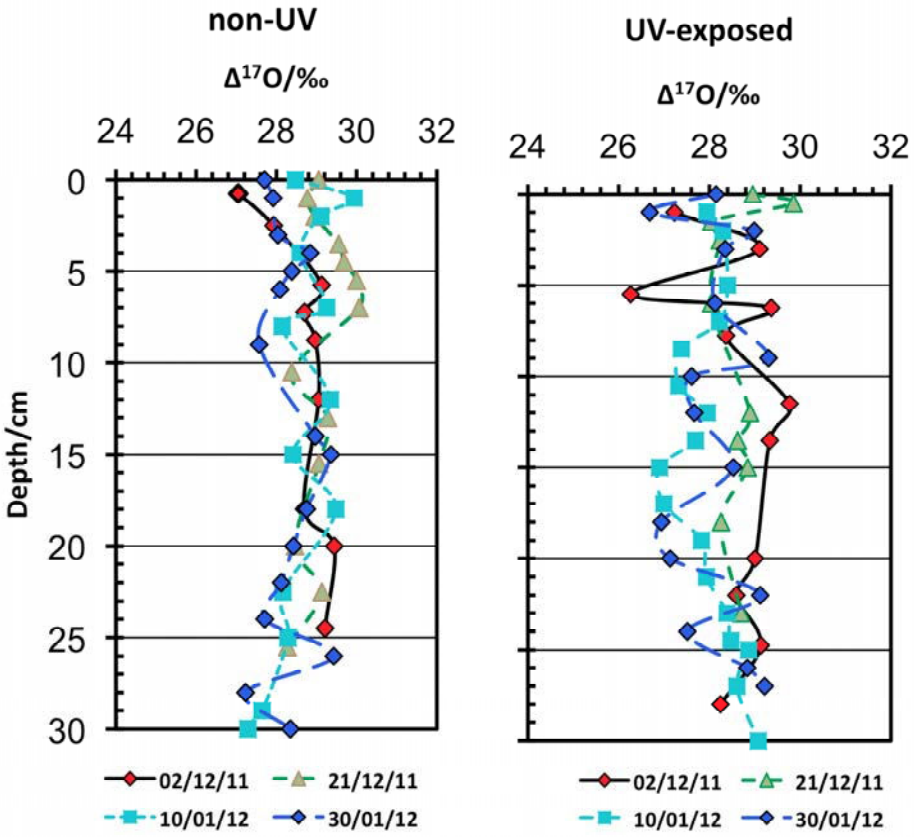

Figure 4.7 *The $\Delta^{17}O$ nitrate in the snow profile with depth. The left plot is for the samples that are not exposed to the solar UV and the right plot for the one exposed to UV light.*

In general, when comparing the stable oxygen isotope ratios of the UV-exposed and non-UV samples, it is difficult to discern any pattern or significant difference between the two sets and the sampling period (**Figs. 4.5 and 4.6**). However, the $\delta^{15}N$ values exhibit significant differences between the two pits.

4.4. DISCUSSION

4.4.1. Post-depositional isotopic effects

Because our experimental approach was based on the comparison of the two pits filled with drifted snow, it was important to ensure that each pit possessed a uniform nitrate distribution with depth and that the two pits were essentially identical. **Figs. 3** and **6** show uniform nitrate mass fraction left in the snow ($f \approx 1$) as well as fairly constant $\delta^{15}N$ profiles (-6 ‰ to -8 ‰) profile until a 30 cm depth for both pits. This observation substantiates that the snow was well homogenized and that both pits had similar initial nitrate composition.

The grey shaded area in **Fig. 4.4** shows the significant nitrate mass loss and ^{15}N isotopic enrichment observed in the top 0 - 7 cm of both in the UV-exposed and non-UV samples. This observation, coupled with the decreasing $\delta^{15}N$ pattern near the surface layers in contrast to the expected enrichment at similar depths, implies that additional non-photolytic processes (e.g., snowdrift, desorption, etc.) may be involved at this depth. Based on this concept, we have divided the two pits into two regions: (i) the top 0 - 7 cm samples, where photolysis and additional processes are expected to act strongly; (ii) samples at 7 - 30 cm depth, where photolysis is the dominant process inducing nitrate mass loss and isotopic fractionation. Below, we discuss the possible causes for nitrate mass loss in the top 7 cm of both pits.

The Concordia site, like most of the sites on the East Antarctic Plateau, possesses a relatively low average wind speed (approximately 2.9 m s^{-1} for the 1984-2003 meteorological record (Zhou et al., 2009;Aristidi et al., 2005). However, there still exists the potential for wind to deposit or remove snow on/from the surface of the two pits.

From the wind speed record at Dome C during the Austral summer 2011/12, higher wind speed events (> 5 m s^{-1}) with potential to induce snowdrift were observed (the wind speed record for the period of this study is provided in **Fig. A.6** of the supplementary material).

Drifted snow on the surface of the snow pits was also observed during our field campaign (see field logbook on the supplementary material). Even if the new snow above the surface level had been removed 1 - 2 times per week using the wooden mark as a reference, the snow may have already mixed with the underlying surface layer and the manual removal might disturb or mix the two layers, even when using extreme caution.

The converging pattern both in the concentration and $\delta^{15}N$ measurements towards a specific value near at the surface may also implicate the presence of surface deposition explained above. For the surface samples, the respective values converge to $f \approx 0.3$ and $\delta^{15}N \approx +10$ to $+14$ ‰ (mainly in UV-exposed samples #2 - 6 and non-UV samples #4 - 6). These values are in contrast with expectations based on the concentration and $\delta^{15}N$ profile observed below 7 cm. Based on the surface snow samples collected near these pits during the experimental season (**Fig. A.7** of supplementary materials), similar nitrate concentration and $\delta^{15}N$ profile with the surface level snow from the two pits during some of the collects were observed, implying deposition of drifted snow on the surface of the pits.

In addition, there might have also been events when sublimation occurred on the surface of the pits, introducing an artifact that the surface level (depth) is consistent which is actually different. In addition, the drifted snow on the surface of the two pits was not always the same: more snow was often deposited on one pit relative to the other, and the deposition was not homogeneous even within a single field. This variability can lead to inconsistency in the surface level reference between collections and mixing of the snow on the surface layers.

Snowfall was not observed during the sampling period and thus the direct deposition of nitrate via snowfall has not been considered. However, even if snowfall had occurred, direct deposition of snow to the experimental pits would have been negligible due to the presence of the plexi-plates.

It should also be noted that desorption may have taken place from the surface of both of the snow pits, an effect that may have been enhanced due to the warming effect of

the plexi-plates. This effect should be manifested in both pits and should affect mainly the top few cm layers. Both pits show comparable loss of nitrate in the top 7 cm, but the $\delta^{15}N$ values are significantly different, with maximum values of 15.0 ‰ and 36.0 ‰ for the non-UV and UV-exposed pits respectively. However, the larger negative isotopic fractionation observed in the UV-exposed samples is probably due to the dominance of photolysis compared to non-photolytic processes present in both pits.

Another possible reason for the observed nitrate mass loss and hence isotopic effects could be photolysis itself in both snow pits. The plexi-plate for the non-UV pit eliminates the majority of UV light below 380 nm. However, 10 - 20 % of the incoming solar UV below 310 nm is transmitted through this plate (**Fig.4.1**), a wavelength range that overlaps with the nitrate UV absorption band. Additionally, at higher solar zenith angles, there might also be direct solar UV coming from the sides of the plexi-plates leading to photolysis. NO_X photoproducts can also be locally reoxidized to form nitrate and re-deposited to the snow surface, as the plexi-plates may have hindered the escape of NO_X to the open atmosphere.

In general, there are multiple processes which can alter the concentration and isotopic composition of nitrate mainly intop 7 cm (**Fig. 4.8**). Identifying these processes and quantifying them is beyond the scope of this study. In this manuscript, we will mainly consider the snow samples between 7 - 30 cm depth.

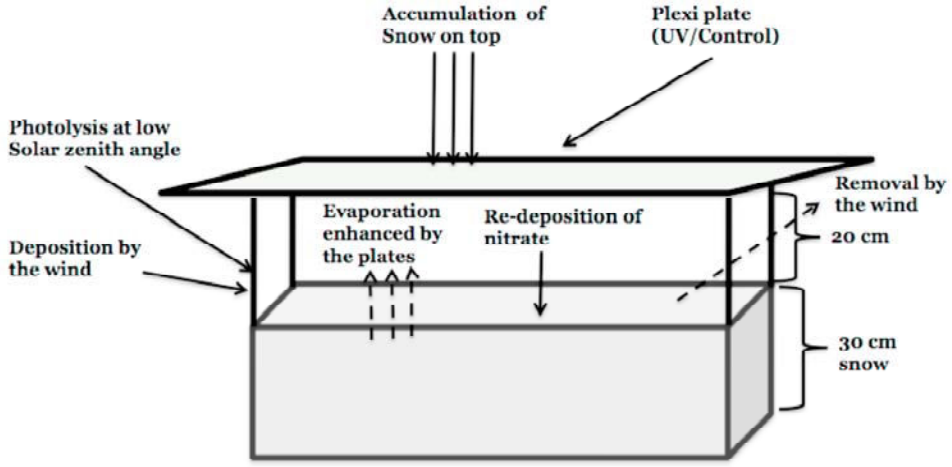

Figure 4.8. *Schematic on the possible external processes that could have affected the surface layers of the two pits. These include evaporation, wind deposition/removal and photolysis.*

4.4.2. Isotopic fractionations

$^{15}\varepsilon$

Due to insignificant changes in nitrate mass and isotopic composition, the linear fits for the first two collections of both pits had a very weak correlation, and are not included in this discussion. A good correlation was observed for samples collected late in the season and a typical Rayleigh plot is shown in **Fig. 4.9**. The calculated nitrogen isotopic fractionations (slopes of the Rayleigh plots) for samples between 7 - 30 cm depth in non-UV and UV-exposed pits are given in Table 2. The samples without UV have small negative isotopic fractionations and varying between (-7.4 ± 2.3) ‰ and (-15 ± 0.9) ‰. In contrast, the UV-exposed snow samples yielded higher negative isotopic fractionations ranging from (-18.0 ± 7.3) ‰ to (-58.3 ± 20.0) ‰ and becoming more negative with sampling time (Table 3). It seems that either $^{15}\varepsilon$ evolves with time (going from 2 to 6) or there is an artifact introduced by excluding the top samples. When compared to deeper snow, excluding the first top 7 cm of the snow pit may induce bias on the derived isotopic fractionations as the extent of the Rayleigh process is significantly reduced. On the other hand, the observed decreasing pattern in $\delta^{15}N$ for the top layer samples implies presence of another process or a different snow with different isotopic signature (**Fig. 4.5**). In an effort to better constrain the observed isotopic fractionations while limiting the influence of biased samples, only data points within the continuity of the deeper samples were kept for the recalculation of the isotopic fractionations (Table 2).

Table 2. The nitrogen isotopic fractionations determined for the samples at 7-30 cm depth. Raw values indicate the derived $^{15}\varepsilon$ values for the 7-30 cm depth and recalculated indicate the values derived after including validated data points above 7 cm.

Sampling No.	$^{15}\epsilon(\pm\mathbf{1}\text{-}\sigma)/‰$ Raw	$^{15}\epsilon(\pm\mathbf{1}\text{-}\sigma)/‰$ Recalculated
non-UV		
2	-12.9 ± 1.9	-12.8 ± 1.9
3	-7.4 ± 2.3	-12.7 ± 3.8
4	-12.9 ± 2.4	-13.2 ± 2.3
5	-13.2 ± 1.1	-14.2 ± 1.4
6	-15.0 ± 0.9	-13.8 ± 2.4
UV-exposed		
2	-18.0 ± 7.3	-72.7 ± 9.7
3	-25.7 ± 13.8	-59.8 ± 20.6
4	-47.8 ± 10.0	-72.3 ±12.9
5	-48.6 ± 18.9	-65.3 ±5.0
6	-58.3 ± 20.0	-69.0 ±11.8

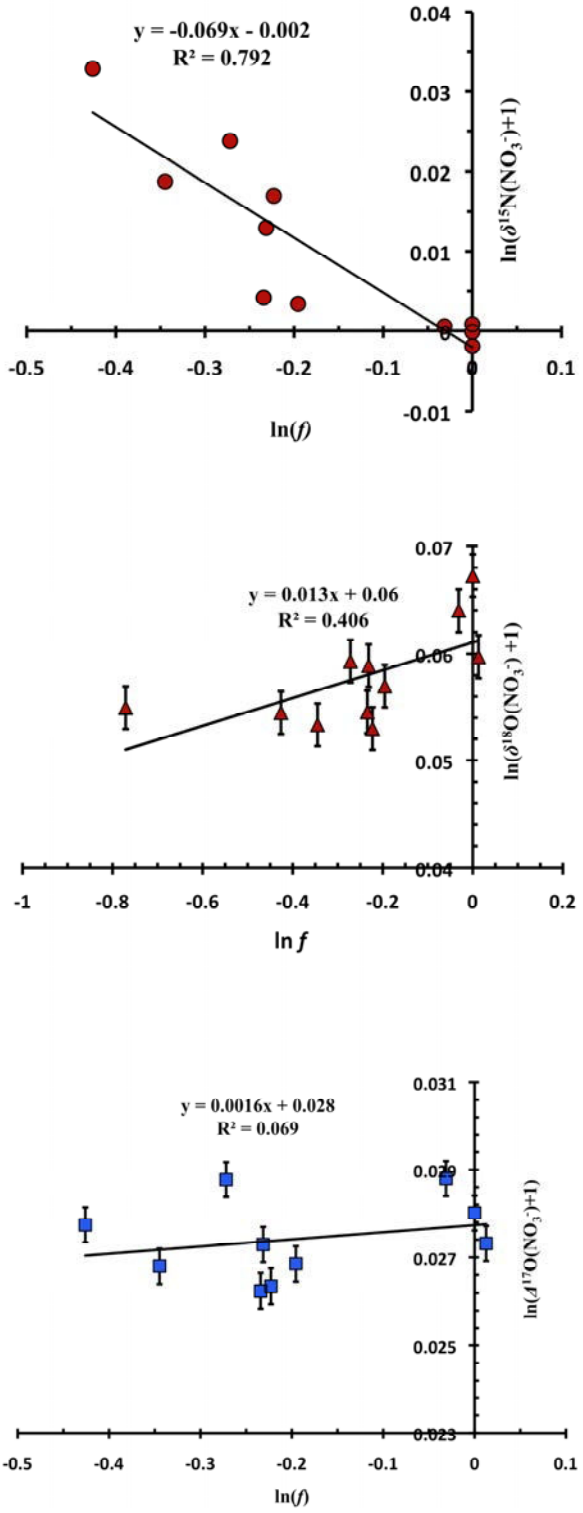

Figure 4.9 *Example of Rayleigh plots obtained in this study, here for the UV-exposed samples on 30/12/2011, to derive their respective $^{15}\varepsilon$, $^{18}\varepsilon$ and ^{17}E values. The error bars correspond to the analytical uncertainty including measuring the isotopic values. In case of ^{15}N, the error bars are smaller than the size of the symbol.*

The new plots based on these corrections are shown in **Fig. 4.10**. Accordingly, a flat pattern with $^{15}\varepsilon$ values ranging between -59.8 ‰ and -73.0 ‰ is obtained, irrespective of the sampling time within the error bars. Similarly, a constant isotopic fractionation with an average value of (-13.3 ± 2.4) ‰ is determined for the non-UV samples. The apparent ($^{15}\varepsilon_{app}$) and photolytic ($^{15}\varepsilon_{photo}$) isotopic fractionations derived in previous field and laboratory studies are shown in Table 3. Our observed average apparent isotopic fractionation of (-67.8 ± 12) ‰ is in good agreement with the previously determined average apparent isotopic fractionations of (-60 ± 10) ‰ (Frey et al., 2009) at Dome C and (-59 ± 10) ‰ for the East Antarctic Plateau (Erbland et al., 2013).

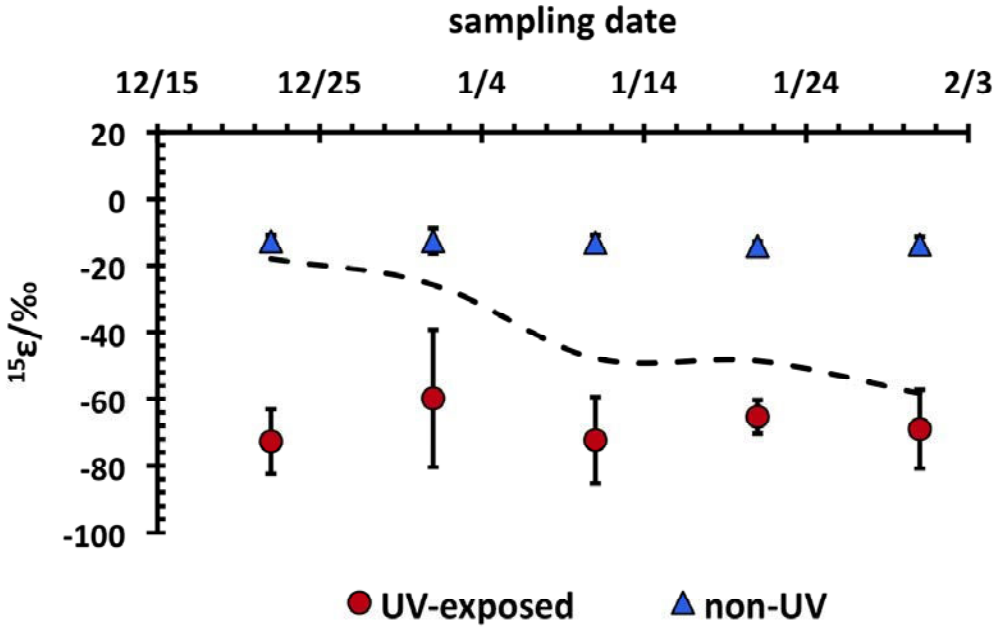

Figure 4.10 *Time evolution of the $^{15}\varepsilon$ values determined for the UV exposed samples with (red) and without (dashed line) some of the best first 7 cm data points included and the non-UV samples (triangles). Errors are determined by the Least square fit method as in Frey et al., 2009.*

Based on the significant differences between the $^{15}\varepsilon$ values calculated for the two experimental treatments, we can clearly conclude that the higher negative isotopic fractionation observed for the UV-exposed samples which possessed an average $^{15}\varepsilon$ values of (-67.8 ± 12.0) ‰ are associated with a process related to solar UV photolysis. However, the small negative nitrogen isotopic fractionation (-13.3 ± 2.4) ‰ observed for the non-UV samples may reflect an impact of mixing of drifted snow with the snow pit's surface snow, sublimation, minor photolysis, or a combination of these processes. In a recent study of post-depositional isotopic effects on the stable isotope ratios of nitrate in snow, it was shown desorption/evaporation and photolysis can occur simultaneously during sunlit periods, with the former process leading to an overall ^{15}N isotopic fractionation close to zero ($^{15}\varepsilon$ = (0.9 ± 1.5) ‰ at -30°C, a temperature relevant during the summer at Dome C), and the latter process inducing stronger negative fractionation ($^{15}\varepsilon$ =

-59 ± 10 ‰) (Erbland et al., 2013). According to our observations, in the non-UV samples, photolysis is the dominant processes due to the solar UV light, and we have determined stronger negative isotopic fractionations. However, we can reasonably assume that the $^{15}\varepsilon$ values for the non-UV samples are driven mainly by mixing of the surface layer snow with drifted snow, and variation in surface level and associated sampling depth inaccuracy, which are observed during the sampling season (see field log book remarks). However, these processes may not impact both pits equally, such as more drifted snow on non-UV sample pit than the UV-exposed pit. Thus, the isotopic fractionation derived for non-UV samples is mainly associated with external factors rather than post-depositional processes such as photolysis. This conclusion is also valid based on the simple difference between the significant mass loss and isotopic fractionations between the UV-exposed and non-UV samples.

Table 3. Apparent isotopic fractionations ($^{15}\varepsilon_{app}$) observed in different previous studies to compare with the observation of this study.

	$^{15}\epsilon/‰$	Experiment type	Reference
$^{15}\epsilon_{app}$	-53.9 ± 9.7	Dome C	Blunier et al 2005[a]
	-50.0 ± 10.0 (DC04)	Dome C	Frey et al 2009[a]
	-71.0 ± 12.0 (DC09)	Dome C	Frey et al 2009[a]
	-59.0 ± 10.0	EAP	Erbland et al[b]
	-67.9 ± 12	Dome C	This study[c]
$^{15}\epsilon_{photo}$	-48.0	ZPE-shift model	Frey et al 2009[d]
	-47.9±6.8	Lab	Berhanu et al[e]
	-52.3 (UV-exposed)	new-ZPE-shift model	This study[f]
	-42.8(UV-exposed)	ZPE-shift model	This study[g]

[a] *Values determined for Dome C*
[b] *An apparent average value derived for different locations in the East Antarctic Plateau*
[c] *The $^{15}\varepsilon$ determined for the UV-exposed samples in this study*
[d] *Determined using the ZPE shift model and using solar actinic flux of Dome C derived from snow TUV model*
[e] *A laboratory result observed using snow from Dome C and a Xe lamp with a UV-filter at 320 nm (significant to Dome C conditions) (Berhanu et al In prep.)*
[f] *Determined using the $\sigma(^{15}NO_3^-)$ values from the modified ZPE-shift derived by Berhanu et al. (In prep.), the plexi plates cut off wavelength for the two pits and the solar irradiance at measured at Dome C (Picard, G. and Libois, Q., personal communication)*

We have calculated the isotopic fractionations associated with photolysis for the samples of both the UV-exposed and non-UV pits applying the ZPE-shift model as described by Frey et al. (2009). The authors of this study calculated an actinic flux for the summer solstice of 2004 at Dome C using the TUV model (Lee-Taylor and Madronich, 2002) (TUV 4.2) and applied the simplified ZPE-shift to determine the absorption cross section of the heavier isotopologue from the lighter isotopologue measured experimentally (Chu and Anastasio, 2003) and determined a $^{15}\varepsilon_{photo}$ of -48 ‰. Following this approach and using an actual solar actinic flux measured at Dome C on 7 January 2012 at 2 pm local time (Ghislan Picard, personal communication) as well as including the UV transmittance effect from the plexi-plates, we calculate a $^{15}\varepsilon_{photo}$ value of -46.2 ‰ and -42.8 ‰ for the non-UV and UV-exposed pits respectively. However, the ΔZPE-shift model prediction for the non-UV samples does not agree with the field observed $^{15}\varepsilon$ values, which averaged (-13.3 ± 2.4) ‰. This is likely due to the minor change in the shape of the solar irradiance and attenuation of incoming light by the plexi-plate uniformly in the wavelength region of interest (i.e., about 15 % of the incoming solar flux penetrates through the plexi plates covering the non-UV pit). Hence, the theoretically derived isotopic fractionations will not be significantly different from the UV-exposed samples. However, the isotopic fractionation observed in the non-UV samples is not due to photolysis as expected based on a simple comparison between the UV exposed and non-UV samples.

The isotopic fractionations determined for the UV-exposed field samples based on ZPE- shift model calculations (-42.8 ‰) are also higher than the field observations. Recently, Berhanu et al. (In prep.) suggested that considering only the ZPE-shift to derive the absorption cross-section of $^{15}NO_3^-$ is not an accurate approximation as the change in the shape of the absorption cross-section should be also be included. According to the four parameter principle by Jost and co-workers, the absorption cross-section of a given molecule can be fitted using an asymmetric Gaussian function σ/E (the absorption cross-section divided by the photon energy, E) which is dependent on the amplitude (A), center (C), width (W) and asymmetry term (S) of the cross-section (Ndengue et al., 2010;Jost, 2008). These four parameters represent the initial ground state wave function, the vertical excitation energy and the slope and curvature of the upper electronic state. A ZPE-shift model disregards these other factors and can provide only a rough approximation of the absorption cross-section of the isotopically substituted species. Considering this principle, Berhanu et al. (In prep.) suggested an apparent ZPE-shift of -53.8 cm^{-1}. However, this value incorporates the actual ZPE-shift and the change in shape of the absorption cross-section due to isotopic substitution. Using this ZPE-shift, a ^{15}N isotopic fractionation of -52.3 ‰ is derived for samples exposed to solar UV, consistent with our field observations.

The isotopic fractionations obtained in the laboratory study of Berhanu et al. (In prep.), where a $^{15}\varepsilon_{photo}$ (-47.9 ± 6.8 ‰), are also less negative than the average $^{15}\varepsilon_{app}$ = (-67.8 ± 12.0) ‰ range observed in the UV-exposed snow pits. The 15 - 20 ‰ differences between the UV-exposed samples and the laboratory study could be due simply to differences in light spectra (i.e., Xe lamp vs. natural incoming solar UV). However, differences in the experimental set-up between the laboratory, where temperature and photochemical product removal can be controlled, and the field set-up where multiple

non-photolytic processes (i.e., desorption/evaporation and deposition) can also drive nitrate processing, complicate the interpretation of the observed differences.

$\delta^{18}O$ and $\Delta^{17}O$

Similar to the $^{15}\varepsilon$ values determined above, we have determined $^{18}\varepsilon$ and ^{17}E values and plotted them versus sampling date in **Fig. 4.11** The non-UV samples yielded $^{18}\varepsilon$ values close to zero (an average value of 0.2 ± 2.6 ‰) due to insignificant change in isotopic values. In contrary, the UV-exposed data sets have nearly constant values ranging 9-13 ‰ (an average value of 12.5 ± 6.7 ‰), in good agreement with previous studies (Table 4).

The ^{17}E values for the non-UV samples were not significantly different from zero whereas the UV-exposed samples yielded an average ^{17}E value of 2.2 ±1.4 ‰ in excellent agreement with previous studies (Table 4). This is presumably a consequence of the "cage effect" whereby the photoproducts of nitrate photolysis are thought to undergo isotopic exchange with the surrounding OH/water ($\Delta^{17}O = 0$), reforming secondary nitrate with $\Delta^{17}O$ values close to zero (McCabe et al., 2005b).

Table 4. Compiled $^{18}\varepsilon$ and ^{17}E values obtained from this study for the UV-exposed samples and previous studies

$^{17}E_{UV}(\pm 1\text{-}\sigma)‰$	$^{18}\epsilon_{UV}(\pm 1\text{-}\sigma)‰$	**Reference**
1.0 ± 0.2	6.0 ± 3.0 (DC 04)	Frey et al. (2009)[a]
2.0 ± 0.6	9.0 ± 2.0 (DC 09)	Frey et al. (2009)[a]
2.0 ± 1.0	8.7 ± 2.4	Erbland et al. (2012)[b]
2.2 ± 1.4	12.5 ± 6.7	This study[c]

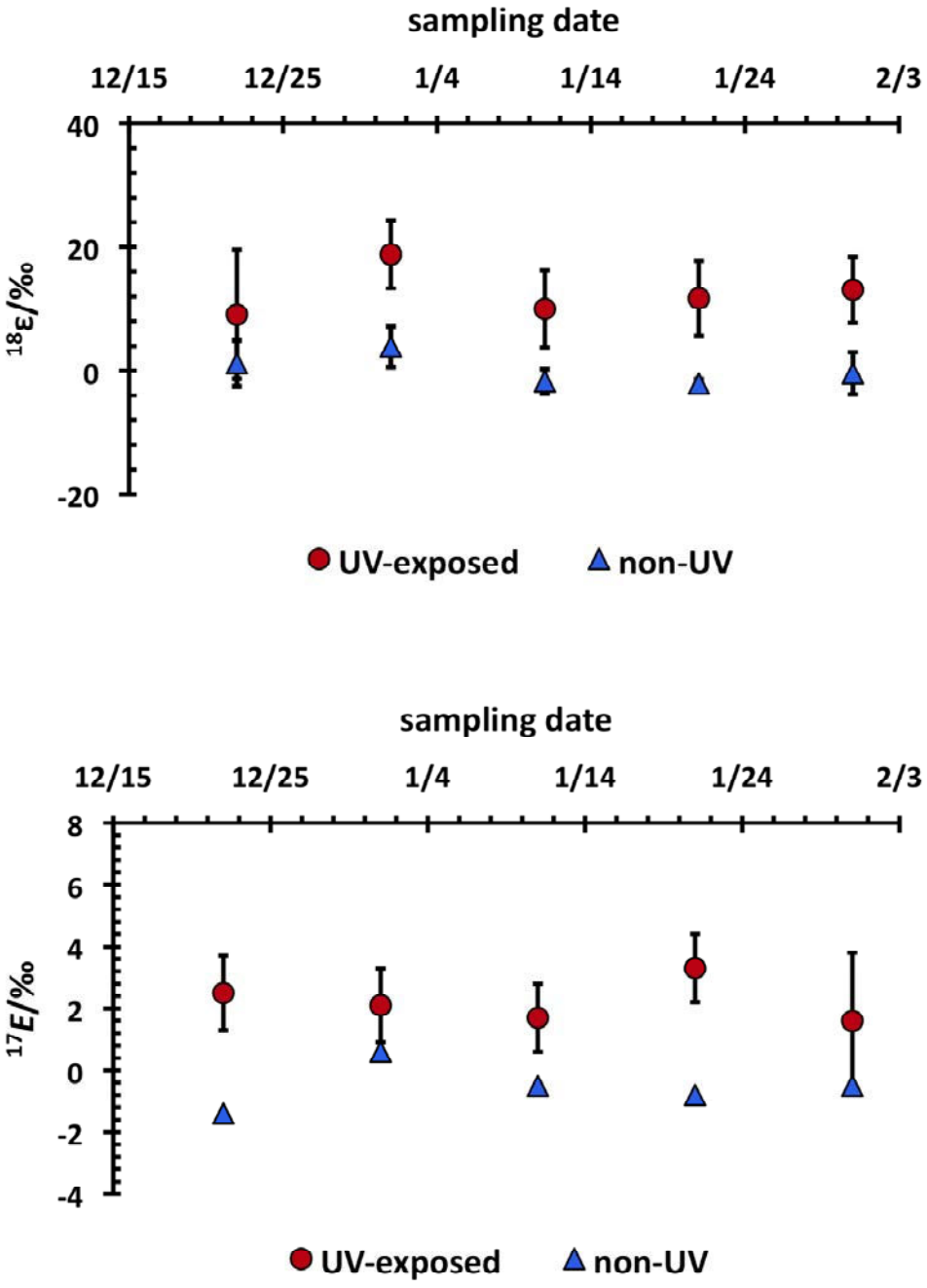

Figure 4.11 *Time evolution of the $^{18}\varepsilon$ (top panel) and ^{17}E (bottom panel) values calculated for the two pits with respect to their sampling date. Errors are determined by the least square fit method from as in Frey et al., 2009.*

Depth dependence of isotopic fractionations

We have determined the depth dependence of the isotopic fractionations for the UV-exposed samples from the concentration and isotopic values of nitrate. The non-UV samples showed no significant change in isotopic values with depth, and they are associated with large errors. Therefore, they are not presented in this manuscript.

Snow sampling at exactly same depth during each sample collection was impossible in the field. Hence, the concentration and $\delta^{15}N$ of nitrate obtained from at least 4 collections at exactly same depth were used to derive the isotopic fractionations. In a few cases, samples within 1 cm depth difference were stacked together to derive the $^{15}\varepsilon$ values. Similar to the case of the derivation of the $^{15}\varepsilon$ values with sampling date, we have followed the $\delta^{15}N$ signal and focused mainly on the 7 - 25 cm depth interval for the $^{15}\varepsilon$ values.

As shown in **Fig. 4.12**, a constant fractionation pattern is exhibited with depth, with an average $^{15}\varepsilon$ value of -59.9 ± 24.7 ‰ in the UV-exposed pit. The large error bars are associated with availability of too few data points to make a Rayleigh fit and a large uncertainty in the depth measurement resulting in the concentration of different depths in a single bin.

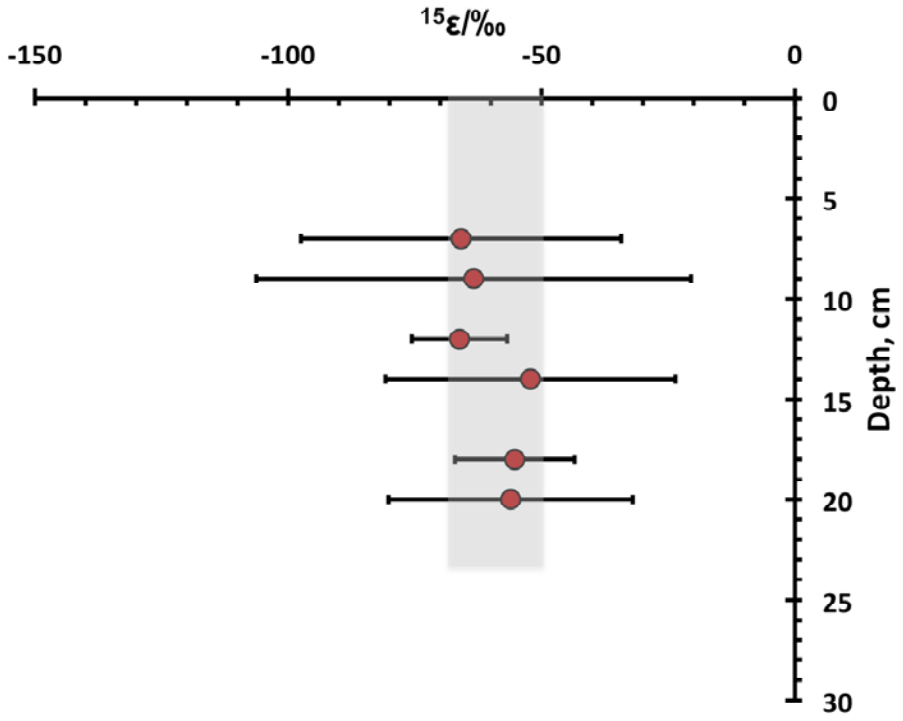

Figure 4.12 *Depth evolution of $^{15}\varepsilon$ for the UV-exposed field. The $^{15}\varepsilon$ is calculated from samples at the same depth from each sampling. Error bars are calculated as in Frey et al. (2009). The shaded region implies the observed $^{15}\varepsilon$ range of -50 ‰ to -70 ‰.*

The depth could have also changed with time, as there might be densification of the snow with time. The relative insensitivity of the $^{15}\varepsilon$ values with depth is actually expected as an even UV light attenuation is observed with depth in snow in a recent laboratory study (Berhanu et al., In prep).

The derived $^{18}\varepsilon$ and ^{17}E values derived with depth have a very weak Rayleigh fitting at lower depths (i.e. below 10 – 15 cm), and are associated with large errors. This is mainly due to the minor changes in the isotopic signal of oxygen when compared to the N isotopes where relatively strong signals were observed.

4.4.5. Conclusions

In a field experiment at Dome C, Antarctica, we have investigated the effect of solar UV radiation on the mass and stable isotope ratios of nitrate in two snow pits (non-UV and UV-exposed) filled with drifted snow. In the UV-exposed pits, we observed a significant nitrate mass loss and isotopic fractionation associated with two processes: photolysis and additional processes including snow surface mixing with drifted snow. The effects of these processes are significant at a 0 - 7 cm depth and affect both the non-UV and UV-exposed samples. Due to the existence of multiple complex processes, it is difficult to consider some of these data points in the determination of the isotopic fractionations. We have determined an average $^{15}\varepsilon$ value of -67.9 ± 12 ‰ for the solar UV-exposed samples by excluding some data points in the top 7 cm, which were thought to be impacted by external process such as deposition. The derived $^{15}\varepsilon$ values are in good agreement with previous estimates based on field observations at Dome C. In contrast, the $^{15}\varepsilon$ values for the non-UV pit, which averaged (-13.3 ± 2.4) ‰, are most likely due to mixing of drifted snow with the surface layers with minor contributions of desorption and photolysis. This is the first experimental study that has demonstrated the strong influence of photolysis on mass loss and isotopic fractionation of nitrate under environmentally relevant conditions. Previous studies of nitrate photolysis in snow were significantly limited due to inadequate replication of natural light conditions, snow quality and the nature of nitrate in snow, depth penetration of the UV-light, as well as temperature and product removal. In contrast, this study is the ultimate replica of photolysis in natural conditions at Dome C. This study clearly demonstrates that photolysis, driven by the solar UV radiation, is the major process inducing mass loss and isotopic fractionation at Dome C, as suggested by previous studies (Erbland et al., 2013) and references therein).

The isotopic fractionations derived for the UV-exposed pits are slightly lower than the predicted $^{15}\varepsilon_{pho}$ value of -47.9 ± 6.8 ‰ based on a laboratory study relevant to the field conditions by Berhanu et al. (In prep.) and derived from the ΔZPE-shift model (-42.8 ‰). Assuming the $^{15}\varepsilon$ values for the non-UV samples to be associated with only non-photolytic process and affect both pits equally, we have obtained a purely photolytic $^{15}\varepsilon$ of -54.6 ‰ for the UV samples. This is in agreement with field observation of undisturbed snow.

We have also determined the depth dependence of the isotopic fractionations and observed the depth independence of $^{15}\varepsilon$ values. However, the paucity of data and the relatively large associated errors indicate that further experimental studies regarding depth dependence of isotopic fractionation are required.

Finally, we should also mention some of the possible limitations of this experimental study. Due to mechanical modification during the filling of the pits with the wind-blown snow, the snow used in this study might not have possessed similar physical properties (i.e. grain size, compactness, optical properties, etc.) identical to the natural snowpack. This might led to modification of scattering properties in the experimental snow pits. The presence of multiple processes on the surface snow layers might have also introduced a small artifact in regards to the derived the $^{15}\varepsilon$ values. However, the experimental design can be further improved. For example, a wire frame may be placed covering the entire pit surface so that the surface level can be fixed at same level during sampling all the time. A laboratory study on desorption of nitrate from snow appropriate to Dome C conditions should also be conducted in the future in order to ascertain the effects of desorption in post-depositional processing of snow nitrate. This will ease the determination of pure photolytic effects with better accuracy.

SUPPLEMENTARY MATERIALS

The actual nitrate concentration measurement data obtained from the IC measurement at the warm lab in Dome C is shown below (Fig. 1). The calculated nitrate fraction left in the snow (*f*) is also given in Fig. 2.

The observed shift in concentration at the deepest part of the profile is probably the result of calibration shift and/or base line drift. The stability of the concentration profile associated to the fact that such variation are not related to the collect date clearly confirm to analytical artifact and not natural changes.

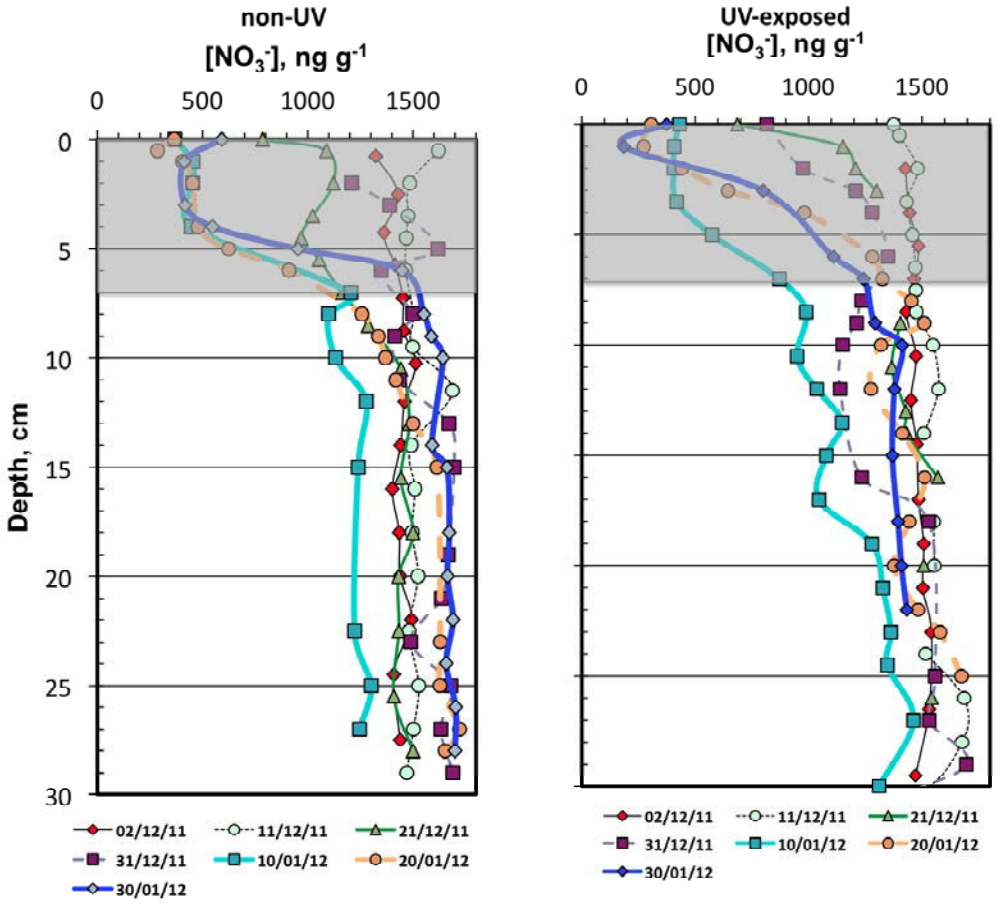

Figure A.1. *Nitrate concentration for the UV-exposed and non-UV samples measured at the warm lab in Dome C. The observed shift in the concentration plot is not suspected to result from loss or gain of nitrate as no correlation with sampling period was found. We suspect the artefact might result from standardization.*

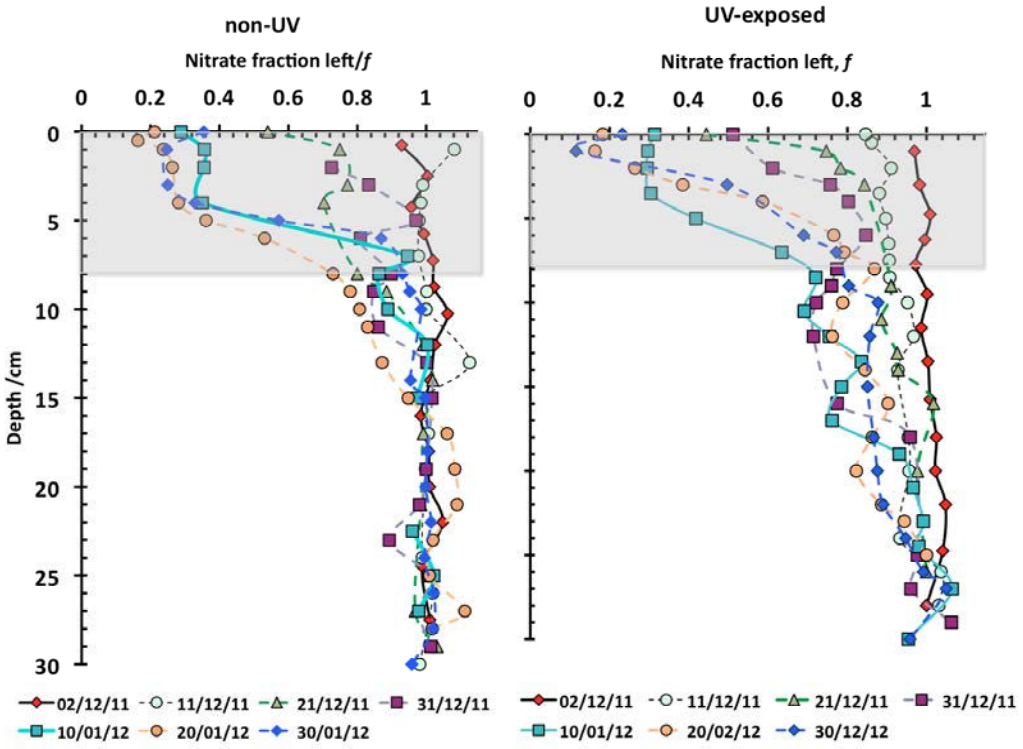

Figure A.2. *The nitrate fraction left in the snow plot for the non-UV and UV-exposed samples.*

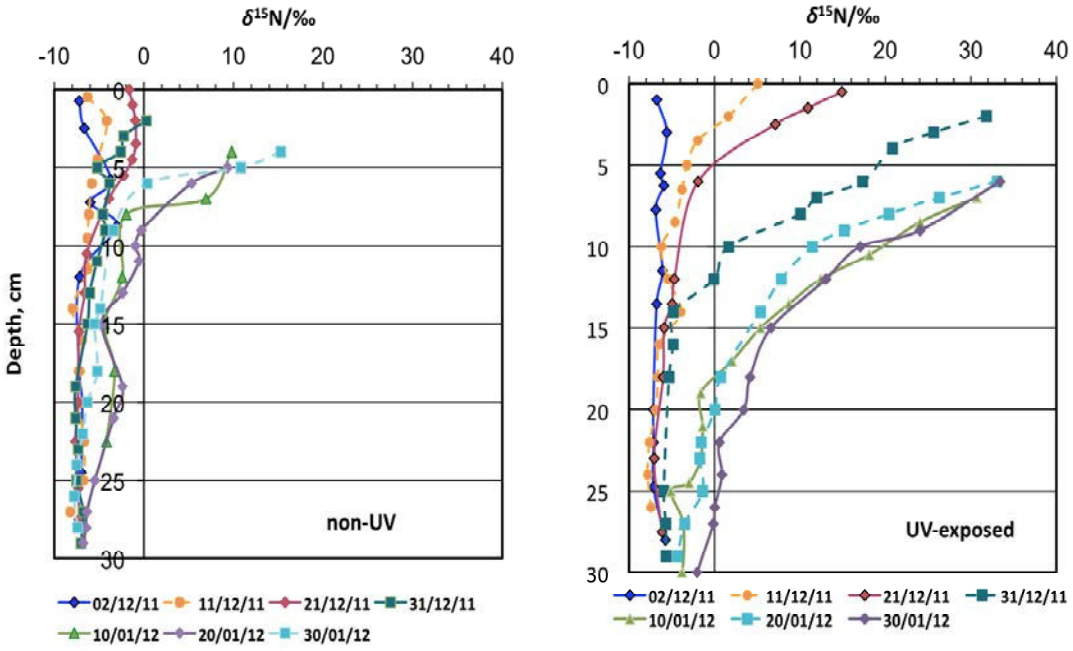

Figure A.3 *The $\delta^{15}N(NO_3^-)$ profile in the snow samples with depth for the non-UV and UV-exposed samples after excluding the data points affected by mixing/drift snow and the experimental setup (see main text above).*

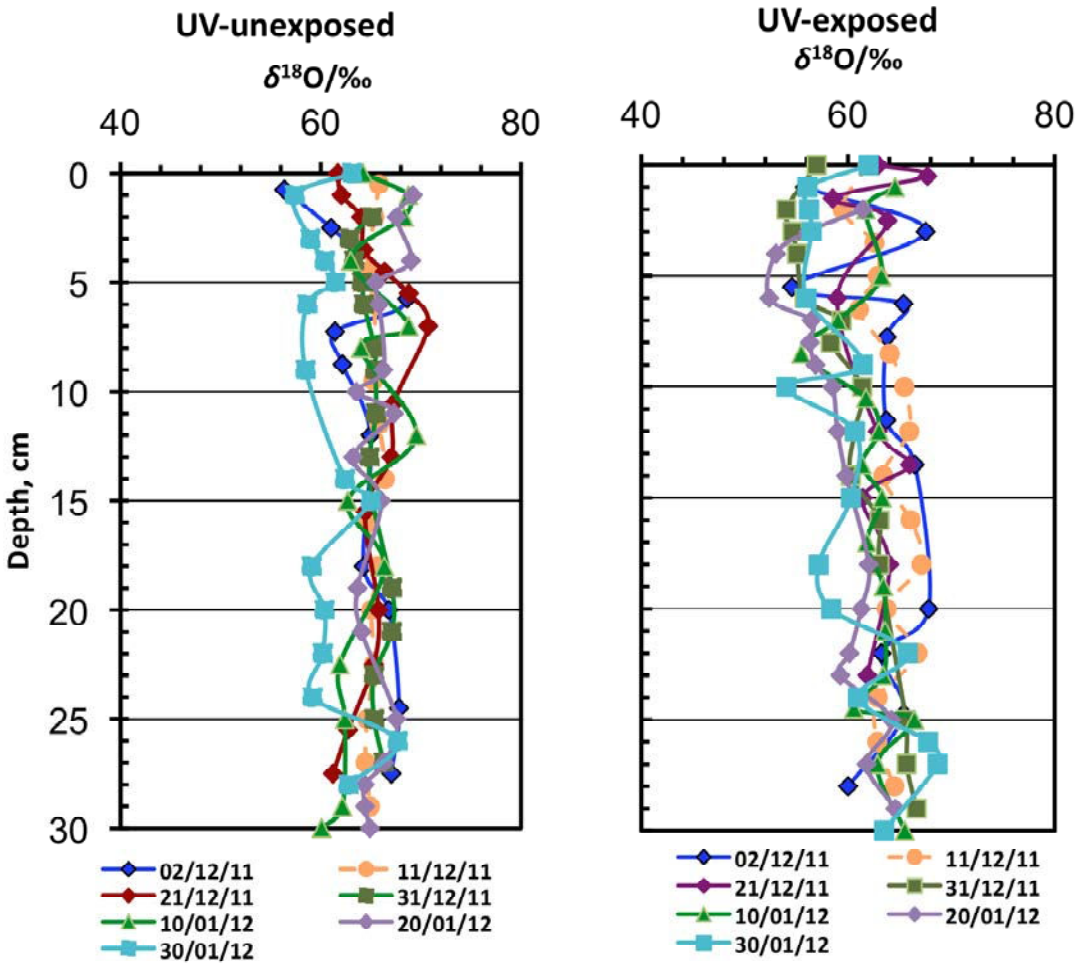

Figure A.4 *Same as Fig. A.3 but here for the $\delta^{18}O(NO_3^-)$ profile in the snow samples with depth for the non-UV (left) and UV-exposed (right) samples.*

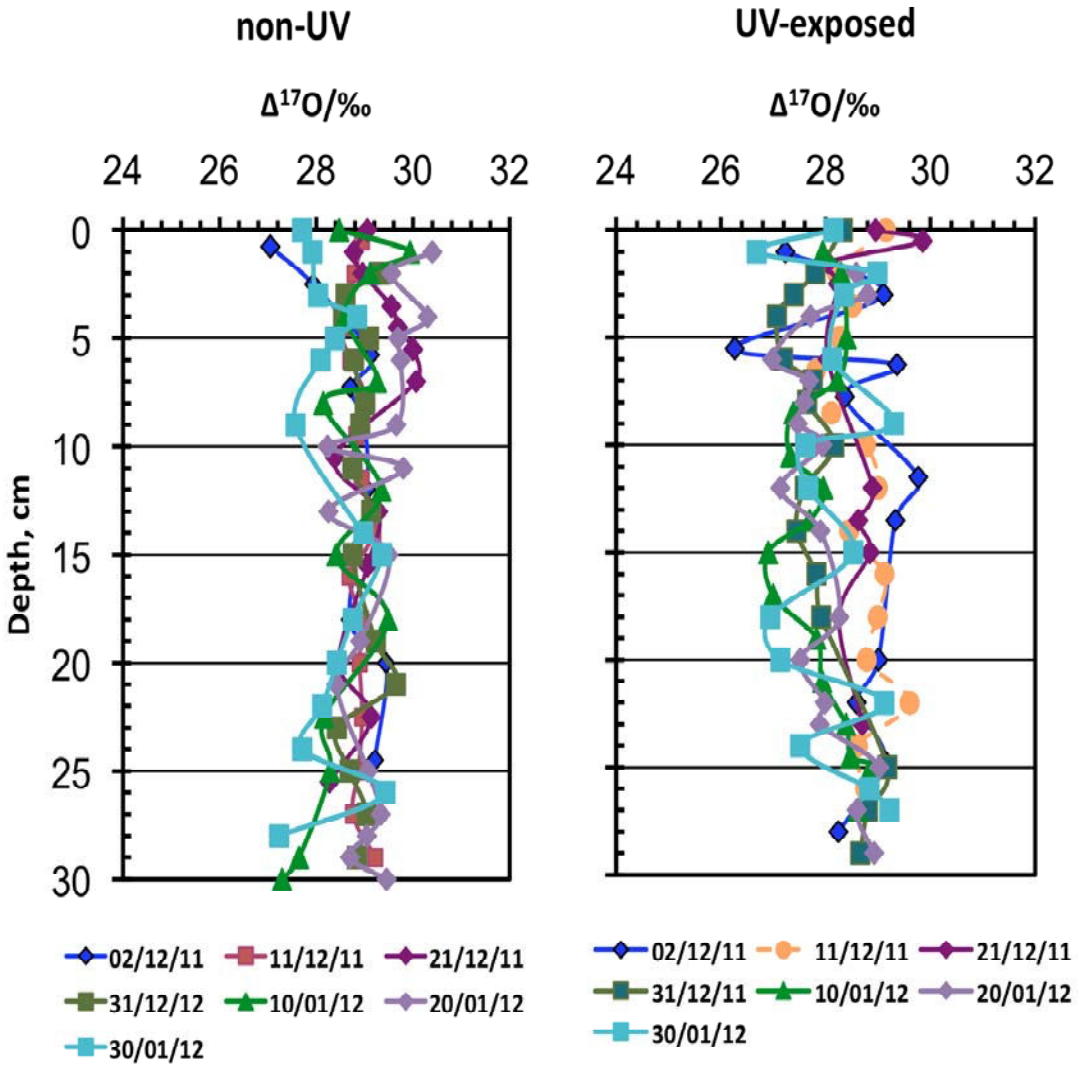

Figure A.5 *Same as Fig. A.3 but here for the $\Delta^{17}O(NO_3^-)$ profile in the snow samples with depth for the non-UV (left) and UV-exposed (right) samples.*

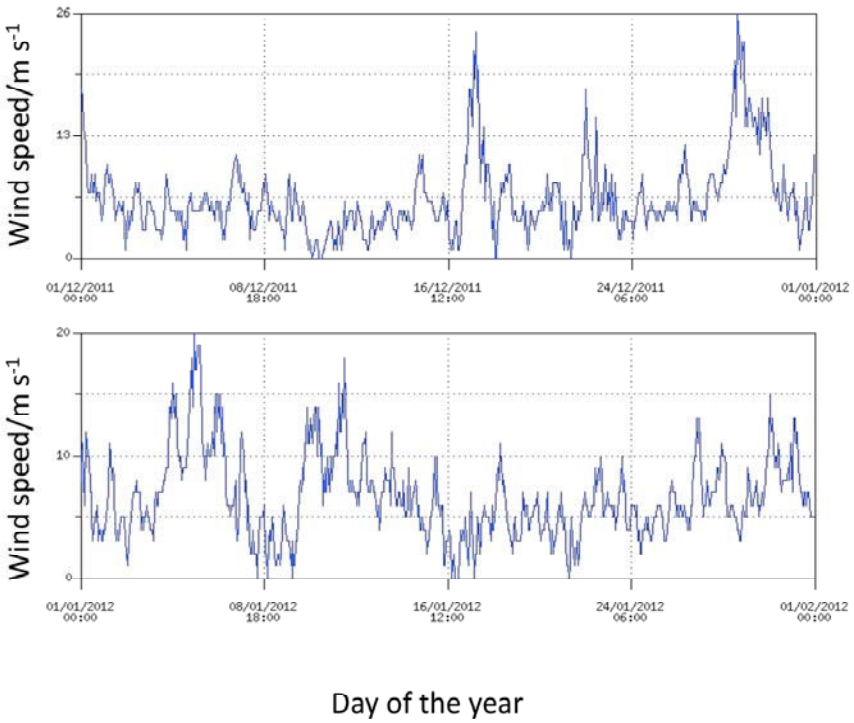

Figure A.6 *The wind speed record at Dome C during December 2011 (top panel) and January 2012 (bottom panel) (http://www.climantartide.it).*

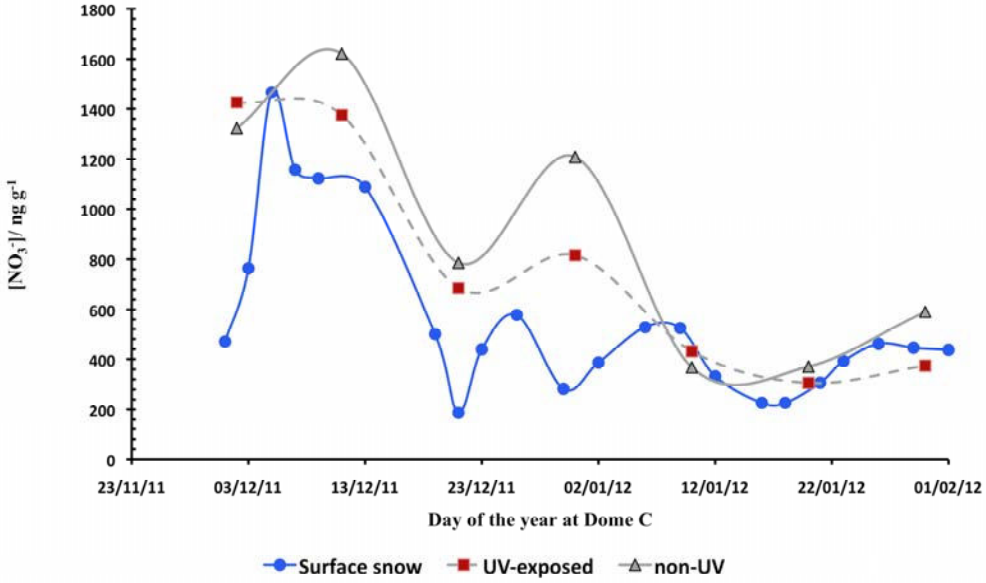

Figure A.7 *The nitrate concentration measured from the surface snow collected near the two snow pits (blue circles), and from the surface of the UV-exposed (brown, squares) and non-UV (grey, triangles) pits.*

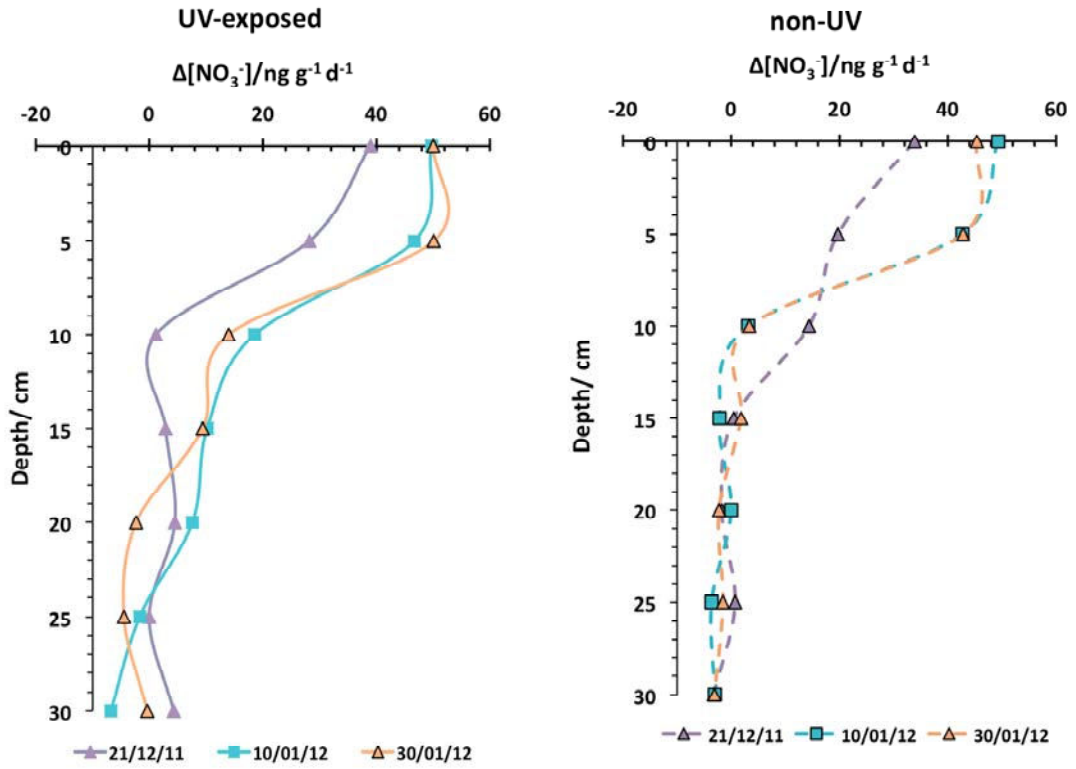

Figure A.8 *The speed of loss of nitrate from the snow pits with depth and for different collections derived based on the change in nitrate amount from its initial amount measured from the first collection (02/12/2011).*

Table A.1. Field observation logbook during the experimental season in Dome C, Antarctica

Date	Observation/Remark
05/12/2011	Sublimation of few millimeters was noticed on non-UV-exposed pit
08/12/2011	Drifted snow on the both pits, and it was swept out
15/12/2011	5 mm sublimation observed in both pits
19/12/2011	Strong wind drifting snow
21/12/2011	Light snowfall, drifted snow was removed from the pits
30/12/2011	Non-UV pit surface was 50 % covered with drifted snow but no drifted snow on the UV-exposed pit
10/01/2012	At the surface level, 50 % of the non-UV and 20 % of the UV-exposed pits were covered with drifted snow
12/01/2012	Drifted snow covering the entire non-UV pit and 20 % of the UV-exposed pit
20/01/2012	2-3 cm drifted snow on non-UV pit and 3 cm drifted snow on UV-exposed pit

Chapter 5

Conclusion and outlook

The main goals of this dissertation have been the understanding of NO_X/nitrate chemistry, and specifically the photochemistry of snow nitrate. Stable isotope ratios are valuable tools in isotope geochemistry with strong potential to provide information about crucial chemical processes. The stable isotope ratios of nitrate ($\delta^{18}O$, $\Delta^{17}O$, $\delta^{15}N$) have been widely used in atmospheric science to infer to the NO_X oxidation pathways and signature of atmospheric ozone as well as to constrain the sources of NO_X (= NO + NO_2). The NO_X emitted in the atmosphere will undergo oxidation through various mechanisms and eventually will become a stable product, nitrate. From the determination of the $\Delta^{17}O$ signal of nitrate obtained from different geographical locations, it is be possible to identify and quantify the oxidation mechanism leading nitrate formation. In polar regions, nitrate will also be deposited in the snow, and it is one of the most abundant anions in polar ice and snow. A thorough analysis of its stable isotopes can then be used as metrics to understand past climatic changes and oxidation capacity of the atmosphere. This information can be obtained from deep ice cores, which preserved the nitrate record on millennial time scales. Despite many existing time-series of ice cores nitrate concentration from various regions in Antarctica such as the EPICA (European Project for Ice Coring in Antarctica) ice core which extends about 3259 m and encompasses 800 ka of information (Wolff et al., 2010) or the Vostok ice core which is about 3623 m and spans about 400 ka (Petit et al., 1997), their interpretation remains complex. This is mainly due to post-depositional process which partly or completely modify the archived information specifically at low snow accumulation sites such as Dome C. Part of this PhD study is framed with the objective to investigate the effect of photolysis on the mass and isotopic composition of snow nitrate. Here are some of the fundamental questions have been answered based on the findings from this study.

5.1. What is the ^{17}O-excess transfer function for the $NO_2 + O_3$ reaction?

Based on the experimental study conducted on the gas phase $NO_2 + O_3$ reaction, an important nighttime nitrate formation pathway, the transferable ^{17}O-excess was quantified by the function: $\Delta^{17}O(O_3^*) = (1.23 \pm 0.19) \times \Delta^{17}O(O_3)_{bulk} + (9.02 \pm 0.99)$. This function is similar to the NO + O_3 transfer function ($\Delta^{17}O(O_3^*) = (1.18\pm 0.07) \times \Delta^{17}O(O_3)_{bulk} + (6.6\pm1.5)$) observed by Savarino et al. (2008) but differs as for the latter, the central oxygen atom of ozone can be transferred with a small probability, (8 ± 5 %). This same gas phase reaction is also different from the liquid phase NO_2^- + O_3 reaction (Michalski and Bhattacharya, 2009) by truly representing the actual reaction conditions in the atmosphere. In the future, modeling studies should incorporate the values obtained from this study to better constrain the nitrate formation pathways relevant to specific conditions (space or time). Additionally, further experimental studies are required to derive the ^{17}O-excess transfer functions for the different nitrate formation pathways including the Br +O_3 reaction, which was not successful during this PhD study.

5.2. What do we learn from the laboratory experiments of photolysis of snow nitrate?

Based on our experimental approach in the laboratory, isotopic fractionations induced by UV-photolysis of nitrate were quantified. The novelty of this work is that it allows to investigate specifically photolysis process and its associated isotopic effects.

The design of this laboratory study enabled better control over key parameters such as temperature, pressure, light conditions (spectral distribution) and product removal compared to previous laboratory study (Blunier et al. 2005). From this study, we have derived nitrogen isotopic fractionations of (-23.2 ± 1.0) ‰, (-38.6 ± 2.8) ‰ and (-47.9 ± 6.8) ‰ for the 280, 305 and 320 nm UV filters respectively. The spectral dependence of isotopic fractionation was experimentally observed with less negative fractionations towards higher energy UV and the opposite observation in lower energy UV region, a trend in agreement with the theory of isotopic shift of cross-section.

5.3. Can we apply the observations in the laboratory to better constrain the absorption cross-section of $^{15}NO_3^-$?

As the experimentally measured absorption cross-section of $^{15}NO_3^-$ is not currently available, the ZPE-shift model was introduced to derive this cross-section from the most abundant isotopologue (Frey et al., 2009). According to this approach, the absorption cross-section of a heavier isotopologue can be derived from the lighter isotopologue by simply shifting the absorption spectra of the most abundant isotopologue by the ΔZPE. For nitrate, a ZPE-shift of -44.8 cm^{-1} was derived and applied to generate the absorption spectra of $^{15}NO_3^-$. Using this model approach, we have derived isotopic fractionations under the laboratory experimental conditions (using actinic fluxes from the Xe lamp in the presence of UV-filters). The model estimates were in fairly good agreement with the values obtained experimentally in the laboratory. In an ideal case where the model perfectly reproduces the experimental conditions, the isotopic fractionations from both approaches should match. However, a recent four-parameter model presented by Jost and co-workers (Ndengue et al., 2010;Jost, 2008) states that even if the ZPE-shift is the major parameter which changes with an isotopic substitution, changes in the width and amplitude of the absorption cross-section of the least abundant isotopologue should also be taken into account. Hence, the small differences between the model estimates and the laboratory observations may arise from ignoring these parameters.

In this study, we went more into the details on effects of isotopic substitution on absorption cross-sections than the approach presented by Frey et al. (2009), and better constrained the absorption cross-section of $^{15}NO_3^-$. In our approach, we matched the results from the laboratory study with the isotopic fractionations derived using the ZPE-shift model under the laboratory conditions (actinic flux of the Xe lamp in the presence of filters) and derived an apparent ZPE-shift of -53.8 cm^{-1}. This apparent value better matches the laboratory values and the model estimates, and it incorporates changes in ZPE, width and amplitude during isotopic substitution.

5.3 How do we validate this newly derived apparent ZPE-shift?

To test the validity of the newly derived apparent ZPE-shift value, we have conducted a field experiment. In this study, we have designed an experimental setup which compares two identical snow pits which were built by filling a locally drifted snow with the same nitrate profile (concentration and isotopic composition) and placed two plexi plates to block/allow solar UV. This experimental design was unique in that it minimizes/prevents non-photolytic effects such as deposition and investigates the effect of photolysis specifically. In this study, we derived an average nitrogen isotopic fractionation of -67.9 ± 12.0 ‰ for the pits exposed to the solar UV.

We have applied the theoretical ZPE-shift model approach based on the newly derived apparent ZPE-shift value and obtained a $^{15}\varepsilon$ value of -55.6 ‰ under Dome C conditions. This value is slightly higher but in good agreement with the experimental values in the field considering the error bars (-67.9 ± 12 ‰).

The nitrogen isotopic fractionation based on this new model prediction is also in good agreement with previous field measurements of average apparent isotopic fractionations of (-59 ± 10) ‰ derived for the East Antarctic Plateau (Erbland et al., 2013) (Note that apparent isotopic fractionation includes fractionations induced by photolysis and additional processes such as desorption and deposition).

Based on these observations, we recommend that the newly derived apparent ZPE-shift should be used to constrain the absorption cross-section of $^{15}NO_3^-$.

5.5 What are the future perspectives to better constrain the field observations?

We are currently applying theoretical calculations to better constrain the ZPE-shift during isotopic substitution using the four parameters model to account for the changes in width, center, asymmetry and amplitude. In addition, the actual ZPE-shift value (-44.8 cm^{-1}) is derived based on fundamental frequencies of $^{14}NO_3^-$ and $^{15}NO_3^-$. This approach may underestimate the ZPE-shit as the anharmonicities of these molecules are not taken into account. Accordingly, if anharmonicities were taken into account, the ZPE-shift will become -47.5 cm^{-1} (Remy Jost, personal communication) and further calculations may be required. In the future, when such framework will be fully developed, we will use the TRANSITS (TRansfer of Atmospheric Nitrate to Stable Isotopes to The Snow) model (Erbland, 2011) will be available to extract the environmental parameters from the observed isotopic fractionations of nitrate trapped in deep ice cores.

TRANSITS is a numerical model which uses variety of measurement inputs such as snow accumulation rate, nitrate flux, solar UV flux, the ozone column, and different optical parameters (quantum yield, absorption cross-sections, absorption/scattering by the snowpack, and so on) and physico-chemical process to constrain the information archived in deep ice cores. The model applies different scenarios such as variability in ozone layer and actinic flux, and provides estimates of concentration and isotopic composition of archived nitrate as well as isotopic fractionations.

It is expected that with a better constrain on the absorption cross-section of $^{15}NO_3^-$, fueled by the better molecular dynamic model, the TRANSITS model will open new

windows into the interpretations of $\delta^{15}N(NO_3^-)$ recorded in deep ice cores. An example of an approach towards such application is described below.

5.6. What can be the applications of these findings in the future?

The purpose of this section of the conclusion is to give directions in the possible applications of the findings from this experimental research. Here, we only provide a qualitative outlook into an example of the use of our findings. A more quantitative interpretation will require the use of a modeling framework (TRANSITS model).

The currently existing ice core nitrate data requires the clear quantification and full understanding of post-depositional process. There are records of very high $\delta^{15}N$ values of nitrate reaching 300 ‰ measured in the Vostok ice core in Antarctica (Erbland, 2011). These $\delta^{15}N$ signals may carry a significant information regarding changes in the ozone layer and variability of the solar radiation within millennial time scales. But the validity of these records lie solely on the clear understanding of post-depositional effects and a well defined mechanism to account for their effects.

The top panel in Figure 5.1 shows the ozone column observed above the Halley station in Antarctica in October from 1955-2005. According to this plot, the ozone column decreases over the years from about 300 DU in 1955 to the lowest levels between 1995 and 2000. Note that the ozone data is provided only for October, and the ozone level may vary at different seasons of the year; however, during this period of the year the ozone hole deepens and extends over the entire continent. The bottom panel shows the $\delta^{15}N(NO_3^-)$ profile of a 6 m snow pit from Dome C which encompass the same period as the ozone column observation. According to Fig. 5.1, the $\delta^{15}N$ values show an increase over the years from about 150 ‰ around 1955 to higher levels reaching 350 ‰. However, we should recall that $\delta^{15}N$ values are the function of isotopic fractionation (ε) and mass loss (f). As the snow accumulation rate during the last 50-60 years was more or less constant, the change in $\delta^{15}N$ values may arise from isotopic fractionation or change in the amount of loss of snow nitrate (f). But how does these parameters impact the $\delta^{15}N$ values?

Isotopic fractionations are dependent on the solar actinic flux reaching the snow nitrate, which in turn depends on the overlying ozone layer that modulates the UV radiation reaching the snow. A decrease in ozone layer will lead to more energetic UV photons reaching the snow nitrate. Referring to the laboratory study in chapter 3, we expect less negative isotopic fractionations towards shorter wavelength regions thus lowering the $\delta^{15}N$ values for the nitrate remaining in the snow in contradiction with our observation in the field (Fig. 5.1). However, decrease in ozone layer accompanied by increase of incoming solar UV flux will lead to a decrease in f, as photolysis rate of nitrate in the snow will be enhanced. This effect will lead to enrichment in ^{15}N of nitrate remaining in the snow and hence higher $\delta^{15}N$ values.

This opposing trend between $^{15}\varepsilon$ and f with the increase of UV radiation is difficult to evaluate. Quantitative interpretation will requires the application of a snow denitrification model (e.g.,TRANSITS). In the future, modeling calculations may provide accurate quantitative estimates of the main parameters influencing $\delta^{15}N$ in snow where the pre and post-period of the ozone hole can be used as a validation case, before

applying the model for deciphering the information buried in ice core on longer time scales.

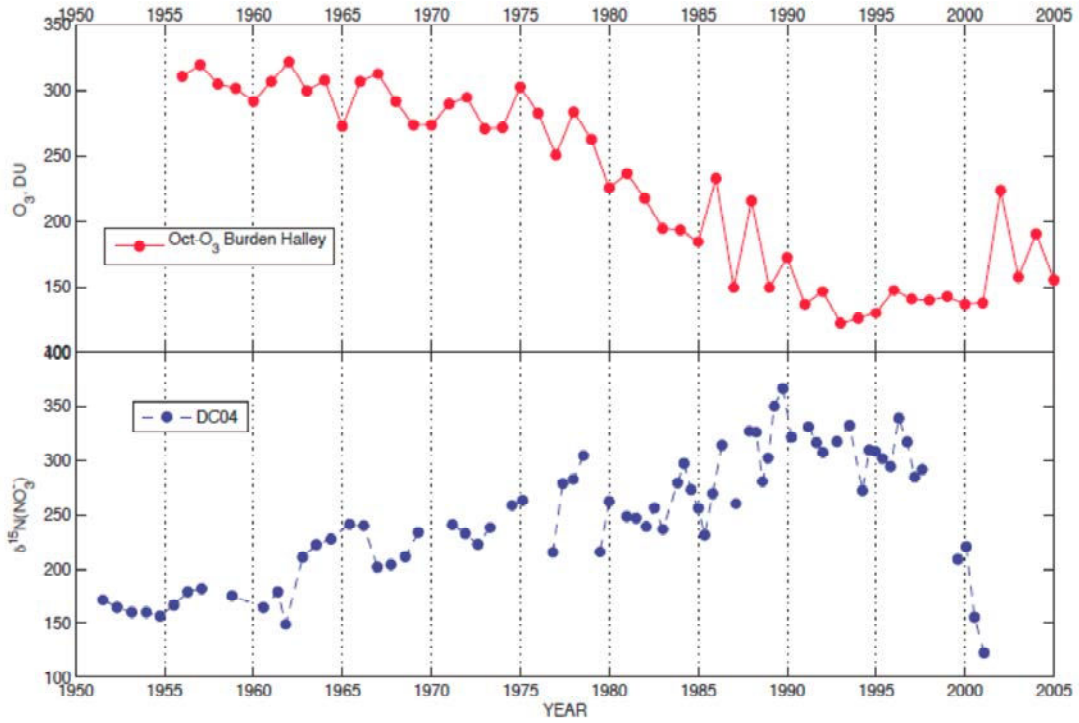

Figure 5.1. *The ozone profile at Halley station in Antarctica observed during October (top) and the $\delta^{15}N(NO_3^-)$ values measured from 6 m surface core at Dome C in 2004 (Unpublished data from M. Frey, S. Morin and J. Savarino)*

Bibliography

Abida, O., Mielke, L. H., and Osthoff, H. D.: Observation of gas-phase peroxynitrous and peroxynitric acid during the photolysis of nitrate in acidified frozen solutions, Chemical Physics Letters, 511, 187-192, 10.1016/j.cplett.2011.06.055, **2011**.

Alexander, B., Savarino, J., Kreutz, K. J., and Thiemens, M. H.: Impact of preindustrial biomass-burning emissions on the oxidation pathways of tropospheric sulfur and nitrogen, J Geophys Res-Atmos, 109, D08303
10.1029/2003jd004218, **2004**.

Alexander, B., Hastings, M. G., Allman, D. J., Dachs, J., Thornton, J. A., and Kunasek, S. A.: Quantifying atmospheric nitrate formation pathways based on a global model of the oxygen isotopic composition (delta O-17) of atmospheric nitrate, Atmospheric Chemistry and Physics, 9, 5043-5056, **2009**.

Allan, B. J., McFiggans, G., Plane, J. M. C., Coe, H., and McFadyen, G. G.: The nitrate radical in the remote marine boundary layer, J Geophys Res-Atmos, 105, 24191-24204, Doi 10.1029/2000jd900314, **2000**.

Aristidi, E., Agabi, K., Azouit, M., Fossat, E., Vernin, J., Travouillon, T., Lawrence, J. S., Meyer, C., Storey, J. W. V., Halter, B., Roth, W. L., and Walden, V.: An analysis of temperatures and wind speeds above Dome C, Antarctica, Astron Astrophys, 430, 739-746, Doi 10.1051/0004-6361:20041876, **2005**.

Atkinson, R.: Atmospheric chemistry of VOCs and NOx, Atmospheric Environment, 34, 2063-2101, 10.1016/s1352-2310(99)00460-4, **2000**.

Atkinson, R., Baulch, D. L., Cox, R. A., Crowley, J. N., Hampson, R. F., Hynes, R. G., Jenkin, M. E., Rossi, M. J., and Troe, J.: Evaluated kinetic and photochemical data for atmospheric chemistry: Volume I - gas phase reactions of O-x, HOx, NOx and SOx species, Atmospheric Chemistry and Physics, 4, 1461-1738, **2004**.

Bainssahota, S. K., and Thiemens, M. H.: Mass-Independent Oxygen Isotopic Fractionation in a Microwave Plasma, J Phys Chem-Us, 91, 4370-4374, Doi 10.1021/J100300a031, **1987**.

Bauguitte, S. J. B., Bloss, W. J., Evans, M. J., Salmon, R. A., Anderson, P. S., Jones, A. E., Lee, J. D., Saiz-Lopez, A., Roscoe, H. K., Wolff, E. W., and Plane, J. M. C.: Summertime NOx measurements during the CHABLIS campaign: can source and sink estimates unravel observed diurnal cycles?, Atmospheric Chemistry and Physics, 12, 989-1002, Doi 10.5194/Acp-12-989-2012, **2012**.

Begun, G. M., and Fletcher, W. H.: Partition Function Ratios for Molecules Containing Nitrogen Isotopes, The Journal of Chemical Physics, 33, 1083, 10.1063/1.1731338, **1960**.

Beine, H., Colussi, A. J., Amoroso, A., Esposito, G., Montagnoli, M., and Hoffmann, M. R.: HONO emissions from snow surfaces, Environ Res Lett, 3, Artn 045005 Doi 10.1088/1748-9326/3/4/045005, **2008**.

Beine, H. J., Honrath, R. E., Domine, F., Simpson, W. R., and Fuentes, J. D.: NOx during background and ozone depletion periods at Alert: Fluxes above the snow surface, J Geophys Res-Atmos, 107, Artn 4584 Doi 10.1029/2002jd002082, **2002**.

Bhattacharya, S. K., Pandey, A., and Savarino, J.: Determination of intramolecular isotope distribution of ozone by oxidation reaction with silver metal, J Geophys Res-Atmos, 113, D03303 10.1029/2006jd008309, **2008**.

Bhattacharya, S. K., Savarino, J., and Luz, B.: Mass-Dependent Isotopic Fractionation in Ozone Produced by Electrolysis, Analytical Chemistry, 81, 5226-5232, 10.1021/ac900283q, **2009**.

Blunier, T.: Isotopic view on nitrate loss in Antarctic surface snow, Geophysical Research Letters, 32, 10.1029/2005gl023011, **2005**.

Blunier, T., Floch, G. L., Jacobi, H. W., and Quansah, E.: Isotopic view on nitrate loss in Antarctic surface snow, Geophysical Research Letters, 32, Artn L13501 Doi 10.1029/2005gl023011, **2005**.

Böhlke, J. K., Mroczkowski, S. J., and Coplen, T. B.: Oxygen isotopes in nitrate: new reference materials for O-18 : O-17 : O-16 measurements and observations on nitrate-water equilibration, Rapid Commun Mass Sp, 17, 1835-1846, Doi 10.1002/Rcm.1123, **2003**.

Bottenheim, J. W., Netcheva, S., Morin, S., and Nghiem, S. V.: Ozone in the boundary layer air over the Arctic Ocean: measurements during the TARA transpolar drift 2006-2008, Atmospheric Chemistry and Physics, 9, 4545-4557, **2009**.

Boxe, C. S., Colussi, A. J., Hoffmann, M. R., Perez, I. M., Murphy, J. G., and Cohen, R. C.: Kinetics of NO and NO2 evolution from illuminated frozen nitrate solutions, Journal of Physical Chemistry A, 110, 3578-3583, Doi 10.1021/Jp055037q, **2006**.

Brenninkmeijer, C., Janssen, C., Kaiser, J., Röckmann, T., Rhee, T. S., and Assonov, S. S.: Isotope effects in the chemistry of atmospheric trace compounds, Chem Rev. , 103, 5125-5162, **2003**.

Brown, S. S., and Stutz, J.: Nighttime radical observations and chemistry, Chem Soc Rev, 41, 6405-6447, Doi 10.1039/C2cs35181a, **2012**.

Burkhart, J. F., Hutterli, M., Bales, R. C., and McConnell, J. R.: Seasonal accumulation timing and preservation of nitrate in firn at Summit, Greenland, J Geophys Res-Atmos, 109, Artn D19302 Doi 10.1029/2004jd004658, **2004**.

Carter, J., and Barwick, V.: Good Practice Guide for Isotope Ratio Mass Spectrometry, 1 ed., edited by: Jim Caret, C. L., Wolfram Meier-Augenstein, Helen Kemp, Sabine Schneiders, Libby Stern, Gerard van der Peijil, **2011**.

Casciotti, K. L., Sigman, D. M., Hastings, M. G., Böhlke, J. K., and Hilkert, A.: Measurement of the oxygen isotopic composition of nitrate in seawater and freshwater using the denitrifier method, Analytical Chemistry, 74, 4905-4912, Doi 10.1021/Ac020113w, **2002**.

Centnerszwer, M., and Bruzs, B.: The Thermal Decomposition of Silver Carbonate, J. Phys. Chem., 29, 733–737, **1925**.

Chen, G., Davis, D., Crawford, J., Nowak, J. B., Eisele, F., Mauldin, R. L., Tanner, D., Buhr, M., Shetter, R., Lefer, B., Arimoto, R., Hogan, A., and Blake, D.: An investigation of South Pole HOx chemistry: Comparison of model results with ISCAT observations, Geophysical Research Letters, 28, 3633-3636, Doi 10.1029/2001gl013158, **2001**.

Chu, L., and Anastasio, C.: Quantum yields of hydroxyl radical and nitrogen dioxide from the photolysis of nitrate on ice, Journal of Physical Chemistry A, 107, 9594-9602, Doi 10.1021/Jp0349132, **2003**.

Clayton, R. N., Mayeda, T. K., Molinivelsko, C. A., and Goswami, J. N.: Oxygen and Silicon Isotopic Composition of Dhajala Chondrules, Meteoritics, 18, 282-282, **1983**.

Coplen, T. B.: Reporting of stable Hydrogen, carbon, and Oxygen isotopic abundances, U.S.Geological survey, Virginia, 273-276, **1994**.

Coplen, T. B.: Guidelines and recommended terms for expression of stable-isotope-ratio and gas-ratio measurement results, Rapid Commun Mass Sp, 25, 2538-2560, Doi 10.1002/Rcm.5129, **2011**.

Cotter, E. S. N.: What controls photochemical NO and NO2 production from Antarctic snow? Laboratory investigation assessing the wavelength and temperature dependence, Journal of Geophysical Research, 108, 10.1029/2002jd002602, **2003**.

Cotter, E. S. N., Jones, A. E., Wolff, E. W., and Bauguitte, S. J. B.: What controls photochemical NO and NO2 production from Antarctic snow? Laboratory investigation assessing the wavelength and temperature dependence, J Geophys Res-Atmos, 108, Artn 4147 Doi 10.1029/2002jd002602, **2003**.

Crawford, J. H., Davis, D. D., Chen, G., Buhr, M., Oltmans, S., Weller, R., Mauldin, L., Eisele, F., Shetter, R., Lefer, B., Arimoto, R., and Hogan, A.: Evidence for photochemical production of ozone at the South Pole surface, Geophysical Research Letters, 28, 3641-3644, Doi 10.1029/2001gl013055, **2001**.

Criss, R. E.: Principles of Stable Isotope Distribution, Oxford, **1999**.

Crutzen, P. J.: ROLE OF NO AND NO2 IN THE CHEMISTRY OF THE TROPOSPHERE AND STRATOSPHERE, Annual Review of Earth and Planetary Sciences, 7, 443-472, 1979.

Davis, D., Nowak, J. B., Chen, G., Buhr, M., Arimoto, R., Hogan, A., Eisele, F., Mauldin, L., Tanner, D., Shetter, R., Lefer, B., and McMurry, P.: Unexpected high levels of NO observed at South Pole, Geophysical Research Letters, 28, 3625-3628, Doi 10.1029/2000gl012584, **2001**.

Davis, D. D., Seelig, J., Huey, G., Crawford, J., Chen, G., Wang, Y. H., Buhr, M., Helmig, D., Neff, W., Blake, D., Arimoto, R., and Eisele, F.: A reassessment of Antarctic plateau reactive nitrogen based on ANTO 2003 airborne and ground based measurements, Atmospheric Environment, 42, 2831-2848, Doi 10.1016/J.Atmosenv.2007.07.039, **2008**.

Dibb, J. E., and Whitlow, S. I.: Recent climate anomalies and their impact on snow chemistry at South Pole, 1987-1994, Geophysical Research Letters, 23, 1115-1118, 10.1029/96gl01039, **1996**.

Dibb, J. E., Talbot, R. W., Munger, J. W., Jacob, D. J., and Fan, S. M.: Air-snow exchange of HNO3 and NOy at Summit, Greenland, J Geophys Res-Atmos, 103, 3475-3486, **1998**.

Dibb, J. E., and Fahnestock, M.: Snow accumulation, surface height change, and firn densification at Summit, Greenland: Insights from 2 years of in situ observation, J Geophys Res-Atmos, 109, Artn D24113 Doi 10.1029/2003jd004300, **2004**.

Domine, F., J., B., Voisin, D., and Donaldson, D. J.: Can We Model Snow Photochemistry? Problems with the Current Approaches, The Journal of Physical Chemistry A, 10.1021/jp3123314, **2013**.

Dominé, F., and Shepson, P. B.: Air-snow interactions and atmospheric chemistry, Science, 297, 1506-1510, Doi 10.1126/Science.1074610, **2002**.

Dominé, F., Taillandier, A. S., Houdier, S., Parrenin, F., Simpson, W. R., and Douglas, T. A.: Interactions between snow metamorphism and climate: Physical and chemical aspects, Physics and Chemistry of Ice, 27-46, **2007**.

Dubey, M. K., Mohrschladt, R., Donahue, N. M., and Anderson, J. G.: Isotope specific kinetics of hydroxyl radical (OH) with water (H2O): Testing models of reactivity and atmospheric fractionation, Journal of Physical Chemistry A, 101, 1494-1500, Doi 10.1021/Jp962332p, **1997**.

Dubowski, Y., Colussi, A. J., and Hoffmann, M. R.: Nitrogen dioxide release in the 302 nm band photolysis of spray-frozen aqueous nitrate solutions. Atmospheric implications, Journal of Physical Chemistry A, 105, 4928-4932, **2001**.

Eisen, O., Frezzotti, M., Genthon, C., Isaksson, E., Magand, O., van den Broeke, M. R., Dixon, D. A., Ekaykin, A., Holmlund, P., Kameda, T., Karlöf, L., Kaspari, S., Lipenkov, V. Y., Oerter, H., Takahashi, S., and Vaughan, D. G.: Ground-based measurements of spatial and temporal variability of snow accumulation in east Antarctica, Rev Geophys, 46, Artn Rg2001 Doi 10.1029/2006rg000218, **2008**.

Erbland, J.: Isotopic constraints on the interpretation of the nitrate record in the Vostok ice core, PhD thesis, University of Grenoble, Grenoble, **2011**.

Erbland, J., Vicars, W. C., Savarino, J., Morin, S., Frey, M., Frosini, E., Vince, E., and Martins, J. M. F.: Air-snow transfer of nitrate on the East Antarctic Plateau – Part 1: Isotopic evidence for a photolytically driven dynamic equilibrium, Atmos. Chem. Phys. Discuss., 12, 28559-28608, 10.5194/acpd-12-28559-2012, **2013**.

Evans, M. J., Jacob, D. J., Atlas, E., Cantrell, C. A., Eisele, F., Flocke, F., Fried, A., Mauldin, R. L., Ridley, B. A., Wert, B., Talbot, R., Blake, D., Heikes, B., Snow, J., Walega, J., Weinheimer, A. J., and Dibb, J.: Coupled evolution of BrOx-ClOx-HOx-NOx chemistry during bromine-catalyzed ozone depletion events in the arctic boundary layer, J Geophys Res-Atmos, 108, 10.1029/2002jd002732, **2003**.

Farquhar, J., and Wing, B. A.: The terrestrial record of stable sulphur isotopes: a review of the implications for evolution of Earth's sulphur cycle, Mineral Deposits and Earth Evolution, 248, 167-177, **2005**.

Farquhar, J., Peters, M., Johnston, D. T., Strauss, H., Masterson, A., Wiechert, U., and Kaufman, A. J.: Isotopic evidence for Mesoarchaean anoxia and changing atmospheric sulphur chemistry, Nature, 449, 706-U705, 10.1038/nature06202, **2007**.

France, J. L., King, M. D., Frey, M. M., Erbland, J., Picard, G., Preunkert, S., MacArthur, A., and Savarino, J.: Snow optical properties at Dome C (Concordia), Antarctica; implications for snow emissions and snow chemistry of reactive nitrogen, Atmospheric Chemistry and Physics, 11, 9787-9801, Doi 10.5194/Acp-11-9787-2011, **2011a**.

France, J. L., King, M. D., Lee-Taylor, J., Beine, H. J., Ianniello, A., Dominé, F., and MacArthur, A.: Calculations of in-snow NO2 and OH radical photochemical production and photolysis rates: A field and radiative-transfer study of the optical properties of Arctic (Ny-Alesund, Svalbard) snow, J Geophys Res-Earth, 116, Artn F04013 Doi 10.1029/2011jf002019, **2011b**.

France, J. L., Reay, H. J., King, M. D., Voisin, D., Jacobi, H. W., Domine, F., Beine, H., Anastasio, C., MacArthur, A., and Lee-Taylor, J.: Hydroxyl radical and NOx production rates, black carbon concentrations and light-absorbing impurities in snow from field measurements of light penetration and nadir reflectivity of onshore and offshore coastal Alaskan snow, J Geophys Res-Atmos, 117, Artn D00r12 Doi 10.1029/2011jd016639, **2012**.

Frey, M. M., Savarino, J., Morin, S., Erbland, J., and Martins, J. M. F.: Photolysis imprint in the nitrate stable isotope signal in snow and atmosphere of East Antarctica and implications for reactive nitrogen cycling, Atmospheric Chemistry and Physics, 9, 8681-8696, Doi 10.5194/Acp-9-8681-2009, **2009**.

Frey, M. M., Brough, N., France, J. L., Traulle, O., Anderson, P. S., King, M. D., Jones, A. E., Wolff, E. W., and Savarino, J.: The diurnal variability of atmospheric nitrogen oxides (NO and NO₂) above the Antarctic Plateau driven by atmospheric stability and snow emissions, Atmospheric Chemistry and Physics Discussions, 12, 22309-22353, 10.5194/acpd-12-22309-2012, **2012**.

Galloway, J. N., Dentener, F. J., Capone, D. G., Boyer, E. W., Howarth, R. W., Seitzinger, S. P., Asner, G. P., Cleveland, C. C., Green, P. A., Holland, E. A., Karl, D. M., Michaels, A. F., Porter, J. H., Townsend, A. R., and Vörösmarty, C. J.: Nitrogen cycles: past, present, and future, Biogeochemistry, 70, 153-226, Doi 10.1007/S10533-004-0370-0, **2004**.

Galloway, J. N., Townsend, A. R., Erisman, J. W., Bekunda, M., Cai, Z. C., Freney, J. R., Martinelli, L. A., Seitzinger, S. P., and Sutton, M. A.: Transformation of the nitrogen cycle: Recent trends, questions, and potential solutions, Science, 320, 889-892, 10.1126/science.1136674, **2008**.

Gane, M. P., Williams, N. A., and Sodeau, J. R.: A reflection-absorption infrared spectroscopy (RAIRS) investigation of the low-temperature heterogeneous hydrolysis of bromine nitrate, Journal of Physical Chemistry A, 105, 4002-4009, 10.1021/jp02328k, **2001**.

Gao, Y. Q., and Marcus, R. A.: Strange and unconventional isotope effects in ozone formation, Science, 293, 259-263, 10.1126/science.1058528, **2001**.

Genthon, C., Town, M. S., Six, D., Favier, V., Argentini, S., and Pellegrini, A.: Meteorological atmospheric boundary layer measurements and ECMWF analyses during summer at Dome C, Antarctica, J Geophys Res-Atmos, 115, Artn D05104 Doi 10.1029/2009jd012741, **2010**.

Gettelman, A., Walden, V. P., Miloshevich, L. M., Roth, W. L., and Halter, B.: Relative humidity over Antarctica from radiosondes, satellites, and a general circulation model, J Geophys Res-Atmos, 111, Artn D09s13 Doi 10.1029/2005jd006636, **2006**.

Gonfiantini, R., Stichler, W., and Rozanski, K.: Standards and Intercomparison materials distributed by the International Atomic Energy Agency, Reference and intercomparison materials for stable isotopes of light elements, **1993**.

Grannas, A. M., Jones, A. E., Dibb, J., Ammann, M., Anastasio, C., Beine, H. J., Bergin, M., Bottenheim, J., Boxe, C. S., Carver, G., Chen, G., Crawford, J. H., Dominé, F., Frey, M. M., Guzmàn, M. I., Heard, D. E., Helmig, D., Hoffmann, M. R., Honrath, R. E., Huey, L. G., Hutterli, M., Jacobi, H. W., Klan, P., Lefer, B., McConnell, J., Plane, J., Sander, R., Savarino, J., Shepson, P. B., Simpson, W. R., Sodeau, J. R., von Glasow, R., Weller, R., Wolff, E. W., and Zhu, T.: An overview of snow photochemistry: evidence, mechanisms and impacts, Atmospheric Chemistry and Physics, 7, 4329-4373, **2007**.

Guenther, J., Erbacher, B., Krankowsky, D., and Mauersberger, K.: Pressure dependence of two relative ozone formation rate coefficients, Chemical Physics Letters, 306, 209-213, Doi 10.1016/S0009-2614(99)00469-8, **1999**.

Hastings, M. G., Steig, E. J., and Sigman, D. M.: Seasonal variations in N and O isotopes of nitrate in snow at Summit, Greenland: Implications for the study of nitrate in snow and ice cores, J Geophys Res-Atmos, 109, Artn D20306 Doi 10.1029/2004jd004991, **2004**.

Hastings, M. G., Jarvis, J. C., and Steig, E. J.: Anthropogenic Impacts on Nitrogen Isotopes of Ice-Core Nitrate, Science, 324, 1288-1288, Doi 10.1126/Science.1170510, **2009**.

Hathorn, B. C., and Marcus, R. A.: An intramolecular theory of the mass-independent isotope effect for ozone. I, J Chem Phys, 111, 4087-4100, **1999**.

Heaton, T. H. E.: 15N/14N ratios of NOx from vehicle engines and coal fired power stations, Tellus, 42(B), 304-307, **1990**.

Hewitt, C. N. A. V. J.: Handbook of Atmospheric Science: Principles and Applications, **2003**.

Hoefs, J.: Stable Isotope Geochemistry, 6th ed., springer, **2009**.

Honrath, R. E., Peterson, M. C., Guo, S., Dibb, J. E., Shepson, P. B., and Campbell, B.: Evidence of NOx production within or upon ice particles in the Greenland snowpack, Geophysical Research Letters, 26, 695-698, **1999**.

Honrath, R. E., Guo, S., Peterson, M. C., Dziobak, M. P., Dibb, J. E., and Arsenault, M. A.: Photochemical production of gas phase NOx from ice crystal NO3-, J Geophys Res-Atmos, 105, 24183-24190, Doi 10.1029/2000jd900361, **2000a**.

Honrath, R. E., Peterson, M. C., Dziobak, M. P., Dibb, J. E., Arsenault, M. A., and Green, S. A.: Release of NOx from sunlight-irradiated midlatitude snow, Geophysical Research Letters, 27, 2237-2240, Doi 10.1029/1999gl011286, **2000b**.

Honrath, R. E., Lu, Y., Peterson, M. C., Dibb, J. E., Arsenault, M. A., Cullen, N. J., and Steffen, K.: Vertical fluxes of NOx, HONO, and HNO3 above the snowpack at Summit, Greenland, Atmospheric Environment, 36, 2629-2640, Pii S1352-2310(02)00132-2 Doi 10.1016/S1352-2310(02)00132-2, **2002**.

Horowitz, L. W., and Jacob, D. J.: Global impact of fossil fuel combustion on atmospheric NOx, J Geophys Res-Atmos, 104, 23823-23840, Doi 10.1029/1999jd900205, **1999**.

Jacobi, H. W., Annor, T., and Quansah, E.: Investigation of the photochemical decomposition of nitrate, hydrogen peroxide, and formaldehyde in artificial snow, J Photoch Photobio A, 179, 330-338, Doi 10.1016/J.Jphotochem.2005.09.001, **2006**.

Jacobi, H. W., Armor, T., Kwakye-Awuah, B., Hilker, B., and Quansah, E.: A mechanism for photochemical reactions in the quasi-liquid layer of snow crystals in polar regions, Physics and Chemistry of Ice, 241-248, **2007**.

Jacobi, H. W., and Hilker, B.: A mechanism for the photochemical transformation of nitrate in snow, J Photoch Photobio A, 185, 371-382, Doi 10.1016/J.Jphotochem.2006.06.039, **2007**.

Janssen, C., Guenther, J., Mauersberger, K., and Krankowsky, D.: Kinetic origin of the ozone isotope effect: a critical analysis of enrichments and rate coefficients, Physical Chemistry Chemical Physics, 3, 4718-4721, **2001**.

Janssen, C., Guenther, J., Krankowsky, D., and Mauersberger, K.: Temperature dependence of ozone rate coefficients and isotopologue fractionation in O-16-O-18 oxygen mixtures, Chemical Physics Letters, 367, 34-38, Pii S0009-2614(02)01665-2 Doi 10.1016/S0009-2614(02)01665-2, **2003**.

Janssen, C.: Intramolecular isotope distribution in heavy ozone ((OOO)-O-16-O-18-O-16 and (OOO)-O-16-O-16-O-18), J Geophys Res-Atmos, 110, 10.1029/2004jd005479, **2005**.

Jarvis, J. C., Hastings, M. G., Steig, E. J., and Kunasek, S. A.: Isotopic ratios in gas-phase HNO(3) and snow nitrate at Summit, Greenland, J Geophys Res-Atmos, 114, D17301 10.1029/2009jd012134, **2009**.

Johnson, M. S., Billing, G. D., Gruodis, A., and Janssen, M. H. M.: Photolysis of nitrous oxide isotopomers studied by time-dependent hermite propagation, Journal of Physical Chemistry A, 105, 8672-8680, Doi 10.1021/Jp011449x, **2001**.

Johnston, J. C., and Thiemens, M. H.: The isotopic composition of tropospheric ozone in three environments, J Geophys Res-Atmos, 102, 25395-25404, **1997**.

Jones, A. E., Weller, R., Wolff, E. W., and Jacobi, H. W.: Speciation and rate of photochemical NO and NO2 production in Antarctic snow, Geophysical Research Letters, 27, 345-348, **2000**.

Jones, A. E., Weller, R., Anderson, P. S., Jacobi, H. W., Wolff, E. W., Schrems, O., and Miller, H.: Measurements of NOxemissions from the Antarctic snowpack, Geophysical Research Letters, 28, 1499-1502, 10.1029/2000gl011956, **2001a**.

Jones, A. E., Weller, R., Anderson, P. S., Jacobi, H. W., Wolff, E. W., Schrems, O., and Miller, H.: Measurements of NOx emissions from the Antarctic snowpack, Geophysical Research Letters, 28, 1499-1502, Doi 10.1029/2000gl011956, **2001b**.

Jost, R.: A new model of low resolution absorption cross section, Adv Quantum Chem, 55, 75-100, Doi 10.1016/S0065-3276(07)00206-7, **2008**.

Kahan, T. F., and Donaldson, D. J.: Photolysis of polycyclic aromatic hydrocarbons on water and ice surfaces, Journal of Physical Chemistry A, 111, 1277-1285, Doi 10.1021/Jp066660t, **2007**.

Kaiser, J., Röckmann, T., Brenninkmeijer, C. A. M., and Crutzen, P. J.: Wavelength dependence of isotope fractionation in N2O photolysis, Atmospheric Chemistry and Physics, 3, 303-313, **2003**.

Kaiser, J., Röckmann, T., and Brenninkmeijer, C. A. M.: Contribution of mass-dependent fractionation to the oxygen isotope anomaly of atmospheric nitrous oxide, Journal of Geophysical Research, 109, 10.1029/2003JD004088, **2004**.

Kaiser, J., Hastings, M. G., Houlton, B. Z., Röckmann, T., and Sigman, D. M.: Triple oxygen isotope analysis of nitrate using the denitrifier method and thermal decomposition of N2O, Analytical Chemistry, 79, 599-607, Doi 10.1021/Ac061022s, **2007**.

Krankowsky, D., Bartecki, F., Klees, G. G., Mauersberger, K., Schellenbach, K., and Stehr, J.: MEASUREMENT OF HEAVY ISOTOPE ENRICHMENT IN TROPOSPHERIC OZONE, Geophysical Research Letters, 22, 1713-1716, **1995**.

Kunasek, S. A., Alexander, B., Steig, E. J., Hastings, M. G., Gleason, D. J., and Jarvis, J. C.: Rnterpreting Delta O-17 of nitrate in ice cores at high accumulation sites, Geochimica Et Cosmochimica Acta, 72, A502-A502, **2008**.

Lee-Taylor, J., and Madronich, S.: Calculation of actinic fluxes with a coupled atmosphere-snow radiative transfer model, J Geophys Res-Atmos, 107, Artn 4796 Doi 10.1029/2002jd002084, **2002**.

Legrand, M., Wolff, E., and Wagenbach, D.: Antarctic aerosol and snowfall chemistry: implications for deep Antarctic ice-core chemistry, Ann Glaciol, 29, 66-72, Doi 10.3189/172756499781821094, **1999**.

Legrand, M. R., and Kirchner, S.: Origins and Variations of Nitrate in Polar Precipitation, Chem Geol, 70, 101-101, **1988**.

Liang, M.-C.: A semianalytic model for photo-induced isotopic fractionation in simple molecules, Journal of Geophysical Research, 109, 10.1029/2004jd004539, **2004**.

Liu, Q., Schurter, L. M., Muller, C. E., Aloisio, S., Francisco, J. S., and Margerum, D. W.: Kinetics and mechanisms of aqueous ozone reactions with bromide, sulfite, hydrogen sulfite, iodide, and nitrite ions, Inorganic Chemistry, 40, 4436-4442, 10.1021/ic000919j, **2001**.

Logan, J. A.: Nitrogen-Oxides in the Troposphere - Global and Regional Budgets, J Geophys Res-Oc Atm, 88, 785-807, Doi 10.1029/Jc088ic15p10785, **1983**.

Lyons, J. R.: Transfer of mass-independent fractionation in ozone to other oxygen-containing radicals in the atmosphere, Geophysical Research Letters, 28, 3231-3234, **2001**.

Mack, J., and Bolton, J. R.: Photochemistry of nitrite and nitrate in aqueous solution: a review, J Photoch Photobio A, 128, 1-13, Doi 10.1016/S1010-6030(99)00155-0, **1999**.

Madsen, D., Larsen, J., Jensen, S. K., Keiding, S. R., and Thogersen, J.: The primary photodynamics of aqueous nitrate: Formation of peroxynitrite, Journal of the American Chemical Society, 125, 15571-15576, Doi 10.1021/Ja030135f, **2003**.

Marcus, R. A.: Mass-independent oxygen isotope fractionation in selected systems. Mechanistic considerations, Adv Quantum Chem, 55, 5-19, Doi 10.1016/S0065-3276(07)00202-X, **2008**.

Mariotti, A., Mariotti, F., and Amarger, N.: The Use of Natural N-15 Isotopic Tracing for the Measurement of Nitrogen Symbiotic Fixation, Physiol Veg, 21, 279-291, **1983**.

Mark, G., Korth, H. G., Schuchmann, H. P., and vonSonntag, C.: The photochemistry of aqueous nitrate ion revisited, J Photoch Photobio A, 101, 89-103, Doi 10.1016/S1010-6030(96)04391-2, **1996**.

Masson-Delmotte, V., Hou, S., Ekaykin, A., and Jouzel, J. a. A., A. and Bernardo, R. T. and Bromwich, D. and Cattani, O. and Delmotte, M. and Falourd, S. and Frezzotti, M. and Gallée, H. and Genoni, L. and Isaksson, E. and Landais, A. and Helsen, M. M. and Hoffmann, G. and Lopez, J. and Morgan, V. and Motoyama, H. and Noone, D. and Oerter, H. and Petit, J. R. and Royer, A. and Uemura, R. and Schmidt, G. A. and Schlosser, E. and Simões, J. C. and Steig, E. J. and Stenni, B. and Stievenard, M. and van den Broeke, M. R. and van de Wal, R. S. W. and van de Berg, W. J. and Vimeux, F. and White, J. W. C.: A Review of Antarctic Surface Snow Isotopic Composition: Observations, Atmospheric Circulation, and Isotopic Modeling*, Journal of Climate, 21, 3359--3387, 10.1175/2007JCLI2139.1, **2008**.

Mauersberger, K., Lammerzahl, P., and Krankowsky, D.: Stratospheric ozone isotope enrichments-revisited, Geophysical Research Letters, 28, 3155-3158, **2001**.

Mayewski, P. A., and Legrand, M. R.: Recent Increase in Nitrate Concentration of Antarctic Snow, Nature, 346, 258-260, **1990**.

McCabe, J. R., Boxe, C. S., Colussi, A. J., Hoffmann, M. R., and Thiemens, M. H.: Oxygen isotopic fractionation in the photochemistry of nitrate in water and ice, J Geophys Res-Atmos, 110, Artn D15310 Doi 10.1029/2004jd005484, **2005a**.

McCabe, J. R., Boxe, C. S., Colussi, A. J., Hoffmann, M. R., and Thiemens, M. H.: dOxygen isotopic fractionation in the photochemistry of nitrate in water and ice, J Geophys Res-Atmos, 110, Artn D15310 Doi 10.1029/2004jd005484, **2005b**.

McCabe, J. R., Thiemens, M. H., and Savarino, J.: A record of ozone variability in South Pole Antarctic snow: Role of nitrate oxygen isotopes, J Geophys Res-Atmos, 112, D12303 10.1029/2006jd007822, **2007**.

McNeill, V. F., Grannas, A. M., Abbatt, J. P. D., Ammann, M., Ariya, P., Bartels-Rausch, T., Dominé, F., Donaldson, D. J., Guzman, M. I., Heger, D., Kahan, T. F., Klan, P., Masclin, S., Toubin, C., and Voisin, D.: Organics in environmental ices: sources, chemistry, and impacts, Atmospheric Chemistry and Physics, 12, 9653-9678, Doi 10.5194/Acp-12-9653-2012, **2012**.

Michalski, G., Savarino, J., Bohlke, J. K., and Thiemens, M.: Determination of the total oxygen isotopic composition of nitrate and the calibration of a Delta O-17 nitrate reference material, Analytical Chemistry, 74, 4989-4993, 10.1021/ac0256282, **2002**.

Michalski, G., Scott, Z., Kabiling, M., and Thiemens, M. H.: First measurements and modeling of Delta O-17 in atmospheric nitrate, Geophysical Research Letters, 30, 1870 10.1029/2003gl017015, **2003**.

Michalski, G., and Bhattacharya, S. K.: The role of symmetry in the mass independent isotope effect in ozone, Proceedings of the National Academy of Sciences of the United States of America, 106, 5493-5496, 10.1073/pnas.0812755106, **2009**.

Miller, C. E.: Photo-induced isotopic fractionation of stratospheric nitrous oxide., Abstr Pap Am Chem S, 219, U312-U312, **2000**.

Miller, C. E., and Yung, Y. L.: Photo-induced isotopic fractionation, J Geophys Res-Atmos, 105, 29039-29051, **2000**.

Miller, M. F.: Isotopic fractionation and the quantification of O-17 anomalies in the oxygen three-isotope system: an appraisal and geochemical significance, Geochimica Et Cosmochimica Acta, 66, 1881-1889, **2002**.

Morin, S., Savarino, J., Bekki, S., Cavender, A., Shepson, P. B., and Bottenheim, J. W.: Major influence of BrO on the NOx and nitrate budgets in the Arctic spring, inferred

from Delta O-17(NO3-) measurements during ozone depletion events, Environmental Chemistry, 4, 238-241, 10.1071/en07003, **2007a**.

Morin, S., Savarino, J., Bekki, S., Gong, S., and Bottenheim, J. W.: Signature of Arctic surface ozone depletion events in the isotope anomaly (Delta O-17) of atmospheric nitrate, Atmospheric Chemistry and Physics, 7, 1451-1469, **2007b**.

Morin, S., Savarino, J., Frey, M. M., Yan, N., Bekki, S., Bottenheim, J. W., and Martins, J. M. F.: Tracing the Origin and Fate of NO(x) in the Arctic Atmosphere Using Stable Isotopes in Nitrate, Science, 322, 730-732, Doi 10.1126/Science.1161910, **2008a**.

Morin, S., Savarino, J., Frey, M. M., Yan, N., Bekki, S., Bottenheim, J. W., and Martins, J. M. F.: Tracing the Origin and Fate of NOx in the Arctic Atmosphere Using Stable Isotopes in Nitrate, Science, 322, 730-732, Doi 10.1126/Science.1161910, **2008b**.

Morin, S., Savarino, J., Frey, M. M., Dominé, F., Jacobi, H. W., Kaleschke, L., and Martins, J. M. F.: Comprehensive isotopic composition of atmospheric nitrate in the Atlantic Ocean boundary layer from 65 degrees S to 79 degrees N, J Geophys Res-Atmos, 114, D05303 10.1029/2008jd010696, **2009**.

Morin, S., Sander, R., and Savarino, J.: Simulation of the diurnal variations of the oxygen isotope anomaly (Δ17O) of reactive atmospheric species, Atmos. Chem. Phys., 11, 3651-3673, 10.5194/acp-11-3653-2011, **2011**.

Morton, J., Barnes, J., Schueler, B., and Mauersberger, K.: Laboratory studies of heavy ozone, J Geophys Res-Atmos, 95, 901-907, **1990**.

Muller, P.: Glossary of Terms Used in Physical Organic-Chemistry, Pure Appl Chem, 66, 1077-1184, Doi 10.1351/Pac199466051077, **1994**.

Nakamura, K., Nakawo, M., Ageta, Y., Goto-Azuma, K., and Kamiyama, K.: Post-depositional loss of nitrate in surface snow layers of the Antarctic Ice Sheet, Bulletin of glaciological research, 17, 11-16, **2000**.

Nanbu, S., and Johnson, M. S.: Analysis of the ultraviolet absorption cross sections of six isotopically substituted nitrous oxide species using 3D wave packet propagation, Journal of Physical Chemistry A, 108, 8905-8913, Doi 10.1021/Jp048853r, **2004**.

Ndengue, S. A., Gatti, F., Schinke, R., Meyer, H. D., and Jost, R.: Absorption Cross Section of Ozone Isotopologues Calculated with the Multiconfiguration Time-Dependent Hartree (MCTDH) Method: I. The Hartley and Huggins Bands, Journal of Physical Chemistry A, 114, 9855-9863, Doi 10.1021/Jp103266m, **2010**.

Peiro-Garcia, J., and Nebot-Gil, I.: Ab initio study of the mechanism and thermochemistry of the atmospheric reaction NO+O-3-NO2+O-2, Journal of Physical Chemistry A, 106, 10302-10310, 10.1021/jp020422q, **2002**.

Peiro-Garcia, J., and Nebot-Gil, I.: Ab initio study of the mechanism of the atmospheric reaction: NO2+O-3 -> NO3+O-2, Journal of Computational Chemistry, 24, 1657-1663, 10.1002/jcc.10299, **2003**.

Perrier, S., Houdier, S., Domine, F., Cabanes, A., Legagneux, L., Sumner, A. L., and Shepson, P. B.: Formaldehyde in Arctic snow. Incorporation into ice particles and evolution in the snowpack, Atmospheric Environment, 36, 2695-2705, Pii S1352-2310(02)00110-3 Doi 10.1016/S1352-2310(02)00110-3, **2002**.

Petit, J. R., Basile, I., Leruyuet, A., Raynaud, D., Lorius, C., Jouzel, J., Stievenard, M., Lipenkov, V. Y., Barkov, N. I., Kudryashov, B. B., Davis, M., Saltzman, E., and Kotlyakov, V.: Four climate cycles in Vostok ice core, Nature, 387, 359-360, Doi 10.1038/387359a0, **1997**.

Platt, U., and LeBras, G.: Influence of DMS on the O-X-NOY partitioning and the NOX distribution in the marine background atmosphere, Geophysical Research Letters, 24, 1935-1938, Doi 10.1029/97gl01821, **1997**.

Qiu, R., Green, S. A., Honrath, R. E., Peterson, M. C., Lu, Y., and Dziobak, M.: Measurements of J(NO3)(-) in snow by nitrate-based actinometry, Atmospheric Environment, 36, 2563-2571, Pii S1352-2310(02)00117-6
Doi 10.1016/S1352-2310(02)00117-6, **2002**.

Roberts, J. M.: THE ATMOSPHERIC CHEMISTRY OF ORGANIC NITRATES, Atmospheric Environment Part a-General Topics, 24, 243-287, **1990**.

Röckmann, T., Kaiser, J., Crowley, J. N., Brenninkmeijer, C. A. M., and Crutzen, P. J.: The origin of the anomalous or "mass-independent" oxygen isotope fractionation in tropospheric N2O, Geophysical Research Letters, 28, 503-506, **2001**.

Röthlisberger, R., Hutterli, M. A., Sommer, S., Wolff, E. W., and Mulvaney, R.: Factors controlling nitrate in ice cores: Evidence from the Dome C deep ice core, J Geophys Res-Atmos, 105, 20565-20572, Doi 10.1029/2000jd900264, **2000**.

Röthlisberger, R., Hutterli, M. A., Wolff, E. W., Mulvaney, R., Fischer, H., Bigler, M., Goto-Azuma, K., Hansson, M. E., Ruth, U., Siggaard-Andersen, M. L., and Steffensen, J. P.: Nitrate in Greenland and Antarctic ice cores: a detailed description of post-depositional processes, Ann Glaciol-Ser, 35, 209-216, **2002**.

Rozanski, K., Froehlich, K., and Mook, W. G.: Environmental isotopes in the hydrological cycle: Principles and applications, edited by: Mook, W. G., UNESCO/IAEA, Paris, **2001**.

Sato, K., Takenaka, N., Bandow, H., and Maeda, Y.: Evaporation loss of dissolved volatile substances from ice surfaces, Journal of Physical Chemistry A, 112, 7600-7607, Doi 10.1021/Jp075551r, **2008**.

Savarino, J., and Thiemens, M. H.: Mass-independent oxygen isotope (O-16, O-17, O-18) fractionation found in H-x, O-x reactions, Journal of Physical Chemistry A, 103, 9221-9229, Doi 10.1021/Jp991221y, **1999**.

Savarino, J., Lee, C. C. W., and Thiemens, M. H.: Laboratory oxygen isotopic study of sulfur (IV) oxidation: Origin of the mass-independent oxygen isotopic anomaly in atmospheric sulfates and sulfate mineral deposits on Earth, J Geophys Res-Atmos, 105, 29079-29088, **2000**.

Savarino, J., Kaiser, J., Morin, S., Sigman, D. M., and Thiemens, M. H.: Nitrogen and oxygen isotopic constraints on the origin of atmospheric nitrate in coastal Antarctica, Atmospheric Chemistry and Physics, 7, 1925-1945, **2007**.

Savarino, J., Bhattacharya, S. K., Morin, S., Baroni, M., and Doussin, J. F.: The NO+O(3) reaction: A triple oxygen isotope perspective on the reaction dynamics and atmospheric implications for the transfer of the ozone isotope anomaly, J Chem Phys, 128, **2008**.

Savarino, J., Morin, S., Erbland, J., Grannec, F., Patey, M. D., Vicars, W. C., Alexander, B., and Achterberg, E. P.: Isotopic composition of atmospheric nitrate in a tropical marine boundary layer, PNAS, **2013**.

Schmidt, J. A., Johnson, M. S., and Schinke, R.: Isotope effects in N2O photolysis from first principles, Atmospheric Chemistry and Physics, 11, 8965-8975, Doi 10.5194/Acp-11-8965-2011, **2011**.

Seinfeld, J. H., and Pandis, S. N.: Atmospheric Chemistry and Physics - From Air Pollution to Climate Change, 2 ed., John Wiley & Sons, 1203 pp., **2006**.

Sigman, D. M., Casciotti, K. L., Andreani, M., Barford, C., Galanter, M., and Bohlke, J. K.: A bacterial method for the nitrogen isotopic analysis of nitrate in seawater and freshwater, Analytical Chemistry, 73, 4145-4153, 2001.

Silva, S. R., Kendall, C., Wilkison, D. H., Ziegler, A. C., Chang, C. C. Y., and Avanzino, R. J.: A new method for collection of nitrate from fresh water and the analysis of

nitrogen and oxygen isotope ratios, J Hydrol, 228, 22-36, Doi 10.1016/S0022-1694(99)00205-X, **2000**.

Simpson, W. R., King, M. D., Beine, H. J., Honrath, R. E., and Zhou, X. L.: Radiation-transfer modeling of snow-pack photochemical processes during ALERT 2000, Atmospheric Environment, 36, 2663-2670, Pii S1352-2310(02)00124-3 Doi 10.1016/S1352-2310(02)00124-3, **2002**.

Simpson, W. R., von Glasow, R., Riedel, K., Anderson, P., Ariya, P., Bottenheim, J., Burrows, J., Carpenter, L. J., Friess, U., Goodsite, M. E., Heard, D., Hutterli, M., Jacobi, H. W., Kaleschke, L., Neff, B., Plane, J., Platt, U., Richter, A., Roscoe, H., Sander, R., Shepson, P., Sodeau, J., Steffen, A., Wagner, T., and Wolff, E.: Halogens and their role in polar boundary-layer ozone depletion, Atmospheric Chemistry and Physics, 7, 4375-4418, **2007**.

Strauss, H., Peters, M., Farquhar, J., Johnston, D., Wiechert, U., and Stogbauer, A.: Multiple sulphur isotopes reflecting compositional changes in Earth's early atmosphere, Geochimica Et Cosmochimica Acta, 71, A978-A978, **2007**.

Taylor, J. R.: An Introduction to Error Analysis: The Study of Uncertainties in Physical Measurements, 2nd ed., **1997**.

Thiemens, M. H., and Heidenreich, J. E.: The mass-independent fractionation of oxygen-a novel isotope effect and its possible cosmochemical implications, Science, 219, 1073-1075, **1983**.

Thiemens, M. H., and Jackson, T.: Production of Isotopically Heavy Ozone by Ultraviolet-Light Photolysis of O-2, Geophysical Research Letters, 14, 624-627, Doi 10.1029/Gl014i006p00624, **1987**.

Thiemens, M. H., and Jackson, T.: New Experimental-Evidence for the Mechanism for Production of Isotopically Heavy O-3, Geophysical Research Letters, 15, 639-642, Doi 10.1029/Gl015i007p00639, **1988**.

Thiemens, M. H., and Jackson, T.: Pressure dependency for heavy isotope enrichment in ozone formation, Geophysical Research Letters, 17, 717-719, **1990**.

Thiemens, M. H.: Atmosphere science - Mass-independent isotope effects in planetary atmospheres and the early solar system, Science, 283, 341-345, **1999**.

Thiemens, M. H.: History and applications of mass-independent isotope effects, Annual Review of Earth and Planetary Sciences, 34, 217-262, 10.1146/annurev.earth.34.031405.125026, **2006**.

Traversi, R., Becagli, S., Castellano, E., Cerri, O., Morganti, A., Severi, M., and Udisti, R.: Study of Dome C site (East Antartica) variability by comparing chemical stratigraphies, Microchem J, 92, 7-14, Doi 10.1016/J.Microc.2008.08.007, **2009**.

Urbini, S., Frezzotti, M., Gandolfi, S., Vincent, C., Scarchilli, C., Vittuari, L., and Fily, M.: Historical behaviour of Dome C and Talos Dome (East Antarctica) as investigated by snow accumulation and ice velocity measurements, Global Planet Change, 60, 576-588, Doi 10.1016/J.Gloplacha.2007.08.002, **2008**.

Urey, H. C.: The Thermodynamic Properties of Isotopic SUbstances, Journal of the Chemical Society, 562-581, **1947**.

Vicars, W. C., Bhattacharya, S. K., Erbland, J., and Savarino, J.: Measurement of the 17O-excess of tropospheric ozone using a nitrite-coated filter, Rapid Commun Mass Sp, 26, 1219-1231, Doi 10.1002/Rcm.6218, **2012**.

Wagenbach, D., Legrand, M., Fischer, H., Pichlmayer, F., and Wolff, E. W.: Atmospheric near-surface nitrate at coastal Antarctic sites, Journal of Geophysical Research, 103, 11007, 10.1029/97jd03364, **1998**.

Wang, Y. H., Choi, Y., Zeng, T., Davis, D., Buhr, M., Huey, L. G., and Neff, W.: Assessing the photochemical impact of snow NOx emissions over Antarctica during ANTCI 2003, Atmospheric Environment, 41, 3944-3958, Doi 10.1016/J.Atmosenv.2007.01.056, **2007**.

Warren, S. G.: Optical-Properties of Snow, Rev Geophys, 20, 67-89, Doi 10.1029/Rg020i001p00067, **1982**.

Warren, S. G., Brandt, R. E., and Grenfell, T. C.: Visible and near-ultraviolet absorption spectrum of ice from transmission of solar radiation into snow, Applied optics, 45, 5320-5334, http://dx.doi.org/10.1364/AO.45.005320, **2006**.

Werner, R. A., and Brand, W. A.: Referencing strategies and techniques in stable isotope ratio analysis, Rapid Commun Mass Sp, 15, 501-519, Doi 10.1002/Rcm.258, **2001**.

Wolff, E. W.: Nitrate in Polar Ice, Ice core studies of global biogeochemical cycles, **1995a**.

Wolff, E. W.: Nitrate in Polar Ice, Ice core studies of global biogeochemical cycles, edited by: Delmas, R. J., Springer Verlag, Berlin, 195-224 pp., **1995b**.

Wolff, E. W., Jones, A. E., Martin, T. J., and Grenfell, T. C.: Modelling photochemical NOX production and nitrate loss in the upper snowpack of Antarctica, Geophysical Research Letters, 29, 10.1029/2002gl015823, **2002**.

Wolff, E. W., Jones, A. E., Bauguitte, S. J. B., and Salmon, R. A.: The interpretation of spikes and trends in concentration of nitrate in polar ice cores, based on evidence from snow and atmospheric measurements, Atmospheric Chemistry and Physics, 8, 5627-5634, Doi 10.5194/Acp-8-5627-2008, **2008**.

Wolff, E. W., Barbante, C., Becagli, S., Bigler, M., Boutron, C. F., Castellano, E., de Angelis, M., Federer, U., Fischer, H., Fundel, F., Hansson, M., Hutterli, M., Jonsell, U., Karlin, T., Kaufmann, P., Lambert, F., Littot, G. C., Mulvaney, R., Rothlisberger, R., Ruth, U., Severi, M., Siggaard-Andersen, M. L., Sime, L. C., Steffensen, J. P., Stocker, T. F., Traversi, R., Twarloh, B., Udisti, R., Wagenbach, D., and Wegner, A.: Changes in environment over the last 800,000 years from chemical analysis of the EPICA Dome C ice core, Quaternary Sci Rev, 29, 285-295, Doi 10.1016/J.Quascirev.2009.06.013, **2010.**

Young, E. D., Galy, A., and Nagahara, H.: Kinetic and equilibrium mass-dependent isotope fractionation laws in nature and their geochemical and cosmochemical significance, Geochimica Et Cosmochimica Acta, 66, 1095-1104, Pii S0016-7037(01)00832-8 Doi 10.1016/S0016-7037(01)00832-8, **2002**.

Yung, Y. L., Demore, W. B., and Pinto, J. P.: Isotopic Exchange between Carbon-Dioxide and Ozone Via O(1d) in the Stratosphere, Geophysical Research Letters, 18, 13-16, Doi 10.1029/90gl02478, **1991**.

Yung, Y. L., and Miller, C. E.: Isotopic fractionation of stratospheric nitrous oxide, Science, 278, 1778-1780, Doi 10.1126/Science.278.5344.1778, **1997**.

Zahn, D.: Exploring the mechanisms of reactions in solution from transition path sampling molecular dynamics simulations, J Chem Theory Comput, 2, 107-114, Doi 10.1021/Ct0501755, **2006**.

Zatko, M. C., Grenfell, T. C., Alexander, B., Doherty, S. J., Thomas, J. L., and Yang, X.: The influence of snow grain size and impurities on the vertical profiles of actinic flux and associated NOx emissions on the Antarctic and Greenland ice sheets, Atmos. Chem. Phys. , 13, 3547-3567, doi:10.5194/acp-13-3547-2013, **2013**.

Zhang, J. S., Miau, T. T., and Lee, Y. T.: Crossed molecular beam study of the reaction Br+O-3, Journal of Physical Chemistry A, 101, 6922-6930, **1997**.

Zhou, M. Y., Zhang, Z. H., Zhong, S. Y., Lenschow, D., Hsu, H. M., Sun, B., Gao, Z. Q., Li, S. M., Bian, X. D., and Yu, L. J.: Observations of near-surface wind and temperature structures and their variations with topography and latitude in East Antarctica, J Geophys Res-Atmos, 114, Artn D17115 Doi 10.1029/2008jd011611, **2009**.

Zhou, X. L., Beine, H. J., Honrath, R. E., Fuentes, J. D., Simpson, W., Shepson, P. B., and Bottenheim, J. W.: Snowpack photochemical production of HONO: a major source of OH in the Arctic boundary layer in springtime, Geophysical Research Letters, 28, 4087-4090, **2001**.

Zhu, C. Z., Xiang, B., Chu, L. T., and Zhu, L.: 308 nm Photolysis of Nitric Acid in the Gas Phase, on Aluminum Surfaces, and on Ice Films, Journal of Physical Chemistry A, 114, 2561-2568, Doi 10.1021/Jp909867a, **2010**.

Annex A

Ag_2O: A new non-mass dependent standard material for oxygen isotope measurements

Tesfaye Ayalneh Berhanu, Joël Savarino, Amaelle Landais, Frédéric Prié, Renato Winkler, Thomas Röckmann, Marion Früchtl, Jan Kaiser, Thomas Blunier, Corentin Reutenauer

The main objective of this part of the thesis was to prepare a reference material for oxygen isotope measurements, a commitment of the INTRAMIF network. The ^{17}O-excess (expressed mathematically as $\Delta^{17}O = \delta^{17}O - 0.52 \times \delta^{18}O$), which is the quantity to describe the deviation from the formal mass dependent rule of $\delta^{17}O \approx 0.52 \times \delta^{18}O$, has been used as a tracer in various scientific studies (See previous chapters for details). Considering the broad scientific research on oxygen non-mass dependent fractionation and its associated effects, an appropriate reference material with non-zeo ^{17}O-excess becomes essential. In this section, we present the experimental approach, the steps followed, the difficulties faced, and finally our recommendations for the production of such reference material.

The experimental studies were conducted at LGGE, and isotopic measurements were compared among other laboratories within the network. The preliminary results from this study have been presented at the INTRAMIF annual meeting in August 2012 in Grenoble and at ISI2012 in Washington DC, USA.

6.1. Background

Stable isotope ratios have been used as an important tool in various scientific areas such as paleoclimate, geochemistry, forensics and so forth.
The isotopic composition of a given sample is expressed in terms of the delta notation (δ), which is the number ratio of the least abundant to the most abundant atom in the given sample (R_{sample}) with respect to a reference material ($R_{reference}$) (mostly expressed in units of per mil, ‰) as:

$$\delta = \left(\left(\frac{R_{sample}}{R_{reference}} \right) - 1 \right) \times 1000 \qquad (6.1)$$

Reference materials consists of natural minerals or compounds usually used in isotope geochemistry with desired isotopic composition, chemical purity, stability and homogeneity (Gonfiantini et al., 1993). Some of the advantages of using reference materials to measure and report the isotopic composition of a given compound are (Criss, 1999):

- As it is difficult to measure the absolute abundance of heavy isotopes due to their rare availability (for eg., D/H ~ 0.00015), performing a relative measurement with a reference of known/accepted isotopic composition will make it easier
- It can account for system variability during isotopic measurements
- Interlaboratory comparisons can be made relatively easily leading to interpretations of results from different labs coherent

Hence, the measured (raw) δ-values for a given compound will be normalized to internationally recognized scales of interest, which are defined using primary reference materials defined below.

Reference materials can be classified into primary (Reference), secondary (calibration), intercomparison materials and in-house standards (Gonfiantini et al., 1993;Carter and Barwick, 2011) (Note that sometimes nomenclature may vary).

6.1.1. Primary reference Materials (PRMs)

These are materials which define the origin of the δ-scale and they have internationally defined δ-values so that there is no need to know their actual isotope ratios (R). They also enable direct comparison between measurements from different laboratories.

Standard Mean Ocean Water (SMOW) was a hypothetical water sample that never physically existed, and was defined by Craig (1961) as reference for $^{2}H/^{1}H$ and $^{18}O/^{16}O$ determinations. Peedee Belemnite (PDB), which consisted of calcium carbonate, is also used to express the natural variation in Carbon isotopes. As SMOW does not have a unique definition and PDB was exhausted, the International Atomic Energy Agency (IAEA) decided to change reporting the isotopic measurements of H, C and O with respect to these standards, and introduced the VSMOW scale for $\delta^{2}H$ and $\delta^{18}O$ and the

VPDB scale for $\delta^{13}C$ measurements (Coplen, 1994). Furthermore, as $\delta^{2}H$ and $\delta^{18}O$ values of VSMOW lie closer to the upper end of the range of abundances of ^{2}H and ^{18}O in naturally occurring materials, the agency recommended $\delta^{2}H$ and $\delta^{18}O$ values at the lower end of the range using a new reference material, Standard Light Antarctic Precipitation (SLAP). Hence, the oxygen and hydrogen isotopic abundances of all isotopic compounds should be normalized using SLAP. Accordingly, a conversion scale was recommended such that:

- $\delta^{2}H_{SLAP/VSMOW} = -428$ ‰
- $\delta^{13}C_{NBS\text{-}18/VPDB} = 1.95$ ‰
- $\delta^{18}O_{SLAP/VSMOW} = -55$ ‰

Note that there is no uncertainty on the isotopic values of the PRMs. It was also suggested to use the standard scale conversion from one scale to another. However, this conversion is not additive but recalculated using equation 5.2. For sample 'a' measured with respect to 'b' and to be normalized on VSMOW scale, the conversion equation can be given by:

$$\delta^{18}O_{a/VSMOW} = \delta^{18}O_{a/b} + \delta^{18}O_{b/VSMOW} + 10^{-3} \times \delta^{18}O_{a/b}\delta^{18}O_{b/VSMOW} \qquad (5.2)$$

Atmospheric nitrogen (Air_N_2) is the isotopic scale for nitrogen isotopic ratio ($^{15}N/^{14}N$), which is prepared by deoxygenation and drying of atmospheric nitrogen (Mariotti et al., 1983). Its wide homogeneity in isotopic composition, abundant availability and easiness to be prepared were main advantageous characteristics of this standard.

However, some of the PRMs are typically valuable materials and may not always be in the appropriate chemical form for simple isotopic standardization or insufficient to fix the scale contraction/expansion of the analytical method employed. These limitations of PRMs made it essential to produce additional reference materials known as secondary reference materials.

6.1.2. Secondary Reference Materials (SRMs)

These are natural or synthetic reference materials, which are carefully anchored to the PRMs so that samples can be accurately normalized to an international scale. These materials have internationally agreed and adopted δ-values but associated with uncertainties (Carter and Barwick, 2011). The IAEA distributes these materials and provides full documentation on their δ-value. A regular update on these values could be obtained from its webpage at www.nucleus.iaea.org. Some of the secondary reference materials distributed by the agency are given in Table 1.

Table 1. List of some of the secondary reference materials distributed by IAEA

Description	NIST RM	Nature	$\delta^{15}N/‰$	$\delta^{18}O/‰$	SD
USGS-32	8558	Potassium nitrate	+180		1
USGS-34	8568	Potassium nitrate	-1.8		0.2
USGS-35	8569	Sodium nitrate	+2.7		0.2
IAEA-602		Benzoic acid		+71.4	0.5
USGS-43		Indian hair		+14.11	0.1
NBS-18	8543	Calcite		-23.2	0.1

6.1.3. Intercomparison materials

These are materials of different chemical nature and isotopic composition prepared to test quality of measurements and monitor long term reproducibility of sample preparation between participating laboratories (Carter and Barwick, 2011). The procedures are managed by Forensic Isotope Ratio Mass Spectrometry (FIRMS, http://www.forensic-isotopes.org/) and the inter laboratory comparison is practiced on yearly basis.

6.1.4. In-house standards

These are reference materials which can be used in daily basis after being calibrated using PRMs or SRMs which are scarce materials for daily use. However, there are a number of requirements for a given material to be considered as appropriate in-house standard. These include the sample should be (Carter and Barwick, 2011):

- Homogeneous
- Abundantly available or easily replaceable
- Stable during storage
- Non-hygroscopic (mainly for H and O measurements)
- Easy and safe to store, handle and transport

6.2. Aim of the study

Currently, except USGS 35 there is no reference material with non-mass dependent nature for oxygen isotopes measurement. USGS 35 was prepared from purified $NaNO_3$ from natural ore in Atacama desert, Chile (Böhlke et al., 2003). This material is widely used for analysis of nitrate samples, and it has isotopic values of $\delta^{17}O$ = 51.5 ‰ and $\delta^{18}O$ = 57.5 ‰. However, sodium nitrate is not in appropriate chemical form practical for applications in fields of isotope geochemistry. In particular, its conversion to O_2, the main working gas to measure the ^{17}O-excess, is difficult.

In order to fill this gap in appropriate reference material with accurately known ^{17}O-excess, Ag_2O is proposed and tested in this experimental study.

The choice of Ag_2O is based on various points including:

- It can be easily decomposed and releases its oxygen atoms

- The pure oxygen gas obtained is a suitable gas for oxygen isotopic measurement (little isobaric interference)
- As it is synthesized from industrial products ($AgNO_3$), it can be produced in large quantities and being scarce or becoming exhausted is not an issue
- It is expected to be homogeneous
- It is easy to produce, handle and transport and potentially stable during storage as it is a solid material

In this PhD study, we have prepared and characterized Ag_2O and perform an interlaboratory comparison between the measurements in Grenoble (LGGE) and collaborating laboratories in Utrecht (IMAU), Paris (LSCE), and Copenhagen (CIC).

6.3. Method development and technical progress

Step 1: Preparation of Ag_2O samples

As a first approach, we have prepared test samples of Ag_2O in very small quantities (typically 1-2 g sample). In this experimental study, solid silver oxide (Ag_2O) was prepared from commercial silver nitrate ($AgNO_3$) (Sigma Aldrich), enriched water (^{16}O = 34.4 %, ^{17}O = 10.6 % and ^{18}O = 55 %, Cambridge Isotope Laboratory) and excess sodium hydroxide (1M NaOH) via R.6.1.

$$2AgNO_3 + 2NaOH \rightarrow 2NaNO_3 + Ag_2O\downarrow + H_2O \qquad (R.6.1)$$

We have mixed 20 µL enriched water was mixed with 130 ml of 1M NaOH, and the mixture was left to equilibrate while stirring for 8 days. The duration of mixing was optimized based on tests conducted with different durations.

The purpose of using enriched water is to incorporate enriched oxygen atoms into Ag_2O so that during its thermal decomposition, oxygen gas with heavy isotopes and accurately known isotopic composition can be obtained. In this way, the ^{17}O-excess can be manipulated to the desired range. In this experimental study, $\Delta^{17}O \approx 20$ ‰ was targeted and the amount of enriched water was determined applying a mathematical calculation during mixing of water solutions with different isotopic composition.

After 8 days, 1-2 g $AgNO_3$ was added slowly and it was left to mix while stirring for additional 11 days. During the entire experiment, the preparation beaker was covered with an Al foil to avoid light and contamination. Again the duration of mixing was optimized based on previous trial experiments. A grayish precipitate was formed immediately after addition of silver nitrate.

Finally, the Ag_2O precipitate was filtered and the solid precipitate was washed with MQ water repeatedly to remove nitrate left from silver nitrate and the excess sodium hydroxide. Complete removal of nitrate was confirmed by measurement of nitrate (QuAAtro nitrate analyzer) which was below 50 ppb.

The Ag_2O precipitate was dried in an oven at 180°C overnight. Then, the Ag_2O samples were carefully transferred into small amber bottles and stored in a desiccator to avoid moisture.

Step 2: Analysis of Ag_2O samples

Before sample analysis, calibration of the mass spectrometer was conducted to determine the amount of oxygen gas produced during decomposition of Ag_2O.

Determination of oxygen yield and calibration of the mass spectrometer

The percentage yield of oxygen gas during thermal decomposition of Ag_2O is calculated based on the molar ratios. Accordingly, during Ag_2O decomposition (R.6.2), for every mole of silver oxide decomposed half a mole of oxygen will be produced i.e. for 100 μmole of Ag_2O in our experiment case, 50 μmole of oxygen is expected.

$$Ag_2O \rightarrow 2Ag + 1/2O_2 \qquad \text{(R.6.2)}$$

In order to determine the amount of oxygen produced, an online technique of calibration was followed and discussed below.

A known amount of pure oxygen gas (50-120 μmole) was filled into a sample tube and introduced to the IRMS dual inlet mode inlet via expansion. The sample bellow is fully expanded (100 % open) during this operation. After few minutes, when the pressure reading in the bellow was stable, all the valves were closed and the pressure reading in the sample bellow was noted. Finally, the valve leading towards the ion source of the MS was opened and the $^{32}O_2$ signal was noted. Based on these measurements, a calibration line of sample amount (μmole), pressure of oxygen gas in the sample bellow (torr) and the $^{32}O_2$ signal (mV) was generated (Fig. 6.1). As the $^{32}O_2$ signal is more reliable method of calibration, it was used in this study to determine the approximate amount of oxygen produced from thermal decomposition of Ag_2O.

The Ag_2O samples were thermally decomposed by carefully transferring about 100 nmol of Ag_2O into a clean quarter inch tube (washed with MQ water, ethanol and acetone and dried overnight in an oven at 200 °C), which was sealed in one side. The tube was then connected to the sample inlet port at the mass spectrometer, and carefully evacuated. Then, a heater which was already at 550°C was connected directly to the quarter inch tube and gaseous products were transferred into the sample bellow, which can be monitored from the rise in pressure in the pressure gauge at the bellow. When decomposition is complete, pressure reading becomes stable, the sample bellow was isolated, and the pressure and $^{32}O_2$ signals were note. The isotopic composition ($\delta^{17}O$ and $\delta^{18}O$) of the oxygen gas were measured using MAT-253 IRMS in the dual inlet mode relative to LGGE#1(working gas at LGGE) with an isotopic composition of $\delta^{17}O$ = 3.533 ‰, $\delta^{18}O$ =7.522 ‰ calibrated versus VSMOW. However, the obtained isotopic compositions in multiple measurements were not reproducible. Additionally, the oxygen gas yield from thermal decomposition of Ag_2O was not consistent based on the molar ratio estimates. The obtained results for the experiments these experiments also showed very small ^{17}O-excess values than expected (about $1/10^{th}$ of the expected ^{17}O-excess value).

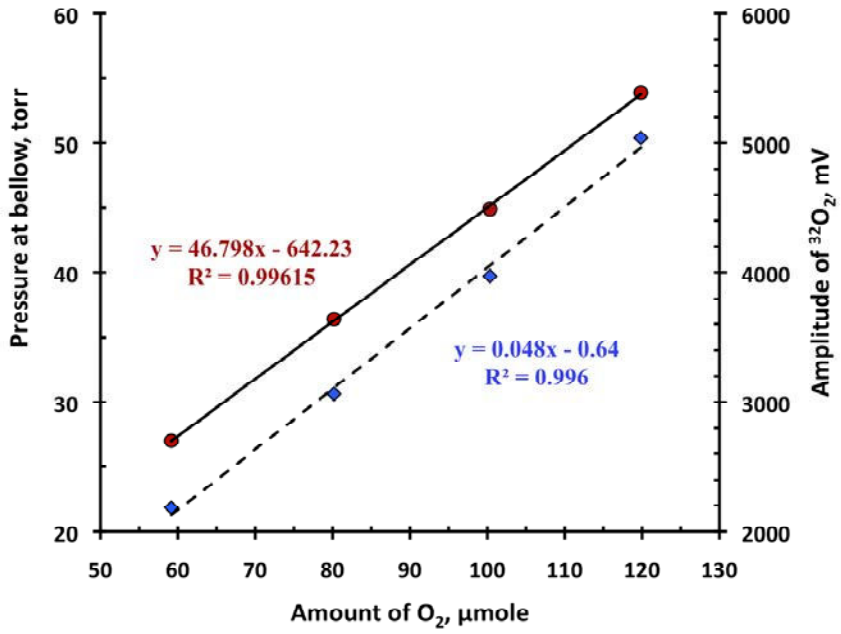

Figure 6.1. *Calibration line for amount of oxygen in micromoles versus oxygen gas pressure in sample bellow (left axis, brown) and $^{32}O_2$ signal for oxygen gas in sample bellow (right axis, blue). The linear correlation enables to determine the amount of oxygen gas yield during decomposition of Ag_2O.*

The CO_2 interference issue

In order to identify the reason behind very low ^{17}O-excess value than expected, an elemental scan was conducted for the oxygen gas produced. Accordingly, significantly big peaks were observed for CO_2 (mass = 44) in all the sample gases (Fig. 6.2). The sources of CO_2 in the oxygen samples could be either the Ag_2O itself or CO_2 leaking into the system. The latter was checked by analysing the oxygen reference gas which was introduced via the sample bellow and there was no CO_2 peak observed confirming the actual CO_2 source was the Ag_2O.

Ag_2O is a strong absorber of atmospheric CO_2 and has a wide application in space science and related fields to remove/recycle CO_2 (as CO_2 scrubber). The absorption of CO_2 in the presence of water can be described by R.6.3 to produce Ag_2CO_3 which can be decomposed thermally above 218°C via R.6.4 (Centnerszwer and Bruzs, 1925).

$$Ag_2O + CO_2 \rightarrow Ag_2CO_3 \qquad \text{(R.6.3)}$$

$$Ag_2CO_3 \rightarrow Ag_2O + CO_2 \qquad \text{(R.6.4)}$$

This implies that during thermal decomposition of Ag_2O, CO_2 is also generated along with O_2, and this can lead to interference and wrong measurements of the isotopic signature of oxygen from Ag_2O.

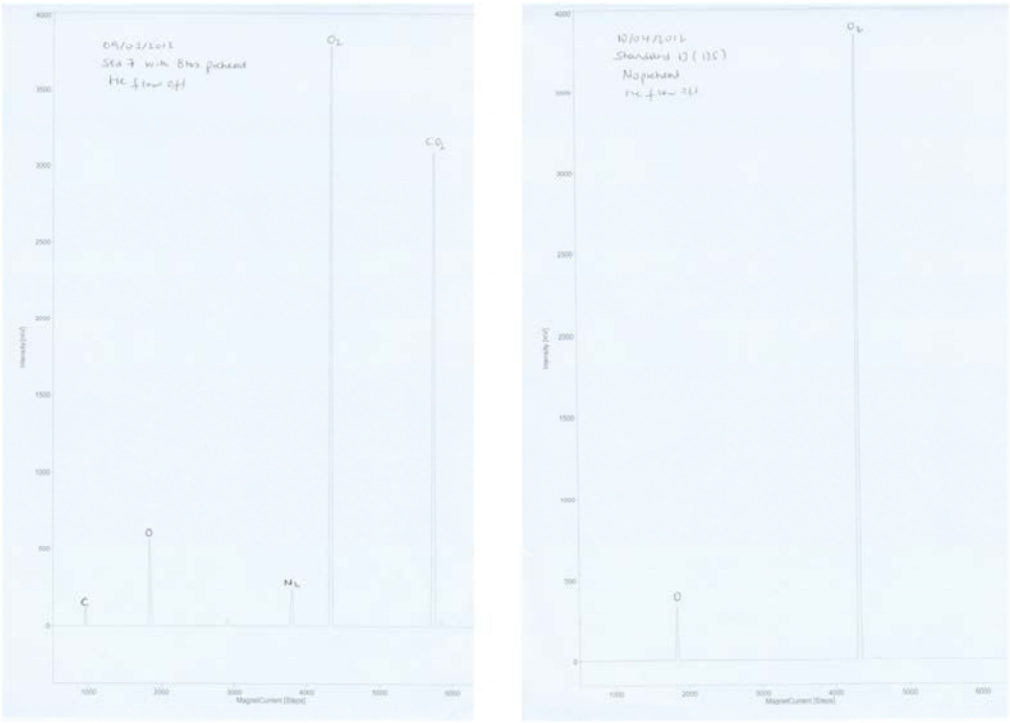

Figure 6.2. *The elemental scans for two oxygen gas samples produced from decomposed Ag_2O in the absence (left) and presence (right) of an Ascarite and Perchlorate traps. In the latter case, there are not observable peaks for C and CO_2.*

In order to prevent the interference associated with CO_2, an Ascarite trap (Granular CO_2 absorbent made of NaOH coated with non-fibrous Silicate) was placed at the top of the quarter inch tubing to remove the emitted CO_2 before entering to the MS for isotopic analysis. As reaction between Ascarite and CO_2 produces water (R.6.5), an additional water trap (Magnesium Perchlorate named simply Perchlorate) was added as shown in Fig. 6.3.

$$CO_2 + 2NaOH \rightarrow Na_2CO_3 + H_2O \qquad \text{(R.6.5)}$$

The Ascarite trap effectively removed the CO_2 produced from the thermal decomposition of silver oxide, and water produced during this step was successfully removed by the perchlorate trap. The elemental scans obtained from oxygen samples obtained in this way are shown in Fig. 6.2.

The general scheme of preparation of the reference silver oxide is summarized in the schematic in Fig. 6.4. Finally, the Ag_2O samples prepared with this procedure were also sent to collaborating laboratories of CIC, LSCE and IMAU for interlab comparison.

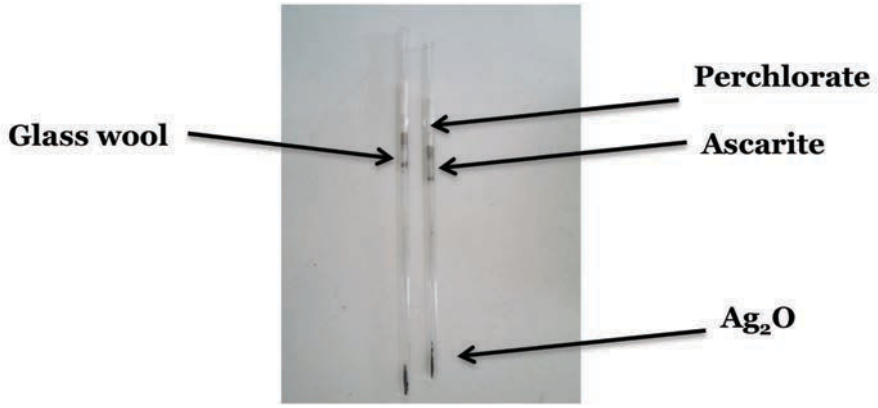

Figure 6.3. *Ag_2O transferred to a quarter inch tube at the bottom and the Ascarite and Perchlorate traps for CO_2 and H_2O respectively placed at the top each separated using a glass wool*

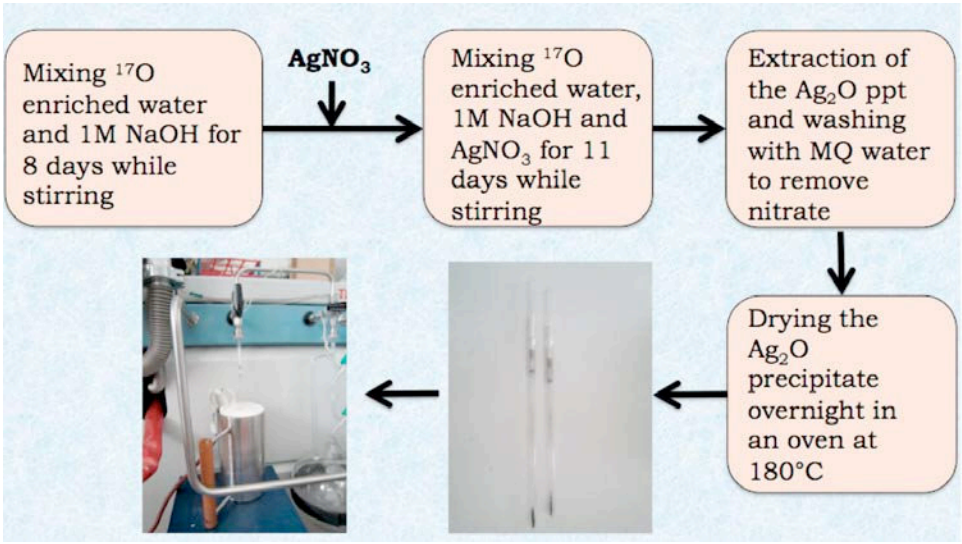

Figure 6.4. *A schematic of the steps followed during the production and analysis of Ag_2O*

6.4. Results and Discussion

6.4.1. Results

Based on the optimised technique of preparation of Ag_2O (shown in the schematic in Fig. 6.4), the oxygen gas produced from Ag_2O has the isotopic composition shown in table 5. These samples were also measured in other laboratories and their values are shown in this table. The Laboratory measurement manual used for these measurements is attached in the Annex.

Table 5. The isotopic composition of Ag_2O standard measured in our lab at LGGE and at other partner labs of LSCE (Paris) and IMAU (Utrecht)

Lab	δ^{17}**O/‰**	δ^{18}**O/‰**	Δ^{17}**O/‰**
LGGE	12.343	-6.169	15.551
	13.193	-5.321	15.960
	13.076	-5.605	15.991
mean	12.871±0.46	-5.698±0.43	15.834±0.25
LSCE	12.066	-5.156	14.747
	12.046	-5.153	14.726
	12.033	-5.142	14.708
mean	12.049±0.016	-5.150±0.007	14.730±0.020
LSCE*	12.904	-4.927	15.467
	12.893	-4.904	15.443
	12.876	-4.892	15.420
mean	12.905±0.014	-4.927±0.018	15.467±0.023
IMAU	10.746	-8.048	14.930
	11.500	-7.043	15.160
	11.041	-8.039	15.220
	10.999	-7.915	15.110
mean	10.970±0.16	-7.630±0.75	15.105±0.125

**LSCE: the measurement was done at LSCE using the reference gas from LGGE (LGGE#1)*

6.4.2. Discussion

The isotopic measurements are fairly reproducible within each lab considering the error bars. However, there exists a significant difference between the results from the three labs. The difference can be associated with:

- Systematic differences arising from differences between instruments, and sample handling and analysis
- Differences between working standards of each laboratory i.e. how well is the working standard of each laboratory calibrated to primary standards
- Stability of the Ag_2O during sample transportation and storage

Systematic difference

During analysis of the Ag_2O samples, there is always an error associated with its measurement. Besides the precision of a given measurement at a specific laboratory, additional errors can be introduced due to variability in sample handling and analysis. Even if a manual for sample handling and analysis was provided for each laboratory, these errors can be minimised but not avoided.

During the analysis of Ag_2O in this study, all the laboratories involved followed similar but not exact same procedure. For example CO_2 trapping and removal of water was done in a fluorination line at LSCE where as the other labs used Ascarite and Perchlorate traps. It may not significantly affect the observations, but it still shows variability in sample handling.

Differences between working standards due to calibration and long-term drift

Differences between the working standards isotopic values of each lab can lead to a significant difference in the measured isotopic values of Ag_2O. It is customary to calibrate the working gas of a given lab with another lab's working gas, which is already calibrated against the VSMOW scale. For example, the working gas LGGE#1 is calibrated against the working gases of laboratories in California, USA and Heidelberg, Germany. However, during this interlab calibration process, errors could be introduced in each step. Additional difference can arise from variation of the laboratory used to calibrate the working gas, and the accuracy of calibration of the working gases of these laboratories. For this purpose, an aliquot of LGGE#1 was sent to the collaborating laboratories and a smaller but significant difference was observed as shown in Table 7. Additionally, each participating lab sent their respective working standards with the corresponding isotopic values (Table 6) and it was measured in LGGE. The long-term drift of the LGGE#1 standard was also tested and there was a minor change of about 0.3 ‰ from its value in 2006.

Table 6. The isotopic composition of the working gases of the laboratories participated in this study. The laboratories obtained these values via intercalibration with other working references and all values are normalized to VSMOW scale.

Lab	δ^{17}**O/‰**	δ^{18}**O/‰**	Δ^{17}**O/‰**
LGGE	3.533	7.522	-0.378
LSCE	5.567	9.901	0.350
IMAU	7.795	14.959	0.016

Table 7. The interlaboratory isotopic composition measurements for the working gases of the different laboratories measured at LGGE using LGGE#1 as reference gas. All the values value are normalised to VSMOW scale and the difference with the values provided by each laboratory (table 6) is given.

Sample	δ^{17}**O/‰**	**Difference**	δ^{18}**O/‰**	**Difference**	Δ^{17}**O/‰**	**Difference**
IMAU	9.335	1.54	18.293	3.33	-0.177	-0.227
	9.379	1.58	18.441	3.48	-0.210	-0.227
LSCE	4.681	-0.89	10.713	0.81	-0.890	-1.24
LGGE#1*	2.493	-1.04	4.768	-2.75	0.023	0.401

**Denotes measurement conducted at IMAU using their reference gas*

Comparing tables 6 and 7, it can be seen that there is a significant difference between the working standards isotopic composition measured at different laboratories. For example the working reference gas of LGGE (LGGE#1) has lower oxygen isotopic values when measured at IMAU. These differences imply that the observed significant difference in isotopic measurement values of Ag_2O can be associated with this effect. As which laboratory had made the right measurement value is unknown, a simple calculation was made assuming the isotopic values of the working gases for each lab measured at LGGE are true values i.e. the isotopic values for the working gases measured at LGGE for the two labs were used instead of the δ^{17}O and δ^{18}O values provided by the labs. The recalculated data in table 8 showed better agreement between the different measurements. However, it can be seen that an improved interlab calibration should be performed to obtain reproducible values.

Table 8. Recalculated oxygen isotopic values for the Ag_2O standard expected to have a ^{17}O excess value about 20‰.

Lab	$\delta^{17}O/‰$	$\delta^{18}O/‰$	$\Delta^{17}O/‰$
LGGE	12.871±0.46	-5.698±0.43	15.834±0.25
LSCE	11.999±0.014	-4.770±0.180	14.923±0.25
IMAU	12.495±0.160	-4.670±0.074	14.147±0.25

6.5. Conclusions and outlook

We took a first approach towards preparing a reference material with non-mass dependent behaviour for oxygen isotopic measurements, Ag_2O, from $AgNO_3$ and enriched water in basic medium. The oxygen gas obtained from the thermal decomposition of Ag_2O showed varying results based on the oxygen isotopic measurements performed at LGGE or in collaborating laboratories. The reason for this difference is not clearly known at this stage of the study. However, the major cause of this difference could be interference from atmospheric CO_2. It is verified in this study that CO_2 could strongly influence the measurements obtained for the oxygen gas due to the strong CO_2 absorption nature of Ag_2O. Additional reason for the variability observed during the interlab measurement can be the inconsistency between the working gases of each laboratory on the VSMOW scale, which may happen during calibration of the working gases. Even if all the laboratories did not participated in this interlab calibration procedure, a significant difference was observed between LGGE, LSCE and IMAU working standards. Further interferences could also arise from sample transportation, handling and storage procedures.

As the final phase of this study is not conducted, a few recommendations can be pointed out. The first approach should be to produce Ag_2O in CO_2 free environment. Even if CO_2 is abundantly available in the atmosphere, using a specific CO_2 free production system where an inert gas can be flushed through the system during equilibration and preparation of Ag_2O steps should be setup. This can lead to a significant improvement on the quality of the reference material.

Secondly, interlab calibration should be performed in more organized, reproducible and careful way. In this experimental study some of the laboratories analysed the Ag_2O samples more than 2 months after they receive these samples. This can lead to errors arising from sample storage and stability, further complicating the source of inconsistency.

Finally, the long-term stability of the Ag_2O product should be tested in a more controlled way. From a single batch of silver oxide, a couple of samples should be placed at different environmental conditions such as in light/dark, in dry/wet condition and at room temperature or in an oven, and the stability should be tested to decide where and how the product should be stored and handled.

Annex B

^{17}O excess transfer during the $Br + O_3 \rightarrow BrO + O_2$ reaction

The main objective of this study was to establish the ^{17}O-excess transfer function during the $Br + O_3 \rightarrow BrO + O_2$ reaction, which is an important chemistry for the polar nitrate. Accordingly, BrO radical formed during ozone depletion events in polar spring can oxidize NO_X and eventually produce $BrNO_3$, which hydrolyses to produce HNO_3 (Morin et al., 2007a). The triangular ozone molecule, with two terminal and central oxygen atoms has a ^{17}O-excess on the terminal oxygen atom and there is a high preference for this terminal atom to be transferred to other compounds during oxidation (Bhattacharya et al., 2008;Savarino et al., 2008). Hence, BrO will have an isotopic anomaly greater than the bulk ozone due to its formation from ozone via terminal oxygen atom transfer which can further incorporate this isotopic anomaly to nitrate. Accordingly, the highest ^{17}O-excess in nitrate (36 ‰) was measured during highest levels of BrO (peak of ozone depletion events, ODE) and lowest levels of ozone. However, the transferable ^{17}O-exces is not experimentally quantified and currently it is assumed that the transfer of a terminal oxygen atom from ozone to BrO and eventually to nitrate is $1.5 \times \Delta^{17}O(O_{3,bulk})$ but it needs to be verified experimentally.

Similar to the $NO_2 + O_3$ reaction presented in chapter 2, we have followed similar idea and used the same experimental procedure (see Chapter 3 method section). In short, ozone was generated via electrical discharge of oxygen gas with $\Delta^{17}O\ (O_3) = 5 – 40$ ‰. Part of this ozone was reacted with Br radical generated from photolysis of Br_2 when exposed to visible light. As the $Br + O_3$ reaction produces highly reactive BrO radicals which can undergo self-addition, and produce extra oxygen ($BrO + BrO \rightarrow Br_2 + O_2$). We have used dimethyl sulfide (DMS) to counteract the self-addition reaction i.e. as soon as BrO is formed, it will react with DMS and the oxygen from BrO will be locked as DMSO, ensuring absence of extra oxygen atom. Oxygen gas produced during this reaction was collected and analyzed for its triple oxygen isotopic composition in addition to the aliquot of initial ozone.

The transfer function ($\Delta^{17}O(O_3^*) = (1.10 \pm 0.21) \times \Delta^{17}O(O_3)_{bulk} + (10.45 \pm 1.07)$) was derived based on the isotopic compositions of the initial ozone and oxygen gas products. However, this function is valid only if the oxygen gas is generated from the $Br + O_3$ reaction only (and not also from side reactions). Unfortunately, BrO radical produced during the reaction undergo fast self-addition reaction producing additional oxygen. DMS can also react slowly with ozone and produce oxygen, leading to additional oxygen atoms.

Hence, under the experimental setup followed in this study, it was not possible to avoid the side reactions and interpretations of the findings from this study were impossible. In the future, this reaction has to be studied in a setup such as an environmental chamber coupled with an FTIR spectroscopy where the reaction progress can be followed online. In addition, using another organic compound than DMS, which may quench BrO effectively, and with no side reaction shall be used to avoid complications arising from multiple oxygen sources.

Annex C

Nitrogen isotopic fractionation between NO and NO_2

Objective

The main objective of this study was to determine the isotopic fractionation of ^{15}N during the NO-NO_2 equilibrium given by:

$$^{14}NO + {}^{15}NO_2 \leftrightarrow {}^{15}NO + {}^{14}NO_2$$

As briefly explained in the previous chapters, nitrate is formed from NO_X via various oxidation mechanisms. These pathways can be inferred from the stable isotopes ratios of nitrate obtained from different sites. The variability in ($\delta^{15}N$) signal of atmospheric nitrate can be associated with variation in NO_X source, partitioning of ^{15}N between NO and NO_2, isotopic fractionation during nitrate formation from NO_X, or transport of atmospheric nitrate (Morin et al. 2009). However, these processes are not currently well constrained, and the focus of this study was to understand the partitioning of ^{15}N between NO-NO_2 equilibrium. Freyer et al. (1991) observed the seasonal variation in $\delta^{15}N$ values for NO_2 collected in Jülich, Germany. Accordingly, relatively higher $\delta^{15}N$ values were measured in autumn and winter when compared to the lower summer and spring measurements. From the measurements of $\delta^{15}N$ and molar ratios of NO_X and NO_2, the authors have indirectly derived an effective ^{15}N exchange constant (K') = 1.018.

In the presented study here, we have followed an approach to directly derive the $\delta^{15}N$ exchange constant during the daytime and nighttime conditions. Note that during the daytime, there is the fast NO-NO_2 interconversion via oxidation with O_3 and photolysis (the Leighton cycle); however, in the nighttime only isotopic exchange will take place.

The ^{15}N fractionation constant between NO and NO_2 during the daytime or nighttime can be determined from the equilibrium concentration of the reactants and products via:

$$K = \frac{\left[{}^{14}NO\right]\left[{}^{15}NO_2\right]}{\left[{}^{15}NO\right]\left[{}^{14}NO_2\right]}$$

where K is the equilibrium constant (note that for isotopic exchange reactions involving a single atom, the fractionation factor (α) is same as the equilibrium constant).

Experimental setup

In order to observe this exchange reaction, an experimental setup was designed using the environmental chamber coupled with FTIR spectroscopy available at CCAR, Copenhagen. With such setup, we were able to measure in-situ the time evolution of the concentration of each species (^{14}NO, ^{15}NO, $^{15}NO_2$, $^{15}NO_2$) while mixed in the reaction chamber.

First, we have prepared enriched $^{15}NO_2$ from $H^{15}NO_3$ solution via decomposition using Cu metal. The $^{15}NO_2$ gas produced was then collected and purified from remaining HNO_3 and NO via cryogenic trapping. A known amount of this gas and an industrial ^{14}NO were introduced into the environmental chamber which was then filled with air to an atmospheric pressure. Then, an IR spectra was recorded at different durations to observe the rate of loss of ^{14}NO and $^{15}NO_2$ and generation of ^{15}NO and $^{14}NO_2$ until no change in peak size is observed, confirming that equilibrium is attained. Then based on each recorded spectras, we have calculated the amount of each species (^{14}NO, $^{15}NO_2$, ^{15}NO and $^{14}NO_2$) from their respective peaks, and using MALT5 computer program (The program enabled to determine the amount of different species from their recorded spectras based on its reference library of calibrated peaks corresponding to different molecules).

Results and difficulties

The main difficulty during this study was the issue of conservation the total NO_X in the system. Accordingly, the total amount of the four species (^{14}NO, $^{15}NO_2$, ^{15}NO and $^{14}NO_2$) in the system was not conserved in this experimental study. We have always observed lower total NO_X level than the sum of the amount of each species denoting possible presence of NO_X sink. This might be associated with wall reactions in which NO_X is lost from the system. Even if we have cleaned the environmental chamber repeatedly with oxidants such as ozone and irradiating with UV-lamps, we could not prevent the loss of NO_X. Under these conditions, it was not possible to further proceed on this experiment.

In the future, such experimental study should be conducted using a similar experimental setup but clean enough to avoid wall reactions.

Annex D

Nitrate preconcentration protocol

The procedures followed during preconcentration of nitrate in the snow samples at the warm lab in Dome C, Antarctica is shortly described below. The basic principle of this method is that an anion exchange resin has different affinity towards anions, and when a liquid sample is poured on these types of resins, anions are trapped one the resin. The trapped ions can be eluted and recovered with another eluent with greater affinity and/or higher concentration to the resin.

The Bio-Rad AG 1-X8 200-400 mesh chloride form is an anion exchange resin with higher affinity for NO_3^- than Cl^- and used in this study.

- 1M NaCl solution was prepared and equal volume of this solution (5 ml each in this case) and the resin were mixed and allowed to settle. The supernatant was discarded and another 10 ml 1M NaCl solution was added. The procedure was repeated three times to have a maximal incorporation of Cl^- ions to the resin and remove any other anions, especially nitrate contamination
- 0.6 ml of this mixture was transferred into the tip of the funnel carefully and it was rinsed 5 times with 5 ml 1M NaCl solution to remove any nitrate that might be present including manufacturing impurities.
- The melted snow sample was then poured into the funnel and left dripping until the entire sample pass through the resin. 10 ml MQ water was added to wash the side of the funnels if there is nitrate left on the walls.
- Finally, the nitrate trapped in the resin was eluted by adding 2 times 5ml of 1M NaCl. Then, the samples were collected in 20 ml plastic cups and then covered with parafilm and kept frozen. Note that the resin has a capacity of 1.2 $mmol.ml^{-1}$ and we used 0.3 ml of resin, which can hold about 360 μmol nitrate that is much bigger capacity than the nitrate available in our samples.

These samples were shipped frozen to Grenoble for analysis of its O and N isotopic composition.

Annex E

Nitrate photolysis experiments – isotopic data correction (provided by Joseph Erbland)

The nitrate photolysis experiment pushes the denitrifier method to its limits. Indeed, the sub-sampling of the snow column leads to samples with nitrate amounts as low as 5 nmol in a few ml. Nitrate pre-concentration on anionic resins is too risky while dealing with nitrate amounts on the order of tens of nanomoles. This is due to a very small blank which would largely affect the measurement. It was therefore decided to run the samples at a fixed volume but with varying nitrate amounts and to apply a size correction to account for that. Following the identical treatment of samples and standards, the latters are prepared in the same way as the samples: in the same matrix (MQ/Dome C water), same volume, nitrate amounts which vary in the same range (usually 5 to 100 nmol).

The correction of the nitrogen isotopic values is undertaken by assuming that the sample N_2 is contaminated with a small N_2 blank which originates whether from a NO_3^- /NO_2^- blank at the bacterial stage, a N_2O blank or a N_2 blank in the N_2O line. A blank at the bacterial stage is very unlikely because the bacteria where flushed with He before the injection of the sample. Also, a N_2O blank from the air is unlikely as well because N_2O levels in the atmosphere are low. The blank is more likely to originate from atmospheric N_2. The size and the isotopic composition of this blank must be determined using the standards at various sizes. Any N isotopic fractionation at the bacterial stage or in the line is ignored.

Let's call A_{bk}, A_{spl} and A_{mes} the respective sizes (in V.s, not in nmol) of the blank, the initial sample and the measured mixture of the two and $\delta^{15}N_{bk}$, $\delta^{15}N_{spl}$ and $\delta^{15}N_{mes}$ the respective isotopic composition in nitrogen of the blank, the initial sample and the measured mixture of the two. We should bear in mind that $\delta^{15}N_{spl}$ refers to the $\delta^{15}N$ of the sample as it would be measured by the mass spectrometer in the absence of the blank. This value still needs to be calibrated to account for any fractionation at the bacterial stage and in the mass spectrometer. The isotopic mass balance of the mixture gives the following schematic and equation:

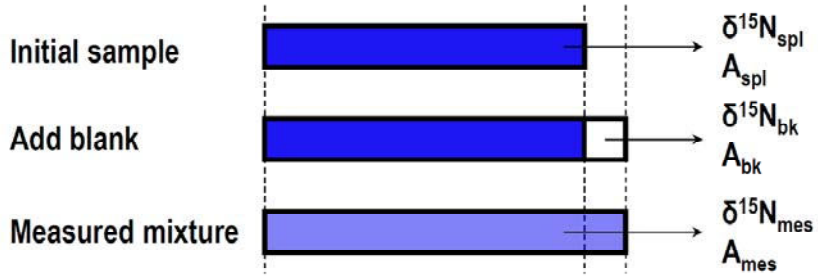

$$\delta^{15}N_{mes}.\ A_{mes} = \delta^{15}N_{bk}.\ A_{bk} + \delta^{15}N_{spl}.\ A_{spl}$$

The following figure shows an example with standards ranging 20 to 100 nmol and for A_{bk} = 0.44 V.s and $\delta^{15}N_{bk}$ = -20 ‰. These values are obtained by varying A_{bk} and $\delta^{15}N_{bk}$ until reducing the standard deviation of the residuals to its minimum value. This approach (calculating the standard deviation of the residuals) is similar to the method employed for standards run at a given amount. The grey lines are obtained for $\delta^{15}N_{spl}$ ranging -60 to 190 ‰ with a 10 ‰ resolution. We can clearly see that $\delta^{15}N_{spl}$ represents an asymptotic value.

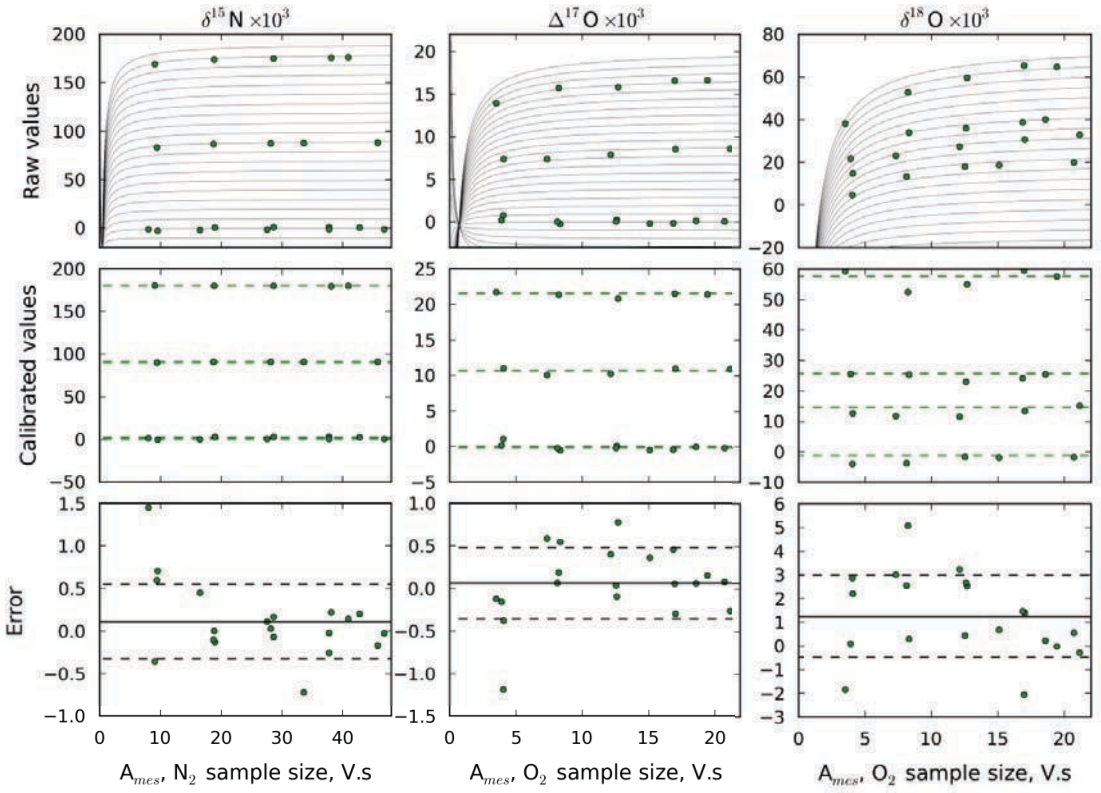

This approach gives a mean error value (solid horizontal line in the lower panels) which is close to 0 ‰ for $\delta^{15}N$ which means that the method does not incorporate a significant bias. The 1-sigma uncertainty reported using this method is 0.5 ‰ which is very satisfactory (at 100 nmol this value can be as low as 0.3 ‰)

For oxygen, it is a little bit more complicated because an isotopic exchange at the bacterial stage must be considered. Focusing on $\Delta^{17}O$, we neglect any isotopic fractionation because we assume that those are mass-dependent. We also neglect any blank effect. Indeed, any atmospheric O_2 blank is considered negligible because the N_2 blank is small. For the sake of simplicity, we also neglect any consumption of O_2 in the gold tube. Let's call A_{IE}, A_{spl} and A_{mes} the respective sizes (in V.s, not in nmol) of the isotopic exchange, the initial sample and the measured mixture of the two and $\Delta^{17}O_{IE}$, $\Delta^{17}O_{spl}$, $\Delta^{17}O_{mes}$ the respective ^{17}O-excess of the isotopically exchanged fraction, the initial sample and the measured mixture of the two. We should bear in mind that $\Delta^{17}O_{spl}$ refers to the $\Delta^{17}O$ of the sample as it would be measured by the mass spectrometer in the absence of the isotopic exchange. This value still needs to be calibrated to account for

any fractionation at the bacterial stage and in the mass spectrometer. The isotopic mass balance of the mixture gives the following schematic and equations:

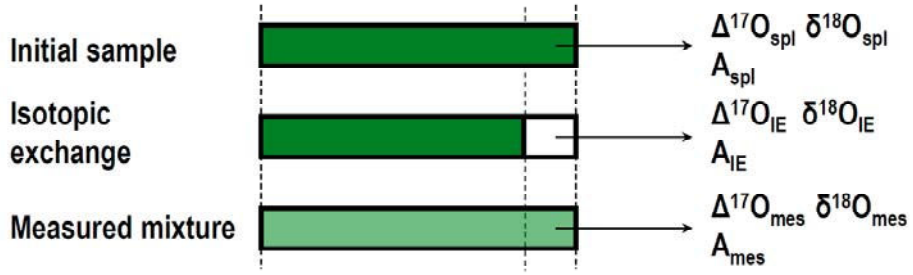

$$\Delta^{17}O_{mes}.\ A_{mes} = \Delta^{17}O.\ (A_{spl} - A_{IE}) + \Delta^{17}O.\ A_{IE}$$

This approach gives a mean error value (solid horizontal line in the lower panels) which is less than 0.1 ‰ for $\Delta^{17}O$ which means that the method does not incorporate a significant bias. The 1-sigma uncertainty reported using this method is 0.5 ‰ which is very satisfactory (at 100 nmol it can easily go down to 0.4‰)

The bias is larger (higher than 1‰) for $\delta^{18}O$, most probably because the oxygen isotopes may well be fractionated at the bacterial stage or further in the analytical process. The correction routine would benefit taking this effect into account. For now, the $\delta^{18}O$ data must be considered with caution.

Summary of activities

In this section the scientific activities during my PhD study is shortly described.

Publications

Tesfaye Ayalneh Berhanu, Joël Savarino, S.K.Bhattacharya, Willliam C. Vicars. **2012**. ^{17}O excess transfer during the $NO_2 + O_3 \rightarrow NO_3 + O_2$ reaction**.** *Journal of Chemical Physics 4, 136.*

Additional three articles are on their final stage to be submitted:

Carl Meusinger, **Tesfaye A Berhanu**, Jospeh Erbland, Joël Savarino and Matthew S. Johnson. Laboratory Study of Nitrate Photolysis in Antarctic Snow, Part 1: Quantum yield and mechanism. *Journal of Chemical Physics* (***to be submitted***).

Tesfaye A Berhanu, Carl Meusinger, Joseph Erbland, Joël Savarino, Matthew S. Johnson and Remy Jost. Laboratory Study of Nitrate Photolysis in Antarctic Snow, Part 2: Isotope Effects and Wavelength Dependence. *Journal of Chemical Physics* (***to be submitted***).

Tesfaye A Berhanu, Jospeh Erbland, William C. Vicars and Joël Savarino. Isotopic effects of nitrate photochemistry in snow: A field study at Dome C, Antarctica. *Atmospheric Chemistry and Physics Discussions* (***to be submitted***).

Conferences

During my PhD study, I have also attended different international conferences and presented my work during these occasions some of which are mentioned below.

Berhanu Tesfaye Ayalneh, Joël Savarino, Amaelle Landais, Frédéric Prié, Renato Winkler, Thomas Röckmann, Marion Früchtl, Jan Kaiser, Thomas Blunier, Corentin Reutenauer. Ag_2O: A new non-mass dependent standard material for oxygen isotope measurements. 6^{th} International Symposium on Isotopomers, Washington D.C., USA June 2012 (***poster presentation***).

Berhanu, Tesfaye; Savarino, Joel; Bhattacharya, S.K; Vicars, W.C. Quantification of isotopic anomaly during the $NO_2 + O_3 \rightarrow NO_3 + O_2$ reaction. 10^{th} Informal conference on Atmospheric and molecular sciences, Copenhagen, Denmark, June 2011 (***poster presentation***).

Berhanu, Tesfaye; Savarino, Joel; Bhattacharya, S.K. Quantification of isotopic anomaly during the $NO_2 + O_3 \rightarrow NO_3 + O_2$ reaction. European Geoscience Union Vienna, Austria, April 2011 (***poster presentation***).

5th International Symposium on Isotopomers, Amsterdam, The Netherlands, June 2010 (***Attended***).

Courses

During the three years of my PhD, I have also attended different courses.

Summer schools

INTRAMIF summer school "Science and society", Paris, August 2011.

INTRAMIF summer school on Mass Independent Isotope Fractionation, Norwich, August 2010.

Supplementary courses

VALORIDOC a course on how to make a CV and search for a job, Grenoble, April 2013.

Oral communications in English, Grenoble, November 2012.

Language courses

Basic French 1, Grenoble, France, November 2010.

Basic French 2, Grenoble, France, April 2011.

Laboratory Study of Nitrate Photolysis in Antarctic Snow, Part 1: Observed Quantum Yield, Domain of Photolysis and Secondary Chemistry

Carl Meusinger,[1] Tesfaye Ayalneh Berhanu,[2,3] Joseph Erbland,[2,3] Joël Savarino,[2,3,a)] and Matthew S. Johnson[1]
[1)] *Department of Chemistry, University of Copenhagen, Copenhagen, Denmark*
[2)] *CNRS, LGGE (UMR5183), F-38041 Grenoble, France*
[3)] *Univ. Grenoble Alpes, LGGE (UMR5183), F-38041 Grenoble, France*

(Dated: August 2, 2013)

Post-depositional processes alter nitrate concentration and nitrate isotopic composition in the top layers of snow at sites with low snow accumulation rates, such as Dome C, Antarctica. Available nitrate ice core records can provide input for studying past atmospheres and climate if such processes are understood. It has been shown that photolysis of nitrate in the snowpack plays a major role in nitrate loss and that the photolysis products have a significant influence on the local troposphere as well as on other species in the snow. For unclear reasons the range of reported quantum yields for the main reaction spans orders of magnitude, constituting the largest uncertainty in models of snowpack NO_x emissions. Here a laboratory study is presented that uses snow from Dome C and minimizes effects of desorption and recombination by flushing the snow with pure N_2 at water vapor equilibrium during irradiation with UV light. A selection of UV filters allowed examination of the effects of the 200 and 300 nm absorption bands of nitrate and to emulate actinic fluxes similar to those in Dome C. Nitrate concentration and actinic flux were measured in the snow and the quantum yield was observed to decrease with increasing exposure to UV radiation. Observed values for the quantum yield lie in the middle of the range of previously reported values and the superposition of photolysis in two photochemical domains of nitrate in snow is proposed: one of photolabile nitrate and one of trapped or buried nitrate. The difference lies in the ability of reaction products to escape the snow crystal, versus undergoing secondary (recombination) chemistry. A metric is developed to render these results applicable to field data. Modeled NO_x emissions may be increased significanty due to the observed quantum yield in this study influencing predicted boundary layer chemistry significantly including ozone concentrations. For the tested snow, the quantum yield changes from 0.44 to 0.05 within what corresponds to weeks of UV exposure in Antarctica. The quantum yield in the 200 nm band was found to be $\sim 1\,\%$, contradicting the predictions of aqueous chemistry. A companion paper present an analysis of the change in isotopic composition of snowpack nitrate based on the same samples as in this study.

PACS numbers: Valid PACS appear here
Keywords: Suggested keywords

I. INTRODUCTION

The nitrogen cycle is central to atmospheric chemistry as it governs photochemistry and oxidant budgets.[1,2] The photochemistry of nitrogen oxides ($NO_x = NO + NO_2$) produces ozone in the troposphere and the NO_x reactions are the most important catalytic cycle removing ozone from the stratosphere.[3] Oxygen atoms are exchanged rapidly between ozone and NO_x, with the result that polar NO_x contains material from atmospheric ozone. Therefore, information on the atmosphere's oxidative capacity is stored in the main sink of the cycle, deposited nitrate.[4] The information contained in ice core records of nitrate buried in polar regions may help in reconstructing the oxidative conditions prevailing in past climatic conditions[5] and in better constraining the nitrogen budget.[6,7] Nitrate is detected easily using e.g. ion chromatography, but post-depositional processes in the snow alter the nitrate concentration and prevent interpretation of the record at sites with low snow accumulation rates.[8–10] Nitrate profiles in the top centimeters of snow from e.g. Dome C, Antarctica, show a significant decrease,[11] while field measurements in summer show increased NO_x emissions above the snow pack at the same locations.[12,13] Elevated polar NO_x levels are suggested to play a central role in remote boundary layer chemistry and cause ozone levels to rise.[14] Laboratory experiments and field studies indicate that desorption and photolysis of nitrate in snow play a key role.

The reported values for the quantum yield of nitrate photolysis in snow, $\Phi_{NO_3^-}$, range from 0.0019 (Chu and Anastasio[15]) to 0.6 (Zhu et al.[16]), depending on the experimental method. Chu and Anastasio froze a prepared aqueous $NaNO_3$ solution, irradiated it with UV light at wavelength longer than 300 nm and detected the resulting OH radicals.[15] They argue that photolysis takes place in the *disordered interface* (DI, sometimes called the *quasi liquid layer*[17]). The small value they obtained for the quantum yield supports the theory that product species are preferably trapped by the aqueous cage effect (see below) potentially lowering the observed quantum yield.[18]

Zhu et al. conducted experiments using HNO_3 ad-

[a)] Electronic mail: jsavarino@lgge.obs.ujf-grenoble.fr

sorbed on an ice film.[16] They detected NO_2 using cavity ring-down spectroscopy and showed that both the absorption cross section and the quantum yield of nitrate have much larger values than reported in liquid phase[15]; both increase by a factor > 100 at 308 nm. Products from adsorbed species seem to leave the ice more easily, increasing the observed quantum yield. In another experiment by the same authors HNO_3 adsorbed on aluminum shows even higher values of $\Phi_{NO_3^-}$. The authors therefore argue that the actual quantum yield for photolysis of HNO_3 adsorbed on ice may be even larger than 0.6 because some of the NO_2 product is dissolved in water/ice.

The difference in the reported quantum yields has a direct impact on modeling studies which try to match the measured NO_x flux from the snow pack with the underlying photochemistry. In a recent study, Frey et al. modeled daytime NO_x emissions in the austral summer at Dome C that matched the observations, but under-predicted nighttime NO_x emissions by a factor of $\sim 3 - 4$.[13] Such studies of the NO_x flux from the snowpack often consider only aqueous chemistry and use the smaller of the reported values for the quantum yield.[13,19,20] These studies all point out that precise knowledge of the quantum yield of nitrate photolysis in snow is among the main uncertainties to current models.

A. Domain of snow photochemistry

The physical and chemical behaviors of species in snow are altered by their microphysical location due to differences in phase and the dielectric constant and electrical fields arising from e.g. salt, dust and phase boundaries, with important implications to snow-atmosphere interactions.[21,22] Potential photochemical reaction sites for chromophores in snow such as nitrate include: bulk ice, water in or on the snow, the DI, the grain boundary (where the Kelvin effect minimizes freezing), the ice surface and inside mineral dust or sea-salt impurities. The term *domain of snow photochemistry* is used here, following Davis et al.,[18] to describe the microphysical properties of the region around the nitrate chromophore that affect its photodissociation. For example the phase and ionic strength of the nearby region will modify the absorption cross section and photoproduct-cage interactions. As summarized in a recent review by Bartels-Bausch et al., the rate constants for a given chemical reaction can differ by orders of magnitude depending on the domain of snow photochemistry.[17]

One example of a domain-specific influence on a photochemical reaction is the *cage effect*. Following photoexcitation in liquids and ice, the surrounding medium may inhibit the initially formed primary products from escaping the cage of water molecules surrounding them. The products loose their excess energy via collisions to the water molecules and often reform the initial compound. This process is called the cage effect and has been observed for many systems including organics in ice[23–25] and nitrate photolysis in aqueous solution.[26] Kurková et al. show that the strength of the cage effect for organic compounds is a function of temperature (stronger recombination at lower temperatures) and microphysical state (frozen solutions show a cage effect at much lower temperature than artificial snow).[24]

In the case of nitrate there is evidence of recombination of photoproducts and of the existence of two reservoirs of nitrate which behave differently upon photoexcitation: In an early study, Dubowski et al. report changes in the nitrate photolysis product distribution over time.[27] This was associated with the depth of different layers allowing for stronger secondary chemistry deeper in the snow. In a similar study, Beine and Anastasio report changes in the photolysis rate of HOOH over time.[28] More recently, Baergen and coworkers saw four orders of magnitude faster nitrate photolysis in grime than in aqueous solution.[29] In addition they observed a background signal associated with photolysis of more strongly bound nitrate. Similarly, Blunier et al. observed a nitrate fraction which could not be photolysed, no matter the length of photolysis.[30] Finally, Thomas et al. set up a chemical model which reproduced NO ratios in the boundary layer (at Summit, Greenland) by assuming a fixed ratio between nitrate in the DI and in the snow grain.[20] Davis et al. were among the first to suggest multiple nitrate reservoirs[18] that result in a superposition of photochemistry from different snow-photochemical domains. The microphysical location appears to control how labile nitrate is with respect to UV light in snow. Therefore, this study distinguishes two domains of nitrate photochemistry in snow: *photolabile* nitrate and *buried* nitrate.

B. Reaction mechanism

Several nitrate photolysis reaction mechanisms have been proposed.[31–35] An overview of the main reactions of concern to this work is shown in Figure 1. The complete mechanism is described in the Appendix, and a short summary is given here.

Even though the aqueous chemistry of nitrogen species[31] is generally not assumed to be representative of snow chemistry,[17] it is a usefull starting point. In the aqueous phase the nitrate ion absorbs light over a wide range of wavelengths and shows two prominent absorption bands at around 200 and 300 nm, as shown in Figure 2. The 200 nm band is about 1000 times stronger than the 300 nm absorption band, but typically plays a smaller role in environmental studies due to the onset of the actinic flux at Earth's surface around 300 nm, cf. Figure 2. The following reaction is generally assumed to be the dominant mechanism in snow

$$NO_3^- + h\nu \xrightarrow{H^+} NO_2 + OH$$

This corresponds to reactions A.1 and A.3 in Figure 1 and the Appendix. NO_2 can enter the gas phase and leave

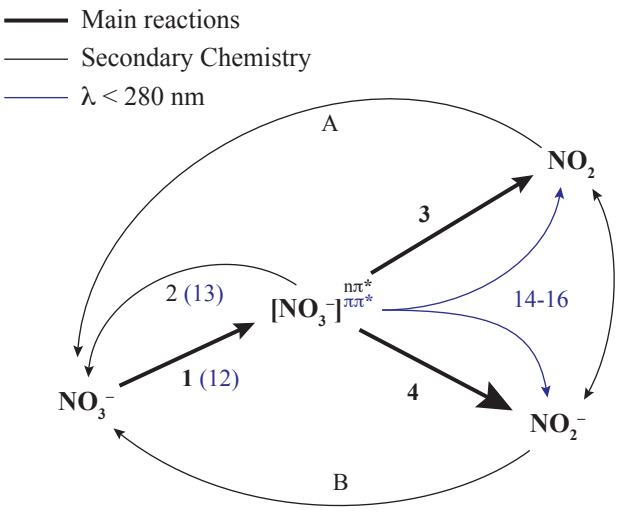

Figure 1. Scheme of the main chemical reactions. The square brackets denote a solvent cage. Product species like NO_2 may leave the system as gases, undergo photolysis or take part in secondary reactions as indicated. Blue color indicates reactions only possible at certain photolysis wavelengths. The numbers refer to reactions in the Appendix.

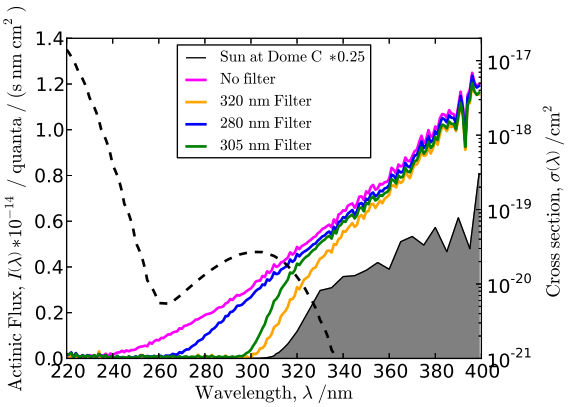

Figure 2. Actinic flux of different sources (left axis) and the liquid phase nitrate absorption cross section (dashed line, right axis). The modeled actinic flux of the sun at Dome C (noon of 1st of January 2012, in Antarctica at 3000 m elevation, with an overhead ozone column of 300 Dobson Units calculated using the TUV model[36]) and the Xe lamp's spectrum measured 1 cm inside the snow (with different filters in place, cf. legend). Note the logarithmic scale on the right.

the system, consistent with observations of elevated NO_2 fluxes from the snowpack.[13,14] NO_2 can also be photolysed or undergo further reaction. Pathways A and B in Figure 1 show reformation of nitrate from its own photoproducts, cf. reactions A.5 - A.11 and A.17 in the Appendix.

Aqueous chemistry on its own may not resemble nitrate snow-phase chemistry for two reasons: i) the superposition of photochemistry of different nitrate domains and ii) the recombination of nitrate due to secondary chemistry (pathways A and B in Figure 1) and the solvent cage (reaction A.2). Both recombination reactions and the cage effect lower the observed quantum yields as the reactant is reformed and might show reaction rates that depend on photoproduct concentrations. Therefore, the presented mechanism does not include reaction rates but it is argued in this study that the effects of superposition of domains and recombination chemistry should be (and for reasons of feasibility even have to be) included in the quantum yield.

Light of wavelengths around 200 nm is not typically present in the troposphere, but plays a role in the stratosphere at sufficient height. Since the deposited nitrate in snow at Dome C is suspected to originate from polar stratospheric clouds (typical altitude 15-20 km), it is exposed to radiation of such wavelengths. At wavelengths shorter than 260 nm, the overall reaction scheme is essentially the same as for longer wavelengths, with strong cage effects and a product pool that might recombine to form nitrate, cf. Figure 1 and the Appendix.

The goal of this work is to study the photolysis of nitrate in natural snow under controlled conditions including light spectrum and temperature while flushing the snow to test for desorption and recombination. This work describes the setup, sample handling, data analysis and interpretation in terms of photochemistry, while the companion paper discusses the implications in terms of stable isotopic composition of nitrate of the same samples. In the present study, the quantum yield is determined by measuring the actinic flux inside the snow and the nitrate concentrations before and after illumination with a Xenon lamp. Two hypotheses are tested:

- Since the rate of reformation of nitrate depends on the concentration of nitrate photoproducts, the quantum yield is dependent on light intensity.
- Since the different domains of nitrate in snow (photolabile vs. buried) show different behavior under UV exposure, these two pools account for the large variation reported in literature values of $\Phi_{NO_3^-}$.

II. THEORY

A. Mass-balance equation

Taking the reaction mechanism in Figure 1, the mass-balance equation for nitrate is as follows:

$$\frac{\mathrm{d}\,c(NO_3^-)}{\mathrm{d}t} = -c(NO_3^-)\,(J_2 + J_3 + J_4) + k_A\,c(NO_2^-) + k_B\,c(NO_2) + J_2\,c\left(NO_3^{-n\pi^*}\right) \quad (1)$$

Here c denotes concentrations; negative terms indicate nitrate loss and positive terms nitrate production. Quantities denoted by J are *first-order rate constants of photolysis* (*photolysis rates* in short) and those denoted by

k are reaction rate constants. The subscripts refer to reactions as given in Figure 1 and in the Appendix, e.g. J_3 and J_4 represent the rates of photolysis producing NO_2 and NO_2^- respectively. Subscripts A and B indicate secondary chemistry reforming nitrate which is not resolved in this study, cf. the Appendix. The total photo absorption rate is $J_1 + J_{12}$ where only $J_1 = J_2 + J_3 + J_4$ is considered in eq. 1, i.e. absorption in the 300 nm band. The effect of reaction A.2, relaxation of $NO_3^{-n\pi^*}$ to NO_3^-, is accounted for by the term $J_2\, c\left(NO_3^{-n\pi^*}\right)$.

In the present study, only nitrate concentrations are measured and therefore the individual terms in eq. 1 can only be discussed indirectly. Nitrate photolysis in snow is assumed here to be a single-step, unidirectional reaction and the right-hand side of eq. 1 can be reduced to a single loss term giving via integration:

$$J^*_{NO_3^-} = \frac{-\ln f}{t} \tag{2}$$

Equation 2 relates the apparent photolysis rate, J^*, to the photolysis time, t, and to the measured fraction of nitrate remaining in snow, $f = x_i(NO_3^-)/x_\circ(NO_3^-)$, with measured nitrate mole fractions, $x(NO_3^-)$ (in ppb = nmol/mol). The subscript i denotes any form of extent, e.g. photolysis time, and $\circ$ denotes the initial sample.

The concept of *apparent* quantities is introduced at this point (denoted by the * symbol) in order to distinguish the apparent photolysis rate (derived from measured nitrate fractions in eq. 2) from the primary photolysis rates in eq. 1. Erbland et al. used apparent quantities in a similar way to describe isotopic measurements in the field which incorporated several convoluted, indistinguishable underlying processes.[37]

B. Apparent photolysis rate and quantum yield

The apparent nitrate photolysis rate, $J^*_{NO_3^-}$, (units of s^{-1}) is defined by:

$$J^*_{NO_3^-}(z) = \int I(\lambda, z)\; \Phi^*_{NO_3^-}(\lambda, z)\, \sigma_{NO_3^-}(\lambda)\, d\lambda \tag{3}$$

Here, I is the *actinic flux* in quanta / (cm^2 s nm), $\sigma_{NO_3^-}$ is the nitrate *absorption cross section* in cm^2 and $\Phi^*_{NO_3^-}$ is the *apparent quantum yield* (dimensionless). The quantities in eq. 3 are given as functions of the depth of the snow layer, z, and wavelength, λ, to emphasize the importance of these parameters. The dependence on temperature, T, and light beam angle is neglected as experiments are done at constant temperature and always with the light beam normal to the snow surface, see below. Most of the quantities in eq. 3 are not sufficiently characterized for nitrate photolysis in snow. The actinic flux, I, for instance, changes nonlinearly in the snow as discussed in detail in the optical properties section. Also, the spectrum of a Xe lamp (used here and in most other studies) is significantly different from that of the sun resulting in different photolysis rates.[11,38] The absorption cross section and quantum yield for nitrate in the liquid phase and HNO_3 in the gas phase have been measured. However, whether those measurements are applicable to nitrate in snow or not is questionable, as the microphysical location of nitrate in ice seems to affect reported values.[15,16] Figure 2 shows some of the quantities of interest for nitrate photolysis.

The apparent quantum yield, $\Phi^*_{NO_3^-}$, was introduced into equation 3 to account for processes in addition to photolysis that alter the nitrate concentration. It therefore implicitly includes the k_A and k_B terms in eq. 1 as well as all J terms. Furthermore, differences in reaction kinetics between different domains of nitrate photolysis in snow are also included in $\Phi^*_{NO_3^-}$. In this way, $c(NO_3^-)$ and I – both of which can be determined in the field – are considered in relation to each other.

Assuming that the quantum yield is independent of λ[15], equation 3 can be rearranged to give

$$\Phi^*_{NO_3^-}(t, z) = \frac{J^*_{NO_3^-}(t, z)}{\int I(\lambda, z)\, \sigma_{NO_3^-}(\lambda)\, d\lambda} \tag{4}$$

Equation 4 allows derivation of the apparent quantum yield from the known actinic flux and an apparent $J^*_{NO_3^-}$ which was calculated from the measured nitrate concentration in snow. As indicated here and shown later, both $J^*_{NO_3^-}$ and $\Phi^*_{NO_3^-}$ are dependent on both depth in the snow and photolysis time.

C. 200 and 300 nm absorption bands

A Xe lamp was used in the present work, allowing study of both the 200 and 300 nm absorption bands of nitrate. J can be divided into contributions from the wavelength regions of these bands:

$$J_{NO_3^-} = J_{200} + J_{300} = \Phi_{200} \int_{220}^{260} I(\lambda)\, \sigma(\lambda)\, d\lambda + \Phi_{300} \int_{260}^{400} I(\lambda)\, \sigma(\lambda)\, d\lambda \tag{5}$$

Here, the * symbol and the depth dependencies of J and I were omitted for clarity and the quantum yield was assumed to be independent of λ.[15]

In order to distinguish the different nitrate absorption bands experimentally, a UV filter with sigmoidal wavelength around 280 nm was used in one of two experiments (#38 & #45) of otherwise identical conditions, i.e. photolysis time, snow type, flow, etc (see Table I). In principle, the experiment with the 280 nm filter (# 45) gives a value for J_{300} which corresponds to the second summand in equation 5, while the experiment with no filter gives $J_{NO_3^-}$ from both absorption bands. However, the UV filter cuts off parts of the 300 nm band which should also

be accounted for. This is done using a factor, g, which is evaluated from the ratio of the photolysis rates (with and without the filter) above 260 nm and is given in Table I. Φ_{200} can then be calculated from equation 5 as

$$\Phi_{200}(z) = \frac{J_{NO_3^-}(z) - J_{300}(z)}{\int_{220}^{260} I(\lambda, z)\,\sigma(\lambda)\,d\lambda} = \frac{J^{38}(z) - g_{280} J^{45}(z)}{\int_{220}^{260} I(\lambda, z)\,\sigma(\lambda)\,d\lambda} \quad (6)$$

Here, superscripts 38 and 45 indicate experiment ID's and g_{280} is the 300 nm band factor for the 280 nm filter. The apparent quantum yield for the 300 nm band, Φ^*_{300}, is derived from equations 4 and 5 :

$$\Phi_{300}(z) = \frac{J_{NO_3^-}(z) - J_{200}(z)}{\int_{260}^{400} I(\lambda, z)\,\sigma(\lambda)\,d\lambda} = \frac{J_{NO_3^-}(z) - \Phi_{200}(z) \int_{220}^{260} I(\lambda, z)\,\sigma(\lambda)\,d\lambda}{\int_{260}^{400} I(\lambda, z)\,\sigma(\lambda)\,d\lambda} \quad (7)$$

D. Optical properties of snow and the Beer-Lambert law

Previous work has shown that the actinic flux, I, changes nonlinearly with depth in a semi-infinite body of snow due to prevalent scattering.[36] In discussion of their Tropospheric Ultraviolet Visible (TUV) model, Lee-Taylor and Madronich document two distinct zones described by the ratio of direct and diffuse light.[36] Undisturbed sunlight has a large fraction of direct light resulting in an amplification of the actinic flux just below the snow surface. Below that zone incoming light undergoes sufficient scattering in the snow, so that effectively all light becomes diffuse.

In the diffuse zone, the depth-profile of I can be fitted assuming a unique exponential decay for each wavelength. The exponential nature of the fit is based on the (modified) Beer-Lambert law

$$I(\lambda, z) = I_0(\lambda) \exp(-z/\eta(\lambda)) \quad (8)$$

where I_0 is the actinic flux measured in the uppermost part of the diffuse zone in the snow and $\eta(\lambda)$ is the (exponential) fitting parameter known as the *e-folding depth* (written as $\eta(\lambda)$ to avoid confusion with the isotopic fractionation, ε). The quantity $\eta(\lambda)$ describes the depth at which 1/e of $I_0(\lambda)$ is lost.

E. Antarctic sunny day equivalent

In order to relate laboratory results to field studies, the exposure to nitrate-active photons is quantified. For this purpose, an actinometric quantity, the *Antarctic sunny day equivalent* numerated as N_{asd}, is introduced. The idea is to illustrate the roles of the different nitrate photochemical domains and the importance of secondary chemistry as a function of absorbed photons under ambient conditions. Starting from the term in the denominator of equation 4 which describes the rate of photon absorption, the total number of photons absorbed by a sample in time t, N_{ph}, is given as

$$N_{ph}(z,t) = t \int I(\lambda, z)\,\sigma_{NO_3^-}(\lambda)\,d\lambda = \frac{t\ J(z,t)}{\Phi(z,t)} \quad (9)$$

N_{ph} is equivalent to the total number of excited nitrate molecules based on the liquid phase absorption cross section $\sigma_{NO_3^-}$. The total number of absorbed photons can be calculated for an experimental sample, N_{ph}^{exp}, and for snow for a typical day in Antarctica, N_{ph}^{sun}, using the sun's actinic flux. It is assumed that the quantum yield determined in this study is applicable to the field in similar conditions. N_{asd} is defined as the ratio of absorbed photons, and Φ cancels:

$$N_{asd} = \frac{N_{ph}^{exp}}{N_{ph}^{sun}} = \frac{t_{exp}\ J_{exp}}{0.5\ t_{sun}\ J_{sun}} \quad (10)$$

J_{sun} is calculated from the modeled actinic flux at Dome C, cf. Figure 2, and the (arbitrary) factor of 0.5 accounts for variations in the actinic flux (e.g. clouds, changes in ozone column and solar zenith angle). A number of $N_{ph}^{sun} \approx 0.5$ is derived for $t_{sun} = 1$ d. A value of $N_{asd} = 1$ indicates that as many photons were absorbed by nitrate in the experiment as in one sunny day in Antarctica, hence the name.

III. METHODS AND MATERIAL

A. Snow

Two batches of snow from Dome C, Antarctica, were used in the experiments. The first batch was collected on January 20th 2009 ca. 10 km South (S 75° 09' 0" E 123° 19' 25") of Concordia station (S 75° 06' 00" E 124° 33' 29"). The first ca. 10 cm of surface snow was scraped, homogenized and placed in a thermally sealed double-walled polyethylene bag. Approximately 5 kg of snow were collected. The second batch was wind-blown snow sampled in vicinity of Concordia station on December 5th 2011. The snow was stored until use at -25 °C in the dark.

The nitrate mole fraction on the day of collection was 570 ppb for the 2009 batch and 1822 ppb for the 2011 batch. Comparison to the mole fractions prior to experiments of around 450 ppb (2009 batch) and 1500 ppb (2011), cf. Table I, indicates only minimal changes during transport and storage due to denitrification by desorption of HNO_3.

All sample preparation before and after the experiments was done in a cold room at LGGE at -15 °C. Inside

Table I. Overview of experiments. The following properties are listed: snow type, starting nitrate mole fraction, average chloride and sulfate mole fractions (all in ppb = nmol/mol), photolysis time, t, UV filter sigmoidal wavelength, $\lambda_{\mathrm{filter}}$, g (indicates how much the filter cuts off the 300 nm band, see section *200 nm band correction* for more details) and gas flow, Q. All experiments were carried out at -30 °C.

Exp #	Snow	$x_\circ(\mathrm{NO_3^-})$	$x(\mathrm{Cl^-})$	$x(\mathrm{SO_4^{2-}})$	t /h	$\lambda_{\mathrm{filter}}$ /nm (g)	Q /(L/min)	Comment
test	Dome C (2009)	230.6	–	–	260	–	1.1	No light, SSA measurement
25	Dome C (2009)	421.1	131.9	95.9	137.8	–	1.1	Ice accumulation in light pathway
26	Dome C (2009)	482.9	103.4	89.8	4.6	–	1.1	
27	Dome C (2009)	466.4	86.1	87.1	88.2	–	1.1	
28	Dome C (2009)	503.2	97.9	76.8	114.4	–	1.1	Reverse flow direction
31	Dome C (2011)	1731.0	436.0	86.3	20.3	–	1.1	
38	Dome C (2011)	1564.8	–	–	162.8	–	2.2	
42	Dome C (2011)	1475.9	414.6	118.0	187.2	305 (2.35)	2.2	
43	Dome C (2011)	1519.4	434.3	158.4	283.2	320 (3.73)	2.2	
44	Dome C (2011)	1434.9	350.0	114.4	139.5	–	2.2	No light
45	Dome C (2011)	1433.9	368.7	102.1	164.0	280 (1.18)	2.2	

the cold room, the snow was kept in the dark in insulated boxes. Before experiments the snow was homogenized by mechanical mixing to ensure a uniform nitrate distribution (both, in terms of concentration and its domain), in all experiments and within each single experiment.

B. Experimental setup

Figure 3 shows an overview of the experiment. The cylindrical (ca. 400 ml) glass cell containing the snow consists of three parts which can be disassembled for filling: two ends with UV transparent Suprasil windows, and a center region where the snow is placed and which has four ports, for temperature and pressure readings, and in- and outflow of the water saturated nitrogen flow. The three parts are held together by metal clamps; sealing o-rings ensure that the closed cell is air tight. A scale was printed on the outside of the cell to guide subsampling after experiments. The snow cell is placed inside an environmental chamber of ca 1 $\mathrm{m^3}$ volume which is temperature controlled via a PC interface. The chamber has ports which allow tubes and optical equipment to reach inside.

A Xenon arc lamp (300 W, LOT Oriel) is placed at one of those ports (outside the chamber), together with an infrared (IR) water filter to reduce the heat flux into the chamber, and a holder to place several optional UV filters to modulate the impinging light spectrum, cf. Figure 2 and Table I. The lamp was adjusted to be collimated at the snow column front, but due to the nature of the two arcs occurring within the lamp, the intensity of the beam was not completely uniform in a plane perpendicular to the optical axis. The snow cell was always placed in the same way relative to the fixed lamp, but small variations could not be avoided. Given the short distance between the lamp and the snow cell, no large changes in the spectrum due to absorption in air were observed.

Water-saturated nitrogen was flowed over the snow during experiments to remove photoproducts. Evaporated liquid nitrogen ($\mathrm{LN_2}$) was used as carrier gas. A part of the $\mathrm{N_2}$ flow was directed through a water bubbler in order to provide a water saturation of ca. 150 % for the set temperature of the environmental chamber and therefore the snow. The super-saturation takes the temperature difference between room and chamber (inside) into account. Since the water vapor pressure scales with temperature, the excess water is collected in a trap inside the chamber. After having been saturated with water vapor at the snow temperature, the flow passes through the snow in the glass cell and exits via a designated port. The flow direction can be changed. All tubes directing the flow are made of stainless steel, as is the excess water trap. The tubing for the pressure gauge and the exit line of the flow are made of Teflon. The temperature was measured using a thermocouple placed in a half-open ethanol-filled glass vial which was introduced into the snow column.

Prior to experiments, the gas line providing the saturated nitrogen flow was heated using a heat gun while flushing with nitrogen to remove any contaminants in the tubes. In between experiments the nitrogen flow was kept above zero to prevent deposition and to sublimate any ice formed in the part of the gas line inside the chamber (including the excess water trap.) The water in the bubbler was renewed regularly; tests of the water after several runs always showed nitrate concentrations below the detection limit.

C. Experimental procedure, sample treatment and subsampling

A known mass of snow was homogenized and transferred into the pre-cleaned and cooled snow cell which had a Teflon sheet wrapped around its inside wall. This sheet ensures efficient removal of the snow after the experiment, as otherwise it sticks to the glass wall. The cell was filled vertically using a plunger which ensures a planar front (i.e. irradiated surface) and then closed

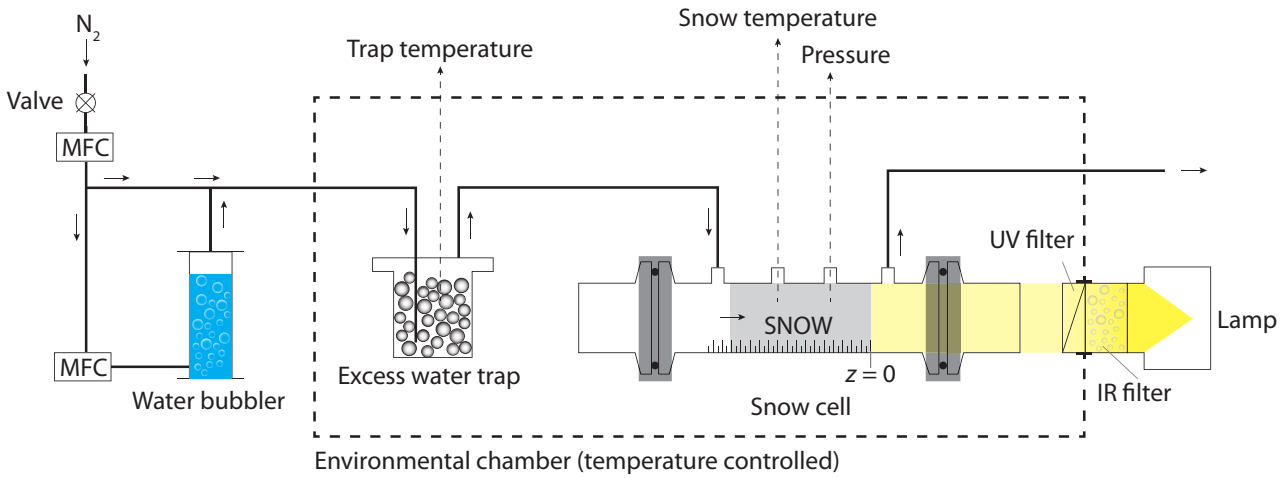

Figure 3. Schematic drawing of the experimental setup and snow cell. The (ca. 400 ml) snow cell has UV transparent Suprasil windows and a printed scale on the outside to guide subsampling after experiments. It is placed, together with the excess water trap, inside a temperature controlled environmental chamber (dashed line). The Xe lamp, IR water filter, optional UV filters and flow preparation setup are partly outside the environmental chamber, but are connected to the snow cell via ports. Pure nitrogen is provided from a liquid nitrogen tank. The flow direction is indicated by the small arrows and can be varied. MFC stands for mass flow controller.

and placed inside the pre-cooled environmental chamber where all tubes and ports were connected. Once the temperature of the snow was stable, the experiment was started by flowing the conditioned stream through the snow and switching on the lamp.

The snow column is usually significantly hardened at the end of an experiment, so that it can be pushed out of the cell easily and sliced into pieces of ca. 1 cm thickness using the scale on the cell. These slices are weighed individually in clean bags and then transferred into two vials each (all pre-cleaned), one for ion concentration and one for isotopic measurements.[39] Sample vials were kept in insulated boxes in the dark in the same cold room until measurement.

D. Specific surface area of the snow, SSA

Test runs without a lamp were performed to ensure the snow is not altered chemically or physically due to the flow system (e.g. desorption, crystal growth). Besides measuring nitrate concentrations as described below, the specific surface area (SSA) of the snow was measured before and after the run. In order to do so, snow samples of the same batch which was used for the experiment were stored in LN_2 to make sure their properties don't change during storage. Also, after the experiments, a portion of the snow was stored in LN_2. The SSA was measured using the DUFISSS instrument (DUal Frequency Integrating Sphere for Snow SSA measurement) described elsewhere[40,41]. Briefly, DUFISS is based on the measurement of the hemispherical infrared reflectance of snow samples using a laser diode at 1310 nm, an integrating sphere, and InGaAs photodiodes. The instrument was calibrated using different reflectance standards prior to measurements. All SSA samples were analyzed at the same time to minimize variation. Samples were removed from the LN_2 dewar some hours before the measurement to allow the snow to equilibrate with the cold room's temperature.

E. Chemical and isotopic analysis

Ion chromatography (Metrohm) was used to measure the nitrate, sulfate and chloride concentrations in each sample. Every set of ion chromatography measurements used freshly prepared standards and eluents.

The stable oxygen and nitrogen isotope ratios of nitrate were measured for each subsample. The results and discussion of this data are presented in the companion paper.[39]

F. Optical characterization

Past work has given considerable attention to describing the physical (e.g. optical) properties of snow to model the actinic flux inside the snow pack (e.g. using the TUV model[36] by Lee-Taylor and Madronich). However, a TUV-snow model cannot be used to calculate the optical behavior inside the snow since the geometry of the snow cell deviates significantly from the assumption of a semi-infinite snow pack. Therefore, an optical detection system consisting of a Maya2000PRO photo-spectrometer (wavelength region 220-400 nm), an optical fibre (solarized, 600 μm diameter) and a cosine corrector (CC-3-UV-

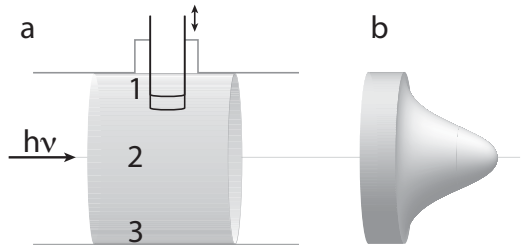

Figure 4. Sketch of the irradiance measurement (a) and beam profile (b) inside the snow column. The optical fibre was inserted in the snow using one of the ports of the snow cell. Measurements were taken at the three positions 1, 2 and 3. The beam profile illustrates the assumed spacial (Gaussian) distribution of the actinic flux inside one disk/subsample of the column (indicated in (a) by the grey cylinder.) The actinic flux is non-zero at the edges (positions 1 and 3).

T) was calibrated using a calibrated light source (DH-2000-CAL, all components Ocean Optics Inc.) in order to measure absolute irradiances. All spectra were corrected for dark noise, the integration times were varied depending on signal strength (up to the instrument maximum of 10 s) and spectra were averaged at least 10 times. The calibration using the DH-2000-CAL lamp was carried out at room temperature. All measurements were performed in a walk-in cold room at -15 °C (the Xe lamp, snow cell and photo-spectrometer were inside the cold room while the PC for data acquisition was kept outside). The manufacturer specified an uncertainty in the calibration spectrum of the calibrated light source of ±5 %.

Figure 4 shows how the absolute irradiance of the Xe lamp was recorded inside the snow column. The optical fibre and cosine corrector were placed at the same depths as for the subsampling using one of the snow cell's ports. The fibre was placed radially at three positions per depth step, see Figure 4 for details. The snow column was refilled at each depth using the same snow (from Dome C) as for the photolysis experiments.

The absolute (Xe lamp) irradiances measured in the snow at positions 1, 2 and 3 (shown in Figure 4) were converted to total actinic fluxes in each layer as follows. First, the field of view of the cosine corrector was taken to be 120 ° based on its geometry. All measured irradiances were corrected accordingly. Irradiances measured at positions 1 and 3 were added, and the data from position 2 doubled, in order to account for the full field of view at both the edge and the center of the snow column. This approximation is valid because snow is highly scattering, i.e. major parts of the radiation along the optical axis are well represented and not excluded, as was tested by longitudinal measurements. As a second approximation, a circular, gaussian distribution of the actinic flux in the base plane of the disk was assumed. Note that the actinic flux obtained using this method is non-zero at the edge, equivalent to a disc-shaped offset of the Gaussian beam profile (b in Figure 4.) Finally, the average of the derived profile is taken as the actinic flux at that specific depth, $I(\lambda, z)$.

This set of data, later denoted as 'Xe lamp irradiances', was used to determine the complete actinic flux inside the snow column. Another set of measurements was taken placing the fibre in position 2 of the first subsample and recording one spectrum per UV filter, labeled 'filter irradiances' below. Together with the first data set, the actinic flux in the total column was derived for each UV filter.

The Xe lamp irradiances are fitted using Beer-Lambert's law (eq. 8), where $I_0 = I(z = 1\text{ cm})$ is the actinic flux 1 cm into the snow. The reference point was chosen to be inside the snow since the front of the snow column reflects a significant portion of the emission of the Xe lamp due to the snow's very high albedo. The obtained set of $\eta(\lambda)$ describes the optical properties of the snow cell. For further data processing, the exponential fit at each wavelength was used to construct a *synthetic* profile of the actinic flux based on the measured value at $z = 1$ cm. Similarly, the filter irradiances measured at $z = 1$ cm can be used to reconstruct the filtered actinic flux at all depths inside the snow cell. In other words, equation 8 is also used to derive $I(\lambda, z)$ for the filtered cases, using the same $\eta(\lambda)$ and substituting $I_0(\lambda)$ for the filtered one. This parametrization allows accurate modeling of the actinic flux for each UV filter.

Using the synthetic instead of the measured actinic flux and assuming a Gaussian beam profile reduces uncertainties in the measurements. Besides the uncertainty in the calibration spectrum uncertainties include: i) The measurement method is intrusive which might allow some photons in the column to be absorbed by the fibre and cosine corrector without being detected, ii) Variations in the placement of the filled snow cell with the probe installed relative to the lamp (angle and side ways) changed the signal within a range of 20 %, iii) Placement of the probes inside the snow was accurate to within ±1 mm, both radially and laterally, iv) The difference in temperatures between the photolysis experiments (-30 °C) and the actinic flux measurements (-15 °C), v) The distance between the lamp and the snow cell was accurate to within ±1 cm; given the low atmospheric absorption in the wavelength region of interest, this plays a minor role.

Table I gives an overview of the experiments presented in this paper. All experiments were conducted using a 300 W Xenon lamp and at -30°C. The total flow of nitrogen, Q, and the duration of irradiation, t, were varied; the actinic flux was changed using UV filters.

IV. RESULTS

A. Snow mass

The masses of the subsamples, weighed after experiments, differed only slightly, ensuring that the results

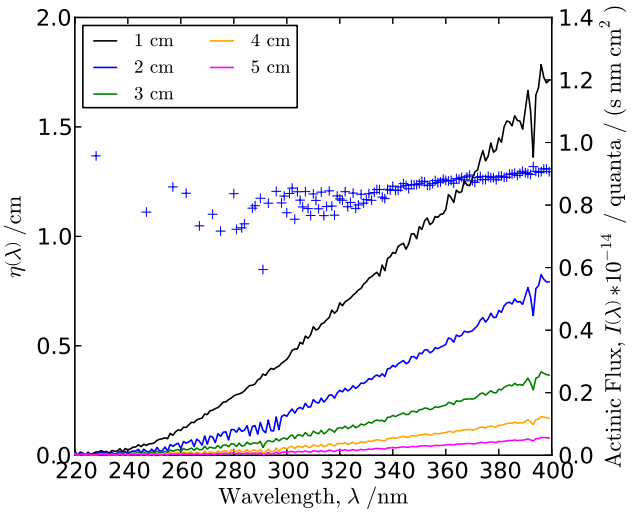

Figure 5. e-folding depths, $\eta(\lambda)$, (crosses, left axis) and actinic fluxes measured without UV filter at different depths, z, as given in the legend (lines, right axis). 1/e of the incoming light is lost after a very short distance into the snow (i.e. ca. 1 cm). Only values of $\eta(\lambda)$ are given for which the exponential fit of the actinic fluxes over depth fulfilled $R^2 > 0.9$, eliminating noisy data below 300 nm.

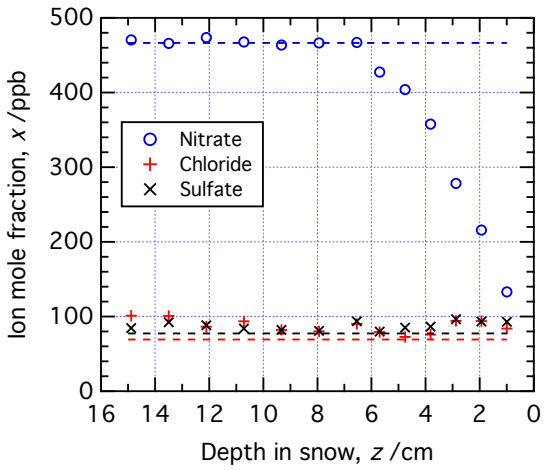

Figure 6. Ion concentration profile in the snow after ca. 86 h of irradiation (experiment #27). The single data points each represent one subsample of approximate 1 cm thickness as described in the text. The dashed lines indicate the respective ion concentrations of the initial snow prior to irradiation.

are comparable to each other. Samples masses were nominally 15 g and the standard deviation of the sample masses was less than 1 g ($n = 8$). The total snow mass weighed before and after photolysis typically differed by less than 1 %.

B. Actinic flux and e-folding depths

Figure 5 shows the profile of the actinic flux as a function of wavelength and depth in the snow column. The amplification in the first couple of millimeters which is predicted for low solar zenith angles by TUV models[36,42] is not observed. This might be because of the low depth-resolution of the measurements, or the non-semi-infinite geometry of the setup.

At a distance of 5 or 6 cm into the snow, the actinic flux decreases more than 10 fold (Figure 5); photolysis deeper in the snow is disregarded as the signal-to-noise ratio decreases accordingly. Equation 4 assumes that the measured actinic flux is the same in all experiments. As noted in Table I experiment #25 had ice accumulating in the light path over time due to humid ambient conditions. This, considered together with the other potential issues concerning the measurement technique itself means that the actinic flux results are a lower limit, since the method is unlikely to measure more photons than are present.

Figure 5 also shows the e-folding depths, $\eta(\lambda)$, as a function of wavelength. Only those values are given for which the fit fulfilled $R^2 > 0.9$, a condition usually not met below 300 nm due to the low actinic fluxes, cf. Figure 5. The e-folding depth was observed to be $\eta(\lambda) \approx 1.2$ cm and rather independent of λ.

C. Physical properties of snow and SSA

The SSA did not change significantly over the course of dark experiments in which there is flow but no light present (data not shown). It can therefore be assumed that the snow did not change due to storage and handling or flow. When handling the snow after photolysis experiments, changes in the front part of the snow were apparent, with notably more hardening for longer experiments. Due to the small amounts of snow available, the change in SSA could not be measured using DUFISS. Therefore, no quantification of the metamorphism is available but they most likely stem from absorption of light. The SSA is expected to decrease with time.

D. Nitrate loss and photolysis rates

Figure 6 shows the mole fractions of NO_3^-, Cl^- and SO_4^{2-} in experiment #27 before and after irradiation. Out of these ions only nitrate is affected with its concentration decreasing in the first 6 cm of the snow column.

Figure 7 shows the nitrate fraction remaining in the snow after photolysis for all experiments. The experiment in the dark with gas flowing (#44) showed no change in the nitrate concentration. Besides being a successful blank test, this strongly suggests that no nitrate desorbed off the snow into the water-saturated flow of nitrogen. All the other experiments show a loss of nitrate

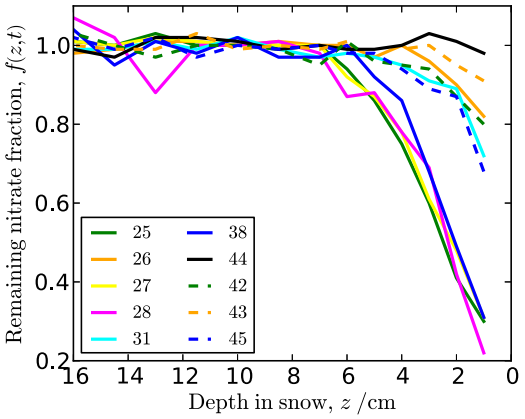

Figure 7. The measured remaining nitrate fraction in the snow after UV exposure. The legend key follows Table I. Depending on the photolysis time, nitrate is lost up to 6 cm depth. Experiment # 26 only shows losses in the first 3 cm and experiment # 43 only in the first 2 cm.

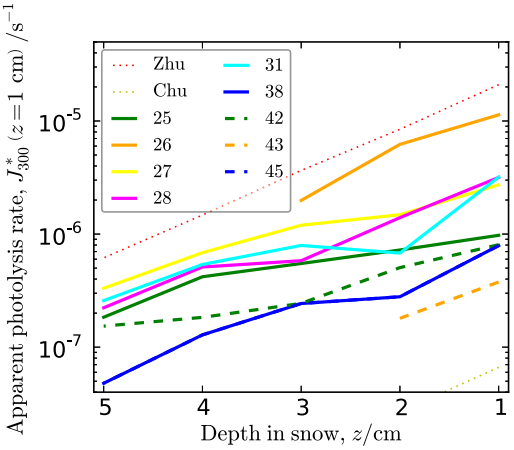

Figure 8. Apparent photolysis rates with depth in snow. Experimental data (full lines) were calculated from measured nitrate losses and the respective photolysis times (eq. 2). Experiments 38 and 45 have the same values due to the applied corrections (see text for details). The dashed lines (top and bottom) were derived by assuming literature values for the quantum yield. Note the log scale on the y-axis.

in the first couple of centimeters in the snow. Depending on the length of UV exposure (photolysis time), nitrate losses occur within the first 6 cm of snow.

Figure 8 shows the derived photolysis rates. Here, all data from experiments 25 - 28, 31 and 38 were corrected for absorption in the 200 nm band, essentially following equation 5. The experiments using UV filters (42, 43 and 45) were corrected using the g factors from equation 6 and Table I. The experimental curves in Figure 8 show two trends: photolysis rates decrease with depth and with photolysis time (the shortest experiment, # 26, has the highest values of J).

Theoretical predictions of nitrate loss using literature values of the quantum yield are also plotted in Figure 8. The quantum yield reported by Chu and Anastasio[15] underestimates the losses while the value by Zhu et al.[16] overestimates the losses. However, the experimental values tend to be closer to the higher values of Zhu et al. The 'Zhu' and 'Chu' curves in Figure 8 assume a constant quantum yield which corresponds to pure photolysis without secondary chemistry. The predicted photolysis rates are time-independent and decrease exponentially with depth. In contrast the slopes of the experimental data tend to larger values of J deeper inside the snow. In summary the experimental nitrate losses cannot be reproduced using the measured actinic flux and literature data for the cross sections and quantum yields.

V. DISCUSSION

A. Loss due to scattering governs the actinic flux profile

An e-folding depth of $\eta(\lambda) \approx 1.2$ cm is significantly lower than reported in ambient measurements (by a factor of 5-20[19,43]). This is due to the geometry of the snow cell: most of the incoming light is lost due to scattering to the glass-walled sides. The glass cell absorbs the UV fraction of the light and does not reflect it back, therefore the boundary conditions are not semi-infinite. This means that beyond a few centimeters into the snow most light is lost, cf. Figure 5.

One of the main assumptions taken when deriving Beer Lambert's law (eq. 8) is that the medium is mainly absorbing and not multiply scattering. However, snow is often used as an example of multiple scattering in the literature[44] and multiple scattering can be seen by digging a hole into fresh snow and observing its blueish glow. Equation 8 is merely used as an exponential fitting function in this context. Further discussion of the extinction coefficient of snow (which could theoretically be derived from $\eta(\lambda)$) is omitted.

B. Desorption-free photolysis system with recombination

As the nitrate concentration and SSA did not change in experiments whit no light present, it is safe to assume that photolysis is the main loss process observed in experiments with the light turned on. In particular, desorption was shown to play no role in the blank experiments. Also, the unchanged snow mass before and after experiments shows that there was no change due to sublimation or condensation. The Cl^- and SO_4^{2-} ion concentrations show that no macroscopic transport of water is present even after long photolysis times and that contamination (e.g. from NaCl) is low. However, the physical properties of the snow did change with the light source switched on and snow metamorphism could in principle make ni-

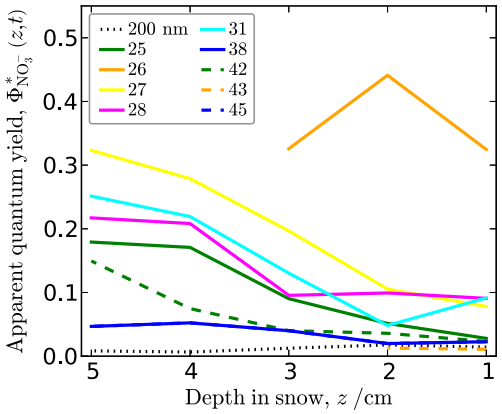

Figure 9. The apparent quantum yield, $\Phi^*_{NO_3^-}(z,t)$, determined for the 300 nm band for different experiments without UV filter (full lines) and with UV filters (dashed lines). See caption of Figure 8 and Table I for details.

trate more available for evaporation. Given the lower loss rates observed at longer photolysis times, desorption does not seem to play a major role under any conditions. In contrast, the production of nitrate via recombination of photolysis products may explain lower apparent photolysis rates relative to theory.

C. The 200 nm absorption band of nitrate

The quantum yield Φ_{200} was found in this study to be ca. 0.01 (independent of depth) which is small but significant given the strength of the 200 nm band. Because aqueous phase nitrogen oxide chemistry[31] suggests that all nitrate which is photolysed around 200 nm recombines (i.e. $\Phi_{200} = 0$), the 200 nm band has not received a lot of attention in snow and ice studies[35] even though the light sources used often emitted photons in the 200 nm region. Therefore, data from experiments using UV lamps without UV filters must be treated with care. The quantum yield determinations by Chu and Anastasio[15] and Zhu et al.[16] used setups without radiation in that range of the UV spectrum. $\Phi_{200} > 0$ clearly contradicts aqueous chemistry predictions, cf. the Appendix. It is very important to note that isotope effects may be different in the 200 nm band; see the companion paper.[39]

D. Superposition of two domains of snow photochemistry

Figure 9 shows the apparent quantum yields derived by relating the predicted number of absorbed photons (derived from the actinic flux measurement) to the apparent photolysis rates (derived from the measured nitrate concentrations) for different experimental conditions (equation 4). All values lie below 0.5 and span a wide range extending to 0.01. The two trends visible in J^* are also found in Φ^*: first, the quantum yield increases with increasing z, and second, the quantum yield decreases with photolysis time. The changes in quantum yield exceed the measurement error of the irradiances. For instance in experiment # 45, Φ^* changes by a factor larger than 3 compared to an error of 20-30 % in the optical measurement which is smoothed by the fitting procedure. More specifically, the measured actinic flux was regarded earlier as an upper limit and therefore the reported quantum yield is a lower limit.

One origin of the depth dependence of the quantum yield is the secondary chemistry terms A and B in the mass-balance equation (eq. 1). Considering that photolysis yields both NO_x and the radicals that oxidize it to reform nitrate, nitrate reformation will have a nonlinear dependence on light intensity. This is consistent with the lower measured quantum yield at the top of the column (Figure 9). However, it seems that secondary chemistry alone falls short in explaining the observed time dependence: the short experiment #26 yielded a high quantum yield at low depths where nitrate was exposed to a high photon flux.

In contrast, both trends can be explained by the superposition of two photochemical domains of nitrate in snow. Considering a system with photolabile and buried nitrate, the former would give a larger quantum yield while the latter will have a smaller quantum yield. In the first hours of the experiment, nitrate is easily photolysed in the front of the snow column. During longer experiments the snow in the back (below 3 cm) is exposed to significant amounts of UV radiation as well, similarly photolysing easily accessible nitrate (hence giving large values of Φ^*.) In the front, the buried nitrate is not photolysed as easily anymore. Over time the curve of the quantum yield shifts to the left in the representation of Figure 9.

It is likely that the values of Φ^* close to 0.35 relate to the photolysis of photolabile nitrate, while the limiting value of $\Phi^* \approx 0.05$ corresponds to photolysis of buried nitrate with a stronger contribution from secondary (recombination) chemistry. This is in line with results of similar experiments in the literature that show changing photolysis rates or two nitrate pools.[18,20,27,29,30]

The highest quantum yields are close to the value of Zhu et al.[16] Therefore it seems likely that samples with such high quantum yields experienced similar conditions as in this reference where HNO_3 was adsorbed on ice.

In order to explain the lower quantum yields a simplified picture of nitric acid solution (i.e. ignoring other ions) is considered here. The phase diagram[45] suggests that the experimental conditions of the present study (nitrate mole fractions, $x\left(NO_3^-\right) = 1 \times 10^{-7} - 1.7 \times 10^{-6}$, -30 °C) fall into a metastable phase where solid solutions of HNO_3 in ice and aqueous HNO_3 solutions coexist. In this framework the experiments by Chu and Anastasio were performed either in the liquid phase or in the same metastable phase (they state a total molality of

5.4 mol/kg corresponding to $x\left(NO_3^-\right) = 8.9\times10^{-2}$). The partitioning coefficient between solid and liquid phases[45] is $\sim 10^{-6}$ for -30 °C and indicates that most nitrate is in the liquid phase in the case of Chu and Anastasio. In the liquid phase nitrate is exposed to surrounding water molecules and a strong cage effect.[26] Chu and Anastasio argue that nitrate is photolysed in the DI in their experiments. The difference between solid solution, DI and aqueous solution is not resolved in the present study, but it is suggested that whichever domain is the prevalent one has a small quantum yield. Another nitrate domain not present in the Chu and Anastasio study is distinguishable due to its higher quantum yield.

The snow used in this study shows nitrate in multiple domains, while the adsorption of HNO_3 resulted predominantly in photolabile nitrate in the work of Zhu et al. and the freezing of an aqueous solution created mostly buried nitrate in Chu and Anastasio's study. The quantum yields found in these studies are a direct result of the specific preparation method used. Because such artificial conditions are not expected to be met fully in the present study or at Dome C, the quantum yields reported here are not equal to the ones reported by the other groups. Instead the quantum yield is always larger than the one by Chu and Anastasio and always smaller than the one by Zhu et al.

Experimental results show the significant role of secondary chemistry in nitrate snow photochemistry. However, the quantum yield does not depend on light intensity alone, rejecting the first hypothesis in the introduction. Instead secondary chemistry has to be viewed in the context of the domain of nitrate snow photochemistry which is consistent with the second hypothesis. Experimental results support to attribute the two literature values of the quantum yield[15,16] to the photolysis of different nitrate pools.

E. Application to UV exposures at Dome C

Figure 10 shows the quantum yields as a function of Antarctic sunny day equivalents for all experiments and shows different snow batches with different symbols. In this visualization, the depth and time dependence of Φ^* is a function of one single variable which is equivalent to UV exposure. An exponential fit describes the decline in the quantum yield well, cf. Table II. The change in quantum yield suggests that after exposure to enough photons all photolabile nitrate has been photolysed and the pool of buried nitrate becomes more prominent, making secondary reaction pathways more important.

As indicated by the fitting curves in Figure 10, the two different batches of snow require different lengths of time before the lower limit of the quantum yield is reached. While the quantum yield levels off over the course of months in the 2009 snow, it only needs about 2-3 weeks in the 2011 (wind-blown) snow to bleach the photoactive nitrate. In the terminology used in this study, this indicates that the 2011 snow has a larger fraction of buried nitrate than the 2009 batch. The local domain of nitrate might be influenced by the much higher chloride concentrations in the 2011 wind blown snow than in the 2009 batch, cf. Table I.[46]

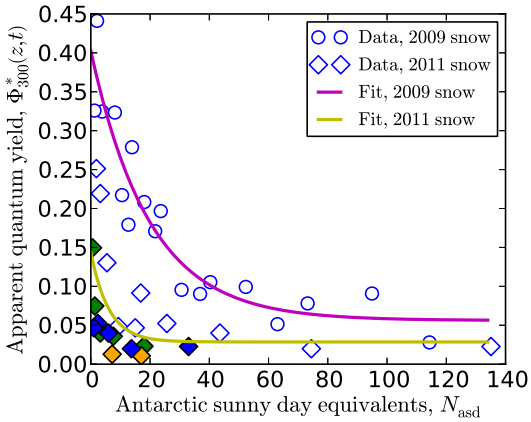

Figure 10. The apparent quantum yield, $\Phi^*_{300}(z,t)$, as a function of Antarctic sunny day equivalents, N_{asd}. Same data as in Figure 9 with colored diamonds for data from experiments 42 (green), 43 (orange) and 45 (blue). Antarctic sunny day equivalents provide a metric of UV exposure to relate the findings of this study to ambient measurements ($N_{asd} = 1$ corresponds roughly to the number of photons absorbed by nitrate in one sunny day in Dome C). The exponential nature of the fit was chosen arbitrarily.

Table II. Determined values and parametrization of the nitrate photolysis quantum yield in snow, $\Phi^*_{NO_3^-}$.

Data	min (N_{asd})	max (N_{asd})	mean	p_0, p_1, p_2, p_3 [a]
2009	0.03 (114)	0.44 (2)	0.18	0.06, 3.11, -43.40, 19.77
2011	0.01 (17)	0.25 (2)	0.07	0.03, 9.99, -27.12, 6.08
all	0.01 (17)	0.44 (2)	0.12	0.05, 23.78, -114.28, 22.15

[a] Fitting function: $p_0 + p_1 \exp\left(-\left(x - p_2\right)/p_3\right)$.

F. Nitrate concentrations and NO_x production at Dome C

All quantum yields found in the present study are larger than the ones used typically in studies which estimate NO_x emission out of the snow pack. If no other chemical or physical processes are assumed to play a role in the snowpack the modeled values of J and predicted NO_x fluxes will significantly increase with the larger quantum yields.

Nitrate concentrations in snow measured in 2007 at Dome C[11] showed concentrations of 330 ng/g in the top layer decreasing down to 30 ng/g at 50 cm depth in snow. The concentration profile is very steep in the first 5 cm after which only 50 ng/g of nitrate is left. There is light down to several tens of cm at Dome C[19] and the nitrate

left at such depths can be assumed to be buried, associated with smaller values of Φ^*. Nitrate is replenished at the top by fresh snow layers and by dry-deposited nitrate, both of which can be assumed to be rather photolabile and therefore to be associated with large quantum yields.

Frey et al. under-predicted nighttime NO_x emissions in austral summer at Dome C by a factor of $\sim 3-4$.[13] The ratio of NO_x fluxes at day over those at night was predicted to be 9 while only a ratio of 2.5 was observed. While it is always bright in Antarctica in austral summer, larger zenith angles reduce the actinic flux deeper in the snow at nighttime. With only the top layers illuminated a higher quantum yield can be associated with night. During daytime light is also present in deeper layers of the snow where only buried nitrate is left to photolyse. Using the largest quantum yield (0.44) for nighttime conditions and the average of largest and smallest quantum yields (0.23) for daytime conditions reduces the day/night NO_x flux ratio to 4.6 and decreases the discrepancy between model and observation. However, the actual fluxes are predicted to increase by a factor of 237 (122) during night (day). Besides the quantum yield, Frey et al. mention the deposition of NO_x photoproducts within the snowpack as one of the main uncertainties in their model. Such a process reduces NO_x fluxes above the snow pack and needs further investigation in order to be parametrized and included in models.

VI. CONCLUSIONS

The photolysis of nitrate was investigated using natural snow in a temperature controlled chamber. The experiments show no desorption of nitrate, while providing a constant gas flow to prevent the deposition of recombined gas-phase products. Two batches of snow, sampled at Dome C, Antarctica, were used. They ensure similar microphysical locations of nitrate in the experiment and field (neglecting effects of transport and storage). Both the actinic flux and the nitrate concentration were measured inside the snow to calculate an apparent quantum yield, Φ^*, which takes secondary chemistry and the photochemical domain into account. The derived values lie between 0.44 and 0.01 – well within the range of those reported previously (0.6 by Zhu et al.[16] and 0.0019 by Chu and Anastasio[15]).

The decrease of the quantum yield with UV exposure is discussed here as a superposition of two domains of nitrate snow photochemistry: photolabile and buried nitrate. It is suggested that the very different quantum yields found in the literature can be viewed as limiting values of photolysis of photolabile nitrate (large Φ) and the photolysis of buried nitrate (small Φ). Photolabile nitrate might correspond to what other authors called surface/adsorbed nitrate and gives rise to a higher quantum yield because reaction products can leave the snow easily. The behavior of buried nitrate might resemble that of nitrate in aqueous solution, bulk ice or the DI. Here the escape of products is inhibited by the cage effect and an enhanced role of secondary (e.g. recombination) chemistry. Buried nitrate is less sensitive to any flow present and results in a much lower quantum yield.

Nitrate concentrations in snow and the actinic flux were measured in field and modeling studies.[19,47] Such studies often assume a single, one-directional photolysis reaction of nitrate with a constant quantum yield in order to predict NO_x emissions out of the snow. They therefore ignore secondary chemistry and the different active domains of nitrate. This study suggests that the commonly used quantum yield is insufficient in reproducing this complex mechanism. The Antarctic sunny day equivalent, N_{asd}, metric was introduced for inter comparison of laboratory and field studies. The results of this study help to decrease the difference between modeled night and daytime NO_x emissions but lead to an over prediction of NO_x fluxes.

The companion paper discusses the stable oxygen and nitrogen isotope ratios of nitrate of the same samples as in this study. By using snow from Dome C, both papers provide the input needed for a refined model to reproduce isotopic data measured in Dome C ice cores.

ACKNOWLEDGMENTS

SSA measurements were performed together with Florent Domine, LGGE, now at Takuvik Joint International Laboratory, Université Laval (Canada) and Samuel Morin, Météo-France/CNRS, CNRM-GAME, Centre d'Etudes de la Neige / Snow Research Center. The authors thank Julia Lee-Taylor for her assistance with the TUV model. The Agence Nationale de la Recherche (ANR) is gratefully acknowledged for its financial support through the OPALE project (Contract NT09-451281). LEFE-CHAT, a scientific program of the Institut National des Sciences de l'Univers (INSU/CNRS), provided partial funding for this study. IPEV is acknowledged for providing access to Concordia station through funding the SUNITEDC program (1011). This work has been supported by a grant from Labex OSUG@2020 (Investissements davenir ANR10 LABX56). The authors also thank IntraMIF and the University of Copenhagen for supporting this research. The research has received funding from the European Community's Seventh Framework Programme (FP7/2007-2013) under grant agreement number 237890.

Appendix: Detailed reaction mechanism

The complete reaction mechanism of nitrate photolysis as shown in Figure 1 is described here. The main excitation in ambient environments is

$$NO_3^- + h\nu\,(\lambda > 260\,\mathrm{nm}) \rightarrow \left[NO_3^-\right]^{n\pi^*} \qquad (A.1)$$

The product is an excited state of the nitrate ion resulting from an $\pi^* \leftarrow$ n transition, abbreviated as nπ^*, Ref. 48. The square brackets denote a compound in a solvent cage. The excited nπ^* nitrate can undergo several reaction pathways, one of them being the back reaction which is promoted by the solvent cage

$$\left[NO_3^-\right]^{n\pi^*} \rightarrow NO_3^- \tag{A.2}$$

The main forward reaction gives NO_2:

$$\left[NO_3^-\right]^{n\pi^*} \xrightarrow{H^+} NO_2 + OH \tag{A.3}$$

Another forward reaction is less likely (1 out of 9, Ref. 49) but forms the important nitrite ion:

$$\left[NO_3^-\right]^{n\pi^*} \rightarrow NO_2^- + O \tag{A.4}$$

Secondary chemistry (thin lines in Figure 1) is described next, starting with nitrite photolysis

$$NO_2^- + h\nu \rightarrow NO + O^- \tag{A.5}$$

and nitrite protonation giving HONO ($pK_a = 3.2$)

$$NO_2^- + H^+ \rightarrow HONO \tag{A.6}$$

The O^- product from reaction A.5 readily forms the OH radical ($pK_a = 11.9$), while the NO product can leave the system as a gas or undergo further reaction, such as reaction with OH:

$$NO + OH \rightarrow HONO \tag{A.7}$$

NO_2 may undergo additional reactions:

$$2\ NO_2 + H_2O \rightarrow NO_2^- + NO_3^- + 2\ H^+ \tag{A.8}$$

with back reaction

$$NO_2^- + OH \rightarrow NO_2 + OH^- \tag{A.9}$$

Another way to form HONO is:

$$NO_2 + NO + H_2O \rightarrow 2\ HONO \tag{A.10}$$

And finally another way to reform nitrate:

$$NO_2^- + OH \rightarrow HOONO \rightarrow NO_3^- + H^+ \tag{A.11}$$

Secondary chemistry as in reactions A.5 - A.11 might depend on light intensity, as these reactions require two photoproducts to react with each other. These reactions may play a larger role in the case of trapped compounds, e.g. after long photolysis times when the photolabile nitrate has been removed. The described secondary chemistry may reform nitrate and is indicated by the A and B terms in Figure 1.

Chemical reaction following UV absorbtion by nitrate at wavelengths below 260 nm is indicated in blue in Figure 1. Essentially the same overall pathway as reactions A.1 and A.3 is possible. This pathway is initiated by the following excitation:

$$NO_3^- + h\nu\,(\lambda < 260\,\text{nm}) \rightarrow \left[NO_3^-\right]^{\pi\pi^*} \tag{A.12}$$

Note the different excitation state of the product compound resulting from a $\pi^* \leftarrow \pi$ transition indicated by $\pi\pi^*$. Madsen and coworkers showed that nearly half of the excited nitrate decays into the ground state[48]:

$$\left[NO_3^-\right]^{\pi\pi^*} \rightarrow NO_3^- \tag{A.13}$$

The other half forms peroxynitrite, $ONOO^-$, Ref. 48:

$$\left[NO_3^-\right]^{\pi\pi^*} \rightarrow ONOO^- \tag{A.14}$$

And only a small portion (8%) decays in a third channel:

$$\left[NO_3^-\right]^{\pi\pi^*} \rightarrow (NO + O_2)^- \tag{A.15}$$

Here, the brackets are adopted from Ref. 48 since the negative charge could not be specifically assigned to either of the products. Peroxynitrite, $ONOO^-$, can isomerize back to nitrate or form the same species:

$$ONOO^- \leftrightarrows (NO + O_2)^- \tag{A.16}$$

NO and O_2 are very likely to react further to give NO_2 and nitrite as indicated in the last reaction:

$$(NO + O_2)^- \rightarrow \cdots \rightarrow NO_2 \text{ and } NO_2^- \tag{A.17}$$

NO_2 and nitrite can participate in the cycles (A and B) shown in Figure 1 the same way as if formed via the 300 nm band excitation.

Aqueous phase nitrogen oxide chemistry suggests[31] that all nitrate photolysed around 200 nm reforms nitrate. This mechanism does not hold in the case of snow and a quantum yield of ca. 1 %, cf. Figure 9, suggests that a small fraction of peroxynitrite, $ONOO^-$, does not reform nitrate. Madsen et al. give a limit of 8 ± 3 % for the primary quantum yield to form $(NO{+}O_2)^-$ but note that this value may act as an upper limit since it does not include secondary reformation of nitrate.[48] Accordingly, their result is in agreement with the quantum yield determined in this study.

REFERENCES

[1] J. H. Seinfeld and S. N. Pandis, *Atmospheric Chemistry and Physics: from Air Pollution to Climate Change* (Wiley, 2006).

[2] J. N. Galloway, F. J. Dentener, D. G. Capone, E. W. Boyer, R. W. Howarth, S. P. Seitzinger, G. P. Asner, C. C. Cleveland, P. A. Green, and E. A. Holland, Biogeochemistry **70** (2004), 10.1007/s10533-004-0370-0.

[3] A. R. Ravishankara, J. S. Daniel, and R. W. Portmann, Science **326** (2009), 10.1126/science.1176985.

[4] J. E. Dibb, R. W. Talbot, J. W. Munger, D. J. Jacob, and S.-M. Fan, J. Geophys. Res. **103** (1998), 10.1029/97JD03132.

[5] M. G. Hastings, E. J. Steig, and D. M. Sigman, J. Geophys. Res. **109**, D20306 (2004).

[6]J. N. Galloway, A. R. Townsend, J. W. Erisman, M. Bekunda, Z. Cai, J. R. Freney, L. A. Martinelli, S. P. Seitzinger, and M. A. Sutton, Science **320** (2008), 10.1126/science.1136674.
[7]D. L. Fibiger, M. G. Hastings, J. E. Dibb, and L. G. Huey, Geophysical Research Letters **40**, 34843489 (2013).
[8]P. Wagnon, R. J. Delmas, and M. Legrand, Journal of Geophysical Research **104** (1999), 10.1029/98JD02855.
[9]R. Roethlisberger, M. A. Hutterli, S. Sommer, E. W. Wolff, and R. Mulvaney, J. Geophys. Res. **105** (2000), 10.1029/2000JD900264.
[10]R. Roethlisberger, M. A. Hutterli, E. W. Wolff, R. Mulvaney, H. Fischer, M. Bigler, K. Goto-Azuma, M. E. Hansson, U. Ruth, M. L. Siggaard-Andersen, and J. P. Steffensen, Annals of Glaciology **35** (2002), 10.3189/172756402781817220.
[11]M. M. Frey, J. Savarino, S. Morin, J. Erbland, and J. M. F. Martins, Atmos. Chem. Phys. **9** (2009), 10.5194/acp-9-8681-2009.
[12]R. E. Honrath, Y. Lu, M. C. Peterson, J. E. Dibb, M. A. Arsenault, N. J. Cullen, and K. Steffen, Atmospheric Environment **36** (2002), 16/S1352-2310(02)00132-2.
[13]M. M. Frey, N. Brough, J. L. France, P. S. Anderson, O. Traulle, M. D. King, A. E. Jones, E. W. Wolff, and J. Savarino, Atmos. Chem. Phys. **13**, 3045 (2013).
[14]R. E. Honrath, S. Guo, M. C. Peterson, M. P. Dziobak, J. E. Dibb, and M. A. Arsenault, J. Geophys. Res. **105** (2000), 10.1029/2000JD900361.
[15]L. Chu and C. Anastasio, The Journal of Physical Chemistry A **107** (2003), 10.1021/jp0349132.
[16]C. Zhu, B. Xiang, L. T. Chu, and L. Zhu, The Journal of Physical Chemistry A **114** (2010), 10.1021/jp909867a, PMID: 20121260.
[17]T. Bartels-Rausch, H.-W. Jacobi, T. F. Kahan, J. L. Thomas, E. S. Thomson, J. P. D. Abbatt, M. Ammann, J. R. Blackford, H. Bluhm, C. Boxe, F. Domine, M. M. Frey, I. Gladich, M. I. Guzmn, D. Heger, T. Huthwelker, P. Kln, W. F. Kuhs, M. H. Kuo, S. Maus, S. G. Moussa, V. F. McNeill, J. T. Newberg, J. B. C. Pettersson, M. Roeselov, and J. R. Sodeau, Atmospheric Chemistry and Physics Discussions **12** (2012), 10.5194/acpd-12-30409-2012.
[18]D. D. Davis, J. Seelig, G. Huey, J. Crawford, G. Chen, Y. Wang, M. Buhr, D. Helmig, W. Neff, D. Blake, R. Arimoto, and F. Eisele, Atmospheric Environment **42** (2008), 10.1016/j.atmosenv.2007.07.039.
[19]J. L. France, M. D. King, M. M. Frey, J. Erbland, G. Picard, S. Preunkert, A. MacArthur, and J. Savarino, Atmos. Chem. Phys. **11** (2011), 10.5194/acp-11-9787-2011.
[20]J. L. Thomas, J. Stutz, B. Lefer, L. G. Huey, K. Toyota, J. E. Dibb, and R. von Glasow, Atmos. Chem. Phys. **11** (2011), 10.5194/acp-11-4899-2011.
[21]F. Domine and P. B. Shepson, Science **297** (2002), 10.1126/science.1074610.
[22]F. Domine, M. Albert, T. Huthwelker, H. W. Jacobi, A. A. Kokhanovsky, M. Lehning, G. Picard, and W. R. Simpson, Atmospheric Chemistry & Physics **8**, 171 (2008).
[23]R. Ruzicka, L. Barakova, and P. Klan, J. Phys. Chem. B **109** (2005), 10.1021/jp044661k.
[24]R. Kurkova, D. Ray, D. Nachtigallova, and P. Klan, Environ. Sci. Technol. **45** (2011), 10.1021/es104095g.
[25]V. F. McNeill, A. M. Grannas, J. P. D. Abbatt, M. Ammann, P. Ariya, T. Bartels-Rausch, F. Domine, D. J. Donaldson, M. I. Guzman, D. Heger, T. F. Kahan, P. Kln, S. Masclin, C. Toubin, and D. Voisin, Atmos. Chem. Phys. **12** (2012), 10.5194/acp-12-9653-2012.
[26]P. Nissenson, D. Dabdub, R. Das, V. Maurino, C. Minero, and D. Vione, Atmospheric Environment **44** (2010), 10.1016/j.atmosenv.2010.08.035.
[27]Y. Dubowski, A. J. Colussi, and M. R. Hoffmann, The Journal of Physical Chemistry A **105** (2001), 10.1021/jp0042009.
[28]H. Beine and C. Anastasio, Journal of Geophysical Research: Atmospheres **116** (2011), 10.1029/2010JD015531.
[29]A. M. Baergen and D. J. Donaldson, Environmental Science & Technology **47** (2013), 10.1021/es3037862.
[30]T. Blunier, G. L. Floch, H. W. Jacobi, and E. Quansah, Geophysical research letters **32** (2005), 10.1029/2005GL023011.
[31]J. Mack and J. R. Bolton, Journal of Photochemistry and Photobiology A: Chemistry **128** (1999), 16/S1010-6030(99)00155-0.
[32]E. S. N. Cotter, A. E. Jones, E. W. Wolff, and S. J. B. Bauguitte, Journal of Geophysical Research (Atmospheres) **108** (2003), 10.1029/2002JD002602.
[33]H.-W. Jacobi and B. Hilker, Journal of Photochemistry and Photobiology A: Chemistry **185** (2007), 10.1016/j.jphotochem.2006.06.039.
[34]C. Boxe and A. Saiz-Lopez, Polar Science **3** (2009), 10.1016/j.polar.2009.01.001.
[35]J. Bock and H.-W. Jacobi, The Journal of Physical Chemistry A **114** (2010), 10.1021/jp909205e.
[36]J. Lee-Taylor and S. Madronich, J. Geophys. Res. **107** (2002), 10.1029/2002JD002084.
[37]J. Erbland, W. C. Vicars, J. Savarino, S. Morin, M. M. Frey, D. Frosini, E. Vince, and J. M. F. Martins, Atmos. Chem. Phys. **13** (2013), 10.5194/acp-13-6403-2013.
[38]H.-W. Jacobi, T. Annor, and E. Quansah, Journal of Photochemistry and Photobiology A: Chemistry **179** (2006), 10.1016/j.jphotochem.2005.09.001.
[39]T. A. Berhanu, C. Meusinger, J. Erbland, J. Savarino, and M. S. Johnson, in prep. (2013).
[40]J. C. Gallet, F. Domine, C. S. Zender, and G. Picard, The Cryosphere **3** (2009), 10.5194/tc-3-167-2009.
[41]F. Domine, R. Salvatori, L. Legagneux, R. Salzano, M. Fily, and R. Casacchia, Cold Regions Science and Technology **46** (2006), 10.1016/j.coldregions.2006.06.002.
[42]W. R. Simpson, M. D. King, H. J. Beine, R. E. Honrath, and X. Zhou, Atmospheric Environment **36** (2002), 10.1016/S1352-2310(02)00124-3.
[43]M. D. King and W. R. Simpson, Journal of Geophysical Research **106** (2001), 1029/2001JD900006.
[44]C. F. Bohren, American Journal of Physics **55** (1987), 10.1119/1.15109.
[45]E. Thibert and F. Domine, The Journal of Physical Chemistry B **102** (1998), 10.1021/jp980569a.
[46]H. J. Beine, A. Amoroso, F. Domin, M. D. King, M. Nardino, A. Ianniello, and J. L. France, Atmos. Chem. Phys. **6** (2006), 10.5194/acp-6-2569-2006.
[47]J. France and M. King, Journal of Glaciology **58** (2012), 10.3189/2012JoG11J227.
[48]D. Madsen, J. Larsen, S. K. Jensen, S. R. Keiding, and J. Thgersen, J. Am. Chem. Soc. **125** (2003), 10.1021/ja030135f.
[49]P. Warneck and C. Wurzinger, The Journal of Physical Chemistry **92** (1988), 10.1021/j100333a022.